UNIVERSITÀ
DEGLI STUDI
DI PADOVA

Sede Amministrativa: Università degli Studi di Padova

Dipartimento di Tecnica e Gestione dei Sistemi Industriali

CORSO DI DOTTORATO DI RICERCA IN: Ingegneria Meccatronica e dell'Innovazione Meccanica del Prodotto

CICLO XXXII

BIOACTIVE SPHENE COATINGS FOR DENTAL IMPLANT APPLICATIONS

Coordinatore: Ch.ma Prof.ssa Daria Battini

Supervisore: Ch.ma Prof.ssa Lisa Biasetto

Dottoranda: Giulia Brunello

Contents:

Abstract

Over the last few decades, due to the aging of the population, prolonged life expectancy and increased demand for esthetic dental procedures, there is an increasing request for dental implant treatment for the replacement of missing teeth. In addition, in presence of an inadequate amount of bone for implant positioning, bone regeneration procedures are required. Among various strategies, which are currently being investigated, synthetic biocompatible three-dimensional structures, known as "scaffolds", produced using different additive manufacturing technologies are attracting growing attention for use in bone tissue regeneration, as personalized bone scaffolds can be designed to fit specific bone defects.

Successful use of bioactive ceramics, as coating materials for dental implants as well as bone substitutes, has been reported. In particular, sintered hydroxyapatite (HA) has been extensively employed in clinical dental practice. However, its low fracture toughness and the occurrence of delamination at the interface with titanium substrates have significantly limited the scope of clinical applications. More recently, a new category of bioactive ceramics, i.e. silicate-based ceramics, has received great attention, due to their remarkable bioactivity and good mechanical properties.

The primary aim of the current project is to develop and test *in vitro* and *in vivo* a specific bioactive silicate-based ceramic, sphene ($CaTiSiO_5$), as coating material for dental implants. Sphene coatings will be prepared using a preceramic polymer containing nanosized active fillers as precursors for the formation of the desired ceramic phase. Coating will be applied by airbrushing, and the samples will undergo heat treatment, in order to transform the precursors into a ceramic coating. Once the sphene-coated implants will be prepared, they will be fully characterized in terms of microstructure analysis, crystalline phase assemblage, physicochemical properties, effect on mesenchymal stem cell behavior *in vitro*, and, finally, osseointegration in a rat model.

Secondary aim of this project consists in the production and characterization of sphene ceramic scaffolds to be utilized as bone substitutes for bone tissue regeneration. These scaffolds will be fabricated by direct ink writing using a preceramic polymer and nano-sized active fillers. The samples will be then characterized, and a particular attention will be given to investigating *in vitro* cytocompatibility and osteoconductive properties, prior to *in vivo* study using rat critical size calvarial defect model.

Chapter 1

Introduction

Abstract

The overall success and long-term life of the medical implants are decisively based on the convenient osseointegration at the hosting tissue-implant interface. Therefore, various surface modifications and different coating approaches have been utilized to the implants to enhance the bone formation and speed up the interaction with the surrounding hosting tissues, thereby enabling the successful fixation of implants.

The first part of this chapter is focused on an overview on bioactive glasses and silicate-based ceramics as coating materials for orthopedic and dental implants. We will briefly present the main metallic implants and discuss their biocompatibility and osseointegration ability depending on their chemical and mechanical properties. In addition, as the main goal of this review, we explore the main properties of bioactive glasses and silica-based ceramics that are used as implant coating materials. The current review provides an overview of these bioactive coatings, with a particular emphasis on deposition methods, coating adhesion to the substrates and apatite formation ability tested by immersion in Simulated Body Fluid (*SBF*). *In vitro* and *in vivo* performances in terms of biocompatibility, biodegradability and improved osseointegration are also examined.

As sphene ($CaTiSiO_5$) represents the object of this thesis, in the second part of this chapter there will be a brief introduction on sphene ceramic, as proposed coating material for improving implant performances.

Keywords: bioactive glass; bioactive silicate ceramic; coating; implants; osseointegration, sphene

1.1. Bioactive glass and silicate-based ceramic coatings on metallic implants: open challenge or outdated topic?

1.1.1. Introduction

Even though ceramics represent the class of materials that are more similar to bone in terms of composition, their intrinsic brittleness makes them not reliable for load bearing applications. For this reason, metallic materials are commonly used for the production of orthopedic and dental implants, thanks to their intrinsic ductility. However, these materials have shown many disadvantages, including the release of toxic ions and the lack of integration at the interface between the bone and the biomaterial [1–3].

Titanium (Ti) and titanium alloys are widely used for the production of both orthopedic and dental implants because of their desirable mechanical features, such as relatively low modulus and good fatigue strength, their corrosion resistance and biocompatibility [4]. The α commercially pure Ti (CpTi) and the α-β Ti-6Al-4V alloy remain the most widely used materials for the intended purposes. Despite the use of stainless steel, in particular of AISI 316L (316L SS), remains widespread due to good mechanical properties and low cost, there are many concerns regarding the release of metal ions from the implant because of corrosion and wear [5]. Compared to stainless steel and cobalt-chromium alloys, Ti and its alloys have shown superior mechanical and biological properties [6–8].

Beside non-resorbable metals, also magnesium (Mg) and Mg alloys are being employed in orthopedics [9–11], but due to their rapid biodegradability [12], they are not good candidates for dental implant applications.

Osseointegration has been considered as a key factor for the long-term success of biomedical implants. In order to obtain improved osseointegration and to shorten the time for osseointegration, enhancing implant stability in the early phases, several implant surface modifications have been explored [13–14].

For instance, the surface roughness has been demonstrated to affect the bone-implant interactions [7], and for this reason several studies have attempted to develop modified surfaces by means of physical and chemical approaches (e.g. sandblasting, acid etching, combination of blasting and etching, electrochemical oxidation and laser treatments).

Coating materials can also be employed to further modify the implant surfaces, in order to improve the performances of metallic implants. Material surface features play a

crucial role in the chemical and biological interaction with the surrounding bone tissue, while the mechanical properties are strongly determined by the bulk of the implant [7]. Poor mechanical properties of monolithic bioceramics and bioactive glasses limit their use in load-bearing applications (see **Figure 1a**). As a consequence, the materials of choice still remain metallic alloys, whose biological properties can be improved by means of coatings (e.g. bioactivity, reduction of corrosion and toxic ion release) [1,9, 15–17].

Metallic biomaterials currently used in orthopedics have a higher elastic modulus (in the range between 44 and 205 GPa) as compared to that of natural bone (17-22 GPa) (see **Figure 1b**), resulting in stress shielding effect that leads to a reduced stimulation of bone formation and remodeling and, subsequently, to the loosening of the implants [18–21]. It means that the implants "shield" the surrounding bone from experiencing adequate loading, which is required for bone growth stimulation, and when the stress level decreases too much, bone resorption may occur. Low elastic modulus, better matching that of bone, reduces the stress-shielding effect, thus favoring bone formation and improving implant osseointegration. The elastic modulus of magnesium is closer to that of natural bone, but its rapid degradability hampers its clinical application [9]. The long-term behavior of implants represents one of the most important concerns, where fatigue fracture is one of the main causes of failure. Indeed, it was recently observed that the bone-implant difference of elastic modulus, not only affects the bone to implant penetration, but also the long-term behavior of the implant itself: the closer the elastic moduli are, the smoother is the bone- to implant stress transmission, thus improving the long-term mechanical behavior of the implant itself [22]. Titanium alloys, such as α-β alloys show an improved fatigue behavior, compared to pure CpTi, but the dissolution of alloys elements may be toxic for the growing bone [23]. For this reason, a novel generation of β-stabilized alloys have been developed (such as Ti-29Nb-13Ta-4.6Zr) showing a Young's module close to that of bone and improved corrosion resistance [24]. Implant geometry can prevent stress-shielding, as described, for instance, in a prospective study evaluating total hip arthroplasties, in which a modified femoral stem design led to a significant improvement in stress-shielding in the proximal femoral bone [25]. Apart from implant macro design and from the development of a porous structure, decreasing the overall stiffness of the prostheses [26], a way to mitigate the effect of stress-shielding consists in improving bone-implant bonding using bioactive coating materials [27, 28].

While the stress shielding effect has been deeply investigated and recognized in the field of long bone researched, its role in implant dentistry is still controversial [29, 30].

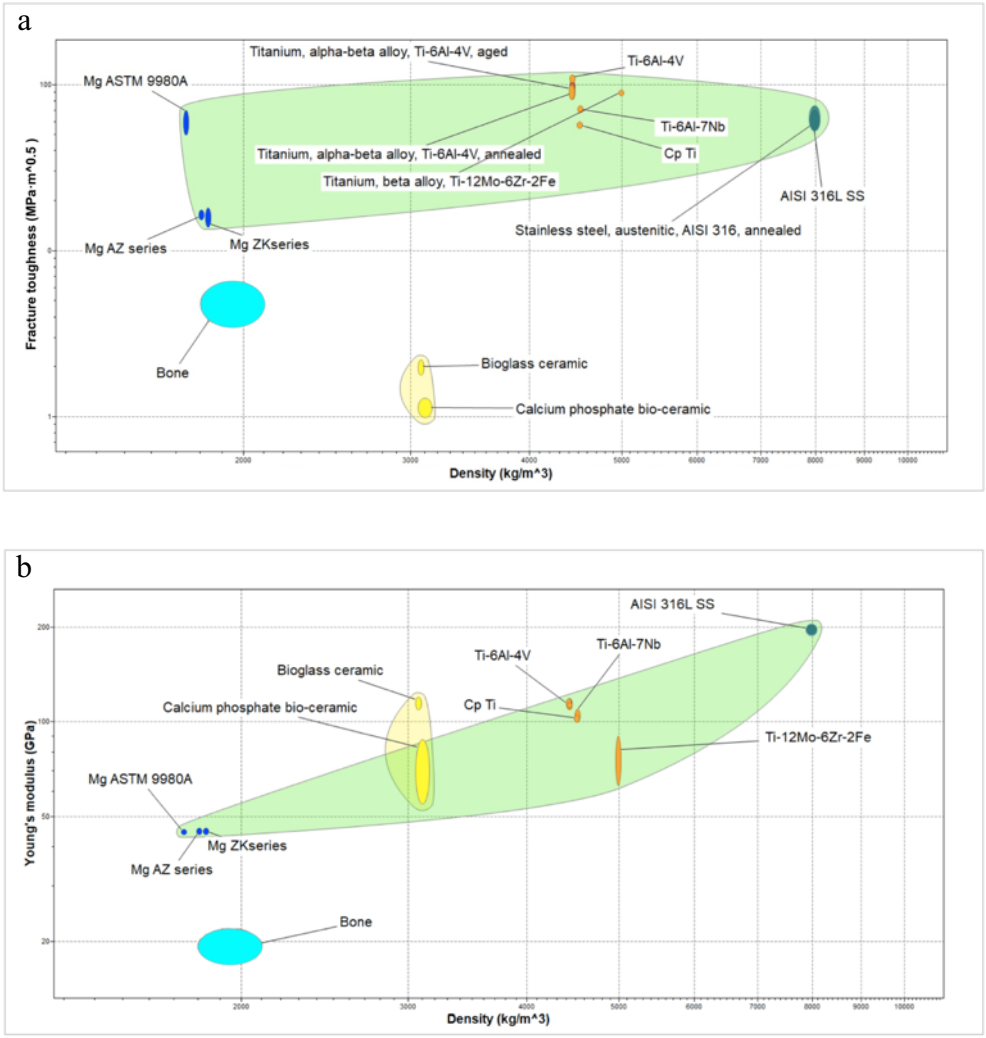

Figure 1 Ashby's maps of: (a) fracture toughness and density; (b) elastic modulus and density of bone, coating materials and most common metallic materials used in orthopedics and implant dentistry. Data elaborated using CES EduPack™ 2018.

Among biomaterials used for coating metallic implants, hydroxyapatite (HA) is one of the most widely used and documented [31,32]. It has been successfully applied, showing promising results for osseointegration, thanks to its resemblance to the inorganic compound of natural bone tissue [33,34]. Unfortunately, early experience with HA coatings revealed frequent delamination of the HA coatings from the substrates and inadequate chemical stability, thus compromising the long-term success of the implants [7,35,36]. Over the last few years, to overcome the limitations of HA coatings, many attempts have been performed to develop chemical stable coatings showing good

adhesion to the substrates and high bioactivity. It has been demonstrated that ceramic materials and bioactive glasses can stimulate bone formation both *in vitro* and *in vivo* [1,15,31,32,37–39]. Moreover, it has been reported the use of coating materials as delivery systems, incorporating antibiotics and antimicrobial agents or bone stimulating molecules, such as growth factors (GFs) [40–43].

The goal of the present PhD thesis is aiming at providing a literature review of most relevant and recent findings on the topic of bioactive glasses and bioactive silicate ceramics as coating materials for metallic biomedical implants, in order to clarify whether the coating approach represents an outdated method or an open challenge for improving implant performances. In this review, the main mechanical features will be introduced, with particular focus on coating roughness, thickness and adhesion to the substrates. Moreover, coating behavior *in vitro* and *in vivo* will be discussed.

1.1.2. Microstructural Features of Metallic Substrates

The material features of commonly used metallic substrates for implant applications will be discussed in the following paragraph. The main mechanical (Young's modulus; Vickers hardness), thermal (coefficient of thermal expansion; melting temperature) and physical (density) properties of these metallic materials are summarized in **Table 1** and compared to those of bone tissue.

Table 1. Different metallic materials and their mechanical, thermal and physical properties in comparison to bone. Data from CES EduPack™ 2018.

Material	E [GPa]	Hv [GPa]	CTE [$10^{-6}K^{-1}$]	Tm [°C]	ρ [Kg/m^3]
CpTi	100 – 105	1.520 – 1.618	8.5 – 9.3	1670	4510 – 4520
Ti-6Al-4V	113 – 115	3.256 – 3.589*	8.7 – 9.1*	1610 –1660	4430
Ti-6Al-7Nb	100 – 110	2.648 – 2.844*	8 – 9.8	1530 – 1590	4510 – 4530
Ti-12Mo-6Zr-2Fe	63.1 – 90.1	3.207 – 3.383*	8.7 – 8.89	1540 – 1620*	4980 – 5000
316L SS	190 – 205	1.667 – 2.158	15 – 18	1380 – 1400	7870 – 8070
Mg	44 – 45.5	0.245 – 0.490	25.5 – 26.5	642 – 650	1730 – 1750
AZ91 Mg alloy	44 – 46	0.588 – 0.598	26 – 26.3	482 – 602	1800 – 1810
ZK61 Mg alloy	44 – 46	0.824 – 0.892*	25 – 26*	470 – 530*	1803 – 1840
Bone	17 – 22	0.196 – 0.392*	10 – 30*	110 – 130*§	1800 – 2100

* estimated values; § Glass Transition Temperature; E = Modulus of Elasticity; Hv = Hardness, Vickers; CTE = Coefficient of Linear Thermal Expansion; Tm = Melting Temperature; $\boldsymbol{\rho}$ = Density.

1.1.2.1 Ti and Ti alloys

Ti and some of its alloys, in particular Ti-6Al-4V, are largely used as implant materials, both in orthopaedics and in dentistry, due to their excellent biocompatibility, high corrosion resistance, and good mechanical properties [44–46]. As compared to CpTi, the α-β Ti-6Al-4V alloy exhibits higher strength, maintaining similar biocompatibility [47]. Main mechanical and thermal properties of Ti and Ti-6Al-4V are summarized in the **Table 1**.

Ti alloys can be classified based on the presence and proportion of α- and β-phases. Alloying elements such as aluminum (Al), carbon (C), oxygen (O) and nitrogen (N) are commonly used to stabilize the α-phase, while elements such as molybdenum (Mo), vanadium (V), niobium (Nb), iron (Fe), manganese (Mn) and chromium (Cr) are considered β-stabilizers [4,48].

Despite their favorable performances for hard tissue replacements, there are still some concerns with the use of many Ti alloys, due to the release of cytotoxic or allergic elements, such as Al [49,50]. This release could be caused by corrosion processes, wear or synergistic combination of both, known as tribocorrosion [49,51]. Elements released into the surrounding tissues may affect peri-implant cell behavior and represent a potential risk for the long-term success of the implants [49,52].

Furthermore, Ti and its alloys seem to insufficiently osseointegrated at the early stage after placement due to their moderate osteoconductivity [53]. As highlighted in a recent review on modern implant surfaces for dental applications [46], there is a high demand for new surfaces able to induce a faster osseointegration and to increase the predictability and success rate of implant treatments, also in areas with low bone quality or in systemically compromised patients, in which bone healing might be impaired. To this aim, several surface modifications of Ti and Ti-alloy implants have been proposed, by means of subtractive processes, additive processes or a combination of both [44,46]. Subtractive treatments include grinding, polishing, blasting, acid-etching and laser texturing. While, additive surface treatments mainly consist in coating depositions by means of different methods, such as plasma-spraying or electrophoretic deposition. Finally, biofunctionalization of surfaces, with peptides, growth factors or drugs, has been

proposed as an alternative promising strategy for improving the implant osseointegration [54–56].

1.1.2.2 Stainless Steel

Stainless steel implants have been widely employed in orthopedics, as temporary fixation devices as well as fixed implants for joint replacements [5]. As compared to other biomaterials, such as Ti, stainless steels are considered inferior in terms of biocompatibility and resistance to corrosion. However, stainless steel is cheaper and suitable for the fabrication of orthopedic implants. For economic issues, there is still a high demand for stainless steel implants, in particular in developing countries, where an affordable healthcare has to be guaranteed to the population [57].

Stainless steels are generally well tolerated by the human body, due to the development of an outer chromium-rich oxide passive layer on the surface. Stainless steels present three main microstructures: ferritic, austenitic and martensitic. On one hand, only ferritic stainless steels do not contain nickel (Ni), whereas only austenitic stainless steels are non-magnetic. Hence, regardless of the presence of Ni, austenitic stainless steels have mainly been used in orthopedics because the absence of ferromagnetism is required. In particular, the most extensively used for biomedical applications is the austenitic stainless steel (AISI 316L, ASTM F-55 and F-138), containing Cr (17–20%), Ni (12–15%), Mo (2–3%) and small quantity of other elements [5,58]. This material, like the other austenitic stainless steels, is characterized by a face-centered cubic (fcc) structure and satisfactory corrosion resistance. Moreover, it possesses acceptable biocompatibility and good mechanical properties also for load-bearing purposes [5].

The major disadvantage of stainless steels is the high elastic modulus as compared to that of natural bone, which may lead to stress shielding. In addition, there are many concerns about the increased risk of localized and systemic reactions associated with the release of metals into the human body, especially of nickel [59]. For instance, allergic reactions are commonly reported when Ni-containing stainless steel devices are implanted.

In order to overcome the adverse effects associated with the release of nickel, nickel-free austenitic stainless steel has been proposed [60]. Among elements which are used in order to stabilize the austenitic microstructure (i.e. nickel, cobalt, carbon, nitrogen, manganese, and copper), nitrogen seems to be the most promising nickel replacement,

because it is a strong austenite forming element and it also improves the mechanical properties and the corrosion resistance of the steel [5,60,61].

The improvement of implant properties can be achieved either by modifying the chemical composition of the stainless steels, such as eliminating Ni content, or by applying a bioactive coating on the surface [5,57].

Coating materials applied onto stainless steel for biomedical purposes have also been investigated.

Tribological stability and reduced amount of metal debris released from the implants have been documented, when bioactive coatings have been deposited [57,62,63].

1.1.2.3 Mg and Mg alloys

In recent years, there has been an increasing interest in Mg and its alloys as orthopedic implant materials, due to their attractive properties, such as biocompatibility and biodegradability [64–66].

The elastic modulus of Mg and Mg alloys is quite similar to that of natural bone. This prevents the occurrence of the "stress-shielding" phenomenon, which is one of the foremost causes of orthopedic implant failures [64,65].

The biodegradability of Mg and Mg alloys can be considered a favorable characteristic, as a second surgery for the removal of the implant in certain orthopedic applications becomes not necessary [67]. Despite the beneficial properties of Mg and its alloys, their degradation rate is too fast, as compared to new bone formation and remodeling around the implants and may lead to an early loss of the mechanical integrity of the bioresorbable implants [67]. Therefore, the application of these materials is currently limited to non-load bearing conditions in most cases.

Although the release of Mg ions is not related to any severe side effect in the human body [68], the rapid release of hydrogen due to the corrosion of the implant is an important issue during the healing process. When the release of gas is too quick, in fact, the gas cannot be absorbed by the body in time, producing the well-known "balloon effect" [69]. However, even if a considerable percentage of patients experienced subcutaneous gas cavities, most of them had no pain or infections after surgery [70].

Many strategies have been developed in order to control the degradation rate and improve the corrosion resistance of Mg implants, including alloying [71], thermal treatment [72] and coating deposition [11].

Several alloying elements, including Al, calcium (Ca), zinc (Zn), zirconium (Zr), strontium (Sr), Mn, etc., have been employed to enhance the properties of biodegradable Mg implants. Intermetallic phases, resulting from the reaction of alloying elements among each other or with Mg, can be found along the grain boundaries or dissolve within the Mg matrix, modifying the mechanical behavior and the corrosion resistance of the material [71]. The general trend is that alloying elements decrease the corrosion rate. However, it is not possible here to quantify their effect in terms of corrosion resistance, since data in literature are not homogeneous [73–74].

The release of metal ions, commonly used as alloying elements, from Mg-based orthopedic implants may give rise to systemic or localized adverse reactions. For instance, an excess amount of Al, which is a constituent of many alloys used in biomedical devices (e.g. AZ31, AZ91 Mg alloys), may lead to neurological disorders or a decrease in osteoclast viability. However, the low concentration of toxic elements is generally well-tolerated by the body [74].

The deposition of bioactive coatings seems to be the most attractive method to reduce the degradation rate and, in the meantime, to improve the biocompatibility and the medium-term mechanical integrity of the both Mg and Mg alloy implants [66].

1.1.3. Microstructure, Physical Features and Applications of Bioactive Glasses and Silica-Based Bioceramics

1.1.3.1 Bioactive Glasses

The first composition, the so-called 45S5 Bioglass® (in wt%: 45% SiO_2, 24.5% CaO, 24.5% Na_2O, 6.0% P_2O_5), was discovered by Hench in the 60's. It has been in the clinical use since the 80's and it remained the most used bioactive glass [75].

The bioactivity of this material is associated with the ability to induce the formation of an apatite layer on its surface upon immersion in Simulated Body Fluid (SBF) solution. It has been extensively demonstrated that bioactive glasses possess high bioactivity [76,77]. Moreover, bioactive glass-ceramic substrates were found to increase osteoblast differentiation and selection of a mature osteoblastic phenotype *in vitro* [78].

With regard to the clinical applications, 45S5 Bioglass has been successfully introduced in alveolar ridge maintenance [79], middle ear replacement [80] and periodontal surgeries [81,82]. 45S5 Bioglass has been successfully incorporated in

toothpastes as an active repair agent, able to mineralize dentin, thus reducing dental hypersensitivity [83]. It has been also proposed as bone substitute material for the treatment of complex bone defects. However, the low mechanical strength and the high brittleness of porous glass scaffolds have limited their application to repair of non-load-bearing bone defects [84]. Interestingly, in particular for bone tissue regeneration purposes, various attempts have been made to regulate the degradation rate and to improve the mechanical strength of bioactive glasses, by modifying their chemical composition by means of the incorporation of metal oxides (e.g. MgO, ZnO, B_2O_3, Al_2O_3) [85]. Bioactive glasses have also been proposed as coating materials for implant devices. A promising approach for increasing the implant bioactivity consists in the deposition of bioactive glasses on bioinert metallic substrates [86]. This allows, on one side, to improve the biological properties of the metallic implants and, on the other side, to overcome the major drawbacks of the glassy phase, which are their poor mechanical properties and their brittle behavior.

Beside the original 45S5 bioglass, more recently a broad variety of bioactive glasses with different chemical compositions have been developed [87]. They contain SiO_2, Na_2O, CaO, and P_2O_5 in different ratio (**Table 2**). In Finland a bioactive glass, known as S53P4, containing higher percentage of silica as compared to 45S5 bioglass was successfully developed, with encouraging results in the treatment of bone defects [88–90]. Glass compounds containing also other elements have been developed, such as 13-93 glass. Both S53P4 and 13-93 bioactive glasses were tested in a frontal sinus and skull bone defect obliteration model *in vivo*, showing enhanced bone healing as compared to synthetic HA [82,91]. In addition, a faster bone recovery was observed in defects treated with S53P4 than in ones filled with 13-93. This is might be related to the presence of Mg in 13-93 glass, reducing its bioactivity. Other bioactive compounds are based on CaO-SiO_2 combinations, like 70S30C, 58S and 77S bioactive glasses [87,92].

Additionally, in order to improve the mechanical properties of bioactive glasses, a new class of materials, known as bioactive glass-ceramics, was developed starting from several glasses undergoing the precipitation of crystalline phases during heat treatment [93–95].

Table 2. Common bioactive glasses (for example, but not limited) used in medical devices and their composition.

Commercial name/Material	Composition (in wt%)	Composition (in mol%)	References
45S5 Bioglass	45% SiO_2, 24.5% CaO, 24.5% Na_2O, 6.0% P_2O_5	46.1% SiO_2, 26.9% CaO, 24.4% Na_2O, 2.6% P_2O_5	[92,96,97]
S53P4	53% SiO_2, 20% CaO, 23% Na_2O, 4% P_2O_5	53.8% SiO_2, 21.9% CaO, 22.7% Na_2O, 1.7% P_2O_5	[92]
BG_Ca	46.9% SiO_2, 42.3% CaO, 4.7% Na_2O, 6.1% P_2O_5	47.2% SiO_2, 45.6% CaO, 4.6% Na_2O, 2.6% P_2O_5	[98]
CaK	46% SiO_2, 41% CaO, 7% K_2O, 6% P_2O_5	47.2% SiO_2, 45.6% CaO, 4.6% K_2O, 2.6% P_2O_5	[86]
13-93	53% SiO_2, 20% CaO, 6% Na_2O, 4% P_2O_5, 12% K_2O, 5% MgO	54.6% SiO_2, 22.1% CaO, 6% Na_2O, 1.7% P_2O_5, 7.9% K_2O, 7.7% MgO	[92,99]
Sr-Bioglass	41.5% SiO_2, 18.7% CaO, 26.2% Na_2O, 9.7% P_2O_5, 3.9% SrO	44.5% SiO_2, 21.5% CaO, 27.2% Na_2O, 4.4% P_2O_5, 2.4% SrO	[92]
70S30C	71.4% SiO_2, 28.6% CaO	70% SiO_2, 30% CaO	[92]
58 S	58% SiO_2, 33% CaO, 9% P_2O_5	60% SiO_2, 36% CaO, 4% P_2O_5	[87]
77 S	77% SiO_2, 14% CaO, 9% P_2O_5	80% SiO_2, 16% CaO, 4% P_2O_5	[87]

1.1.3.2 Silica-based Ceramics

Bioceramics are commonly used in several applications in medicine, including orthopedics and dentistry [100]. A new family of bioceramics, silica-based ceramics have been afforded a considerable amount of importance as coating materials on the surface of biomedical implants, as well as bone substitutes [101–103].

The main silica-based ceramics used for medical devices are reported in **Table 3**.

There is an increasing evidence that silicon (Si) can promote the new bone formation [104], as confirmed by both *in vitro* and *in vivo* studies. Contrary to conventional calcium phosphate ceramics, such as hydroxyapatite or β-tricalcium phosphate (β-TCP), the presence of Si in the composition of silica-based ceramics contributes to their bioactive properties. Moreover, owing to the wide range of chemical compositions, it is possible to tailor formulations of silica-based ceramics in order to meet specific application requirements, in terms of mechanical properties, bioactivity and degradation rate [101,105–107]. For instance, the incorporation of trace elements, such Mg or Zn, into Ca-Si ceramics has a considerable influence on the mechanical properties of ceramics, both on bending strength and on fracture toughness. In particular, bulk silicate ceramics with $MgO–CaO–SiO_2$ (e.g. akermanite, bredigite, diopside, merwinite) or $ZnO–CaO–SiO_2$ (e.g. hardystonite) ternary oxides presented fracture toughness values in the range of 1.24 – 3.5 $MPam^{1/2}$, higher than those of $CaSiO_3$ and hydroxyapatite (≤ 1 $MPam^{1/2}$) [105].

In addition, it is worth noting that most bioactive glasses and silica-based ceramics possess elastic modulus similar to that of human bone (**Table 2** and **Table 3**), making them good candidates for orthopedic implants.

Table 3. Common silica-based ceramics used in medical devices and their composition, mechanical, thermal and physical properties (dense structure).

System	Materials	Compositions	CTE [$10^{-6}K^{-1}$]	E [GPa]	ρ [Kg/m^3]	Ref.
Binary oxides	Wollastonite	$CaSiO_3$	10 – 13	52	2900	[108–109]
	Dicalcium silicate	Ca_2SiO_4	8.5	10 – 40	3150	[110–111]
	Tricalcium silicate	Ca_3SiO_5	_	24.9 – 36.7	3210	[112–114]
	Dimagnesium silicate	Mg_2SiO_4	_	_	3271	[115]

	Magnesium silicate	$MgSiO_3$	_	_	2600 – 2800	[116]
	Zinc silicate	Zn_2SiO_4	_	_	3300	[116]
	Strontium silicate	$SrSiO_3$	10.9	_	3650	[113,116]
Ternary oxides	Akermanite	$Ca_2MgSi_2O_7$	9.9	42 – 56	2961	[117–119]
	Bredigite	$Ca_7MgSi_4O_{16}$	_	43	3400	[120,121]
	Diopside	$CaMgSi_2O_6$	8.4	170	3200	[122,123]
	Merwinite	$Ca_3MgSi_2O_8$	_	31 – 49	3150 – 3330	[119,124, 125]
	Hardystonite	$Ca_2ZnSi_2O_7$	11.2	37	3392	[118]
	Sphene	$CaTiSiO_5$	6	_	3539	[126,127]
	Baghdadite	$Ca_3ZrSi_2O_9$	_	82 – 120	3480	[128,129]

1.1.4. Deposition Methods and Physical Properties of the Coatings

Bioactive glasses and silica-based ceramics have been investigated as coating materials for both resorbable and non-resorbable metallic substrates, using a variety of synthesis and deposition methods. As superficial features, in particular the roughness and the thickness of the coatings, are of great importance for the characterization of the devices prior to other *in vitro* biological or *in vivo* test, these properties have been also reported in **Table 4**.

Even though the surface roughness-osseointegration relationship is well-known, however, there are still unclear aspects as reported in Wennerberg & Albrektsson [130] regarding implant dentistry. For instance, the key morphological parameters are not standardized, hence, it is tough making comparisons between different studies. In this review, we are comparing the average roughness profile (Ra), as it is the most frequently used parameter in the investigated articles.

Coating thickness has been reported as well, because it strongly affects the dissolution time in body fluids. In addition, when coatings undergo a thermal treatment after deposition, the higher the coating thickness the higher are the induced thermal stresses, with consequences on adhesion strength to the substrate, so as on the mechanical integrity of the coating itself (i.e. cracks initiation) [131].

Even if porosity may be considered a key parameter for *in vitro* performances of the coating, we observed a lack of data in the literature, for this reason these values could not be considered in the present review.

Table 4. Synthesis and deposition methods of bioactive coatings onto metallic substrates and their average roughness and thickness.

		Substrate	Coating material	Synthesis method	Deposition method	Coating Ra [µm]	Average coating thickness [µm]	Ref
Ti-BASED SUBSTRATES	CERAMICS	CpTi	Sphene	Polymer-derived ceramics route	Airbrushing	4.1 – 6.5	50 – 100	[132]
		CpTi	Sphene	Polymer-derived ceramics route	Airbrushing	3.1 – 8.4	133.8	[133]
		CpTi	Sphene	Polymer-derived ceramics route	Airbrushing	0.5 – 1.4	120	[134]
		CpTi	Sphene	Polymer-derived ceramics route	Airbrushing	3.9	–	[37]
		Ti-6Al-4V	Sphene	Solid phase reaction	Plasma-spraying	7.5	–	[135]
			Hardystonite	Solid phase reaction	Plasma-spraying	7.5	–	
		Ti	Sphene	Liquid phase reaction	Micro-arc oxidation	–	≤ 21	[136]
		Ti-6Al-4V	Sphene	Sol-gel	Dip-coating	–	–	[137]
		Ti-6Al-4V	Sphene	Sol-gel	Plasma-spraying	10	150	[127]
		Ti-6Al-4V	Sphene	Sol-gel	Spin-coating	0.4	0.5 – 1	[138]
		Ti-6Al-4V	Hardystonite	Sol-gel	Plasma-spraying	12.1	170	[139]
		Ti-6Al-4V	Hardystonite	Solid phase reaction	Plasma-spraying	7.7	15 – 18	[140]
			Sr-substituted hardystonite	Solid phase reaction	Plasma-spraying	7.2	15 – 18	
		Ti-6Al-4V	Akermanite	Sol-gel	Plasma-spraying	–	400	[141]
		Ti-6Al-4V	Baghdadite	Solid state reaction	Plasma-spraying	9.8	120	[142]
		Ti-6Al-4V	Bredigite	Sol-gel	Plasma-spraying	–	200	[143]

		Ti-6Al-4V	Diopside	Commercially available powder	Plasma-spraying	8.3	200 – 300 [123]
		Ti-6Al-4V	Dicalcium silicate	–	Plasma-spraying	–	380 [144]
		Ti-6Al-4V	Wollastonite	Commercially available powder	Plasma-spraying	–	350 – 400 [145]
		Ti-6Al-4V	Wollastonite	Liquid phase reaction	Atmosphere plasma spraying (+hydrothermal technology)	–	120 – 150 [53]
	GLASSES & GLASS-CERAMICS	Ti-6Al-4V	Wollastonite glass-ceramic	Commercially available powder	Thermal spraying	9	100 – 150 [146]
			Wollastonite (36.77 in wt%)-diopside (63.23 in wt%) glass-ceramic	Commercially available powder (wollastonite); solid state reaction (diopside)	Thermal spraying	11	130 – 200
		Ti-6Al-4V	Bioactive glass-ceramic with glass phase (SiO_2–Al_2O_3–CaO–P_2O_5–CaF_2) and with fluorapatite ($Ca_5(PO_4)_3F$) and diopside	Melting and crystallization	Airbrushing	0.4 – 1	53 [147]
		Ti-6Al-4V	Bioactive glass in mol%: 23.41SiO_2, 3.18 $CaCO_3$, 51.45 $SrCO_3$, 8.67 MgO, 4.62 Na_2CO_3, 4.62 K_2CO_3, 3.47 ZnO, 5.20 $Ca_3(PO_4)_2$	Melting	Plasma-spraying	11.9	50-100 [148]
		Ti-6Al-4V	BG_Ca	Melting	Plasma-spraying	–	30 – 40 [98]
		CpTi	Bioactive glass (in mol%: 2.3 K_2O, 2.3 Na_2O, 45.6 CaO, 2.6 P_2O_5, 47.3 SiO_2) + HA	Melting	High velocity suspension flame spraying	–	30 [149]
					Suspension plasma spraying	–	≤50

		Ti-6Al-4V	CaK	Melting	Pulsed electron deposition	–	1	[86]
			45S5 bioglass	Melting	Pulsed electron deposition	–	1	
		CpTi	45S5 bioglass	Melting	High velocity suspension flame spraying	–	41 – 83	[150]
		Ti	HA + Bioactive glass S53P4	Commercially available powder	Radiofrequent magnetron sputtering	1.5 – 2	2 – 3	[151]
		Ti	HA + Bioactive glass S53P4	Commercially available powder	Radiofrequent magnetron sputtering	1.2	2.1	[152]
		Ti-6Al-4V	Bioactive glass in wt%: 59.1 SiO_2, 19.2 CaO, 5.46 P_2O_5, 9.4 B_2O_2, 22.24 Na_2O, 1.0 TiO_2	Melting	Vitreous enameling technique	–	70 – 100	[153]
		Ti grade 4	$xCaO\cdot(1-x)SiO_2$ bioactive glass ($0.0 \leq x \leq 0.60$)	Sol-gel	Dip-coating	–	–	[1]
		Ti grade 4	70S30CxA bioactive glass (in mol%: 70 SiO_2 (S), 30 CaO (C), x Ag_2O (A), with $0.08 \leq x \leq 0.27$)	Sol-gel	Dip-coating	–	–	[154]
STAINLESS STEEL SUBSTRATES	**CERAMICS**	316L SS	Hardystonite	Sol-gel	Electrophoretic deposition	–	14	[155]
		316L SS	Hardystonite	Sol-gel	Electrophoretic deposition	_	_	[156]
	GLASSES, GLASS-	316L SS	Wollastonite glass-ceramic	Commercially available powder	Thermal spraying	10	100 – 150	[146]
			Wollastonite (36.77 in wt%)-diopside (63.23 in wt%) glass-ceramic	Commercially available powder (wollastonite); solid state reaction (diopside)	Thermal spraying	13	130 – 200	

		316L SS	Hybrid organic-inorganic + wollastonite	Sol-gel	Dip-coating	–	1.1	[62]
		316L SS	Hybrid organic-inorganic + wollastonite	Sol-gel	Dip-coating	–	1.1	[157]
		316L SS	Hybrid organic-inorganic + 45S5 Bioglass	Sol-gel	Dip-coating	–	4.2	[57]
			Hybrid organic-inorganic + 45S5 Bioglass with Ca partially substituted with 2mol% of Sr	Sol-gel	Dip-coating	–	4.2	
Mg-BASED SUBSTRATES	**CERAMICS**	Mg alloy (AZ91)	Diopside + bredigite + fluoridated HA	Sol-gel	Anodic spark deposition + electrophoretic deposition	–	–	[66]
		Mg alloy (AZ91)	Merwinite	Sol-gel	Plasma electrolytic oxidation + electrophoretic deposition	7	250	[67]
		Mg alloy (AZ91)	Diopside	Sol-gel	Micro-arc oxidation + electrophoretic deposition	–	–	[65]
		Mg alloy (ZK60)	Dimagnesium silicate – Magnesium oxide	Liquid phase reaction	Micro-arc oxidation	–	–	[11]
		Mg alloy (ZK61)	Dimagnesium silicate + Magnesium oxide + Clinoenstatite	Liquid phase reaction	Micro-arc oxidation	–	10	[158]
	GLASS-CERAMICS	Mg alloy (AZ31)	45S5 glass–ceramic	Sol-gel	Dip-coating	–	1	[159]
		Mg alloy (AZ31)	45S5 glass–ceramic	Sol-gel	Dip-coating	–	0.5 – 1.0	[160]
		Mg alloy (AZ31B)	45S5 glass–ceramic	Sol-gel	Dip-coating	–	–	[161]

		Mg alloy (AZ31)	45S5 glass–ceramic	Sol-gel	Dip-coating	–	1.1	[162]
		Mg-Ca (1.4 wt%) alloy	RKKP*	Liquid phase reaction	Pulsed laser deposition	–	100	[69]

* RKKP: glass-ceramic material, RKKP stands for Ravaglioli A, Krajewski A, Kirsch M, Piancastelli A, a coating material with the following composition (in wt%): 43.68 SiO_2, 24 β-$Ca_3(PO_4)_2$, 18.40 CaO, 4.92 CaF_2, 4.53 Na_2O, 2.78 MgO, 0.19 K_2O, 1.00 Ta_2O_5, 0.50 La_2O_3.

The bioceramic coatings can be realized by means of production processes involving the synthesis and the deposition of the ceramics directly on the substrates (e.g. Micro-Arc Oxidation or Plasma Spraying) [11, 65, 158].

Other processes comprise a first step, in which the precursors for glass or ceramic synthesis are mixed for example, with a sol-gel technique [57, 62, 65-67, 155-157] or from preceramic polymers [37, 132-134], followed by a second step consisting in the deposition of a solution containing the precursors onto the substrates. When the deposition process occurs at high temperatures, such as in case of plasma [146] or thermal spaying [98], no post-depositional heat treatment is required. Whereas, when the deposition is carried out at room temperature (dip-coating, spin-coating or spray-coating), a heat treatment has to be applied for removing the solvent used in the preparation of the coating and developing the desired bioactive coating.

Regarding bioactive glass and glass-ceramic coatings, they are usually obtained by melt-quenching route or by sol-gel process [82,93] and they are then applied onto the substrates in a second moment, followed by heat treatment.

Several silica-based bioceramics were used to coat Ti and Ti-6Al-4V substrates, including sphene [37,127,132–138], hardystonite [135,139,140], Sr-substituted hardystonite [140], arkemanite [141], baghdadite [142], bredigite [143], diopside [123], dicalcium silicate [144] and wollastonite [53,145].

These coatings possess a Ra in the range of 0.4 – 12.1 μm. The great variability depends not only on the deposition method and on the roughness of the substrate, but also on the dimension of the powders and on the synthesis technique. Rougher surfaces were obtained using plasma spraying, with Ra values above 5 μm. Ra below 5 μm have been found when other deposition methods have been applied (i.e. spray-coating and spin-coating).

Surface roughness of sphene ceramic coatings, prepared by the preceramic polymer processing route and deposited by spraying coating using an automated airbrush, varied with the composition of the solution and with the deposition time. The reduction of deposition time (1 sec) and the use of nano-sized active precursors resulted in coating with Ra of 3.5 ± 0.5 μm [133]. Consistently, sphene-coated CpTi samples produced with the same method exhibited Ra and average surface roughness (Sa) of 3.9 ± 0.7 μm and 3.6 ± 0.5 μm, respectively [37]. However, lower values are reported in Biasetto et al. [134] using the same solution and deposition technique, but this might be related to the use of different Ti substrates.

Atomic force microscopy (AFM) analysis revealed a surface roughness of 0.38 ± 0.04 μm of sphene coatings synthesized via sol-gel and deposited by means of spin-coating [138]. The thickness of the silicate ceramic coatings on Ti-based substrates presented minimum values of 0.5 μm up to 400 μm. The lowest values were observed when spin-coating was applied [138]. With this technique it is possible to deposit thin coating layers below 10 μm. Thicker coatings were produced with airbrushing deposition, with reported values around 100-150 μm [132–134]. Coating deposited using plasma spraying showed a broad variability, from 10 μm [136,140] to 400 μm [141,145].

Also bioactive glass and glass-ceramics coatings on Ti-based substrates were investigated [1, 86,98,146–154].

Surface roughness of these coatings is frequently not reported in the analyzed papers. When available, Ra had values ≤ 2 μm in samples prepared using airbrushing and radio frequency magnetron sputtering techniques [147,151,152]. Higher surface roughness with Ra around 10 μm was observed in wollastonite and wollastonite-diopsite glass-ceramic coatings deposited by thermal spraying [146] and in Sr-substituted bioactive glass coating applied by plasma spraying [148].

In Bellucci et al. [86], two different bioactive glass-ceramic coatings, 45S5 Bioglass and CaK, were deposited onto Ti-6Al-4V substrates using pulse electron deposition (PED) technique. An increase in the amount of crystallinity caused by the thermal sintering was found for both the coatings. Even though CaK was less crystalline than 45S5 bioglass before heat treatment, after annealing the crystallinity of CaK samples increased to a higher extent, becoming much more crystalline than 45S5 ones. As a consequence, the authors suggested that the increased roughness after sintering of 16.6% for 45S5 and 13.2% for CaK samples, could be ascribed to an increase in crystallinity. In

addition, as a consequence of an increase in roughness, an increase in water contact angle values were reported for both the coatings after annealing. This is a positive surface characteristic, because, contrary to hydrophobic ones, it has been widely demonstrated that hydrophilic surfaces can favor cells attachment, proliferation and differentiation [163].

Furthermore, as regards the thickness, values between 1 and 200 μm were observed. The thinnest coatings (1–3 μm) were obtained by PED [86] and radio frequency magnetron sputtering [151,152]. The thickness of a bioactive glass coating produced using the conventional vitreous enameling technique was found to be around 70 and 100 μm [153]. In Sanyal et al. [147], Scanning Electron Microscopy (SEM) analysis on cross-sections of the glass-ceramic coated Ti-6Al-4V substrates revealed that the coating thickness was about 53 ± 10 μm, showing lower values as compared to those of bioceramic coatings also deposited by airbrushing [132–134]. Both high velocity suspension flame spraying (HVSFS) and suspension plasma spraying (SPS) techniques allowed for the deposition of bioactive coating with a thickness below 50 μm [149].

Spraying techniques allowed obtaining a wide range of coating thickness, from 30 to 200 μm [98,146,148,150]. 45S5 bioglass coatings deposited onto Ti substrates, differing in thickness (41–83 μm) and porosity, were produced using HVSFS technique modifying the parameter settings [150]. Pre-heating of the substrates was fundamental in reducing the rapid cooling of glass droplets, thus allowing the deposition of a first thin layer containing abundant fine porosity. The structure of the coatings showed a through-thickness microstructural gradient, with denser and thicker layers on the top, thanks to the increasingly warm glass surface, which more slowly cooled the impinging droplets.

Wollastonite and wollastonite-diopside glass ceramic coatings, for the same number of torch passes, were characterized by a thickness of about 100–150 μm and 130–200 μm, respectively [146], as visible in **Figure 2**. Interestingly, the boundaries between adjacent layers associated to each torch pass were clearly detectable on SEM cross-sectional images.

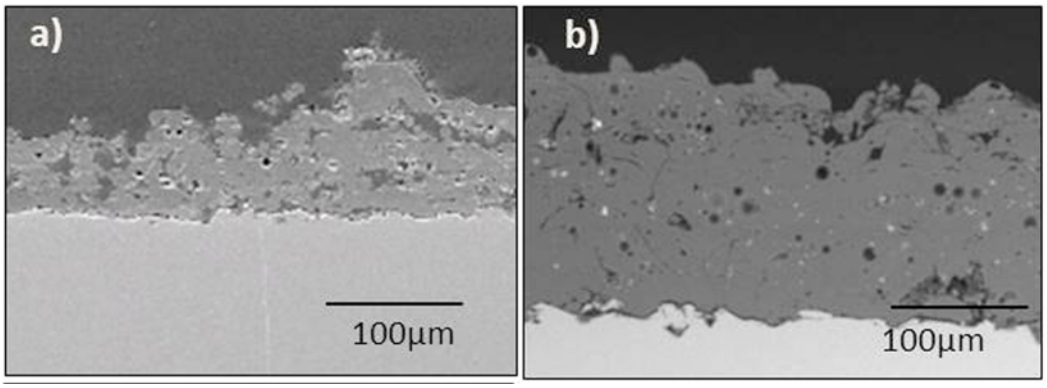

Figure 2. SEM micrographs of the cross section of: (a) wollastonite and (b) wollastonite-diopside glass ceramic coat-ings deposited on Ti6Al4V substrate, from Garcia et al., 2018 [146]

Bioactive glasses and silica-based ceramics coatings deposited onto Ti and Ti alloys have been largely investigated, whilst fewer works have focused on the development of coated stainless steel substrates for biomedical applications.

The coatings applied onto stainless steel substrates analyzed in this review were mainly synthetized by sol-gel technique and deposited by electrophoretic deposition (EPD) [155,156] or dip-coating [57,62,157]. Garcia et al. [146], instead, deposited wollastonite and wollastonite-diopside coatings by thermal spraying. These authors are the only one who reported the surface roughness of the coatings. Wollastonite-diopside coatings deposited onto stainless steel substrates exhibited higher Ra and Rz (the mean peak to valley height) values than wollastonite ones, which might be due to the coarser size of the wollastonite-diopside feedstock powders. In addition, the authors suggested that the higher roughness of the grit blasted stainless steel substrates (Ra 5±1 µm; Rz 44±5 µm), as compared to that of grit blasted Ti-6Al-4V substrates (Ra 3.8±0.2 µm; Rz 25±2 µm), could have contributed to the final coating roughness, with 316L SS system achieving the highest values. Moreover, wollastonite-diopside coatings were found to be thicker and denser than wollastonite coatings.

As demonstrated by SEM cross-section illustration of hardystonite coating on 316L SS, a crack-less coating of 14 µm was obtained using electrophoretic method [155].

Hybrid organic–inorganic coatings containing wollastonite [62,158] or bioactive glass [57] particles presented mean surface roughness of 1.1 µm and 4.2 µm, respectively.

Besides non-resorbable metals, also resorbable metals such as Mg alloys were successfully coated with bioactive glass-ceramics or silica-based ceramics. Bioactive silicate ceramics were applied onto Mg alloys of both AZ and ZK groups, using several

deposition techniques. In order to enhance the corrosion resistance of ZK60 Mg alloy substrates, a rough and porous coating composed of MgO and Mg_2SiO_4 was deposited by micro-arc oxidation (MAO) technique [11]. Using the same deposition process, Yu et al. [158] fabricated coatings containing MgO, Mg_2SiO_4 and a small quantity of $Mg_2Si_2O_6$. SEM analysis on cross-section identified a coating layer with an average thickness of about 10 μm, characterized by a denser inner part, acting as a barrier decelerating the degradation rate of the substrate in corrosive body fluid.

Various coatings containing diopside, merwinite or a combination of diopside, bredigite and fluoridated hydroxyapatite were applied to AZ91 Mg alloy using a combination of EPD method with other methods [65–67]. Among these studies, only in one [67] the average roughness and thickness were reported. The merwinite coating possessed a mean roughness of 7 ± 1 μm and a thickness of approximately 250 ± 20 μm.

Eventually, bioactive 45S5 glass–ceramic coatings, deposited onto Mg alloy AZ31 substrates using dip-coating technique, exhibited an average thickness ~1 μm [159,160–162]. In Rau et al. [69], RKKP glass-ceramic coatings on Mg-Ca alloy were characterized by a coating thickness about 100 μm. Moreover, the surface resulted composed of agglomerates, with root mean squared roughness (Rms) of 295 ± 30 nm, and of fine-texture aggregates, with Rms of 47 ± 4 nm.

1.1.5. Coating-Substrate Adhesion Strength

Obtaining high coating-substrate adhesion is the most important purpose of coating deposition.

To investigate the interface characteristics, several methods have been applied. Most of the studies analyzed the presence of gaps at the interface or of cracks, along with coating thickness, on cross-section SEM or Optical Microscope images [57,98,155].

Scratch tests are commonly performed to obtain information about the adhesion strength at the interface between metal implants and coatings. The normal and tangential loads of the scratch are usually reported as a function of distance; in addition, friction coefficient can be reported as well. After scratch tests, SEM or Optical Microscope images are helpful for the analysis of scratch lines and crack patterns. Moreover, EDS analysis can be performed on the scratched surface to better assess the tracks surface composition and the partial or complete removal of the coating material [86,98,132,133,147].

Other methods to investigate the adhesion of the coatings to the substrates included the tensile adhesion test according to ASTM D4541 [164] or ASTM C633-13 [165] standards, in which the force at which the failure occurs and the characteristics of the failure are recorded in order to measure the bonding strength of the coating [153,164–167]. Moreover, nano-indentation tests on cross-sections are widely conducted to assess the interfacial strength between the coating and the metallic substrate [168]. Furthermore, the occurrence of delamination of the coatings can also be recorded *in vivo* studies [169].

The adhesion of the coating to the substrate is widely investigated in literatures when a non-resorbable metallic implant is used. Whereas, studies regarding resorbable metallic implants, such as Mg and Mg alloys ones, are mainly focused on the coating effectiveness in delaying the degradation of the implants, by means of dissolution testing and electrochemical corrosion. Main findings of literature review are summarized in **Table 5**.

Table 5. Coating-substrate adhesion strength

		Substrate	Coating material	Test performed	Adhesion strength [MPa]	Ref
Ti-BASED SUBSTRATES	CERAMICS	CpTi	Sphene	Scratch test	–	[132]
		CpTi	Sphene	Scratch test	–	[133]
		CpTi	Sphene	Scratch test	–	[134]
				Nanoindentation	–	
		Ti-6Al-4V	Sphene	ASTM C-633	41.0 ± 3.5	[135]
			Hardystonite	ASTM C-633	27.0 ± 3.9	
		Ti-6Al-4V	Sphene	ASTM C-633	33.2 ± 2.4	[127]
		Ti-6Al-4V	Sphene	Scratch test	17.4 ± 0.9	[138]
		Ti-6Al-4V	Hardystonite	ASTM C-633	33.4 ± 2.2	[139]
		Ti-6Al-4V	Hardystonite	ASTM C-633	27 ± 4	[140]
			Sr-substituted hardystonite	ASTM C-633	35 ± 6	
		Ti-6Al-4V	Akermanite	ASTM C-633	38.7 – 42.2	[141]
		Ti-6Al-4V	Baghdadite	ASTM C-633	28 ± 4	[142]
		Ti-6Al-4V	Bredigite	ASTM C-633	41.1 – 49.8	[143]
		Ti-6Al-4V	Diopside	ASTM C-633	32.5 ± 2.8	[123]

		Ti-6Al-4V	Dicalcium silicate	ASTM C-633	38.9 ± 3.5	[144]
		Ti-6Al-4V	Wollastonite	ASTM C-633	27.4 – 42.8	[145]
	GLASSES & GLASS-CERAMICS	Ti-6Al-4V	Wollastonite glass-ceramic	Microindentation test	–	[146]
			Wollastonite (36.77 in wt%)-diopsite (63.23 in wt%) glass-ceramic	Microindentation test	–	
		Ti-6Al-4V	Bioactive glass-ceramic with glass phase (SiO_2–Al_2O_3–CaO–P_2O_5–CaF_2) and with fluorapatite and diopside	Scratch test	–	[147]
		Ti-6Al-4V	BG_Ca	Scratch test	–	[98]
		Ti-6Al-4V	CaK	Scratch test	–	[86]
			45S5 bioglass	Scratch test	–	
STAINLESS STEEL	GLASS-CERAMICS	316L SS	Wollastonite glass-ceramic	Microindentation test	–	[146]
			Wollastonite (36.77 in wt%)-diopside (63.23 in wt%) glass-ceramic	Microindentation test	–	
Mg-BASED	GLASS-CERAMICS	Mg alloy (AZ31B)	45S5 glass–ceramic	Tensile adhesion test	14.2 – 26.8	[161]
		Mg alloy (AZ31)	45S5 glass–ceramic	Tensile adhesion test	10.1 – 27	[162]

Among various bioceramics, hydroxyapatite $Ca_{10}(PO_4)_6(OH)_2$, a calcium phosphate ceramic, is probably the most thoroughly researched material for coating purposes, due to its biocompatibility and similarity to natural bone [46,170]. Since the 1980s, plasma-sprayed HA coatings have been successfully deposited onto metallic implants, mainly Ti-

based ones, in order to accelerate and improve the implant osseointegration. However, the prognosis of these implants remains controversial. Even positive long-term results in both load-bearing and non-load-bearing applications have been reported [171–174], poor bond strength of the HA layer to metallic implants has been documented [169]. The failure normally occurred at the interface between the coating and the implant, as confirmed by both mechanical and *in vivo* studies [169,175]. Recently, silicate substituted HA was developed with the main purpose of improving the HA bioactivity [176]. SiO_4^{4-} substituted HA was deposited on CpTi substrates by RF Magnetron sputtering, giving coatings with a thickness less than one micron and a nano-sized structure. On one hand, the introduction of Si in HA reduced the elastic modulus and coatings with the Young's modulus very similar to the substrates were obtained. On the other hand, scratch tests showed that the introduction of Si increased the material loss and penetration depth during scratch tests [177].

The mismatch of CTE, as in the case of HA, which possesses a CTE in the range between 10 and 14 (10^{-6} $°C^{-1}$), and Ti-based substrates (see **Table 1**), is likely to be responsible of the delamination of the coating, determining the loosening of the implant [123,127]. Furthermore, the increased rate of delamination at the substrate-coating interface over time in clinical settings might reflect the continuous increase of the strength at coating-bone level during the healing phase [169].

The bonding strength, required by the international standard (ISO 13779-2) [178], for bioactive HA coating implants is 15 MPa. When the bonding strength between the silicate bioceramic coating and the Ti-based substrate was measured in accordance with ASTM C-633, the mean values were always higher than 15 MPa [123,127,135,139–145].

In one study [138], the adhesion strength of both sphene and HA coatings on Ti-6Al-4V substrates was assessed by scratch test. The results revealed enhanced bonding strength of the sphene coating, compared with HA, with Hertz stress values of 17.4 ± 0.9 MPa and of 9.8 ± 0.6 MPa, respectively.

Furthermore, good adhesion of sphene ($CaTiSiO_5$) coatings deposited by airbrushing onto CpTi was observed [132–134]. This might be due to the reduced difference between the coefficient of thermal expansion of CpTi and $CaTiSiO_5$ compared to the one of CpTi and HA.

Bellucci and co-workers [86] also examined the adhesion of the coatings to the substrates using micro-scratch tests. A correlation between the mechanical resistance and

the crystallinity was found. In particular, coatings 45S5 before sintering exhibited the lower critical load (Lc) at which partial delamination of the coating occurred (Lc ~ 0.4 N); sintered 45S5 samples (Lc ~ 0.8 N) and as-deposited CaK samples (Lc ~ 1.1 N) showed similar intermediate values, while sintered CaK coatings resulted to be the most resistant (Lc 4.5 N). The authors underlined that high crystallinity is usually considered a drawback for bioglasses, however sintered CaK glass showed promising properties for implant applications which should be further investigated. The new CaK composition may be promising for the production of implant coatings, with improved properties as compared to the well-documented 45S5 Bioglass.

SPS bioactive glass coatings on Ti-6Al-4V were developed and various sets of spray parameters were analyzed in order to determine the role of process parameters on coating features [98]. Amorphous coatings were successfully produced, with a limited crystallization of the glass leading to the formation of silicate-based secondary phases, i.e. wollastonite ($CaSiO_3$) and Ca_2SiO_4. The mechanical properties of the samples resulted to be slightly worse than, for instance, those reported in Altomare and co-workers [150], who investigated the 45S5 bioglass coatings deposited by HVSFS. However, the elastic modulus of BGCa1–BGCa5 coatings was similar to that of the cortical bone [98]. Therefore, as indicated by the authors, it might contribute in the reduction of the stress shielding effect. Moreover, all the coatings showed a good adhesion to the substrates, with critical load values in the range 18-21 N.

Regarding resorbable metallic substrates, the bonding strength of 45S5 glass–ceramic coatings deposited by dip-coating to Mg alloys was investigated using tensile adhesion tests [161,162].

In Niu et al. [161], the coated samples were thermally treated at 480 °C for 90 min under different pressures and the influence of the pressure on the bonding strength was analyzed. The minimum value was obtained when the treatment was performed without pressure (14.2 ± 2.0 MPa). Intermediate values were achieved with Ar pressure at 0.3 and 0.9 MPa, with bonding strength of 17.5 ± 1.9 MPa and 22.7 ± 2.2 MPa, respectively. The maximum value (26.8 ± 2.7 MPa) was obtained with pressure at 0.6 MPa.

In another work, the influence of the heat treatment temperature on the adhesion of the bioactive coating to the Mg alloy was investigated [162]. Increasing the temperature (from 300 °C to 500 °C), an improved cohesion strength of the coating was observed, consisting in a strong interface between the glass and the glass–ceramic particles.

Meanwhile, a deterioration of the adhesion strength between the coating and the substrate occurred. Therefore, these opposite trends resulted in a maximum bonding strength when samples where heat treated at 450 °C (27.0 ± 2.9 MPa), which is closed to what obtained by Niu et al. [161].

Si-HA coatings were deposited on Mg-based substrates. In these experiments coatings of few micron thickness were obtained and showed a positive response to cell proliferation, due to a reduction of corrosion rate [179].

In **Figure 3**, coating-substrate adhesion strength vs coating thickness is reported for those references where data are available. As it can be observed, adhesion strength for bioactive glass or bioceramic coatings on Ti-based substrates tends to slightly increase at increasing coating thickness, when plasma spray is used as deposition technique [123,127,139–145]. Only one data is available for alternative techniques (i.e. spin-coating) [138] and one for coatings deposited on Mg-based substrates [162], so no conclusion can be drawn.

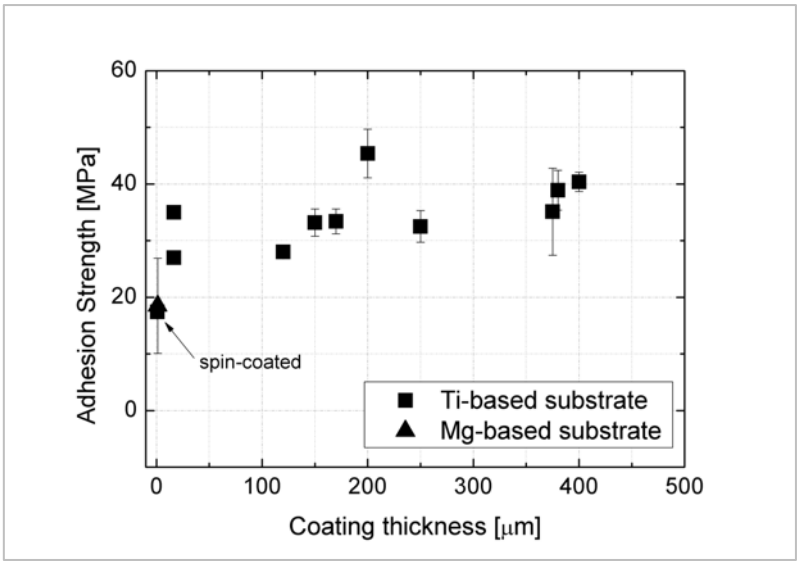

Figure 3. Adhesion strength and thickness of bioactive coatings. Data obtained by merging data available in Table 4 and Table 5.

However, it should be noted that the adhesion strength limit of 15 MPa defined for HA can be reached and overcome, using alternative coatings compositions and deposition methods. A further limit for adhesion strength is that it should be tested in *ex-vivo* experiments, in order to evaluate the ideal adhesion strength value of the coatings once applied *in vivo* or in humans.

1.1.6. Experiments in SBF Solution

In order to reduce the number of animal studies, various preliminary tests have been developed for screening the bioactive materials, such as the implant coating materials. The ability of a biomaterial to bond to living bone is often preliminarily assessed by investigating the ability of apatite to form on its surface in SBF [180–182]. When implanted *in vivo*, bioactive glasses were found to bond to the surrounding bone by forming on their surface a silica-rich layer and a calcium phosphate film. The capability to induce the formation of a calcium phosphate film *in vivo* was demonstrated to be reproducible in a cell-free solution (SBF), with ion concentrations similar to those of human blood plasma reproduced [180]. The original SBF was composted (in mM) of 142.0 Na^+, 5.0 K^+, 1.5 Mg^{2+}, 2.5 Ca^{2+}, 148.8 Cl^-, 4.2 HCO_3^-, and 1.0 HPO_4^{2-}, but it lacked the SO_4^{2+} ions contained in human blood plasma [183,184]. This composition was then corrected by Kokubo et al. by adding also SO_4^{2+} ions [185,186].

In order to evaluate the *in vitro* apatite-mineralization ability, samples are soaked in SBF solution and analyzed at different time points. To characterize the morphological modifications of the surfaces and the formation of apatite crystals, various analyses can be performed, including SEM observations combined, sometimes, with Energy Dispersive X-Ray Spectroscopy (EDS), surface roughness measurements, Fourier-transform infrared (FTIR) spectroscopy and X-ray diffraction (XRD) analysis. The variation of ion concentrations in SBF can also be measured, using, for instance, Inductively Coupled Plasma Optical Emission Spectrometry (ICP-OES), Inductively Coupled Plasma Atomic Emission Spectrometry (ICP-AES) or Inductively Coupled Plasma Mass Spectrometry (ICP-MS). The concentration of different ions is, not only, determined before and after soaking at different time points, but the dissolution kinetics of ions can, also, be obtained from the released concentrations.

The bioactivity of bioactive glasses, glass-ceramics and of silica-based ceramics deposited onto metallic substrates, was confirmed in several *in vitro* studies (see **Table 6**), thus indicating that these coatings might be suitable for the clinical applications, for improving the bonding of the metallic implantable devices with the surrounding bone tissue.

All the studies, reported in Table 6, focused on the surface analysis of the coating after soaking in SBF. Whereas, only in a few of them, the chemical analysis of the solution was performed [66,141,143,144,146,147,150].

It is worth noting that most of the authors conducted the tests at different time points, in order to monitor the modifications in the coating structure and the apatite-forming ability over time. The longer soaking time was 33 days [62,157]. In Wang et al. [53], 7 days represented the longest immersion time, instead in the other papers the maximum soaking time was at least double the time span.

Table 6. In vitro apatite forming ability of the coatings, assessed by immersion SBF.

		Substrate	Coating material	Control	Soaking time (days)	Surface analysis	Ion release concen-tration	Main results	Ref
Ti-BASED SUBSTRATES	SILICATE CERAMICS	Ti-6Al-4V	Sphene	–	21	SEM, EDS	–	Presence of nanocrystals of apatite on the surface.	[138]
		Ti-6Al-4V	Hardystonite	–	28	SEM, EPMA	–	After 28 days two layers were present on the coating surface: a) top layer: apatite layer, composed of Ca and P with a Ca/P molar ratio ~1.6; b) deeper layer: silica-rich layer, maybe as a consequence of ionic exchange between Ca^{2+} in the coating and H^{+} in SBF.	[139]
		Ti-6Al-4V	Akermanite	–	2, 6, 14	SEM, EDS, FTIR	ICP-OES	- After 2 days: some apatite particles on the surface; - after 6 days: thick layer of apatite; - after 14 days: apatite layer (3 μm thick), silicon rich layer, original akermanite layer; - high weight loss rate over the first 6 days, then very low.	[141]
		Ti-6Al-4V	Baghdadite	–	14, 28	SEM, EDS; XRD	–	Apatite formation already obvious after 14 days of immersion.	[142]

		Ti-6Al-4V	Bredigite	–	2, 6, 14	SEM, EDS, FTIR, XRD	ICP-OES	- Presence of apatite layer after 2 days, becoming denser after 6 days of soaking; - after 14 days from outside to inner: apatite layer (thickness ~10 μm), silicon-rich layer and bredigite coating layer.	[143]
		Ti-6Al-4V	Diopside	–	5, 15	SEM, EDS	–	- After 5 days: isolated granular crystals composed of calcium and phosphorous; - after 15 days: coating completely covered by apatite layer.	[123]
		Ti-6Al-4V	Dicalcium silicate	–	2, 7, 14, 21	SEM, EDS, XRD	ICP-AES	- After 2 days: a carbonate-containing HA layer was formed on the surface of coating, with the presence of an intermediate silica-rich layer; - the thickness of carbonate-containing HA layer increased over time.	[144]
		Ti-6Al-4V	Wollastonite	Calcium silicate coating (without HT)	1, 3, 7	SEM, EDS, XRD, FTIR	_	HT at 180°C for 24 h enhanced apatite-mineralization ability of the coatings.	[53]
	GLASSES & GLASS-CERAMICS	Ti-6Al-4V	Wollastonite glass-ceramic Wollastonite (36.77 in wt%)-diopside (63.23 in wt%) glass-ceramic	_	7, 14	SEM, EDS	ICP-AES	Wollastonite glass-ceramic coating exhibited significantly higher dissolution rate than wollatonite-diopsite glass-ceramic coating.	[146]
		Ti-6Al-4V	Bioactive glass-ceramic with glass phase (SiO^2–Al^2O^3–CaO–P^2O^5–CaF^2) and with fluorapatite and diopside	_	7, 14, 21	SEM, EDS	_	- Formation of fluorapatite layer onto the coating surface. - Si and Mg elements were significantly increased in the SBF solution with the increase in soaking time, instead Ca, P and F elements were decreased.	[147]
		Ti-6Al-4V	BG_Ca	–	1, 3, 7, 14	SEM,	–	- All the coatings developed a surface	[98]

					EDS, XRD, micro-Raman spectroscopy		layer of hydroxy-carbonated-apatite; - the reaction kinetics were influenced by the coatings' porosity and degree of crystallinity.	
		CpTi	Bioactive glass (in mol%: 2.3 K_2O, 2.3 Na_2O, 45.6 CaO, 2.6 P_2O_5, 47.3 SiO_2) + HA	HA	1, 3, 7, 14	SEM, XRD, micro-Raman spectroscopy	_	- Porous SPS bioactive glass coatings more rapidly dissolved in SBF, as compared to HVSFS bioactive glass coatings; - SPS HA was more stable than HA HVSFS coating	[149]
		CpTi	45S5 bioglass	Bulk glass	1, 3, 7, 14, 28	SEM, EDS, XRD, micro-Raman spectroscopy	ICP-OES	- After 1 day presence of HA layer on the sample surface; - after 28 days the glass coating was replaced by precipitated HA film.	[150]
		Ti grade 4	$xCaO\cdot(1-x)SiO_2$ bioactive glass ($0.0 \leq x \leq 0.60$)	Uncoated	7, 21	SEM, EDS	–	- After 7 days: uncoated samples showed fewer bone-like apatite globular grains in comparison to coated samples; - precipitate increased with the increased in exposure time to SBF.	[1]
		Ti grade 4	70S30CxA bioactive glass (in mol%: 70 SiO_2 (S), 30 CaO (C), x Ag_2O (A), with $0.08 \leq x \leq 0.27$)	Uncoated	21	SEM, EDS	–	- Coated samples showed the surface covered by apatite globular crystals; - coated samples were more bioactive than uncoated ones.	[154]
STAINLESS STEEL SUBSTRATES	CERAMICS	316L SS	Hardystonite	–	3, 7, 14	SEM, EDS, XRD	–	- After 3 days: no changes in coating morphology; - after 7 and 14 days: presence of cauliflower-shaped apatite on the surface; - increasing cracks by the time of immersion.	[155]
	GLASSES,	316L SS	Wollastonite glass-ceramic Wollastonite (36.77% in wt%)-diopside (63.23% in	–	7, 14	SEM, EDS	ICP-AES	Wollastonite glass-ceramic coating exhibited significantly higher dissolution rate than wollatonite-diopsite glass-ceramic coating.	[146]

			wt%) glass-ceramic					
		316L SS	Hybrid organic-inorganic + wollastonite	–	5, 33	SEM, EDS, XRD	–	An apatite-like layer was observed on the surface, mainly composed of Ca and P. [62]
		316L SS	Hybrid organic-inorganic + wollastonite	–	5, 33	SEM, EDX	–	- After 5 days: a Ca-P rich phase was detected in proximity to wollastonite particles; - after 33 days: presence of numerous Ca-P rich compounds [157]
		316L SS	Hybrid organic-inorganic + 45S5 Bioglass ——— Hybrid organic-inorganic + 45S5 Bioglass with Ca partially substituted with 2mol% of Sr	a) stainless steel b) double layer of TMS	30	SEM, micro-Raman assays	–	Formation of HA on both test surfaces. [57]
Mg-BASED SUBSTRATES	CERAMICS	Mg alloy (AZ91)	Diopside + bredigite + fluoridated HA	a) coated Mg alloy (ASD/AZ 91) b) Mg alloy (AZ91)	3, 7, 14, 21, 28	SEM, EDS, FTIR	ICP	Amount of degradation and precipitates on the surface: composite/ASD/AZ91 > ASD/AZ91 > AZ91. [66]
		Mg alloy (ZK61)	Dimagnesium silicate + Magnesium oxide + Clinoenstatite	–	7, 14	SEM, EPMA, FTIR	–	Quick growing of the apatite layer. [158]
	GLASS-CERAMICS	Mg alloy (AZ31)	45S5 glass–ceramic	Uncoated	1, 7, 14	SEM, EDS	–	- Enhanced corrosion resistance of coated sample over the first 7 days; - after 14 days of soaking, reduced corrosion resistance also in the coated samples due to the cracking of the coating. [159]
		Mg alloy (AZ31)	45S5 glass–ceramic	Uncoated	1, 3, 5, 7	SEM, EDS	_	Samples with the thickest coating, 3A500, showed lower (2.31%) mass loss than A500 [160]

			(72.71%), 2A500 (72.24%) and uncoated (78.04%) samples, along with a lower pH variation of m-SBF after 7 days.

ASD = Anodic Spark Deposition; EPMA = Electron Probe Micro-Analyzer; HT = Hydrothermal Treatment; TMS = TEOS (tetraethoxysilane) – MTES (methyltriethoxysilane) – SiO_2

Bioactive silicate ceramics possess a distinct apatite mineralization ability in SBF. In accordance with what reported by Wu & Chang [101], who indicated that wollastonite, dicalcium silicate, and bredigite, among the silica-based ceramics, had the best apatite forming abilities and fastest dissolutions in SBF. The apatite could be detected after 1 or 2 days of soaking, when Ti-based substrates coated with these bioceramics were immersed in SBF [53,143,144].

Interestingly, wollastonite samples, produced by means of atmosphere plasma spraying (APS) in combination with hydrothermal technology (HT), were found to possess a better bone-like apatite formation ability after the heat treatment, which could be due to their nano-sheet-like topography providing more sites for apatite nucleation [53].

A longer time for the induction of the apatite layer formation was reported for other coatings, such as akermanite [141], sphene [138], hardystonite [139], baghdadite [142] and diopside coatings [123]. However, it has to be noted that in some works the tests were performed after a minimum time of 14 days, so no data are available regarding the early phases after immersion [138,139,142].

Additionally, the bioactive glass and glass-ceramic coated Ti-based substrates were tested in in SBF [1, 98,146,147,149,150,154]. In Sanyal et al. [147], Ti-6Al-4V with a glass-ceramic coating, containing fluorapatite and diopside, showed a good bioactivity, as indicated by high concentration of Ca, P, F elements on the coating surface after soaking in SBF for 21 days. The formation of a fluorapatite layer was further confirmed by the elemental composition analyses of the solutions at different time points, showing an increase in Si and Mg concentrations and a decrease in Ca, P and F element concentrations with the increase in the soaking time.

Encouraging results were also obtained with suspension plasma sprayed bioactive glass coatings, composed of 4.7 Na_2O, 42.3 CaO, 6.1 P_2O_5 and 46.9 SiO_2 (in wt%), produced using several sets of spray parameters and applied on rough Ti-6Al-4V disks

(Ra = 3.4 μm) [98]. The degree of crystallinity and porosity of the different samples, which were mainly related to the spray distance, influenced the kinetic reaction in SBF, particularly, in the first days of soaking. In fact, the crystalline phase (wollastonite) reacted with SBF, but at a lower rate as compared with the glassy one. It is worth noting, that, regardless of differences in the reaction rate among the samples, after 14 days of immersion all the surfaces were covered by a hydroxyapatite layer, replacing the gradually resorbed original coating, as shown in **Figure 4**.

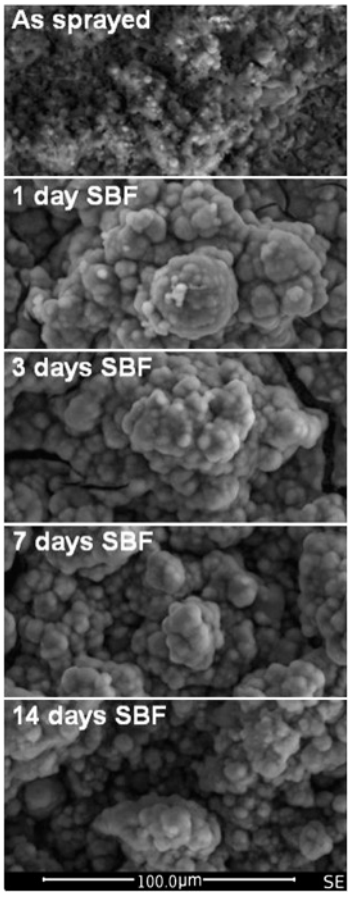

Figure 4. Surface evolution of the samples (BGCa3) immersed in SBF for increasing times, from Cattini et al., 2013 [98].

Different *in vitro* behavior was noticed, when CpTi bioglass-coated samples were produced by different methods [149,150]. The bioactivity of 45S5 bioglass coatings was characterized by soaking in SBF up to 28 days [150]. In order to verify whether the deposition process could affect the *in vitro* behavior of 45S5 bioglass, bulk 45S5 bioglass was tested as well. Coated samples and bulk bioglass presented the comparable interactions with SBF. After 1 day of immersion, a hydroxyapatite layer was

distinguishable on all the samples, as confirmed by XRD patterns and micro-Raman spectra. At 28 days of soaking, the whole glass coating was replaced by the precipitated hydroxyapatite. SEM observations of the surfaces and of cross-sectional SEM micrographs, microcracks were detected, with larger ones on samples immersed in SBF for longer times. It is interesting to note that the samples did not release measurable amounts of Ti ions, as well as Al or Zr ions.

In Bolelli et al. [149], the apatite precipitation occurred on both HA and bioactive glass samples after soaking in SBF. Among the bioactive glass samples, the SPS coatings reacted more rapidly than the HVSFS coatings, due to their high porosity and to the related larger surface area in contact with the SBF. Despite the poor mechanical properties exhibited by SPS bioactive glasses, which had already lost their mechanical integrity after one week of immersion in SBF. They could be useful for specific applications, such as for the release of functional bioactive polymers. Multilayered coatings could also be designed, with a more stable inner layer deposited using HVSFS technique and an outer SPS layer, in order to tailor the resorbability and reactivity of the coatings to specific need.

Furthermore, when the apatite forming ability of two bioactive glasses, deposited onto Ti grade 4 substrates, was compared to that of uncoated samples, better results were observed with the coated samples [1,154]. Positive *in vitro* results were also obtained when 316L SS) was used as a substrate.

In Bagherpour et al. [155], hardystonite coatings showed no change in their morphology after 3 days of soaking in SBF, while a cauliflower-shaped apatite was observed after one and two weeks of immersion. These observations further confirm the longer time required by hardystonite to induce the apatite formation, as compared to other biosilicates [101].

In Garcia et al. [146], it is not specified if 316L SS and/or Ti-based substrates were used for checking the *in vitro* bioactivity of the coatings. The attention was focused of the behavior of wollastonite and wollastonite-diopside glass-ceramic coatings in contact with the SBF. The incorporation of diopside was found to be a useful tool for adjusting the dissolution rate of wollastonite and, in the meantime, for enhancing the mechanical stability of the coating.

316L SS implants, characterized by a double-layer hybrid organic-inorganic sol-gel coating with the dispersion of wollastonite particles deposited using dip-coating

technique, were able to induce hydroxyapatite deposition on their surface, when immersed in SBF up to 33 days [62,157]. Consistently, hybrid organic-inorganic sol-gel coatings containing particles either of 45S5 bioglass or of 45S5 glass (in which calcium was partially substituted strontium), exhibited hydroxyapatite deposition ability when immersed in SBF for 30 days [57].

Due to the rapid degradability of Mg and Mg alloys, a bioactive coating is expected to protect the substrate from the corrosive body fluid, thus favoring the maintenance of the mechanical integrity of the implants during the healing process. The *in vitro* behavior of a ceramic coating on Mg-based substrate, obtained by microarc oxidation using electrolyte containing silicate salts, was investigated by immersion in SBF for 7 and 14 days. SEM-EDS analyses revealed the presence of apatite on the coating surface after 7 days of soaking, while after 14 days a homogeneous bone-like apatite layer was detected on the surface, indicating a quick thickening of the apatite layer [158]. In a recent work of Razavi et al. [66], anodic spark deposition (ASD), followed by EPD of an outer composite layer composed of diopside, bredigite, and fluoridated HA, was used to improve the properties of AZ91 Mg alloy. The coated samples resulted to moderate the degradation rate, when immersed in SBF up to 28 days, as compared to AZ91 Mg alloy and AZ91 Mg alloy with only the intermediate layer deposited by ASD. SEM analysis revealed the presence of cracks on the surfaces, as a consequence of the degradation, especially on uncoated AZ91 specimens. Moreover, composite/ASD/AZ91 samples showed a lower amount of weight loss and of Mg ion release into the solution, corroborating the protective effect of the coating against corrosion. Similarly, compression tests performed before and after soaking resulted in a less pronounced loss of mechanical integrity in composite/ASD/AZ91. The compressive strength of the samples decreased from 230 MPa, before soaking, to 100, 130 and 195 MPa for uncoated, ASD/AZ91, and composite/ASD/AZ91 specimens, respectively.

Crack-free glass–ceramic coating, characterized by a glassy Si-based phase and a crystalline phase $Na_2Ca_2Si_3O_9$, acted as a protective barrier for the Mg alloy substrate, as confirmed by the immersion tests in SBF [159]. In accordance with these findings, Dou et al. [160] reported that optimized 45S5 glass–ceramic coatings produced onto Mg alloy through sol–gel and dip-coating method reduced the degradation of the substrate, improving the corrosion resistance in modified simulated body fluid. Although also

thinner coatings protected the substrates for degradation up to 3 days of soaking, a better protective effect over time was noticed with thicker coating (~1 μm).

1.1.7. In Vitro Experiments

In vitro tests, aiming to investigate the behavior of cells seeded onto implant surfaces, are considered a fundamental tool to preliminary determine the coating/tissue interaction on a cellular level. Among the studies analyzed in the present review (see **Table 4**), *in vitro* tests using different kind of cells were performed to assess the biocompatibility, the osteoinductive properties and the antimicrobial ability of bioactive glass and glass-ceramic and silica-based ceramics (see **Table 7**). As revealed by SEM images, both Ti- and Mg-based coated substrates were found to sustain cellular growth *in vitro* (see **Figure 5**).

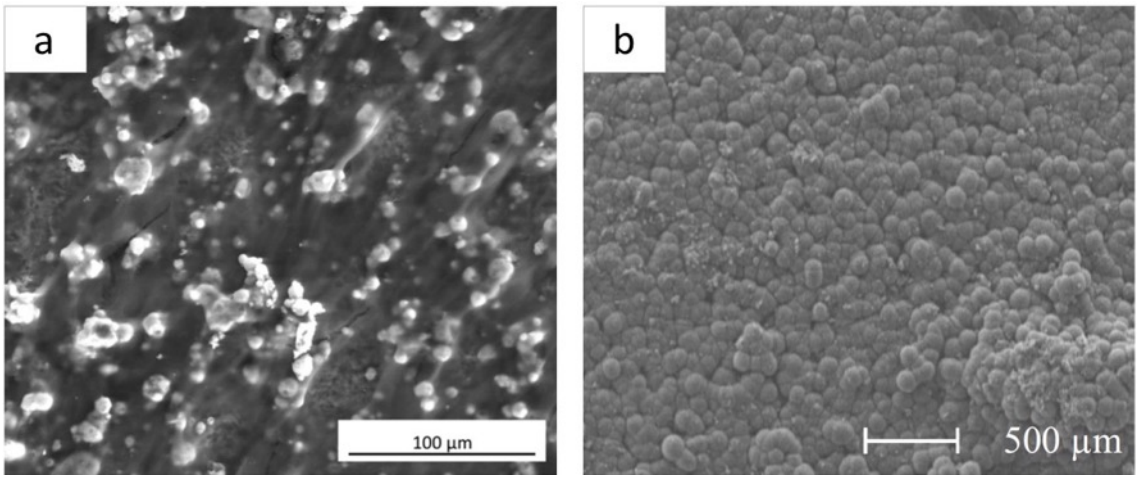

Figure 5. SEM images of cells grown on: (a) sphene-coated CpTi substrate after 21 days of culture in Osteo-genic Differentiation Medium; from Elsayed et al., 2018 [37]; (b) bioceramic coating composed of diopside, bredigite, and fluoridated hydroxyapatite deposited on Mg alloy (AZ91) after 7 days of culture; modified from Razavi et al., 2018 [66].

It is important to point out that most of the studies limited the investigation to cell viability by means of colorimetric assays, such as MTT (3-(4,5-dimethylthiazol-2-yl)-2,5-diphenyltetrazolium bromide) assay, MTS (3-(4,5-dimethylthiazol-2-yl)-5-(3-carboxymethoxyphenyl)-2-(4-sulfophenyl)-2H-tetrazolium) or WST-8 (2-(2-Methoxy-4-nitrophenyl)-3-(4-nitrophenyl)-5-(2,4-disulfophenyl)-2H- tetrazolium sodium salt) assay.

Table 7. Bioactive coatings: in vitro experiments.

		Substrate	Coating material	Control	Cells	Test performed	Main results	Ref
Ti-BASED SUBSTRATES	CERAMICS	CpTi	Sphene	Uncoated	hADSCs	- MTT assay - SEM analysis - Immunofluorescence - Alzarin Red S staining - rt-PCR	- Sphene-based coating significantly better supported cell attachment and proliferation, than CpTi samples. - When cells were seeded in the presence of Osteogenic Differentiation Medium for 21 days, a significantly higher accumulation of calcium deposits on sphene coatings than on uncoated samples was observed.	[37]
		Ti-6Al-4V	Sphene Hardystonite	Uncoated	Primary human osteoblasts	- SEM analysis - MTS assay - rt-PCR	- After 7 days of culture, cell proliferation rate on hardystonite coatings was higher when compared with those on sphene coatings and Ti-6Al-4V samples ($p < 0.05$). - Both coatings were able to enhance the expression of bone-related genes.	[135]
		Ti-6Al-4V	Sphene	HA-coated (Uncoated)	Human osteoblast-like cells	- SEM analysis - MTS assay - ICP-AES - ALP activity	- After 7 days of culture, significantly higher cell proliferation and ALP activity on sphene coatings, than on HA- coated and uncoated substrates were observed ($p < 0.05$).	[127]

						- After 7 days of culture, no detectable levels of Ti ions and minor amounts of Ca and Si ions released from sphene coatings.	
		Ti-6Al-4V	Hardystonite	Uncoated	MC3T3-E1 cells (a mouse calvaria-derived osteoblast-like cell line)	- SEM analysis - MTS assay	- Hardystonite showed no toxic effect on cells. - After 24 h incubation, cells on hardystonite coating were more elongated, spread and confluent than on uncoated samples.	[139]
		Ti-6Al-4V	Hardystonite Sr-substituted hardystonite	HA-coated	Canine BMMSCs	- Immunofluorescence - rt-PCR - ICP-OES - ALP activity - Calcium deposition assay	- After 14 days of culture, the expression levels for BMP-2, ALP and osteocalcin cells cultured on strontium-substituted hardystonite coatings were the highest, followed by hardystonite and then by HA coatings.	[140]
		Ti-6Al-4V	Akermanite	HA-coated	Rabbit BMMSCs	- SEM analysis - MTT assay	- After 1 day, cells on HA coating were similar in appearance to those on akermanite coating, but with fewer minor filopodia. After 7 days of culture, more cells were detected on akermanite coating than on HA one. - After 1 day of culture no significant differences in cell proliferation rate between the 2 groups; cells on the akermanite	[141]

						coatings showed a higher proliferation rate than that on HA coatings at both 3 and 7 days of culture ($p < 0.05$ and $p < 0.01$, respectively).	
		Ti-6Al-4V	Bredigite	- HA-coated - blank control	Rabbit BMMSCs	- SEM analysis - MTT assay	- Cells cultured on bredigite coating for 1 day presented an elongated morphology and were firmly attached to the surface. After 3 days of culture, the bredigite coating presented numerous cells on its surface, characterized by a net-like morphology. - After 3 and 7 days of culture, cells on bredigite coating had a higher proliferation rate than that on HA coating and blank control.	[143]
		Ti-6Al-4V	Wollastonite	–	Rat BMMSCs	- MTT assay - ICP-AES - Immunofluorescence - ALP activity - qRT-PCR	- Cells seeded on the HT treated coatings presented higher cell viability and proliferation than untreated coatings at all time points (1,4 and 7 days) ($p < 0.05$). - Quantitative results of ALP activity cells cultured on HT treated and untreated coatings revealed higher ALP activity on HT treated samples at all time points (4, 7 and 10 days) ($p < 0.05$).	[53]

						- HT treatment enhanced the expression of osteogenic genes and angiogenic factors.	
	GLASSES & GLASS-CERAMICS	CpTi	45S5 bioglass	Uncoated	Human osteosarcoma cell line MG63	- MTT assay - SEM analysis	- After 24 h of culture, cells spread over the coated surface. After 7 days, it appeared covered by a cell layer. - Coated samples supported an increasing cell viability overtime, similarly to uncoated samples.	[150]
		Ti grade 4	$xCaO\cdot(1-x)SiO_2$ bioactive glass ($0.0 \leq x \leq 0.60$)	Uncoated	NIH 3 T3 murine fibroblasts cells	WST-8 assay	- After 24 h of culture, the cells grown on uncoated samples showed lower viability than on all coated samples ($p < 0.05$). - The best results were obtained with $0.3CaO\cdot SiO_2$ and $0.4CaO\cdot SiO_2$ coatings, which were homogeneous and crack-free, contrary to SiO_2, $0.5CaO\cdot SiO_2$ and $0.6CaO\cdot SiO_2$ coatings.	[1]
		Ti grade 4	70S30CxA bioactive glass (in mol%: 70% SiO_2 (S), 30% CaO (C), x% Ag_2O (A), with $0.08 \leq x \leq 0.27$	Uncoated	NIH 3 T3 murine fibroblasts cells	WST-8 assay	- Higher percentage of viable cells on coated samples than on uncoated ones. - The coating with the lower content of Ag resulted to be the most biocompatible.	[154]
Mg-CERAMIC		Mg alloy (AZ91)	Diopside + bredigite + fluoridated HA	a) Uncoated b) ASD coated	L-929 fibroblast cell line	- MTT assay - SEM analysis	- Increase in cell viability from 2 to 7 days of culture in all samples.	[66]

						- At all time points (2, 5 and 7 days) cell viability was as follows: diopside + bredigite + fluoridated HA coated > ASD coated > uncoated.	
		Mg alloy (AZ91)	Diopside	a) Uncoated b) MAO coated	L-929 fibroblast cell line	MTT assay	- Cell viability of all samples increased with the culture time. - At all time points (2, 5 and 7 days) cell viability was as follows: diopside coated > MAO coated > uncoated. - Diopside coated samples had significantly higher cell viability than that of uncoated samples at all time intervals ($p < 0.05$).	[65]
		Mg alloy (ZK60)	Dimagnesium silicate – Magnesium oxide	Uncoated	Human osteoblast-like cells (MG63) and NIH 3 T3 murine fibroblasts cells	- CellTiter-96 cytotoxicity test - SEM analysis	Dimagnesium silicate – magnesium oxide coatings, with or without gallic acid, favored osteoblast-like cell proliferation.	[11]

ALP = alkaline phosphatase; BMMSCs = Bone Marrow Mesenchymal Stem Cells; BMP = Bone Morphogenic Protein; hADSCs =Human Adipose-Derived Stem Cells; qRT-PCR = Quantitative Reverse Transcription Polymerase Chain Reaction; rt-PCR = Real Time Polymerase Chain Reaction.

1.1.7.1. In vitro behavior of Ti-based substrates coated by bioactive silica-based ceramics

Different silica-based ceramic coatings deposited onto Ti substrates, characterized by a rough surface with Ra in the range between 3.9 and 12.1 μm, were all able to support cell attachment and proliferation [37,127,135,139,140].

Regardless of the synthesis and deposition methods, sphene coatings were found to promote cell proliferation and differentiation [37,127,135]. Plasma-sprayed sphene-coated showed better results in terms of cell proliferation and alkaline phosphatase (ALP)

activity than both plasma-sprayed HA coating and uncoated Ti-6Al-4V samples [127]. The authors speculated that the excellent cellular bioactivity might be due to the release of minor amounts of Ca and Si ions from the sphene coatings. In a good agreement with the latter work [127], also the results obtained by other researchers, who suggested that the dissolution of Ca and Si ions from sphene coatings might lead to beneficial effects by promoting cell proliferation and differentiation [37,135].

Furthermore, cell proliferation rate on hardystonite coatings was found to be higher than on sphene coatings and uncoated Ti-6Al-4V substrates. The authors suggested that it could be caused by the release of zinc ions from the hardystonite coatings [135]. In accordance with the previous study, in Li et al. [139] cells were able to attach and spread on hardystonite coating surface, whereas fewer cells were counted on uncoated Ti-6Al-4V.

Moreover, comparable cell adhesion was observed on hardystonite and strontium-substituted hardystonite, in both cases superior than that on uncoated and HA-coated samples. Nevertheless, cell differentiation was superior on strontium-substituted hardystonite coatings compared to all the other groups. As both silica-based coatings had similar surface topography, it was suggested that the release of Sr ions, rather than surface topography, was responsible of the higher differentiation on strontium-substituted hardystonite compared to hardystonite ones [140,187,188].

Both akermanite and bredigite coatings stimulated the attachment and proliferation of bone marrow stem cells in a greater extent than HA coatings. Therefore, it is likely that the Mg and Si ions released from the coatings contributed to the improvement in cell proliferation *in vitro* [141,143].

Furthermore, calcium silicate coatings were fabricated by a combination of atmosphere plasma spraying and hydrothermal technology. The HT treatment allowed the glassy phase to be transformed into a nano-structured phase with high crystallinity. This not only significantly reduced the degradation rate of the coatings, but also enhanced their biological properties, even though no significant differences in the concentration of Si ions in culture medium was observed between the two groups (i.e. HT treated and not) [53].

Beside morphological aspects, such as roughness and crystallite size, cell proliferation seems to be affected by the interaction with released ions from the coating, capable of promoting at different levels cell growth, depending on their chemical characteristics.

More detailed investigations should be necessary in order to clarify the role of the ions on cell growth, as well as the chemical characteristics in favor of cell proliferation.

1.1.7.2. In vitro behavior of bioactive glass coated Ti-based substrates

It would be interesting to investigate the role of surface roughness and coating adhesion to substrate on *in vitro* behavior of bioactive coatings. However, no data is available on bioactive glass coated titanium substrates.

Bioactive glasses deposited onto Ti-based substrates by means of different techniques were found to favor cell growing as compared to uncoated samples [1,150,154]. Bioactive calcium silicate glasses produced using sol-gel and dip-coating technique were found to improve the *in vitro* responses of the titanium substrates [1]. Similar findings were observed using bioactive calcium silicate glass coatings fabricated using the same synthesis and deposition techniques but characterized by the addition of limited amounts of Ag_2O [15]. HVSFS-deposited 45S5 bioglass coatings presented no cytotoxicity [150]. Moreover, when human osteosarcoma cells were seeded onto coated and uncoated samples, cell viability increased overtime in the first week on both 45S5 bioglass and control samples, with no statistical differences between the two groups.

1.1.7.3. In vitro behavior of Mg-based substrates coated by bioactive silica-based ceramics

Regarding resorbable metallic substrates coated by bioactive silica-based ceramics, various studies indicated that these coatings are able to enhance the *in vitro* responses of the implants compared to uncoated samples [11,65,66]. No data is available in these studies about coating roughness. Only in Lee et al. [11], it is underlined that the implant surface, became rough and coarse with several pores after coating deposition, had a positive effect on osteoblast-like cell adhesion and proliferation. Moreover, the addition of gallic acid positively and adversely affect the growth of bone-like cell and fibroblast, respectively.

1.1.7.4. Antibacterial properties of bioactive coatings

Biomaterial-associated infections are still common problems in both orthopedics and dentistry. Surface modifications of metallic substrates, including the deposition of

coatings with antimicrobial properties, can prevent the occurrence of implant-related infections [189,190]. In two studies, the antibacterial properties of Ti-based substrates coated with hardystonite [139] and with a bioactive glass containing silver (Ag) [154] were investigated. In both the works, *Staphylococcus aureus*, a common pathogen causing implant-related infections [191] was used for antibacterial tests. The inhibitory effect of zinc ions on bacteria was confirmed, as demonstrated by the marked decrease of total colony forming unit (CFU) of *S. aureus* after 18 h of interaction with hardystonite-coated samples as comparted to Ti-6Al-4V substrates [139]. In Catauro et al. [154], the antibacterial effect of silver contained in the coatings was confirmed. In fact, a uniform layer of bacteria was detectable on uncoated substrates, while the number of bacteria decreased with the increase of Ag content in the coatings. Nevertheless, high percentages of silver were found to negatively affect coating biocompatibility, probably due to the nitrate ions released from the coating. Therefore, bioactive glass coatings with 0.14 % of Ag_2O resulted to be the best compromise in terms of both antimicrobial and biological properties. The incorporation of ions, such as Ag or Zn ions, in calcium silicate coatings could represent a valid tool to reduce implant-related infections.

1.1.8. In Vivo Experiments

Utilization of animals needs to follow strict rules in terms of ethical issues, design and execution of the study as well as extrapolation of the results [192–194]. In an effort to minimize the number of *in vivo* animal studies, alternative methods for assessing the bioactivity and the biocompatibility of implantable devices, such as immersion in SBF, have been developed and extensively used in pre-clinical phases [180].

However, once the safety and the osteoconductive property of the material has been determined, further *in vivo* tests are required to confirm these findings before the clinical use in humans [192–194].

Since some bioactive glass-based and silicate ceramic coatings have shown promising *in vitro* properties, *in vivo* tests have been performed in several animal models to investigate the ability of the coatings to promote the new bone formation and neovascularization. Among the analyzed studies (see **Table 4**), in only 10 works *in vivo* studies were carried out. The main results are reported in **Table 8**. Briefly, bone-implant contact (BIC%), which represents the percentage of the implant surface in contact with the surrounding bone on a microscopic level, is one of the mostly used parameters to

measure implant osseointegration. It can be noted that, when reported [137,140,152], higher values were achieved by implants with silicate-based and HA coatings as compared to uncoated ones. The beneficial effect of bioactive coatings was also confirmed by the higher failure load registered during push-out testes with silicate-based bioactive coatings compared to control HA-coated and uncoated implants [137,140,148]. Moreover, silicate-based ceramic coatings were found to protect Mg substrates from fast corrosion, thus improving bone healing [65,67].

Table 8. Bioactive coatings: in vivo experiments.

		Sub-strate	Coating material	Study model*	N. test im-plants	Control implants§	Sacrifice [wks]	Assessment methods	BIC %	Main results	Ref
Ti-BASED SUBSTRATES	**CERAMICS**	Ti-6Al-4V	Sphene	Merino sheep (femur) (n=10)	20	a) uncoated (n=20) b) HA-coated (n=20)	6	- Histological analysis - Histomorphometric analysis - Push-out testing	In cortico-cancellous bone: - sphene-coated ~75% - HA coated ~75% - uncoated ~15% In cortical bone: - sphene-coated ~75% - HA coated ~80% - uncoated ~62 %	- In cortico-cancellous bone, significantly higher BIC % in sphene- and HA-coated implants, than in uncoated ones. - Uncoated implants in corticocancellous site: fibrous tissue and lack of ALP and TRAP staining at the interface. - Push-out tests: significantly higher failure load with sphene-coated implants compared to uncoated ones in cortical bone.	[137]
		Ti-6Al-4V	Hardystonite / Sr-substituted hardystonite	Beagle dog (femur) (n=12)	12+12	a) uncoated (n=12) b) HA-coated (n=12)	12	- Sequential fluorescent labeling - Micro- CT analysis - Push-out test - Histomorphometric analysis	- Sr-substituted hardystonite 51.20±9.08 - hardystonite 36.97±8.72 - HA 27.72 ±5.48 - uncoated < 10	- BIC% of Sr-substituted hardystonite-coated implants was higher than those of hardystonite ($p < 0.05$) and HA ($p < 0.01$). - Push-out test (loading rate of 5 mm/min): Sr-substituted hardystonite-coated implants possessed the highest failure load (388.84±100.51 N).	[140]
	GLASSES &	Ti-6Al-4V	Bioactive glass (SrBG)	New Zealand rabbit (femur and tibia) (n=27)	54	HA-coated (n=54)	6,12, 24	- Push-out test - SEM analysis - Histological analysis - Histomorphometric analysis	Quantified using Osteomeasure software (OsteoMetrics)	- No significant differences in BIC% between the 2 groups at any time point. - Push-out: significant difference in maximal shear strength at 24 wks between the 2 groups	[148]

									(p = 0.028). Maximal shear strength increased over time in bioactive glass-coated samples, but no similar increase in the control group.	
		Ti	HA + Bioactive glass S53P4	Beagle dog (mandible) (n=16)	16 ($HABG_{High}$) + 16 ($HABG_{Low}$)	HA-coated (n=16)	4, 12	- Histological analysis - Histomorphometric analysis	At 4 wks: - HA 41.5±19.7 - $HABG_{Low}$ 45.1±19.3 - $HABG_{High}$ 29.7±12.5 At 12 wks: overall BIC% ranged from 40.5% to 31.1% with no significant differences between the groups.	- After 4 wks, in $HABG_{High}$ group BIC% was lower than in the other groups ($P < 0.05$). - After 12 wks, no significant differences in overall BA%, BIC% and 1st BIC among the groups.	[151]
		Ti	HA + Bioactive glass S53P4 (HABG)	Saanen goat (iliac crest) (n=8)	32	a) Uncoated (n=32) b) HA-coated (n=32)	4	- Removal torque testing - Histological analysis - Histomorphometric analysis	Monocortical: - Uncoated 40.7±13.2 - HA-coated 44.8±21.7 - HABG-coated 54.2±18.4 Bicortical: - Uncoated 57.5±8.5 - HA-coated 65.7±11.3 - HABG-coated 66.7±11.5	HABG-coated implants showed higher ($p < 0.05$) BIC% in both monocortical and bicortical implant placements in comparison with uncoated implants.	[152]
STAINLESS STEEL SUBSTRATES	**GLASSES, GLASS-CERAMICS &COMPOSITES**	316L SS	Hybrid organic-inorganic + wollastonite	Hokkaido rat (femur) (n=4)	Unclear	Uncoated (n unclear)	8.5	- Histological analysis - SAXS analysis	- ~ 60 coated	- After 60 days, newly formed bone around coated implants and fibrous tissue around uncoated implants. - Uniform mean thickness of Ca/P rich crystals in the new bone tissue (~ 2 nm).	[62]
		316L SS	Hybrid organic-inorganic + wollastonite	Hokkaido rat (femur) (n=4)	Unclear	–	8.5	- Surface analysis (SEM, EDS, AFM) - Histological analysis - Nanoindentation	–	After 60 days, newly formed bone around coated implant, characterized by the presence of osteocyte lacunae and laminar structure.	[157]
		316L SS	Hybrid organic-inorganic + 45S5 Bioglass	Wistar–Hokkaido rat (femur) (n=6)	Unclear	Uncoated (n unclear)	4, 8	- SEM analysis - Micro-Raman Spectroscopy	–	- Thickness of newly formed bone: at 8 wks ~50 μm for all the samples, but at 4 wks lower bone thickness around uncoated implants.	[57]

			Hybrid organic-inorganic + 45S5 Bioglass with Ca partially substituted with 2mol% of Sr						- At 4 wks post-op, a better mineralized tissue in samples with Sr-substituted bioactive glass than in those with 45S5 Bioglass coating.	
Mg-BASED SUBSTRATES	**CERAMICS**	Mg alloy (AZ91)	Merwinite	Rabbit (femur: greatee trochanter) (n=3)	1	a) Uncoated (n=1) b) PEO-coated (n=1)	8	- Blood tests – - Radiographs - Histological analysis - Histomorphometric analysis - Measurement of implant weight loss	- On 2- wks post-op radiographs: uncoated samples showed higher gas formation than PEO-coated ones, while no gas on test samples. - 2 months post-op new bone volume: merwinite (44 %) > PEO-coated (31 %) > uncoated (27 %). - 2 months post-op: weight loss for uncoated, PEO-coated and merwinite coated implants was 25, 16, and 5 mg/cm^2, respectively.	[67]
		Mg alloy (AZ91)	Diopside	Rabbit (femur: greatee trochanter) (n not specified)	Not specified	a) Uncoated (n not specified) b) MAO coated (n not specified)	8	- Blood tests – - Radiographs - Histological analysis - Histomorphometric analysis - Measurement of implant weight loss	- No gas formation was clinically observed in any group. - On 2- wks post-op radiographs: uncoated samples showed higher gas formation than MAO-coated ones, no gas on test samples. - 2 months post-op, volume percentage of newly formed bone around implants: diopside coated (65%) > MAO-coated (31%) > uncoated (27%) samples. - 2 months post-op: the weight loss for uncoated, MAO-coated and diopside coated implants was 25, 16, and 7 mg/cm^2, respectively.	[65]

* sample size (number of animals) into brackets; § number of control implants into brackets; BA%= peri-implant bone area percentage; BIC = Bone-Implant Contact; PEO: Plasma Electrolytic Oxidation; SAXS = angle X-ray scattering; TRAP = Tartrate-Resistant Acid Phosphatase; wks = weeks.

Six studies evaluated implants placed in the long bones (femur and tibia) of rats, [57,62,157] or rabbits [65,67,148], while in the remaining 4 studies implants were tested in larger animal models [137,140,151,152].

The inclusion of one or multiple control groups in the study design is considered of particular interest [192]. Concerning this aspect, in all studies apart from one [157] coated implants were compared to control implants.

As good adhesion of the coating to the substrate is crucial for the success of the implants, it would be interesting to verify if mechanical test could predict the bonding of the coating once implanted *in vivo*. Unfortunately, in only one paper preliminary adhesion tests prior to *in vivo* phase are reported [140], so any comparison between the studies can't be carried out.

As shown in **Figure 6**, metallic implants coated by bioactive coating were found to induce the new bone formation *in vivo*.

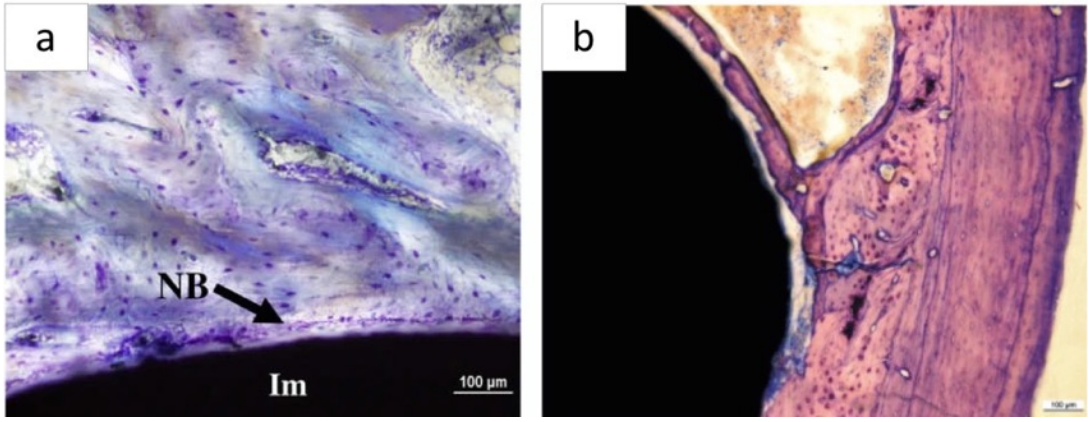

Figure 6. Histological morphology of the interface between the implant and the bone tissue of: (a) sphene-coated Ti-6Al-4V implant after 6 weeks of healing (Toluidine blue); from Ramaswamy et al., 2009 [137] (b) stainless steel implant coated with hybrid organic-inorganic bioactive coating containing wollastonite after 60 days of healing (Toluidine blue); from Ballarre et al, 2011 [157]. Im, implant; NB, new bone.

1.1.8.1. In vivo evaluation of bioactive coatings on Ti-based implants

HA has been extensively used as coating material for Ti implants. Interestingly, in the 5 studies analyzing the osseointegration of coated Ti-based implants, the test samples were always compared to HA-coated implants, while only three times to uncoated implants.

In Ramaswamy et al. [137], a similar bone to implant contact percentage was obtained by both sphene- and HA-coated Ti–6Al–4V implants. Contrary to uncoated samples, no

fibrous tissue was detected around the coated implants, as also indicated by the expression of ALP and by the presence of osteoclasts at the interface. Moreover, sphene-coated implants exhibited higher push-out values than uncoated implants, confirming the ability to strongly bond to the bone tissue.

Accordingly, in another study investigating silica-based ceramic coatings in a dog model, a better osseointegration was observed in presence of hardystonite and strontium-substituted hardystonite when compared to HA-coated and uncoated Ti implants [140]. It was demonstrated that strontium-substituted hardystonite-coated implants presented the highest osseointegration, followed in order by hardystonite-coated, HA-coated and, finally, uncoated implants.

The beneficial effect of strontium, in combination with a bioactive glass, was also demonstrated. In Newman et al. [148], strontium-substituted bioactive glass-coated implants exhibited superior push-out strength than HA-coated controls, with a trend for increasing maximal shear strength over time. Interestingly, this is the only paper, among the ones analyzed in the present review, in which three different implantation periods were used (i.e. 6, 12 and 24 weeks). This characteristic was of help in the evaluation of this tendency. Moreover, it is to note that the majority of bioactive glass coating dissolved over a 6-week time, thus stimulating bone formation around the implants.

The biological performances of Ti dental implants coated with composite HA/bioactive glass coatings were compared to those of HA-coated implants in both dog mandible [151] and goat iliac crest models [152].

When inserted in the healed sites in the mandible of Beagle dogs, implants with a high amount of bioactive glass ($HABG_{High}$) showed significantly lower BIC% in comparison both HA- and $HABG_{Low}$-coated implants at 4 weeks post-operatively [151]. Nevertheless, after 12 weeks of healing, histomorphometical analysis revealed no significant differences between the experimental groups.

Furthermore, histological and histomorphometrical assessments, performed at 4 and 12 weeks after implantation in a goat iliac crest model, revealed that the incorporation of bioactive glass into the HA coating had significantly improved implant osseointegration as compared to uncoated implants [152]. However, similar results in terms of BIC% could be observed between HA- and HABG coated implants after 12 weeks of healing.

1.1.8.2. In vivo evaluation of bioactive coatings on stainless steel implants

Regarding stainless steel substrates, hybrid organic–inorganic coatings containing wollastonite [62,157] or bioactive glass [57], produced by sol-gel technique and deposited by dip-coating, were tested in rat femur models.

In vivo osseointegration ability of hybrid organic–inorganic coatings functionalized with wollastonite was analyzed after 60 days of implantation. The newly formed bone around coated implants was characterized by osteoid and osteocyte lacunae, as well as by a laminar structure presenting osteoblasts at the interface [62,157]. In addition, in Ballarre et al. [62] a fibrous tissue encapsulating the uncoated control implants was observed.

Consistently with these findings, also the use of bioactive glass particles as a disperse phase in sol-gel protective coatings was found to enhance the bioactivity of stainless steel implants [57]. An improved bone regeneration was documented for both kinds of coated implants as compared to uncoated ones. Nevertheless, coatings containing Sr-substituted bioactive glass were found to induce higher bone mineralization in the surrounding bone tissues than Bioglass 45S5-coated ones, in particular at the early phases after implantation.

1.1.8.3. In vivo evaluation of bioactive coatings on Mg-based implants

As previously mentioned, the main criticism of the use of Mg implants is their rapid degradability, leading to the early loss of the integrity of the implant and to undesired bubble formation. These two critical aspects were analyzed in both the animal studies on coated Mg alloys included in the present review. Resorbable Mg alloy implants coated with bioactive silica-based ceramics were tested in an experimental rabbit model [65,67].

The *in vivo* biocompatibility of double layer diopside/MAO coated AZ91 magnesium implants was examined in comparison with uncoated and MAO coated implants [65]. As mentioned above, one of the main drawbacks of Mg alloys is the formation of hydrogen gas due to the rapid corrosion of the implant [69]. Contrary to control implants, no bubble formation was visible on radiographs of diopside coated samples 2 weeks after surgery. As confirmed by histological analysis of 2 months post-op, the volume percentage of newly formed bone around diopside coated samples was approximately the double of that of control implants. Moreover, a limited implant weight loss of 2 months after implantation was observed in the test group compared to the control ones [65].

Using the same animal model, Razavi et al. [67] evaluated the biocompatibility of merwinite/PEO coating on the Mg alloy implants. As in the previous work, no gas bubbles were observed around implants with the bioceramic coating, whereas a few bubbles were detectable around PEO-coated samples and to a greater extent around uncoated implants. Additionally, the animals were sacrificed at two months post-operatively also in this work [67]. In accordance with what reported in the previous study [65], the new bone volume percent was higher in the test group than in the control group. However, a lower amount of new bone formation was reported for merwinite/PEO coated implants (44%) than for diopside/MAO coated ones (65%). Similarly to the previous study, implant weight loss at the end of the *in vivo* examination was higher in absence of bioceramic coating, thus confirming the role of silica-based ceramic coatings in protecting magnesium substrates from fast corrosion.

In the studies included in the present review, numerous silica-based bioactive coatings were applied. Despite the variety of animal models adopted and the numerous substrates and bioactive coatings utilized, a common trend towards an improved osseointegration of coated samples as compared to uncoated ones was observed in the majority of the studies.

1.1.9. Conclusions

Mechanical and *in vitro* biological analyses have demonstrated that bioactive glass-based and silicate ceramic coatings could be promising coating materials for orthopedic and dental applications. When optimized process parameters are used, new coatings deposited onto metallic implants seem to have appropriate adhesive properties to the substrates, overcoming the main drawbacks related to the use of previous generation of HA implants. Moreover, coatings deposited onto Mg alloy substrates were found to play a crucial role as protective barriers retarding the contact between the Mg alloy and the solution, thus favoring the maintenance of the mechanical integrity over a longer period of time. The bioactivity of the coatings has been investigated mainly by means of SBF immersion tests. Bioactive glass and silicate-based ceramic coatings showed sufficient efficiency of the apatite mineralization in SBF, higher than that of hydroxyapatite. The apatite forming ability and dissolution rate mainly depended on the chemical composition and structure of these coatings as well as the coating process, which controlled the total porosity and surface area of the coatings, in contact with the SBF. These parameters are

useful tools for adjusting the coated implant performance in terms of dissolution rate, apatite formation and the mechanical stability of the coating. It has to be noted that available *in vivo* data on metallic implants coated with bioactive glass/glass-ceramics or silica-based ceramics are limited. Hence, it seems fundamental to expand the knowledge on the influence of chemical composition, mechanical properties and surface features of the coatings on implant performances *in vitro*, but also in preclinical study in animal models, and then in human clinical trials.

1.2. Bioactive Sphene ($CaTiSiO_5$) Ceramic coatings for Dental Implants

1.2.1. Introduction

From the analysis of the current literature presented in the previous section (see **Section 1.1**), silicate ceramics have emerged as promising coating materials for both orthopedic and dental applications. Among silicate bioceramics, sphene has recently received significant attention for its potential use in medical devices, however it is still a largely unexplored area of research.

Sphene or titanite ($CaTiSiO_5$) is an orthosilicate mineral. Its structure is characterized by [TiO_6] octahedra and [SiO_4] tetrahedra. The former link to create kinked chains by sharing O atoms at the corner, and the latter link the chains of the octahedra [195,196]. The crystal structure of sphene is represented in **Figure 7** and its main features are listed in **Table 9**.

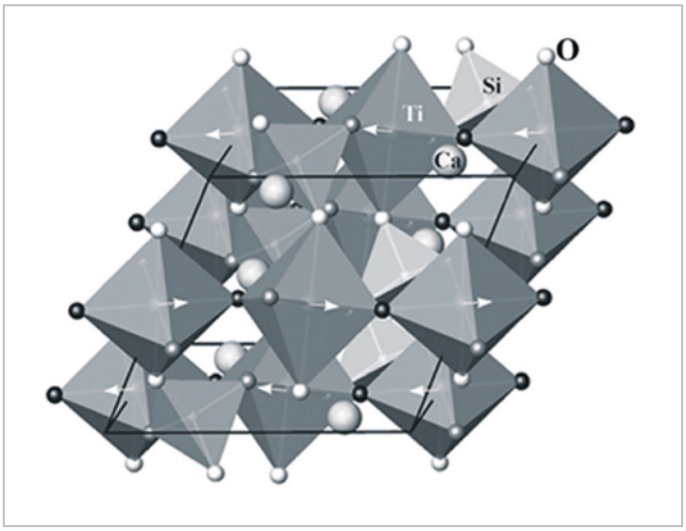

Figure 7. Crystal structure of sphene, mod. From Fan et al., 2018 [196]

Table 9. Composition, thermal and physical properties (dense structure) of sphene [126,127,197].

Characteristic	Value
Composition	$CaTiSiO_5$
ϱ [Kg/m^3]	3539
E [GPa]	112.3*

CTE [$10^{-6}K^{-1}$]	6

CTE = coefficient of linear thermal expansion; E = Modulus of Elasticity; ϱ = density; * value obtained by nanoindentation.

Sphene is predominantly used for nuclear waste disposal [198-200]. Apart from being intended for radioactive waste immobilization, sphene ceramic has been recently proposed as a coating material for dental and orthopedic applications [127,132,135-138].

It has been demonstrated that the dissolution of soluble silicon (Si) and calcium (Ca) ions from bioactive glasses promotes new bone formation [201], however their high degradation rate is considered a hindrance to their use as coating materials.

In this context, sphene-based coatings have received great attention, due to their bioactivity, slow dissolution rate and high bonding strength, thanks to the similarity of sphene CTE to that of the Ti-based substrates [101,138]. Hence, sphene seems to be a promising candidate as implant coating material.

An overview on this biomaterial, which represents the object of the present thesis, is here provided.

1.2.2. Overview of current literature about the use of sphene as coating material for biomedical applications

Researches regarding bioactive coatings started about a decade ago. For this reason, the starting point of my project consisted in the review of the current literatures about the use of sphene ceramic as bioactive coating on titanium implants.

1.2.2.1 Method

The Scopus database was used as searching tool to find articles that were published in the English language between 2006 and 2016, about the use of sphene ceramic as coating material deposited onto Ti or Ti alloy substrate for dental and orthopedic applications. The search was executed with various combinations of the following keywords: “implant”, “sphene”, “titanite”, “coating” in the publications title, abstract and keywords. A similar search on Medline (PubMed) was performed for completeness. Only original articles published in peer-reviewed journals were considered.

1.2.2.2 Results and Discussion

Literature review identified 6 published articles which met the inclusion criteria. The publications consisted of 5 *in vitro* studies [127,132,135,136,138] and 1 includes both *in vitro* and *in vivo* animal study [137]. In the latter *in vitro* tests were performed using pure sphene ceramic disks, therefore only the findings from *in vivo* tests will be discussed.

Sphene ceramics were produced as coatings on Ti6Al4V or commercially pure Ti substrates using various synthesis and deposition methods. The reported substrate roughness ranged from a minimum of 0.1 μm to a maximum of 2.15 μm. The main features of the substrates and of the coating productive process are summarized in **Table 10**.

Table 10. Main features of the substrates and of the coating productive process.

Substrate	Substrate Ra [μm]	Synthesis method of $CaTiSiO_5$	Synthesis temperature [°C]	Coating deposition method	Ref.
CpTi plates	2.1	Polymer-derived ceramics route	950	Airbrushing	[132]
Ti-6Al-4V discs	–	Solid phase reaction	1290	Plasma-spraying	[135]
Ti plates	–	Liquid phase reaction	400 – 900	Micro-Arc Oxidation	[136]
Ti–6Al–4V cylindrical implants	0.1	Sol-gel	875	Dip-Coating	[137]
Ti-6Al-4V discs	0.5	Sol-gel	1100	Plasma-spraying	[127]
Ti-6Al-4V discs	0.1	Sol-gel	875	Spin-coating	[138]

The reported thickness of coatings varied approximately from 1 to 150 μm (**Table 11**). This property is related to the production process. The thickest coatings were produced by plasma-spraying, which were characterized by a highly dense inner microstructure and rough surface [127]. In Biasetto et al. [132], thickness of the coatings, applied using the

airbrush coating technique, was controlled by modifying the deposition process parameters. Whereas thinner coatings were produced by Micro-Arc Oxidation (MAO) [136] or spin-coating [138].

Table 11. Roughness and thickness of sphene-based coatings.

Roughness (method)	Coating roughness Ra [µm]	Thickness (method)	Coating thickness [µm]	Ref.
Stylus profilometer	4-6.5	FEG-SEM	50 – 100	[132]
Stylus profilometer	7.5	_	_	[135]
_	_	SEM	≤ 21	[136]
AFM	10	SEM	150	[127]
AFM	0.38 ± 0.04	SEM	0.5-1	[138]

*AFM: Atom Force Microscopy;

X-ray diffraction (XRD) analysis is commonly applied to characterize ceramic materials for biomedical devices, as the crystallinity of the ceramic coating as well as the crystalline phase composition are believed to influence the biological response to the coatings [202]. Coating characterization is reported in **Table 12**.

Table 12. X-ray diffraction (XRD) characterization of the coatings.

Sphene ($CaTiSiO_5$)	Titanium dioxide (TiO_2)	Perovskite ($CaTiO_3$)	Ref.
X	X	X	[132]
X	–	–	[135]
X	–	–	[136]
X	–	X	[127]
X	–	–	[138]

The adhesion strength of sphene coatings has been reported in 4 articles (see **Table 13**). Sphene coatings exhibited improved bonding strength, when compared to hydroxyapatite coatings [138]. Higher bonding strength values are reported in Wu et al. [127]. Consistently, on SEM cross section no microcracks were observed at the interface between plasma-sprayed sphene coating and the Ti-6Al-4V substrate. In all cases the values obtained for sphene coatings were higher than 15 MPa required by international standard for bioactive HA coating implants (ISO 13779-2). In addition, an improved bonding strength was achieved with sphene-based coatings, as compared to 10-20 MPa commonly reported for HA coatings [203-205].

Table 13: Adhesion strength of the coatings to the substrates.

Test performed	Adhesion strength of sphene coating [MPa]	Control coating material	Adhesion strength of control coating [MPa]	Ref.
Scratch test	70.5±7.5	–	–	[132]
ASTM C-633	41.0±3.5	Hardystonite	27.0±3.9	[135]
ASTM C-633	33.2±2.4	–	–	[127]
Scratch test	17.4±0.9	Hydroxyapatite	9.8±0.6	[138]

For the evaluation of the chemical stability of the coatings, in three studies the samples were tested by immersion in the buffer solution of tris-(hydroxymethyl)-aminomethane (Tris, $(CH_2OH)_3CNH_2$) and hydrochloric acid (HCl) with a pH of 7.4 (see **Table 14**). Sphene-coated samples presented a significantly improved chemical stability compared to HA coatings, as confirmed by the profile element distribution and the dissolution kinetics of calcium ions after immersion in Tris-HCl [138]. These findings are in agreement with Wu et al. [127], confirming the higher chemical stability of sphene compared to that of HA. In addition, the morphology of coatings after 7 days of soaking in Tris-HCl was analyzed by scanning electron microscopy (SEM) images, showing no visible alterations on sphene-coated samples. Whereas, detectable surface modifications were identified on HA coatings.

Wang et al. [135] used hardystonite ($Ca_2ZnSi_2O_7$) coatings as controls. In this work, not only Ca, but also the concentrations of other ions (i.e. silicium, zirconium and titanium) released in the Tris-HCl buffered solution were investigated. The released amount of Ca and Si ions from hardystonite-coated samples was significantly higher ($p < 0.05$) than that from the sphene-coated ones. It is worth noting, that only trace amount (0.014 ppm) of Ti ions was released from the sphene coating, which is unlucky to provoke any toxic effects in humans [206].

Table 14. Chemical stability in Tris-HCl buffer solution

Soaking time in Tris-HCl (days)	pH of the solution	Concentration of ions in the solution (ICP-AES)*	Ref.
7	Higher increase in pH values after immersion of hardystonite coatings when compared with that for sphene coatings	Higher release of Ca and Si ions from hardystonite-coated samples than that from sphene-coated ones ($p < 0.05$)	[135]
1, 3, 7	–	Sphene coating: lower dissolution kinetics constant compared with that of HA coating	[127]
1, 3, 7	–	Sphene coating: lower Ca dissolution kinetics (0.00025) compared with that of HA coating (0.00138)	[138]

* ICP-AES: Inductively Coupled Plasma Atomic Emission Spectroscopy

Apatite formation ability in simulated body fluids (SBF), which is a common test to preliminary assess *in vitro* the bioactivity of a material, was used only by Wu et al. [138]. SEM coupled with energy-dispersive spectrometer (EDS) confirmed the presence of a layer of apatite on sphene-coated Ti–6Al–4V samples after soaking in SBF for 21 days.

Moreover, when osteoblast-like cells were cultured for 7 days onto sphene-coated Ti-based substrates, positive results in terms of cell attachment, spreading and proliferation were observed [127,135]. Interestingly, when compared to uncoated and HA-coated Ti-

6Al-4V control samples, a significantly higher cell proliferation and alkaline phosphatase activity was found when cells had been seeded onto sphene coatings ($p < 0.05$) [127].

Finally, *in vivo* bone formation around Ti6Al4V implants coated with sphene was demonstrated in sheep femurs after 6 weeks, showing bone to implant contact (BIC%) measurements and push-out strength values comparable to that of hydroxyapatite coatings [137]. From the analysis of histological sections stained with toluidine blue, similar BIC% values, above 70% in both cortico-cancellous and the cortical bone, where found for both sphene- and HA-coated implants. Whereas a significant reduction in bone-implant contact was observed when cortico-cancellous uncoated Ti–6Al–4V implants were used, due to the formation of a band of fibrous tissue at the interface between the implant and the bone. Regarding the push-out mechanical testing, it showed comparable results for sphene- and HA-coated sample, higher than those of uncoated Ti-Al6-4V, when implants where placed in cortico-cancellous bone. In addition, when inserted in cortical bone, sphene-coated implants presented similar values to those of HAp-coated implants, but significantly higher values than uncoated Ti–6Al–4V.

In conclusion, sphene ceramics seem to be safe and promising materials as coating for orthopedic and dental implants. However, it is still a relatively unexplored area of research and further pre-clinical studies are needed before clinical application.

References

1. Catauro, M.; Papale, F.; Bollino, F. Coatings of titanium substrates with xCaO · (1- x)SiO2 sol-gel materials: characterization, bioactivity and biocompatibility evaluation. Mater. Sci. Eng. C Mater. Biol. Appl. 2016, 58, 846–851. DOI: 10.1016/j.msec.2015.09.033.

2. Moritz, N.; Rossi, S.; Vedel, E.; Tirri, T.; Ylänen, H.; Aro, H.; Närhi, T. Implants coated with bioactive glass by CO2-laser, an in vivo study. J. Mater. Sci. Mater. Med. 2004, 15, 795–802. DOI: 10.1023/B:JMSM.0000032820.50983.c1.

3. Beloti, M.M.; Rollo, J.M.; Itman Filho, A.; Rosa, A.L. In vitro biocompatibility of duplex stainless steel with and without 0.2% niobium. J. Appl. Biomater. Biomech. 2004, 2, 162–168. DOI: 10.1177/228080000400200306.

4. Liu, X.; Chu, P.K.; Ding, C. Surface modification of titanium, titanium alloys, and related materials for biomedical applications. Mater. Sci. Eng. R Rep. 2004, 47, 49–121. DOI: 10.1016/j.mser.2004.11.001.

5. Talha, M.; Behera, C.K.; Sinha, O.P. A review on nickel-free nitrogen containing austenitic stainless steels for biomedical applications. Mater. Sci. Eng. C Mater. Biol. Appl. 2013, 33, 3563–3575. DOI: 10.1016/j.msec.2013.06.002.

6. Niinomi, M. Mechanical properties of biomedical titanium alloys. Mater. Sci. Eng. A 1998, 243, 231–236. DOI: 10.1016/S0921-5093(97)00806-X.

7. Palmquist, A.; Omar, O.M.; Esposito, M.; Lausmaa, J.; Thomsen, P. Titanium oral implants: surface characteristics, interface biology and clinical outcome. J. R. Soc Interface 2010, 7, S515–S527. DOI: 10.1098/rsif.2010.0118.focus.

8. Li, X.; Ma, X.Y.; Feng, Y.F.; Ma, Z.S.; Wang, J.; Ma, T.C.; Qi, W.; Lei, W.; Wang, L. Osseointegration of chitosan coated porous titanium alloy implant by reactive oxygen species-mediated activation of the PI3K/AKT pathway under diabetic conditions. Biomaterials 2015, 36, 44–54. DOI: 10.1016/j.biomaterials.2014.09.012.

9. Staiger, M.P.; Pietak, A.M.; Huadmai, J.; Dias, G. Magnesium and its alloys as orthopedic biomaterials: a review. Biomaterials 2006, 27, 1728–1734. DOI: 10.1016/j.biomaterials.2005.10.003.

10. Lin, D.J.; Hung, F.Y.; Jakfar, S.; Yeh, M.L. Tailored coating chemistry and interfacial properties for construction of bioactive ceramic coatings on magnesium biomaterial. Mater. Des. 2016, 89, 235–244. DOI: 10.1016/j.matdes.2015.09.144.

11. Lee, H.P.; Lin, D.J.; Yeh, M.L. Phenolic Modified Ceramic Coating on Biodegradable Mg Alloy: The Improved Corrosion Resistance and Osteoblast-Like Cell Activity. Materials 2017, 10, 696. DOI: 10.3390/ma10070696.

12. Zhang, F.; Cai, S.; Xu, G.; Shen, S.; Li, Y.; Zhang, M.; Wu, X. Corrosion behavior of mesoporous bioglass-ceramic coated magnesium alloy under applied forces. J. Mech. Behav. Biomed. Mater. 2016, 56, 146–155. DOI: 10.1016/j.jmbbm.2015.11.029.

13. Wang, H.Y.; Zhu, R.F.; Lu, Y.P.; Xiao, G.Y.; He, K.; Yuan, Y.F.; Ma, X.N.; Li, Y. Effect of sandblasting intensity on microstructures and properties of pure titanium microarc oxidation coatings in an optimized composite technique. Appl. Surf. Sci. 2014, 292, 204–212. DOI: 10.1016/j.apsusc.2013.11.115.

14. Civantos, A.; Martínez-Campos, E.; Ramos, V.; Elvira, C.; Gallardo, A.; Abarrategi, A. Titanium coatings and surface modifications: toward clinically useful bioactive implants. ACS Biomater. Sci. Eng. 2017, 3, 1245–1261. DOI: 10.1021/acsbiomaterials.6b00604.

15. Catauro, M.; Bollino, F.; Papale, F. Biocompatibility improvement of titanium implants by coating with hybrid materials synthesized by sol-gel technique. J Biomed Mater Res A. 2014, 102, 4473–4479. DOI: 10.1002/jbm.a.35116.

16. Midha, S.; Kim, T.B.; van den Bergh, W.; Lee, P.D.; Jones, J.R.; Mitchell, C.A. Preconditioned 70S30C bioactive glass foams promote osteogenesis in vivo. Acta Biomater. 2013, 9, 9169–9182. DOI: 10.1016/j.actbio.2013.07.014.

17. Niinomi M. Recent metallic materials for biomedical applications. Met. Mater. Trans. A 2002, 33, 477–486. DOI: 10.1007/s11661-002-0109-2.

18. Deen, J.T.; Clay, T.B.; Iams, D.A.; Horodyski, M.; Parvataneni, H.K. Proximal tibial resorption in a modern total knee prosthesis. Arthroplast. Today. 2017, 4, 244–248. DOI: 10.1016/j.artd.2017.10.005.

19. Inoue, K.; Suenaga, N.; Oizumi, N.; Yamaguchi, H.; Miyoshi, N.; Taniguchi, N.; Munemoto, M.; Egawa, T.; Tanaka, Y. Humeral bone resorption after anatomic shoulder arthroplasty using an uncemented stem. J. Shoulder Elbow Surg. 2017, 26, 1984–1989. DOI: 10.1016/j.jse.2017.04.012.

20. Spormann, C.; Durchholz, H.; Audigé, L.; Flury, M.; Schwyzer, H.K.; Simmen, B.R.; Kolling, C. Patterns of proximal humeral bone resorption after total shoulder arthroplasty with an uncemented rectangular stem. J. Shoulder Elbow Surg. 2014, 23, 1028–1035. DOI: 10.1016/j.jse.2014.02.024.

21. Cilla, M.; Checa, S.; Duda, G.N. Strain shielding inspired re-design of proximal femoral stems for total hip arthroplasty. J. Orthop. Res. 2017, 35, 2534–2544. DOI: 10.1002/jor.23540.

22. Bayata, F.; Yildiz, C. The Mechanical behaviors of various dental implant materials under fatigue. Adv. Mater. Sci. Eng. 2018, 2018, 5047319. DOI: 10.1155/2018/5047319.

23. Cui, W.; Liu, Y. Fatigue behavior of Ti50Zr alloy for dental applications. J Alloy. Compd. 2019, 793, 212–219. DOI: 10.1016/j.jallcom.2019.04.165.

24. Najdahmadi, A.; Zarei-Hanzaki, A.; Farghadani, E. Mechanical properties enhancement in Ti–29Nb–13Ta–4.6Zr alloy via heat treatment with no detrimental effect on its biocompatibility. Mater. Design 2014, 54, 786–791. DOI: 10.1016/j.matdes.2013.09.007.

25. Herrera, A.; Mateo, J.; Lobo-Escolar, A.; Panisello, J.J.; Ibarz, E.; Gracia, L. Long-term outcomes of a new model of anatomical hydroxyapatite-coated hip prosthesis. J. Arthroplasty 2013, 28, 1160–1166. DOI: 10.1016/j.arth.2012.06.033.

26. Dallago, M.; Fontanari, V.; Torresani, E.; Leoni, M.; Pederzolli, C.; Potrich, C.; Benedetti, M. Fatigue and biological properties of Ti-6Al-4V ELI cellular structures with variously arranged cubic cells made by selective laser melting. J Mech Behav Biomed Mater. 2018, 78, 381–394. DOI: 10.1016/j.jmbbm.2017.11.044.

27. Vladescu, A.; Mihai Cotrut, C.; Ak Azem, F.; Bramowicz, M.; Pana, I.; Braic, V.; Birlik, I.; Kiss, A.; Braic, M.; Abdulgader, R.; Booysen, R.; Kulesza, S.; Monsees, T.K. Sputtered Si and Mg doped hydroxyapatite for biomedical applications. Biomed. Mater. 2018, 13, 025011. DOI: 10.1088/1748-605X/aa9718.

28. Hedia, H.S.; Fouda, N. Design optimization of cementless hip prosthesis coating through functionally graded material. Comput. Mater. Sci. 2014, 87, 83–87. DOI: 10.1016/j.commatsci.2014.02.007.

29. Wiskott, H.W.; Belser, U.C. Lack of integration of smooth titanium surfaces: a working hypothesis based on strains generated in the surrounding bone. Clin. Oral Implants Res. 1999, 10, 429–444. DOI: 10.1034/j.1600-0501.1999.100601.x.

30. Korabi, R.; Shemtov-Yona, K.; Rittel, D. On stress/strain shielding and the material stiffness paradigm for dental implants. Clin. Implant Dent. Relat. Res. 2017, 19, 935–943. DOI: 10.1111/cid.12509.

31. Nagano, M.; Nakamura, T.; Kokubo, T.; Tanahashi, M.; Ogawa, M. Differences of bone bonding ability and degradation behaviour in vivo between amorphous calcium phosphate and highly crystalline hydroxyapatite coating. Biomaterials 1996, 17, 1771–1777. 10.1016/0142-9612(95)00357-6.

32. Lin, D.Y.; Wang, X.X. A novel method to synthesize hydroxyapatite coating with hierarchical structure. Colloids Surf. B Biointerfaces 2011, 82, 637–640. DOI: 10.1016/j.colsurfb.2010.09.025.

33. Roy, M.; Bandyopadhyay, A.; Bose, S. Induction plasma sprayed nano hydroxyapatite coatings on titanium for orthopaedic and dental implants. Surf. Coat. Technol. 2011, 205, 2785–2792. DOI: 10.1016/j.surfcoat.2010.10.042.

34. Tsui, Y.C.; Doyle, C.; Clyne, T.W. Plasma sprayed hydroxyapatite coatings on titanium substrates. Part 1: Mechanical properties and residual stress levels. Biomaterials 1998, 19, 2015–2029. DOI: 10.1016/S0142-9612(98)00103-3.

35. Kweh, S.W.; Khor, K.A.; Cheang, P. An in vitro investigation of plasma sprayed hydroxyapatite (HA) coatings produced with flame-spheroidized feedstock. Biomaterials 2002, 23, 775–785. DOI: 10.1016/S0142-9612(01)00183-1.

36. Bauer, T.W.; Geesink, R.C.; Zimmerman, R.; McMahon, J.T. Hydroxyapatite-coated femoral stems. Histological analysis of components retrieved at autopsy. J. Bone Joint Surg. Am. 1991, 73, 1439–1452. DOI: 10.1302/0301-620X.81B1.0810148.

37. Elsayed H, Brunello G, Gardin C, Ferroni L, Badocco D, Pastore P, Sivolella S, Zavan B, Biasetto L. Bioactive sphene-based ceramic coatings on cpTi substrates for dental implants: an in vitro study. Materials 2018, 11, 2234. DOI: 10.3390/ma11112234.

38. Bloyer, D.R.; Gomez-Vega, J.M.; Saiz, E.; McNaney, J.M.; Cannon, R.M.; Tomsia, A.P. Fabrication and characterization of a bioactive glass coating on titanium implant alloys. Acta materialia 1999, 47, 4221–4224. DOI: 10.1016/S1359-6454(99)00280-3.

39. Yang, H.; Zhu, Q.; Qi, H.; Liu, X.; Ma, M.; Chen, Q. A facile flow-casting production of bioactive glass coatings on porous titanium for bone tissue engineering. Materials 2018, 11, 1540. DOI: 10.3390/ma11091540.

40. Fu, Y.C.; Chen, C.H.; Wang, C.Z.; Wang, Y.H.; Chang, J.K.; Wang, G.J.; Ho, M.L.; Wang, C.K. Preparation of porous bioceramics using reverse thermo-responsive hydrogels in combination with rhBMP-2 carriers: in vitro and in vivo evaluation. J. Mech. Behav. Biomed. Mater. 2013, 27, 64–76. DOI: 10.1016/j.jmbbm.2013.06.009.

41. Hankenson, K.D.; Gagne, K.; Shaughnessy, M. Extracellular signaling molecules to promote fracture healing and bone regeneration. Adv. Drug. Deliv. Rev. 2015, 94, 3–12. DOI: 10.1016/j.addr.2015.09.008.

42. Kose, N.; Çaylak, R.; Pekşen, C.; Kiremitçi, A.; Burukoglu, D.; Koparal, S.; Doğan, A. Silver ion doped ceramic nano-powder coated nails prevent infection in open fractures: In vivo study. Injury 2016, 47, 320–324. DOI: 10.1016/j.injury.2015.10.006.

43. Sivolella, S.; Stellini, E.; Brunello, G.; Gardin, C.; Ferroni, L.; Bressan, E.; Zavan, B. Silver nanoparticles in alveolar bone surgery devices. J. Nanomater. 2012, 2012, Article ID 975842. DOI: 10.1155/2012/975842

44. Jäger, M.; Jennissen, H.P.; Dittrich, F.; Fischer, A.; Köhling, H.L. antimicrobial and osseointegration properties of nanostructured titanium orthopaedic implants. Materials 2017, 10, 1302. DOI: 10.3390/ma10111302.

45. Niinomi, M. Mechanical biocompatibilities of titanium alloys for biomedical applications. J. Mech. Behav. Biomed. Mater. 2008, 1, 30–42. DOI: 10.1016/j.jmbbm.2007.07.001.

46. Pellegrini, G.; Francetti, L.; Barbaro, B.; Del Fabbro, M. Novel surfaces and osseointegration in implant dentistry. J. Investig. Clin. Dent. 2018, 9, e12349. DOI: 10.1111/jicd.12349.

47. Shah, F.A.; Trobos, M.; Thomsen, P.; Palmquist, A. Commercially pure titanium (cp-Ti) versus titanium alloy (Ti6Al4V) materials as bone anchored implants - Is one truly better than the other? Mater. Sci. Eng. C Mater. Biol. Appl. 2016, 62, 960–966. DOI: 10.1016/j.msec.2016.01.032.

48. Zakaria, M.Y.; Sulong, A.B.; Muhamad, N.; Raza, M.R.; Ramli, M.I. Incorporation of wollastonite bioactive ceramic with titanium for medical applications: An overview. Mater. Sci. Eng. C Mater. Biol. Appl. 2019, 97, 884–895. DOI:10.1016/j.msec.2018.12.056.

49. Costa, B.C.; Tokuhara, C.K.; Rocha, L.A.; Oliveira, R.C.; Lisboa-Filho, P.N.; Costa Pessoa, J. Vanadium ionic species from degradation of Ti-6Al-4V metallic implants: In vitro cytotoxicity and speciation evaluation. Mater Sci Eng C Mater Biol Appl. 2019, 96, 730–739. DOI: 10.1016/j.msec.2018.11.090.

50. Xu, W; Li, M.; Wen, C.; Lv, S.; Liu, C.; Lu, X.; Qu, X. The mechanical properties and in vitro biocompatibility of PM-fabricated Ti-28Nb-35.4Zr alloy for orthopedic implant applications. Materials 2018, 11, 531. DOI:10.3390/ma11040531.

51. Okazaki, Y.; Gotoh, E. Comparison of metal release from various metallic biomaterials in vitro. Biomaterials 2005, 26, 11–21. DOI: 10.1016/j.biomaterials.2004.02.005.

52. Atapour, M.; Pilchak, A.L.; Frankel, G.S.; Williams, J.C. Corrosion behavior of beta titanium alloys for biomedical applications. Mater. Sci. Eng. C Mater. Biol. Appl. 2011, 31, 885–891. DOI: 10.1016/j.msec.2011.02.005.

53. Wang, X.; Zhou, Y.; Xia, L.; Zhao, C.; Chen, L.; Yi, D.; Chang, J.; Huang, L.; Zheng, X.; Zhu, H.; Xie, Y.; Xu, Y.; Lin, K. Fabrication of nano-structured calcium silicate coatings with enhanced stability, bioactivity and osteogenic and angiogenic activity. Colloids Surf. B Biointerfaces 2015, 126, 358–366. DOI: 10.1016/j.colsurfb.2014.11.044.

54. Sevilla, P.; Cirera, A.; Dotor, J.; Gil, F.J.; Galindo-Moreno, P.; Aparicio, C. In vitro cell response on CP-Ti surfaces functionalized with TGF-β1 inhibitory peptides. J. Mater. Sci. Mater. Med. 2018, 29, 73. DOI: 10.1007/s10856-018-6082-0.

55. Yang, D.H.; Yoon, S.J.; Lee, D.W. Preparation and evaluation of dexamethasone (DEX)/Growth and Differentiation Factor-5 (GDF-5) surface-modified titanium using β-cyclodextrin-conjugated heparin (CD-Hep) for enhanced osteogenic activity in vitro and in vivo. Int. J. Mol. Sci. 2017, 18, 1695. DOI: 10.3390/ijms18081695.

56. Zhou, W.; Jia, Z.; Xiong, P.; Yan, J.; Li, Y.; Li, M.; Cheng, Y.; Zheng, Y. Bioinspired and biomimetic AgNPs/gentamicin-embedded silk fibroin coatings for robust antibacterial and osteogenetic applications. ACS Appl. Mater. Interfaces 2017, 9, 25830–25846. DOI: 10.1021/acsami.7b06757.

57. Omar, S.; Repp, F.; Desimone, P.M.; Weinkamer, R.; Wagermaier, W.; Ceré, S.; Ballarre, J. Sol–gel hybrid coatings with strontium-doped 45S5 glass particles for enhancing the performance of stainless steel implants: electrochemical, bioactive and in vivo response. J. Non-Cryst. Solids 2015, 425, 1–10. DOI: 10.1016/j.jnoncrysol.2015.05.024.

58. Sedriks, A.J. Corrosion of Stainless Steels. Wiley, New York, 1996.

59. Prasad, K.; Bazaka, O.; Chua, M.; Rochford, M.; Fedrick, L.; Spoor, J.; Symes, R.; Tieppo, M.; Collins, C.; Cao, A.; Markwell, D.; Ostrikov, K.K.; Bazaka, K. Metallic biomaterials: current challenges and opportunities. Materials 2017, 10, 884. doi: 10.3390/ma10080884.

60. Sumita, M.; Hanawa, T.; Teoh, S.H. Development of nitrogen-containing nickel-free austenitic stainless steels for metallic biomaterials-review. Mater. Sci. Eng. C Mater. Biol. Appl. 2004, 24, 753–760. DOI: 10.1016/j.msec.2004.08.030.

61. Thomann, U.I.; Uggowitzer, P.J. Wear–corrosion behavior of biocompatible austenitic stainless steels. Wear 2000, 239, 48–58. DOI: 10.1016/S0043-1648(99)00372-5.

62. Ballarre, J.; Liu, Y.; Mendoza, E.; Schell, H.; Díaz, F.; Orellano, J.C.; Fratzl, P.; García, C.; Ceré, S.M. Enhancing low cost stainless steel implants: bioactive silica-based sol-gel coatings with wollastonite particles. Int. J. Nano Biomaterials 2012, 4, 33–53. DOI: 10.1504/IJNBM.2012.048216.

63. Ballarre, J.; López, D.A.; Cavalieri, A.L. Frictional and adhesive behavior of organic–inorganic hybrid coatings on surgical grade stainless steel using nano-scratching technique. Wear 2009, 266, 1165–1170. DOI: 10.1016/j.wear.2009.03.029.

64. Farraro, K.F.; Kim, K.E.; Woo, S.L.; Flowers, J.R.; McCullough, M.B. Revolutionizing orthopaedic biomaterials: The potential of biodegradable and bioresorbable magnesium-based materials for functional tissue engineering. J. Biomech. 2014, 47, 1979–1986. DOI: 10.1016/j.jbiomech.2013.12.003.

65. Razavi, M.; Fathi, M.; Savabi, O.; Razavi, S.M.; Heidari, F.; Manshaei, M; Vashaee, D.; Tayebi, L. In vivo study of nanostructured diopside (CaMgSi2O6) coating on magnesium alloy as biodegradable orthopedic implants. Appl. Surf. Sci. 2014, 313, 60–66. DOI: 10.1016/j.apsusc.2014.05.130.

66. Razavi, M.; Fathi, M.; Savabi, O.; Tayebi, L.; Vashaee, D. Improvement of in vitro behavior of an Mg alloy using a nanostructured composite bioceramic coating. J. Mater. Sci. Mater. Med. 2018, 29, 159. DOI: 10.1007/s10856-018-6170-1.

67. Razavi, M.; Fathi, M.; Savabi, O.; Vashaee, D.; Tayebi, L. In vivo biocompatibility of Mg implants surface modified by nanostructured merwinite/PEO. J. Mater. Sci. Mater. Med. 2015, 26, 184. DOI: 10.1007/s10856-015-5514-3.

68. Song, G. Control of biodegradation of biocompatable magnesium alloys. Corros. Sci. 2007, 49, 1696–1701. DOI: 10.1016/j.corsci.2007.01.001.

69. Rau, J.V.; Antoniac, I.; Fosca, M.; De Bonis, A.; Blajan, A.I.; Cotrut, C.;,Graziani, V.; Curcio, M.; Cricenti, A.; Niculescu, M.; Ortenzi, M.; Teghil, R. Glass-ceramic coated Mg-Ca alloys for biomedical implant applications. Mater.

Sci. Eng. C Mater. Biol. Appl. 2016, 64, 362–369. DOI: 10.1016/j.msec.2016.03.100.

70. Witte, F. The history of biodegradable magnesium implants: a review. Acta Biomater. 2010, 6, 1680–1692. DOI: 10.1016/j.actbio.2010.02.028.

71. Ding, Y.; Wen, C.; Hodgson, P.; Li, Y. Effects of alloying elements on the corrosion behavior and biocompatibility of biodegradable magnesium alloys: a review. J. Mater. Chem. B 2014, 2, 1912–1933. DOI: 10.1039/c3tb21746a.

72. Li, L.; Gao, J.; Wang, Y. Evaluation of cyto-toxicity and corrosion behavior of alkali-heat-treated magnesium in simulated body fluid. Surf. Coat. Technol. 2004, 185, 92–98. DOI: 10.1016/j.surfcoat.2004.01.004.

73. Li, X.; Liu, X.; Wu, S.; Yeung, K.W.K.; Zheng, Y.; Chu, P.K. Design of magnesium alloys with controllable degradation for biomedical implants: From bulk to surface. Acta Biomater. 2016, 45, 2–30. DOI: 10.1016/j.actbio.2016.09.005.

74. Agarwal, S.; Curtin, J.; Duffy, B.; Jaiswal, S. Biodegradable magnesium alloys for orthopaedic applications: A review on corrosion, biocompatibility and surface modifications. Mater Sci Eng C Mater Biol Appl. 2016, 68, 948–963. DOI: 10.1016/j.msec.2016.06.020.

75. Hench, L.L. The story of Bioglass. J. Mater. Sci. Mater. Med. 2006, 17, 967–978. DOI: 10.1007/s10856-006-0432-z.

76. Cao, W.; Hench, L.L. Bioactive materials. Ceram. Int. 1996, 22, 493–507. DOI: 10.1016/0272-8842(95)00126-3.

77. Hench, L.L.; Paschall, H.A. Direct chemical bond of bioactive glass-ceramic materials to bone and muscle. J. Biomed. Mater. Res. 1973, 7, 25–42. DOI: 10.1002/jbm.820070304.

78. Xynos, I.D.; Hukkanen, M.V.; Batten, J.J.; Buttery, L.D.; Hench, L.L.; Polak, J.M. Bioglass 45S5 stimulates osteoblast turnover and enhances bone formation In vitro: implications and applications for bone tissue engineering. Calcif. Tissue Int. 2000, 67, 321–329. DOI: 10.1007/s002230001134

79. Stanley, H.R.; Hall, M.B.; Clark, A.E.; King, C.J. 3rd; Hench, L.L.; Berte, J.J. Using 45S5 bioglass cones as endosseous ridge maintenance implants to prevent alveolar ridge resorption: a 5-year evaluation. Int. J. Oral Maxillofac. Implants 1997, 12, 95–105.

80. Rust, K.R.; Singleton, G.T.; Wilson, J.; Antonelli, P.J. Bioglass middle ear prosthesis: long-term results. Am. J. Otol. 1996, 17, 371–374.

81. Hench, L.L. Bioceramics: from concept to clinic. J. Am. Ceram. Soc. 1991, 74, 1487–1510. DOI: 10.1111/j.1151-2916.1991.tb07132.x

82. Jones, J.R. Review of bioactive glass: from Hench to hybrids. Acta Biomater. 2013, 9, 4457–4486. DOI: 10.1016/j.actbio.2012.08.023.

83. Du Min, Q.; Bian, Z.; Jiang, H.; Greenspan, D.C.; Burwell, A.K.; Zhong, J.; Tai, B.J. Clinical evaluation of a dentifrice containing calcium sodium phosphosilicate (novamin) for the treatment of dentin hypersensitivity. Am. J. Dent. 2008, 21, 210–214.

84. El-Rashidy, A.A.; Roether, J.A.; Harhaus, L.; Kneser, U.; Boccaccini, A.R. Regenerating bone with bioactive glass scaffolds: A review of in vivo studies in bone defect models. Acta Biomater. 2017, 62, 1–28. DOI: 10.1016/j.actbio.2017.08.030.

85. Tripathi, H.; Rath, C.; Kumar, A.S.; Manna, P.P.; Singh, S.P. Structural, physico-mechanical and in-vitro bioactivity studies on SiO(2)-CaO-P(2)O(5)-SrO-Al(2)O(3) bioactive glasses. Mater. Sci. Eng. C Mater. Biol. Appl. 2019, 94, 279–290. DOI: 10.1016/j.msec.2018.09.041.

86. Bellucci, D.; Bianchi, M.; Graziani, G.; Gambardella, A.; Berni, M.; Russo, A.; Cannillo, V. Pulsed Electron Deposition of nanostructured bioactive glass coatings for biomedical applications. Ceram. Int. 2017, 43, 15862–15867. DOI: 10.1016/j.ceramint.2017.08.159.

87. Drouet, C.; Leriche, A.; Hampshire, S.; Kashani, M.; Stamboulis, A.; Iafisco, M.; Tampieri, A. Types of ceramics: Material class. In: Advances in Ceramic Biomaterials (Materials, Devices and Challenges); Palmero, P.; Cambier, F.; Barra, E.D., Eds; Woodhead Publishing: Sawston, Cambridge, UK, 2017, chapter 2, 21–82, DOI: 10.1016/B978-0-08-100881-2.00002-6.

88. Kinnunen, I.; Aitasalo, K.; Pöllönen, M.; Varpula, M. Reconstruction of orbital floor fractures using bioactive glass. J. Craniomaxillofac. Surg. 2000, 28, 229–234. DOI: 10.1054/jcms.2000.0140

89. van Gestel, N.A.; Geurts, J.; Hulsen, D.J.; van Rietbergen, B.; Hofmann, S.; Arts, J.J. Clinical applications of S53P4 Bioactive glass in bone healing and osteomyelitic treatment: a literature review. Biomed. Res. Int. 2015, 2015, 684826. DOI: 10.1155/2015/684826.

90. Tanner, M.C.; Heller, R.; Westhauser, F.; Miska, M.; Ferbert, T.; Fischer, C.; Gantz, S.; Schmidmaier, G.; Haubruck, P. Evaluation of the clinical effectiveness of bioactive glass (S53P4) in the treatment of non-unions of the tibia and femur:

study protocol of a randomized controlled non-inferiority trial. Trials 2018, 19, 299. DOI: 10.1186/s13063-018-2681-9.

91. Peltola, M.J.; Aitasalo, K.M.; Suonpää, J.T.; Yli-Urpo, A.; Laippala, P.J.; Forsback, A.P. Frontal sinus and skull bone defect obliteration with three synthetic bioactive materials. A comparative study. J. Biomed. Mater. Res. B Appl. Biomater. 2003, 66, 364–372. DOI: 10.1002/jbm.b.10023.

92. Maçon, A.L.; Kim, T.B.; Valliant, E.M.; Goetschius, K.; Brow, R.K.; Day, D.E.; Hoppe, A.; Boccaccini, A.R.; Kim, I.Y.; Ohtsuki, C.; Kokubo, T.; Osaka, A.; Vallet-Regí, M.; Arcos, D.; Fraile, L.; Salinas, A.J.; Teixeira, A.V.; Vueva, Y.; Almeida, R.M.; Miola, M.; Vitale-Brovarone, C.; Verné, E.; Höland, W.; Jones, J.R. A unified in vitro evaluation for apatite-forming ability of bioactive glasses and their variants. J. Mater. Sci. Mater. Med. 2015, 26, 115. DOI: 10.1007/s10856-015-5403-9.

93. Montazerian, M.; Zanotto, E.D. History and trends of bioactive glass-ceramics. J. Biomed. Mater. Res. A 2016, 104, 1231–1249. DOI: 10.1002/jbm.a.35639.

94. Peitl, O.; LaTorre, G.P.; Hench. L.L. Effect of crystallization on apatite layer formation of bioactive glass 45S5. J. Biomed. Mater. Res. 1996, 30, 509–514. DOI: 10.1002/(SICI)1097-4636(199604)30:4<509::AID-JBM9>3.0.CO;2-T

95. Peitl, O.; Zanotto, E.D.; Hench, L.L. Highly bioactive P2O5–Na2O–CaO–SiO2 glass-ceramics. J. Non-Cryst. Solids 2001, 292, 115–126. DOI: 10.1016/S0022-3093(01)00822-5.

96. Thompson, I.D.; Hench, L.L. Mechanical properties of bioactive glasses, glass-ceramics and composites. Proc. Inst. Mech. Eng. H 1998, 212, 127–136. DOI: 10.1243/0954411981533908.

97. Bellucci, D.; Cannillo, V.; Sola, A. Coefficient of thermal expansion of bioactive glasses: Available literature data and analytical equation estimates. Ceram. Int. 2011, 37, 2963–2972. DOI: 10.1016/j.ceramint.2011.05.048.

98. Cattini, A.; Łatka, L.; Bellucci, D.; Bolelli, G.; Sola, A.; Lusvarghi, L.; Pawłowski, L.; Cannillo, V. Suspension plasma sprayed bioactive glass coatings: Effects of processing on microstructure, mechanical properties and in-vitro behavior. Surf. Coat. Technol. 2013, 220, 52–59. DOI: 10.1016/j.surfcoat.2012.10.076.

99. Boccaccini, A.R.; Brauer, D.S.; Hupa, L. Bioactive glasses: Fundamentals, technology and applications. Royal Society of Chemistry: London, UK. 2016. DOI: 10.1039/9781782622017.

100. Prakasam, M.; Locs, J.; Salma-Ancane, K.; Loca, D.; Largeteau, A.; Berzina-Cimdina, L. Biodegradable Materials and Metallic Implants-A Review. J. Funct. Biomater. 2017, 8, 44. DOI: 10.3390/jfb8040044.

101. Wu, C.; Chang, J. A review of bioactive silicate ceramics. Biomed. Mater. 2013, 8, 032001. DOI: 10.1088/1748-6041/8/3/032001.

102. Juraski, A.C.; Rodas, A.C.D.; Elsayed, H.; Bernardo, E.; Soares, V.O.; Daguano, J. The in vitro bioactivity, degradation, and cytotoxicity of polymer-derived wollastonite-diopside glass-ceramics. Materials 2017, 10, 425. DOI: 10.3390/ma10040425.

103. Elsayed, H.; Sinico, M.; Secco, M.; Zorzi, F.; Colombo, P.; Bernardo, E. B-doped hardystonite bioceramics from preceramic polymers and fillers: Synthesis and application to foams and 3D-printed scaffolds. J. Eur. Ceram. Soc. 2017, 37, 1757–1767. DOI: 10.1016/j.jeurceramsoc.2016.12.002.

104. Götz, W.; Tobiasch, E.; Witzleben, S.; Schulze, M. Effects of silicon compounds on biomineralization, osteogenesis, and hard tissue formation. Pharmaceutics 2019, 11, 117. DOI: 10.3390/pharmaceutics11030117.

105. Mohammadi, H.; Sepantafar, M.; Ostadrahimi, A. The role of bioinorganics in improving the mechanical properties of silicate ceramics as bone regenerative materials. J. Ceram. Sci. Tech. 2015, 6, 1–8. DOI: 10.4416/JCST2014-00043.

106. Zocca, A.; Elsayed, H.; Bernardo, E.; Gomes, C.M.; Lopez-Heredia, M.A.; Knabe, C.; Colombo, P.; Günster, J. 3D-printed silicate porous bioceramics using a non-sacrificial preceramic polymer binder. Biofabrication 2015, 7, 025008. DOI:10.1088/1758-5090/7/2/025008.

107. Elsayed, H.; Zocca, A.; Bernardo, E.; Gomes, C.M.; Günster, J.; Colombo, P. Development of bioactive silicate-based glass-ceramics from preceramic polymer and fillers. J. Eur. Ceram. Soc. 2015, 35, 731–739. DOI: 10.1016/j.jeurceramsoc.2014.09.020.

108. Heimann, R.B.; Lehmann, H.D. Bioceramic Coatings for Medical Implants: Trends and Techniques. John Wiley & Sons, 2015. DOI: 10.1002/9783527682294.

109. Long, L.H.; Chen, L.D.; Bai, S.Q.; Chang, J.; Lin, K.L. Preparation of dense β-CaSiO3 ceramic with high mechanical strength and HAp formation ability in simulated body fluid. J. Eur. Ceram. Soc. 2006, 26, 1701–1706. DOI: 10.1016/j.jeurceramsoc.2005.03.247.

110. Gou, Z.R.; Chang, J.; Zhai, W.Y. Preparation and characterization of novel bioactive dicalcium silicate ceramics J. Eur. Ceram. Soc. 2005, 25, 1507–1514. DOI: 10.1016/j.jeurceramsoc.2004.05.029.

111. Heimann, R.B. Important Ceramic Phase Systems. In: Classic and advanced ceramics: from fundamentals to applications. John Wiley & Sons, 2010, pp. 55–97. DOI: 10.1002/9783527630172.ch3.

112. Zhao, W.; Chang, J. Preparation and characterization of novel tricalcium silicate bioceramics. J. Biomed. Mater. Res. A 2005, 73, 86–89. DOI: 10.1002/jbm.a.30242.

113. Thieme, C.; Rüssel, C. Thermal expansion behavior of SrSiO3 and Sr2SiO4 determined by high-temperature X-ray diffraction and dilatometry. J. Mater. Sci. 2015, 50, 5533–5539. DOI:10.1007/s10853-015-9100-3.

114. Bullard, J.W. A determination of hydration mechanisms for tricalcium silicate using a kinetic cellular automaton model. J. Am. Ceram. Soc. 2008, 91, 2088–2097. DOI: 10.1111/j.1551-2916.2008.02419.x.

115. Tan, Y.M.; Tan, C.Y.; Ramesh, S; The, Y.C.; Ching, Y.C.; Lwin, N.; Yap, B.K.; Agrawal, D. Study on the effects of milling time and sintering temperature on the sinterability of forsterite (Mg2SiO4). J. Ceram. Soc. Jpn. 2015, 123, 1032–1037. DOI: 10.2109/jcersj2.123.1032.

116. McColm, I.J. Dictionary of Ceramic Science and Engineering. Springer Netherlands, 2013. DOI: 10.1007/978-94-007-0916-4.

117. Wu, C.; Chang, J. A novel akermanite bioceramic: preparation and characteristics. J. Biomater. Appl. 2006, 21, 119–129. DOI: 10.1177/0885328206057953.

118. Haussühl, S.; Liebertz, J. Elastic and thermoelastic properties of synthetic Ca2MgSi2O7 (åkermanite) and Ca2ZnSi2O7 (hardystonite). Phys. Chem. Miner. 2004, 31, 565–567. DOI: 10.1007/s00269-004-0416-9.

119. Chen, X.; Ou, J.; Wei, Y.; Huang, Z.; Kang, Y.; Yin, G. Effect of MgO contents on the mechanical properties and biological performances of bioceramics in the MgO-CaO-SiO2 system. J. Mater. Sci. Mater. Med. 2010, 21, 1463–1471. DOI: 10.1007/s10856-010-4025-5.

120. Wu, C.; Chang, J.; Wang, J.; Ni, S.; Zhai, W. Preparation and characteristics of a calcium magnesium silicate (bredigite) bioactive ceramic. Biomaterials 2005, 26, 2925–2931. DOI: 10.1016/j.biomaterials.2004.09.019.

121. Wu, C.; Chang, J. Synthesis and in vitro bioactivity of bredigite powders. J. Biomater. Appl. 2007, 21, 251–263. DOI: 10.1177/0885328206062360.

122. Nonami, T.; Tsutsumi, S. Study of diopside ceramics for biomaterials. J. Mater. Sci. Mater. Med. 1999, 10, 475–479. DOI: 10.1023/A:1008996908797.

123. Xue, W.; Liu, X.; Zheng, X.; Ding, C. Plasma-sprayed diopside coatings for biomedical applications. Surf. Coat. Tech. 2004, 185, 340–345. DOI: 10.1016/j.surfcoat.2003.12.018.

124. Hafezi-Ardakani, M.; Moztarzadeh, F.; Rabiee, M.; Talebi, A.R.; Abasi-shahni, M.; Fesahat, F.; Sadeghian, F. Sol-gel synthesis and apatite-formation ability of nanostructure merwinite (Ca3MgSi2O8) as a novel bioceramic. J. Ceram. Process Res. 2010, 11, 765–768.

125. Ou, J.; Kang, Y.; Huang, Z.; Chen, X.; Wu, J.; Xiao, R.; Yin, G. Preparation and in vitro bioactivity of novel merwinite ceramic. Biomed. Mater. 2008, 3, 015015. DOI: 10.1088/1748-6041/3/1/015015.

126. Pantić, J.; Urbanovich, V.; Poharc-Logar, V.; Jokić, B.; Stojmenović, M.; Kremenović, A.; Matović, B. Synthesis and characterization of high-pressure and high-temperature sphene (CaTiSiO5). Phys. Chem. Minerals 2014, 41, 775–782 DOI: 10.1007/s00269-014-0693-x.

127. Wu, C.; Ramaswamy, Y.; Liu, X.; Wang, G.; Zreiqat, H. Plasma-sprayed CaTiSiO5 ceramic coating on Ti-6Al-4V with excellent bonding strength, stability and cellular bioactivity. J. R. Soc. Interface 2009, 6, 159–168. DOI: 10.1098/rsif.2008.0274.

128. Schumacher, T.C.; Volkmann, E.; Yilmaz, R.; Wolf, A.; Treccani, L.; Rezwan, K. Mechanical evaluation of calcium-zirconium-silicate (baghdadite) obtained by a direct solid-state synthesis route. J. Mech. Behav. Biomed. Mater. 2014, 34, 294–301. DOI: 10.1016/j.jmbbm.2014.02.021.

129. Al-Hermezi, H.M.; McKie, D.; Hall, A.J. Baghdadite, a new calcium zirconium silicate mineral from Iraq. Mineral. Mag. 1986, 50, 119–123. DOI: 10.1180/minmag.1986.050.355.15.

130. Wennerberg, A; Albrektsson, T. On implant surfaces: a review of current knowledge and opinions. Int. J. Oral Maxillofac. Implants 2010, 25, 63–74.

131. Lynn, A.K.; DuQuesnay, D.L. Hydroxyapatite-coated Ti-6Al-4V part 1: the effect of coating thickness on mechanical fatigue behaviour. Biomaterials 2002, 23, 1937–1946. DOI: 10.1016/S0142-9612(01)00321-0.

132. Biasetto, L.; Elsayed, H.; Bonollo, F.; Colombo, P. Polymer-derived sphene biocoating on cp-Ti substrates for orthopedic and dental implants. Surf. Coat. Technol. 2016, 301, 140–147. DOI: 10.1016/j.surfcoat.2016.01.018.

133. Biasetto, L.; Elsayed, H. Sphene silicate ceramic coatings on cpTi substrates: Process upgrade. Surf. Coat. Technol. 2017, 321, 416–424. DOI: 10.1016/j.surfcoat.2017.05.018.

134. Biasetto, L.; Bertolini, R.; Elsayed, H.; Ghiotti, A.; Bruschi, S. Use of cryogenic machining to improve the adhesion of sphene bioceramic coatings on titanium substrates for dental and orthopaedic applications. Ceram. Int. 2019, 45, 5941-5951. DOI: 10.1016/j.ceramint.2018.12.063.

135. Wang, G.; Lu, Z.; Liu, X.; Zhou, X.; Ding, C.; Zreiqat, H. Nanostructured glass-ceramic coatings for orthopaedic applications. J. R. Soc. Interface 2011, 8, 1192–1203. DOI: 10.1098/rsif.2010.0680.

136. Cheng, S.; Wei, D.; Zhou, Y. Formation and structure of sphene/titania composite coatings on titanium formed by a hybrid technique of microarc oxidation and heat-treatment. Appl. Surf. Sci. 2011, 257, 3404–3411. DOI: 10.1016/j.apsusc.2010.11.034.

137. Ramaswamy, Y.; Wu, C.; Dunstan, C.R.; Hewson, B; Eindorf, T; Anderson, G.I.; Zreiqat, H. Sphene ceramics for orthopedic coating applications: an in vitro and in vivo study. Acta Biomater. 2009, 5, 3192–3204. DOI: 10.1016/j.actbio.2009.04.028.

138. Wu, C.; Ramaswamy, Y.; Gale, D.; Yang, W.; Xiao, K.; Zhang, L.; Yin, Y.; Zreiqat, H. Novel sphene coatings on Ti-6Al-4V for orthopedic implants using sol-gel method. Acta Biomater. 2008, 4, 569–576. DOI: 10.1016/j.actbio.2007.11.005.

139. Li, K.; Yu, J.; Xie, Y.; Huang, L; Ye, X; Zheng, X. Chemical stability and antimicrobial activity of plasma sprayed bioactive Ca2ZnSi2O7 coating. J. Mater. Sci. Mater. Med. 2011, 22, 2781–2789. DOI: 10.1007/s10856-011-4454-9.

140. Zhang, W.; Wang, G.; Liu, Y.; Zhao, X.; Zou, D.; Zhu, C.; Jin, Y.; Huang, Q.; Sun, J.; Liu, X.; Jiang, X.; Zreiqat, H. The synergistic effect of hierarchical micro/nano-topography and bioactive ions for enhanced osseointegration. Biomaterials 2013, 34, 3184–3195. DOI: 10.1016/j.biomaterials.2013.01.008.

141. Yi, D.; Wu, C.; Ma, X.; Ji, H.; Zheng, X.; Chang, J. Preparation and in vitro evaluation of plasma-sprayed bioactive akermanite coatings. Biomed. Mater. 2012, 7, 065004. DOI: 10.1088/1748-6041/7/6/065004.

142. Liang, Y.; Xie, Y.; Ji, H.; Huang, L.; Zheng, X. Excellent stability of plasma-sprayed bioactive Ca3ZrSi2O9 ceramic coating on Ti–6Al–4V. Appl. Surf. Sci. 2010, 256, 4677–4681. DOI: 10.1016/j.apsusc.2010.02.071.

143. Yi, D.; Wu, C.; Ma, B.; Ji, H.; Zheng, X.; Chang, J. Bioactive bredigite coating with improved bonding strength, rapid apatite mineralization and excellent cytocompatibility. J. Biomater. Appl. 2014, 28, 1343–1353. DOI: 10.1177/0885328213508165.

144. Liu, X.; Tao, S.; Ding C. Bioactivity of plasma sprayed dicalcium silicate coatings. Biomaterials 2002, 23, 963–968. DOI: 10.1016/S0142-9612(01)00210-1.

145. Liu, X.Y.; Ding, C.X. Characterization of plasma sprayed wollastonite powder and coatings. Surf. Coat. Technol. 2002, 153, 173–177. DOI: 10.1016/S0257-8972(01)01666-8.

146. Garcia, E.; Miranzo, P.; Sainz, M.A. Thermally sprayed wollastonite and wollastonite-diopside compositions as new modulated bioactive coatings for metal implants. Ceram. Int. 2018, 44, 12896–12904. DOI: 10.1016/j.ceramint.2018.04.100.

147. Sanyal, S.; Shukla, M.; Dandapat, N.; Ghosh, S. In vitro evaluation of bioactive glass ceramic coating for application on Ti6Al4V based biomedical implants. J. Non-Cryst. Solids 2018, 500, 22–29. DOI: 10.1016/j.jnoncrysol.2018.04.043.

148. Newman, S.D.; Lotfibakhshaiesh, N.; O'Donnell, M.; Walboomers, X.F.; Horwood, N.; Jansen, J.A.; Amis, A.A.; Cobb, J.P.; Stevens, M.M. Enhanced osseous implant fixation with strontium-substituted bioactive glass coating. Tissue Eng. Part A 2014, 20, 1850–1857. DOI: 10.1089/ten.TEA.2013.0304.

149. Bolelli, G.; Bellucci, D.; Cannillo, V.; Gadow, R.; Killinger, A.; Lusvarghi, L.; Müller, P.; Sola, A. Comparison between Suspension Plasma Sprayed and High Velocity Suspension Flame Sprayed bioactive coatings. Surf. Coat. Technol. 2015, 280, 232–249. DOI: 10.1016/j.surfcoat.2015.08.039.

150. Altomare, L.; Bellucci, D.; Bolelli, G.; Bonferroni, B.; Cannillo, V.; De Nardo, L.; Gadow, R.; Killinger, A.; Lusvarghi, L.; Sola, A.; Stiegler, N. Microstructure and in vitro behaviour of 45S5 bioglass coatings deposited by high velocity suspension flame spraying (HVSFS). J. Mater. Sci. Mater. Med. 2011, 22, 1303–1319. DOI: 10.1007/s10856-011-4307-6.

151. van Oirschot, B.A.; Alghamdi, H.S.; Närhi, T.O.; Anil, S.; Al Farraj Aldosari, A.; van den Beucken, J.J.; Jansen, J.A. In vivo evaluation of bioactive glass-based

coatings on dental implants in a dog implantation model. Clin. Oral Implants Res. 2014, 25, 21–28. DOI: 10.1111/clr.12060.

152. van Oirschot, B.A.; Meijer, G.J.; Bronkhorst, E.M.; Närhi, T.; Jansen, J.A.; van den Beucken, J.J. Comparison of different surface modifications for titanium implants installed into the goat iliac crest. Clin. Oral Implants Res. 2016, 27, 57–67. DOI: 10.1111/clr.12529.

153. Mistry, S.; Roy, R.; Kundu, B.; Datta, S.; Kumar, M.; Chanda, A.; Kundu, D. Clinical outcome of hydroxyapatite coated, bioactive glass coated, and machined Ti6Al4V Threaded dental implant in human jaws: a short-term comparative study. Implant Dent. 2016, 25, 252–260. DOI: 10.1097/ID.0000000000000376.

154. Catauro, M.; Bollino, F.; Papale, F.; Vecchio Ciprioti, S. Investigation on bioactivity, biocompatibility, thermal behavior and antibacterial properties of calcium silicate glass coatings containing Ag. J. Non-Cryst. Solids 2015, 422, 16–22. DOI: 10.1016/j.jnoncrysol.2015.04.037.

155. Bagherpour, I.; Naghib, S.M.; Yaghtin, A.H. Synthesis and characterisation of nanostructured hardystonite coating on stainless steel for biomedical application. IET Nanobiotechnol. 2018, 12, 895–902. DOI: 10.1049/iet-nbt.2017.0275.

156. Bagherpour, I. Fabrication of hardystonite nano-bioceramic coating on 306L stainless steel substrate using electrophoretic method and evaluation of its corrosion resistance to improve medical performance. In: The Minerals, Metals & Materials Series (eds) TMS 2019 148th Annual Meeting & Exhibition Supplemental Proceedings. The Minerals, Metals & Materials Series. Springer, Cham, 2019, pp. 143–154. DOI: 10.1007/978-3-030-05861-6_13.

157. Ballarre, J.; Seltzer, R., Mendoza, E.; Orellano, J.C.; Mai, Y.W.; García, C.; Ceré, S.M. Morphologic and nanomechanical characterization of bone tissue growth around bioactive sol–gel coatings containing wollastonite particles applied on stainless steel implants. Mater Sci Eng C Mater Biol Appl. 2011, 31, 545–552. DOI: 10.1016/j.msec.2010.11.030.

158. Yu, H.; Dong, Q.; Dou, J.; Pan, Y.; Chen, C. Structure and in vitro bioactivity of ceramic coatings on magnesium alloys by microarc oxidation. Appl. Surf. Sci. 2016, 388, 114–119. DOI: 10.1016/j.apsusc.2016.03.028.

159. Ye, X.; Cai, S.; Dou, Y.; Xu, G.; Huang, K.; Ren, M.; Wang, X. Bioactive glass–ceramic coating for enhancing the in vitro corrosion resistance of biodegradable Mg alloy. Appl. Surf. Sci. 2012, 259, 799–805. DOI: 10.1016/j.apsusc.2012.07.127.

160. Dou, Y.; Cai, S.; Ye, X.; Xu, G.; Huang, K.; Wang, X.; Ren, M. 45S5 bioactive glass–ceramic coated AZ31 magnesium alloy with improved corrosion resistance. Surf. Coat. Technol. 2013, 228, 154–161. DOI: 10.1016/j.surfcoat.2013.04.022.

161. Niu, S.; Cai, S.; Liu, T.; Zhao, H.; Wang, X.; Ren, M.; Huang, K.; Wu, X. 45S5 bioactive glass-ceramic coated magnesium alloy with strong interfacial bonding strength by "superplasticity diffusion bonding". Mater. Lett. 2015, 141, 96–99. DOI: 10.1016/j.matlet.2014.11.057.

162. Shen, S.; Cai, S.; Xu, G.; Zhao, H.; Niu, S.; Zhang, R. Influence of heat treatment on bond strength and corrosion resistance of sol-gel derived bioglass-ceramic coatings on magnesium alloy. J. Mech. Behav. Biomed. Mater. 2015, 45, 166–174. DOI: 10.1016/j.jmbbm.2015.02.005.

163. Gittens, R.A.; Scheideler, L.; Rupp, F.; Hyzy, S.L.; Geis-Gerstorfer, J.; Schwartz, Z.; Boyan, B.D. A review on the wettability of dental implant surfaces II: Biological and clinical aspects. Acta Biomater. 2014, 10, 2907–2918. DOI: 10.1016/j.actbio.2014.03.032.

164. ASTM D4541 2009 Standard test method for pull-off strength of coatings using portable adhesion ASTM Int.

165. ASTM International. Available online: https://www.astm.org/Standards/C633 (accessed on 09 Sept 2019)

166. Fletcher, J.F.; Barnes, D.J. Pull-Off Adhesion Testing of Coatings–Improve Your Technique. 2017 Available on line: https://www.elcometer.com/images/stories/PDFs/Pull-Off_Adhesion_Testing_of_Coatings_Improve_Your_Technique.pdf (Access on 5 June 2019).

167. Chen, Q.; Cabanas-Polo, S.; Goudouri, O.M.; Boccaccini, A.R. Electrophoretic co-deposition of polyvinyl alcohol (PVA) reinforced alginate-Bioglass® composite coating on stainless steel: mechanical properties and in-vitro bioactivity assessment. Mater Sci Eng C Mater Biol Appl. 2014, 40, 55–64. DOI: 10.1016/j.msec.2014.03.019.

168. Kleinbichler, A.; Pfeifenberger, M.J.; Zechner, J.; Moody, N.R.; Bahr, D.F.; Cordill, M.J. New insights into nanoindentation-based adhesion testing. JOM 2017, 69, 2237–2245. DOI: 10.1007/s11837-017-2496-2.

169. Sun, L.; Berndt, C.C.; Gross, K.A.; Kucuk, A. Material fundamentals and clinical performance of plasma-sprayed hydroxyapatite coatings: a review. J Biomed Mater Res. 2001, 58, 570–592. DOI: 10.1002/jbm.1056.

170. Xuereb, M.; Camilleri, J.; Attard, N.J. Systematic review of current dental implant coating materials and novel coating techniques. Int. J. Prosthodont. 2015, 28, 51–59. DOI: 10.11607/ijp.4124.

171. Røynesdal, A.K.; Ambjørnsen, E.; Støvne, S.; Haanaes, H.R. A comparative clinical study of three different endosseous implants in edentulous mandibles. Int. J. Oral Maxillofac. Implants. 1998, 13, 500–505.

172. Capello, W.N.; D'Antonio, J.A.; Feinberg, J.R.; Manley, M.T. Ten-year results with hydroxyapatite-coated total hip femoral components in patients less than fifty years old. A concise follow-up of a previous report. J. Bone Joint Surg. Am. 2003, 85, 885–889. DOI: 10.2106/00004623-200305000-00017.

173. Nelissen, R.G.; Valstar, E.R.; Rozing, P.M. The effect of hydroxyapatite on the micromotion of total knee prostheses. A prospective, randomized, double-blind study. J. Bone Joint Surg. Am. 1998, 80, 1665–1672. DOI: 10.2106/00004623-199811000-00014.

174. Magyar, G.; Toksvig-Larsen, S.; Moroni, A. Hydroxyapatite coating of threaded pins enhances fixation. J. Bone Joint Surg. Br. 1997, 79, 487–489. DOI:10.1302/0301-620X.79B3.0790487.

175. Inadome, T.; Hayashi, K.; Nakashima, Y.; Tsumura, H.; Sugioka, Y. Comparison of bone-implant interface shear strength of hydroxyapatite-coated and alumina-coated metal implants. J. Biomed. Mater. Res. 1995, 29, 19–24. DOI: 10.1002/jbm.820290104.

176. Surmeneva, M.A.; Chaikina, M.V.; Zaikovskiy, V.I.; Pichugin, V.F.; Buck, V.; Prymak, O.; Epple, M.; Surmenev, R.A. The structure of an RF-magnetron sputter-deposited silicate-containing hydroxyapatite-based coating investigated by high-resolution techniques. Surf. Coat. Technol. 2013, 218, 39–46. DOI: 10.1016/j.surfcoat.2012.12.023.

177. Surmeneva, M.A.; Mukhametkaliyev, T.M.; Tyurin, A.I.; Teresov, A.D.; Koval, N.N.; Pirozhkova, T.S.; Shuvarin, I.A.; Shuklinov, A.V.; Zhigachev, A.O.; Oehr, C.; Surmenev, R.A. Effect of silicate doping on the structure and mechanical properties of thin nanostructured RF magnetron sputter-deposited hydroxyapatite films. Surf. Coat. Technol. 2015, 275, 176–184. DOI: 10.1016/j.surfcoat.2015.05.021.

178. ISO Standards. Available online: https://www.iso.org/standard/64617.html (accessed on 09 Sept 2019).

179. Dehghanian, C.; Aboudzadeh, N.; Shokrgozar, M.A. Characterization of silicon-substituted nano hydroxyapatite coating on magnesium alloy for biomaterial

application. Mater. Chem. Phys. 2018, 203, 27–33. DOI: 10.1016/j.matchemphys.2017.08.020.

180. Kokubo, T.; Takadama, H. How useful is SBF in predicting in vivo bone bioactivity? Biomaterials 2006, 27, 2907–2915. DOI: 10.1016/j.biomaterials.2006.01.017.

181. Kheradmandfard, M.; Fathi, M.H.; Ahangarian, M.; Zahrani, E.M. In vitro bioactivity evaluation of magnesium-substituted fluorapatite nanopowders. Ceram. Int. 2012, 38, 169–175. DOI: 10.1016/j.ceramint.2011.05.157.

182. Liu, S.; Li, H.; Zhang, L.; Yin, X.; Guo, Y. In simulated body fluid performance of polymorphic apatite coatings synthesized by pulsed electrodeposition. Mater Sci Eng C Mater Biol Appl. 2017, 79, 100–107. DOI: 10.1016/j.msec.2017.05.037.

183. Kokubo, T.; Kushitani, H.; Sakka, S.; Kitsugi, T.; Yamamuro, T. Solutions able to reproduce in vivo surface-structure changes in bioactive glass-ceramic A-W. J. Biomed. Mater. Res. 1990, 24, 721–734. DOI: 10.1002/jbm.820240607.

184. Filgueiras, M.R.; La Torre, G.; Hench, L.L. Solution effects on the surface reactions of a bioactive glass. J. Biomed. Mater. Res. 1993, 27, 445-453. DOI: 10.1002/jbm.820270405.

185. Kokubo T. Bioactive glass ceramics: properties and applications. Biomaterials 1991, 12, 155–163. DOI: 10.1016/0142-9612(91)90194-f.

186. Ohtsuki, C.; Kushitani, H.; Kokubo, T.; Kotani, S.; Yamamuro, T. Apatite formation on the surface of Ceravital-type glass-ceramic in the body. J. Biomed. Mater. Res. 1991, 25, 1363–1370. DOI: 10.1002/jbm.820251105.

187. Elsayed, H.; Gardin, C.; Ferroni, L.; Zavan, B.; Colombo, P.; Bernardo, E. Highly porous Sr/Mg-doped hardystonite bioceramics from preceramic polymers and reactive fillers: direct foaming and direct ink writing. Adv. Eng. Mater 2019, 21, 1800900. DOI: 10.1002/adem.201800900.

188. Elsayed, H.; Zocca, A.; Franchin, G.; Bernardo, E.; Colombo, P. Hardystonite bioceramics from preceramic polymers. J. Eur. Ceram. Soc. 2016, 36, 829–835. DOI: 10.1016/j.jeurceramsoc.2015.10.034.

189. Chouirfa, H.; Bouloussa, H.; Migonney, V.; Falentin-Daudré, C. Review of titanium surface modification techniques and coatings for antibacterial applications. Acta Biomater. 2019, 83, 37–54. DOI: 10.1016/j.actbio.2018.10.036.

190. Chen, Y.K.; Zheng, X.B.; Xie, Y.T.; Ji, H.; Ding, C.X. Antibacterial properties of vacuum plasma sprayed titanium coatings after chemical treatment. Surf. Coat. Technol. 2009, 204, 685–690. DOI: 10.1016/j.surfcoat.2009.09.010.

191. Oliveira, W.F.; Silva, P.M.S.; Silva, R.C.S.; Silva, G.M.M.; Machado, G.; Coelho, L.C.B.B.; Correia, M.T.S. Staphylococcus aureus and Staphylococcus epidermidis infections on implants. J. Hosp. Infect. 2018, 98, 111–117. DOI: 10.1016/j.jhin.2017.11.008.

192. Pearce, A.I.; Richards, R.G.; Milz, S.; Schneider, E.; Pearce, S.G. Animal models for implant biomaterial research in bone: a review. Eur. Cell. Mater. 2007, 13, 1–10. DOI: 10.22203/eCM.v013a01.

193. Wancket, L.M. Animal models for evaluation of bone implants and devices: comparative bone structure and common model uses. Vet. Pathol. 2015, 52, 842–850. DOI: 10.1177/0300985815593124.

194. Stadlinger, B.; Pourmand, P.; Locher, M.C.; Schulz, M.C. Systematic review of animal models for the study of implant integration, assessing the influence of material, surface and design. J. Clin. Periodontol. 2012, 39, 28–36. DOI: 10.1111/j.1600-051X.2011.01835.x.

195. Liferovich, R.P.; Mitchell, R.H. Solid solutions of niobium in synthetic titanite. Can. Mineral. 2006, 44, 1089–1097. DOI: 10.2113/gscanmin.44.5.1089.

196. Fan, G.; Dang, J.; Lv, X.; Hu, M. Effect of basicity on the crystallization behavior of TiO2–CaO–SiO2 ternary system slag. Cryst. Eng. Comm. 2018, 20, 5422–5431. DOI: 10.1039/c8ce01078a.

197. Awin, E.W.; Matović, B; Maletaškić, J; Urbanovich, V; Kumar, R. Mechanical properties of ultra-high pressure sintered sphene (CaTiSiO5). Process Appl Ceram, 2016, 10, 295–298. DOI: 10.2298/PAC1604295A.

198. Hayward, P.J.; Cecchetto, E.V. Development of sphene-based glass ceramics tailored for Canadian waste disposal conditions. In The Scientific Basis for Nuclear Waste Management, Ed. Topp S.J., Elsevier, New York, USA. 1982, 91–97. DOI: 10.1557/PROC-6-91.

199. Hayward, P.J.; Doern, D.C.; George, I,M. Dissolution of a sphene glass-ceramic, and of its component sphene and glass phases in Ca-Na-Cl brines. J. Am. Ceram. Soc. 1990, 73, 544–511. DOI: 10.1111/j.1151-2916.1990.tb06551.x.

200. Maletaškić, J.; Matović, B.; Stanković, N.; Prekajski Djordjević, M.; Luković, J.; Yoshida, K.; Yano, T. Phase evolution of sphene based ceramics during

annealing. Energy Procedia 2017, 131, 407–412. DOI: 10.1016/j.egypro.2017.09.457.

201. Hench, L.L.; Jones, J.R. Bioactive glasses: frontiers and challenges. Front. Bioeng. Biotechnol. 2015, 3, 194. DOI: DOI: 10.3389/fbioe.2015.00194.

202. Prevéy, P.S. X-ray diffraction characterization of crystallinity and phase composition in plasma-sprayed hydroxyapatite coatings. J. Therm. Spray Techn. 2000, 9, 369–376. DOI: 10.1361/105996300770349827.

203. Khor, K.A.; Gu, Y.W.; Pan, D.; Cheang, P. Microstructure and mechanical properties of plasma sprayed HA/YSZ/Ti-6Al-4V composite coatings. Biomaterials 2004, 25, 4009–4017. DOI: 10.1016/j.biomaterials.2003.10.089.

204. Zheng, X.; Huang, M.; Ding, C. Bond strength of plasma-sprayed hydroxyapatite/Ti composite coatings. Biomaterials 2000, 21, 841–849. DOI: 10.1016/s0142-9612(99)00255-0.

205. Ning, C.Y.; Wang, Y.J.; Chen, X.F.; Zhao, N.R.; Ye, J.D.; Wu, G. Mechanical performances and microstructural characteristics of plasma-sprayed bio-functionally gradient HA-ZrO2-Ti coatings. Surf. Coat. Technol. 2005, 200, 2403–2408. DOI: 10.1016/j.surfcoat.2005.05.004.

206. Hildebrand, H.; Hornez, J. Biological response and biocompability. In Metals as biomaterials. Eds. Helsen J.A. & Breme H.J., Wiley, Chichester, UK. 1998, 265–290.

Chapter 2

Bioactive Sphene-Based Ceramic Coatings on CpTi Substrates for Dental Implants: An In Vitro Study

Abstract

Surface modifications of titanium dental implants have been widely investigated, in order to improve the osseointegration at the interface between the implant and the surrounding bone.

After successful production and mechanical characterization of sphene-based coatings on commercially pure (cp) Ti substrates (Prof. L. Biasetto, DTG-UNIPD, in collaboration with Elsayed H, DII-UNIPD), critical aspects, such as the chemical stability and the *in vitro* biocompatibility, needed to be assessed before testing this new material *in vivo*.

Motivated by the positive results obtained with nano-sized precursors, instead of micro-sized active fillers, and by the improvement in coating deposition using an automatic airbrush, rather than a manual airbrush, sphene ($CaTiSiO_5$) bioactive coatings were synthesized via the preceramic polymer processing route, using nano-sized active fillers as precursors, and were deposited by means of an automatic airbrush onto CpTi plates. Already optimized suspension composition and processing setup were utilized.

This chapter is focused on the evaluation of sphene ($CaTiSiO_5$) bioactive coating on the *in vitro* osteogenic differentiation of Human Adipose-Derived Stem Cells (hADSCs). Different analyses were conducted on the samples, including Scanning Electron Microscopy (SEM) analysis, surface roughness measurements and X-ray diffraction analysis. The chemical stability of the coatings was evaluated by soaking the samples in Tris-HCl buffer solution. *In vitro* studies were performed by means of proliferation test of hADSCs seeded on coated and uncoated samples after 21 days. Methyl Thiazolyl-Tetrazolium (MTT) test and immunofluorescent staining with phalloidin confirmed the *in vitro* biocompatibility of both uncoated and coated samples. *In vitro* osteogenic differentiation of the cells was evaluated using Alizarin Red S staining and quantification assay and real-time PCR (Polymerase Chain Reaction). When hADSCs were cultured in the presence of Osteogenic Differentiation Medium, a significantly higher accumulation of calcium deposits onto the sphene-coated surfaces than on uncoated substrates was detected. Osteogenic differentiation on both samples was confirmed by PCR. The analyses proved that the produced sphene-based bioceramic coating possesses good chemical stability and supports stem cell adhesion, proliferation and differentiation *in vitro*, making it a good candidate for orthopedic and dental implants.

Keywords: implant; titanium; osseointegration; biocompatibility; bioactive ceramic coatings; sphene

2.1. Introduction

Commercially pure titanium (CpTi) and its alloys represent the materials of choice for manufacturing orthopedic and dental implants because of their high mechanical properties, good corrosion resistance and excellent biocompatibility [1–4].

The successful outcome of the dental implants mainly depends on the osseointegration at bone-implant level. In recent years, several surface treatments have been applied to Ti implants with the aim of increasing the speed and success rate of osseointegration [5,6]. Surface modifications included acid etching, isothermal oxidation, hydrothermal synthesis method, and combination of sandblasting and acid etching (SLA) [5,6].

Bioactive coatings appear to be promising materials favoring a faster and more enhanced osseointegration [1]. Several different coatings were reported in the literature, including hydroxyapatite, bioglass, proteins, polysaccharides, drugs, calcium phosphate, and calcium silicate [7–11].

Hydroxyapatite (HA), an osseoconductive material, can induce direct formation of bone tissue around implants, thanks to its unique chemical composition similar to that of the inorganic mineral part of bone tissue [9,12]. Despite its excellent biological properties, there are concerns for using HA-coated Ti-6Al-4V implants. However, the mismatch of their thermal expansion coefficients may cause delamination at coating-substrate interface, compromising the long-term success of osseointegrated implants [13,14].

In addition, $CaO–SiO_2$-based bioglasses have been investigated as coating materials. However, they have demonstrated poor bonding strength, due to the higher thermal expansion coefficient compared to that of Ti-6Al-4V [15,16], and high degradation rate [17–21].

Cp-Ti possess an average CTE (Coefficient of Thermal Expansion) of 8.9 (10^{-6} C^{-1}), Ti alloys an average CTE of 9.2 (10^{-6} C^{-1}). Hydroxyapatite shows CTE in the range between 10 and 14 (10^{-6} C^{-1}), while sphene has a CTE of 6 (10^{-6} C^{-1}). SiO_2-CaO bioactive glasses show CTE ranging between 8.5 and 19 (10^{-6} C^{-1}).

However, the clinical applications of bioglasses are limited by their low bending strength, high brittleness, low fracture toughness and workability. To overcome the major drawbacks related to the use of bioglass, several silicate-based ceramics were produced and tested as bioactive materials for bone tissue regeneration. Moreover, when compared to $CaSiO_3$ ceramics and tricalcium phosphate TCP (TriCalcium Phosphate), sphene ($CaTiSiO_5$) ceramics drove higher bone-derived cell attachment, spreading, proliferation and differentiation. CaTiSiO5 ceramics have shown significantly higher chemical stability. Also, they have shown better chemical and biological properties compared to HA ceramics.

Sphene ($CaTiSiO_5$) bioactive coatings on titanium substrates were produced using various methods, such as plasma-spraying [14], sol-gel method [22], a hybrid technique of microarc oxidation coupled with heat treatment [23], and airbrush spray coating [24]. These studies have proved their chemical stability, excellent bonding strength (improved compared to HA coatings), bioactivity and cellular biocompatibility. Taken together, these results suggest that sphene ceramics may be potential candidates for bioactive coatings for orthopedic and dental implants. This reduced difference between CTE of CpTi and $CaTiSiO_5$ compared to that of CpTi and HA, is known to be the main property responsible for their improved adhesion [14,22–26].

Recently, our research group deposited sphene coatings from a preceramic polymer precursor “Silicone” onto Ti plates by the airbrush spray technique. Coatings exhibited excellent adhesion to the substrates and homogeneous deposition mode [24,27].

The novelty of this procedure compared to those reported in the literature consists both of the development of sphene synthesis via preceramic polymers route and nano-sized precursors, as well as in the deposition technique. The main advantages of the proposed technology can be summarized as follow:

- The use of preceramic polymer together with nano-sized precursors allowed for the improvement of reaction efficiency to produce sphene as well as an optimized suspension useful for spray coating via airbrush.
- The use of spray coating is a low-cost technique capable of producing coatings possessing a controlled morphology (roughness and thickness) and thereby improved adhesion to the metallic substrate.

- Compared to high temperature coating techniques, such as plasma coating, the spray coating used in this work is performed at room temperature and further heating of the samples at relatively low temperature.
- The optimized composition of the bioceramic coating together with its improved adhesion to the substrate is the result of the synergic effect of synthesis of sphene via preceramic polymer route and the deposition technique we used.

The primary objective of the current research consists of evaluating the effect of polymer-derived sphene-coated Ti substrates on the osteogenic differentiation of Adipose-Derived Stem Cells (ADSCs) *in vitro*. The secondary aim consists of assessing sphene coating composition, its *in vitro* chemical stability, and its micrometer-scale profile- and areal-topography.

2.2. Experimental Procedure

2.2.1. Samples Preparation and Coating Deposition

Sphene ($CaTiSiO_5$) bioactive ceramic coating on Titanium plates (CpTi) was developed by using a preceramic polymer "silicone" approach as previously reported [24,27]. Preceramic silicone "polymethylsiloxane" (commercially available and known as "SILRES® MK", Wacker-Chemie GmbH, München, Germany), isopropanol, nano-sized $CaCO_3$ powder (PlasmaChem, Berlin, Germany, 90 nm) and nano-sized TiO_2 powders (Evonik Degussa GmbH, Essen, Germany, 21 nm) were used as starting materials.

Briefly, to prepare the coating suspension, SILRES® MK silicone resin powder was used as SiO_2 precursor. The MK silicone was placed in isopropyl alcohol. Active fillers of nanoparticles of $CaCO_3$, and TiO_2 were mixed with the MK silicone under magnetic stirring. The total solid content load in the suspension was ~48 vol%. The addition of active fillers was in stoichiometric molar ratio that allows developing the sphene bioceramic as a final ceramic product after sintering at relative lower temperature (i.e., 950 °C).

The suspension was homogenized using a sonic bath for 15 min and then transferred into an automatic airbrush (Prona-RA-C2, PronaTools, Toronto, Canada M3J 3A1) for

spray coating deposition. During the coating process, the silicone-fillers mixture was kept homogenous by magnetic stirring.

Rectangular plates of 13 X 13 X 3 mm^3 size of commercially pure Ti grade 2 (Torresin Titanio s.r.l, Padova, Italy) were used as substrates. The chemical composition of the CpTi plates, as given by the producer (wt%), was: Fe 0.060, O 0.140, N 0.004, H 0.003, C 0.016, Ti 99.78. Before coating deposition, the CpTi plates were ultrasonically cleaned with acetone, alcohol, and deionized water for ten minutes for each passage, and finally the titanium substrates were dried using compressed air. The use of CpTi instead of Ti alloys as substrate was driven by the choice of restricting the field of study to dental implants.

After many preliminary tests, the processing setup was optimized. The distance between the substrate and nozzle distance was fixed to be 35 cm. The diameter of nozzle of the airbrush was of 1 mm. The air inlet was set at three bars and a deposition time of 1 s was chosen (**Figure 1**). After deposition process, the plates were left to dry in air at room temperature. Then, the coated samples were heat-treated in static air at 950 °C for 1 h (using 5 °C/min as heating rate).

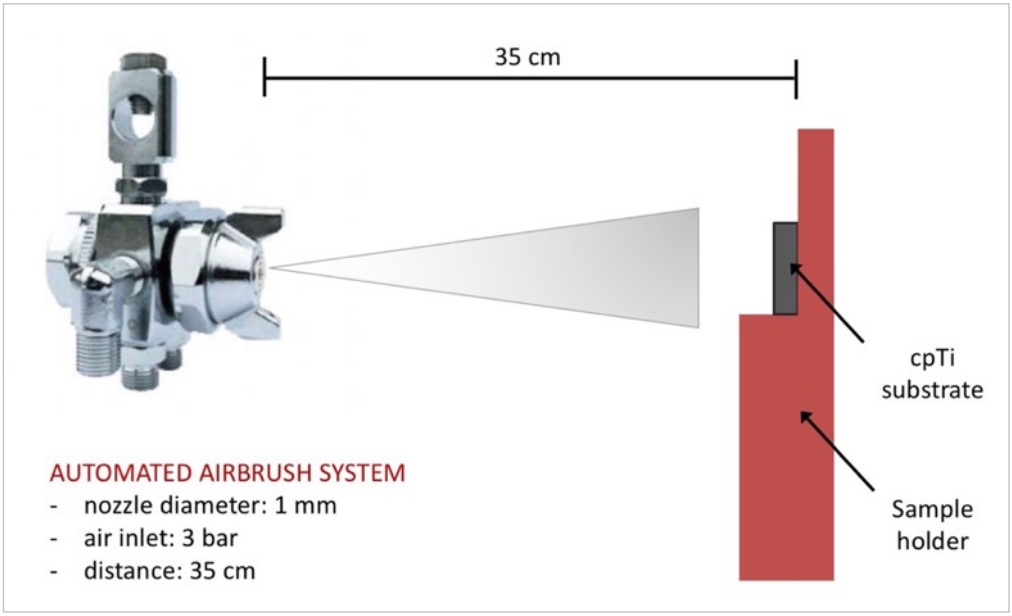

Figure 1. Schematic drawing of the experimental set up used for coating the CpTi plates.

2.2.2. Surface and Coating Characterization

The morphology of the surface of both uncoated (CpTi) and sphene-coated (Sphene) CpTi plates was investigated by Field Emission Gun Scanning Electron Microscopy (FEG-SEM, Quanta 250 Fei, Eindhoven, The Netherlands).

X-ray diffraction (XRD) patterns of the coatings, after thermal treatment, were collected with an X-ray diffractometer (XRD Bruker D8 Advance, Milano, Italy) operated with Cu-K α radiation 40 mA and 40 mV. The Rietveld refinement was subsequently applied to quantitatively analyze the XRD data using MAUD (Materials Analysis Using Diffraction) software and COD (Crystallography Open Database).

Surface topography was investigated using a stylus profilometer (Form Talysurf i-Series, Taylor Hobson Ltd., Leicester, UK), a high-resolution system for both profile- and areal-topography measurements. For 2D profile measurements (Ra and Rz), two plates of each group (CpTi and Sphene) were analyzed and a total of 3 scans (evaluation length equal to 5 mm) were extracted from the surface of each sample. For 3D areal measurements, at least 4 squared areas of 0.5 mm _ 0.5 mm, extracted from the same surface, in at least two samples per group (CpTi and Sphene) were examined by 3D scanning. Areal parameter Sa and Sz were selected to describe the surface topography. Profile and areal data were filtered to eliminate waviness as well as form components of surface topography by applying a Gaussian filter with a sampling length equal to 0.8 mm, in accordance with ISO 4288 and ISO 25178. Data evaluation was performed with Talymap analysis software (Taylor Hobson Ltd., Leicester, UK).

2.2.3. Chemical Stability

The chemical stability of the sphene-coated CpTi substrates was evaluated in Tris-HCl buffer solution. The coated samples were immersed in the buffer solution of tris-(hydroxymethyl) aminomethane (Tris, $(CH_2OH)_3CNH_2$) and hydrochloric acid (HCl) with a pH value of 7.4 and were examined at 1, 3 and 7 days. The ratio of plate surface area to Tris-HCl solution volume was 0.1 cm^2/mL.

Before and after soakings, dried coated samples were analyzed by means of a stylus profilometer (Form Talysurf i-Series) to evaluate changes in surface roughness. The roughness values of 3 different tracks (5 mm evaluation length) and 4 square areas (0.5 mm _ 0.5 mm) per sample were recorded. The following profile roughness parameters, Ra and Rz, and areal parameters, Sa and Sz, were selected.

The variation of Ca, Si and Ti concentrations in the Tris-HCl solution was measured by Inductively Coupled Plasma Optical Emission Spectrometry (ICP-OES; iCAP 7400 ICP-OES, Thermo Fisher Scientific, Cambridge, UK) and confirmed by Inductively Coupled Plasma Mass Spectrometry (ICP-MS, Agilent Technologies 7700 _ ICP-MS system, Agilent Technologies International Japan, Ltd., Tokyo, Japan). The ICP-MS was tuned daily using a tuning solution containing 10 μg L^{-1} ^{140}Ce, ^{7}Li, ^{205}Tl, and ^{89}Y (Agilent Technologies, UK). A 100 μg L^{-1} solution of ^{45}Sc and ^{115}In (Aristar, BDH, UK) prepared in HNO_3 1.4% was used as internal standard through addition to the sample solution via a T-junction.

All calibrations of Ca, Si and Ti were obtained in Tris-HCl solution using the multi-standard CCS-5 (Inorganic-Ventures) for Si and Ti (100 mg L^{-1}), and multi-standard IMS-120 (Ultra Scientific Multistandard) for Ca (1000 mg L^{-1}). All regressions were linear with a determination coefficient (R^2) larger than 0.999. Five samples for each time point were taken and measured five times. Data were given as mean ± standard deviation. The dissolution kinetics of Ca, Si and Ti were obtained from the released concentrations.

2.2.4. Human ADSCs Isolation and Cell Culture

Human ADSCs (hADSCs) were isolated from the adipose tissue of healthy patients undergoing cosmetic surgery procedures. Tissue collection protocol received a favorable ethical opinion by the Local Bioethical Committee, Padova University and all participants provided written consent.

In addition, all experiments performed with human-derived materials were conducted in accordance to the relevant guidelines and regulations. The tissues were digested, and the cells isolated and expanded as described in Gardin et al. [28].

2.2.5. Seeding of hADSCs

hADSCs were seeded on both uncoated and sphene-coated samples, in a 12-well plate, with a density of 2 X 10^4 cells/sample. The cells were cultured in DMEM (Dulbecco's Modified Eagle's Medium) High Glucose or Osteogenic Differentiation Medium, at 37 °C and 5% CO_2, for 21 days. Osteogenic Differentiation Medium was made of DMEM High Glucose supplemented with 10 nM dexamethasone, 10 mM b-glycerophosphate, and 10 ng mL^{-1} of basic fibroblast growth factor. Both media were completed with 10% fetal bovine serum and 1% penicillin/streptomycin.

After 21 days of culture, Methyl Thiazolyl-Tetrazolium (MTT) test, Scanning Electron Microscopy (SEM) analysis, immunofluorescent staining with phalloidin, Alizarin Red S staining and quantification, and real-time PCR were carried out.

2.2.6. MTT Assay

To assess the proliferation rate of hADSCs grown on both uncoated and coated samples, a colorimetric mitochondrial viability assay was performed as described by Denizot and Lang [29] with minor modifications. After removing the culture medium, the samples were incubated in 1 mL of 0.5 mg/mL MTT solution in phosphate buffered saline (PBS) for 3 h at 37 °C. The MTT solution was then removed, and each sample was extracted with 0.5 mL of 10% dimethyl sulfoxide in isopropanol for 30 min at 37 °C. For each sample, Optical Density (O.D.) values, at 570 nm, were recorded in duplicate on 200 μL aliquots using a multilabel plate reader (Victor 3, Perkin Elmer, Milan, Italy).

2.2.7. SEM Analysis

For SEM imaging, hADSCs grown on both uncoated and sphene-coated samples for 21 days were fixed in 2.5% glutaraldehyde in 0.1 M cacodylate buffer for 1 h, then progressively dehydrated in ethanol. Cell spreading and morphology were evaluated using FEG-SEM (Quanta 250 Fei, Eindhoven, The Netherlands).

2.2.8. Immunofluorescence

Cell adhesion to the scaffolds surface was evaluated by immunofluorescent staining with phalloidin. Briefly, cells were fixed in 4% paraformaldehyde in PBS for 10 min, then permeabilized with 0.1% triton X-100 in PBS for 30 min at room temperature. 5 mg/mL phalloidin were then used for fluorescent staining of actin filaments, whereas nuclear staining was performed with 2 $\mu g\ mL^{-1}$ Hoechst H33342 solution for 5 min. Image acquisition was obtained with an inverted optical microscope DMI4000 B (Leica Microsystems,Wetzlar, Germany).

2.2.9. Alizarin Red S Staining and Quantification

The formation of extracellular mineral deposits onto uncoated and sphene-coated samples was detected by Alizarin Red S staining and quantification. Cells were fixed in

4% paraformaldehyde in PBS for 10 min at room temperature. Then, cells were stained adding 0.5 mL of 40 mM freshly prepared Alizarin Red S solution (pH 4.2) for 20 min at room temperature. After washing with double-distilled water, the Alizarin Red S stained areas were extracted with 0.5 mL of 10% cetylpyridinium chloride solution for 1 h at room temperature under gentle agitation. For each sample, O.D. values at 570 nm were recorded in duplicate on 200 µL aliquots using a Victor 3 plate reader.

2.2.10. Real-Time PCR

Total RNA was extracted from hADSCs, cultured on both uncoated and sphene-coated samples for 21 days, with a Total RNA Purification Plus Kit (Norgen Biotek Corporation, Thorold, ON, Canada). For the first-strand cDNA synthesis, 1 µg of total RNA of each sample was reverse transcribed with a SensiFAST™ cDNA Synthesis Kit (Bioline, London, UK), following the manufacturer's protocol. Human primers were selected for each target gene using a Primer 3 software. Real-time PCRs were run using the chosen primers at a concentration of 400 nM and SensiFAST™ SYBR No-ROX Kit (Bioline) on a Rotor-Gene 3000 (Corbett Research, Sydney, Australia). The thermal cycling conditions were as follow: 2 min denaturation at 95 °C; 40 cycles of 5 s denaturation at 95 °C; annealing for 10 s at 60 °C; and 20 s elongation at 72 °C. Differences in gene expression were calculated by normalizing to the expression of the Transferrin Receptor (TFRC) housekeeping gene.

2.2.11. Statistical Analysis

One-way analysis of variance (ANOVA) was used for data analysis. t-tests were used to determine data significance ($p < 0.05$). All tests were performed using SPSS 16.0 software (SPSS Inc., Chicago, IL, USA) (licensed to the University of Padua, Padova, Italy).

2.3. Results

2.3.1. Surface Characterization

FEG-SEM images of uncoated CpTi and sphene-coated surfaces are shown in **Figure 2a,b**, respectively. Sphene coating is characterized by a homogenous grey substrate,

composed of tetragonal crystals <1 μm, and "white islands" growing on it. These white agglomerates appear to be composed of vertically aggregated spherical particles. As reported in previous work [27], EDS (Energy Dispersive X-ray Spectrometry) analysis identified Ti, O, Si and Ca in areas corresponding to these white spherical structures. Instead, in the grey phase Ti and O were mainly present.

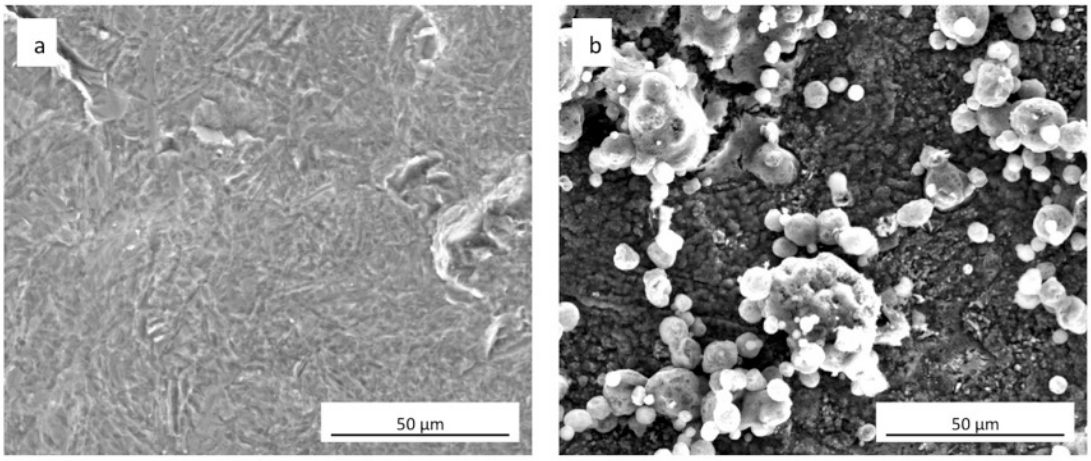

Figure 2. Surface morphology (SEM-FEG) of (a) as-received uncoated CpTi and (b) sphene-coated CpTi.

The coating composition was further investigated by XRD analysis and Rietveld refinement (**Figure 3**) that showed the presence of rutile (TiO_2, 60 wt%) followed by sphene ($CaTiSiO_5$, 31 wt%) and perovskite ($CaTiO_3$, 9 wt%). The as-received TiO_2 powders, used as a filler to develop the sphene ceramic, are characterized by a weight percentage ratio of 80 to 20 between anatase and rutile, as claimed in the manufacturer's datasheet. Anatase and rutile are the two main polymorphs of titanium oxide. They both exhibit tetragonal crystalline structure but obey different space groups. Anatase is a metastable phase, and the transformation to the stable rutile structure occurs as irreversible phase transformation in the range between 600 °C and 700 °C [30]. The treatment at 950 °C, performed in air, may have induced the nucleation and growth of rutile crystals before sphene synthesis, to yield a final weight percentage ratio of 60 wt% rutile. The higher stability of rutile compared to anatase may have inhibited the reaction to produce sphene at this temperature. It has indeed been reported in the literature that the formation of sphene by the sol-gel method is complete at 1300 °C [31]. As previously reported [24], the choice of keeping the temperature at 950 °C was driven by the need for preserving the structure of the CpTi plate without affecting the bonding of the coating to

the substrate. Further studies are ongoing aimed at increasing the amount of sphene produced by the preceramic polymer precursor route.

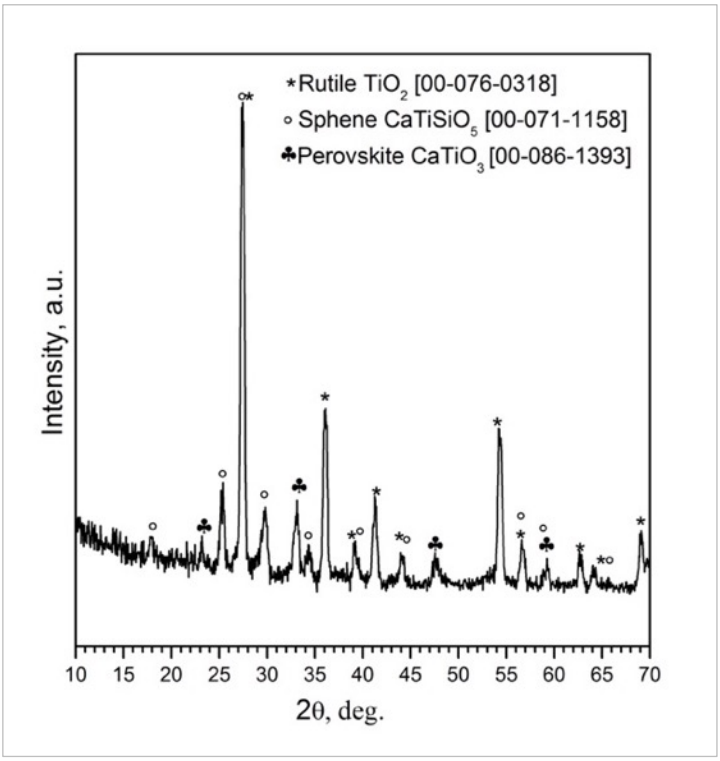

Figure 3. XRD pattern of sphene-coated CpTi after heat treatment at 950 °C in air for 1 h.

Surface roughness was investigated by means of a profilometer. 2D profile measurements (Ra and Rz) and 3D areal measurements (Sa and Sz) of uncoated (CpTi) and sphene-coated (Sphene) CpTi substrates are reported in **Table 1** and **Figure 4.**

A clear difference in the values of Ra and Rz between the CpTi substrate and the sphene-coated substrate can be observed in the 2D measurements. However, this difference is smoothed in the 3D areal measurements. Indeed, the surface of the CpTi substrate is characterized by a flatter morphology (**Figure 4a**) than the sphene-coated sample (**Figure 4b**). The sphene coating presents a high number of peaks homogeneously distributed, while the CpTi substrate presents a limited number of peaks, but characterized by a wider area. The yellow and red peaks in **Figure 4b** well correspond to the edges of the white agglomerates detected by SEM observations (**Figure 2b**).

2.3.2. Chemical Stability

The 2D roughness data after Tris-HCl immersion test show a slight increase after 1 day of soaking time. However, this increase in roughness values shows an almost constant trend after 3 and 7 days.

In accordance to these data, 3D maps of sphene after immersion in Tris-HCl solution (**Figure 4c,d**) demonstrated a reduction in the numbers of peaks after the dissolution test, with a similar pattern of peak and valley distributions at 1, 3 and 7 days after soaking. This is confirmed by Sa and Sz values that were reported in **Table 1**.

Table 1. Linear and surface roughness of as-received CpTi, sphene-coated CpTi, and sphene-coated CpTi after 1 and 7 days of chemical etching in Tris-HCl. Values are expressed as mean (standard deviation).

Samples	Ra [µm]	Rz [µm]	Sa [µm]	Sz [µm]
CpTi	2.82 (0.30)	14.30 (1.38)	3.51 (0.65)	25.15 (5.28)
Sphene	3.94 (0.75)	23.70 (3.74)	3.64 (0.47)	28.09 (3.58)
Sphene Tris-HCl, 1 day	4.66 (0.41)	27.80 (2.05)	4.39 (1.07)	37.28 (6.49)
Sphene Tris-HCl, 3 days	3.66 (0.52)	22.29 (2.85)	4.69 (0.37)	37.70 (6.57)
Sphene Tris-HCl, 7days	4.48 (0.37)	27.74 (2.81)	3.99 (0.45)	34.58 (4.96)

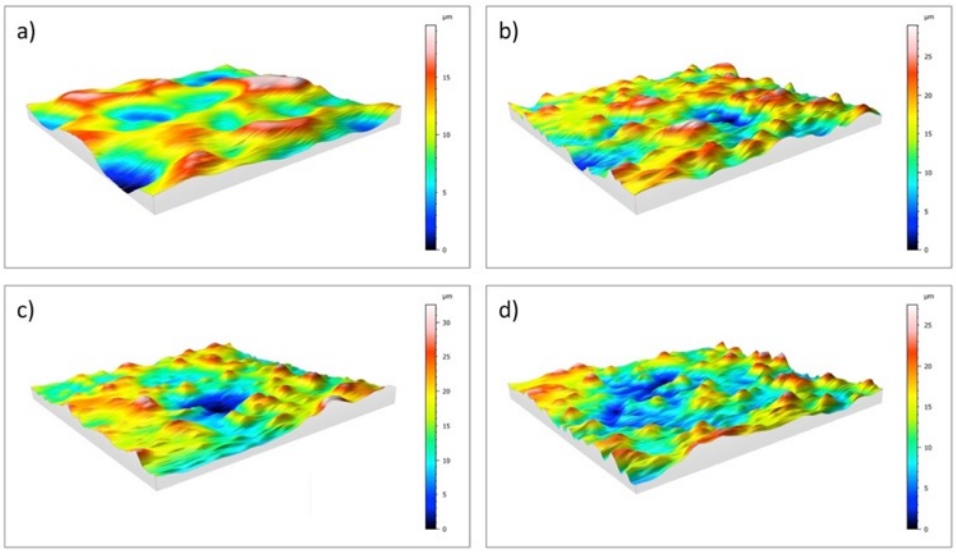

Figure 4. 3D maps of: (a) uncoated CpTi; (b) sphene-coated CpTi; (c) sphene-coated CpTi after 1 day in Tris-HCl buffer solution; (d) sphene-coated CpTi after 7 days in Tris-HCl buffer solution.

Figure 5 shows ICP analysis of Ca, Si and Ti ion release of the sphene coating in Tris-HCl solution at different time points. The average concentrations of Ca and Si ions, after 1 day of soaking, are 0.069 mM and 0.045 mM, respectively. Similar concentration levels were found after 3 and 7 days of immersion in Tris-HCl solution. Only trace amount of Ti ions released from the coating was detected (0.001–0.002 mM).

These findings are consistent with the above mentioned areal-topography measurements and suggest that the dissolution occurs only in the first hours after soaking.

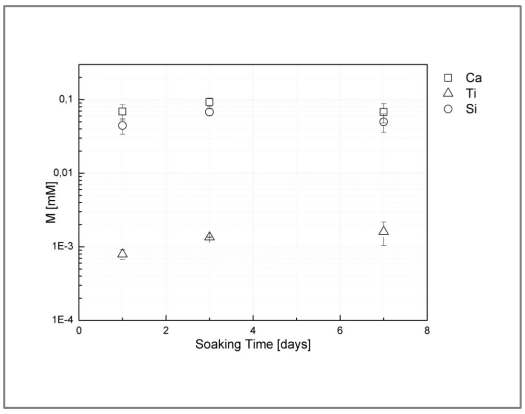

Figure 5. Ca, Ti and Si ion release of sphene-coated samples, after 1, 3, and 7 days of soaking time.

2.3.3. Cell Proliferation

The MTT assay proved that hADSCs were able to proliferate on both sphene-coated and uncoated samples (**Figure 6**). The O.D. values recorded for cells loaded on coated samples were found to be significantly ($p < 0.05$) higher to those observed for the controls in both the experimental conditions. Moreover, from MTT results, it was shown that hADSCs' proliferation was higher when hADSCs were cultured in Osteogenic Differentiation Medium compared to in DMEM High Glucose, in particular for the sphene-coated samples.

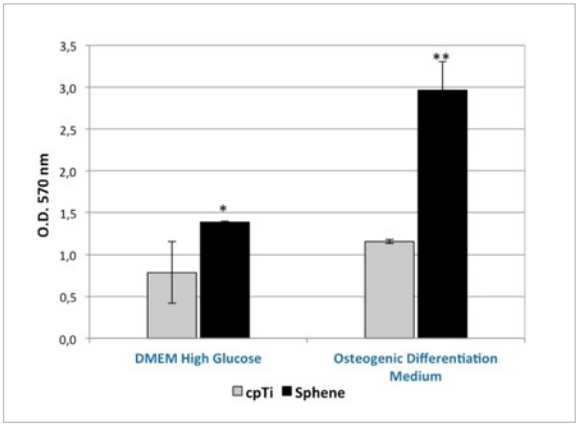

Figure 6. MTT assay of hADSCs cultured for 21 days on uncoated CpTi samples (CpTi) and on sphene-coated

2.3.4. Cell Adhesion and Morphology

The SEM analyses showed how hADSCs anchored to the surface of the specimens (**Figure 7a–d**). The cells were extremely flat with the typical star morphology associated with the osteoblastic-like phenotype and their distribution was similar, independent of the culture medium used (**Figure 7a,c**). After 21 days of culture onto the sphene-coated surfaces, cells showed short and thin filopodia when grown in DMEM High Glucose (**Figure 7b**); whereas they appeared flat and overlapped when cultured in the presence of the Osteogenic Differentiation Medium (**Figure 7d**). In both cases, the sphene coating remained intact during the culturing time, thus demonstrating its chemical stability.

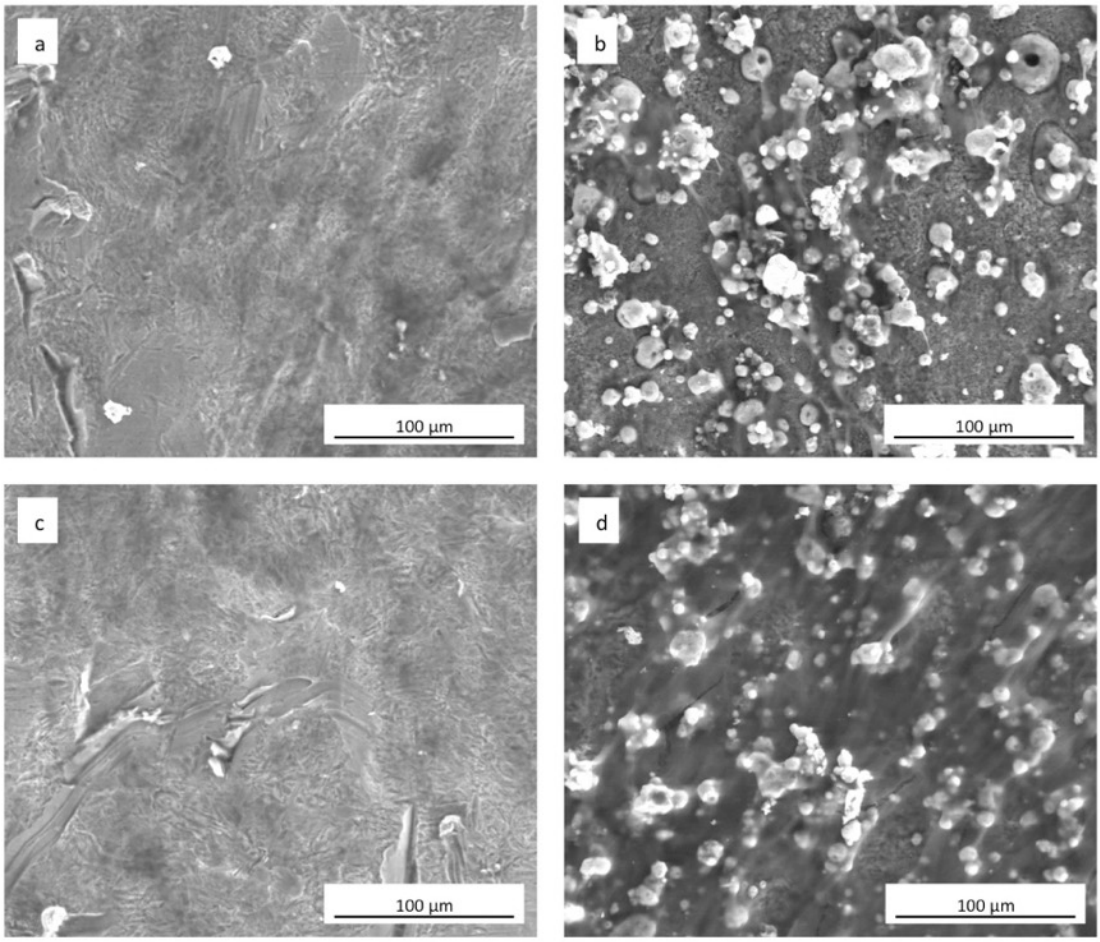

Figure 7. SEM images (1000 X magnification) of hADSCs grown for 21 days on (a) uncoated CpTi in DMEM High Glucose; (b) sphene-coated CpTi in DMEM High Glucose; (c) uncoated CpTi in Osteogenic Differentiation Medium; (d) sphene-coated CpTi in Osteogenic Differentiation Medium.

2.3.5. Cytoskeletal Organization

Staining with fluorescent phalloidin showed that cells were able to attach and spread on both the CpTi (**Figure 8a,c**) and sphene-coated samples (**Figure 8b,d**). After 21 days of culture, hADSCs had completely colonized the surfaces and formed a continuous layer with no significant differences between the experimental conditions. In vivo, such as in periosteum, osteoblasts are aligned with the collagen they produce and also on system cells are aligned to the collagen substrate. Cytoskeletal stresses and tension increase with increasing ECM (ExtraCellular Matrix) stiffness. The cytoskeleton provides a structural frame for the cell through Focal adhesions. Focal adhesion forms when adapter proteins link the cytoskeleton to integrins, which permits cells to adhere to the substrate. A variety of signaling proteins are also associated with focal adhesions, including focal adhesion kinase (FAK), an important mediator of signaling at these centers. Forces are also

transmitted to the substrate at these sites. Osteogenic differentiation can also be affected by the substrate properties where cells are seeded. On our samples, we can confirm that the shape of a cell follows the steps that occur *in vivo*.

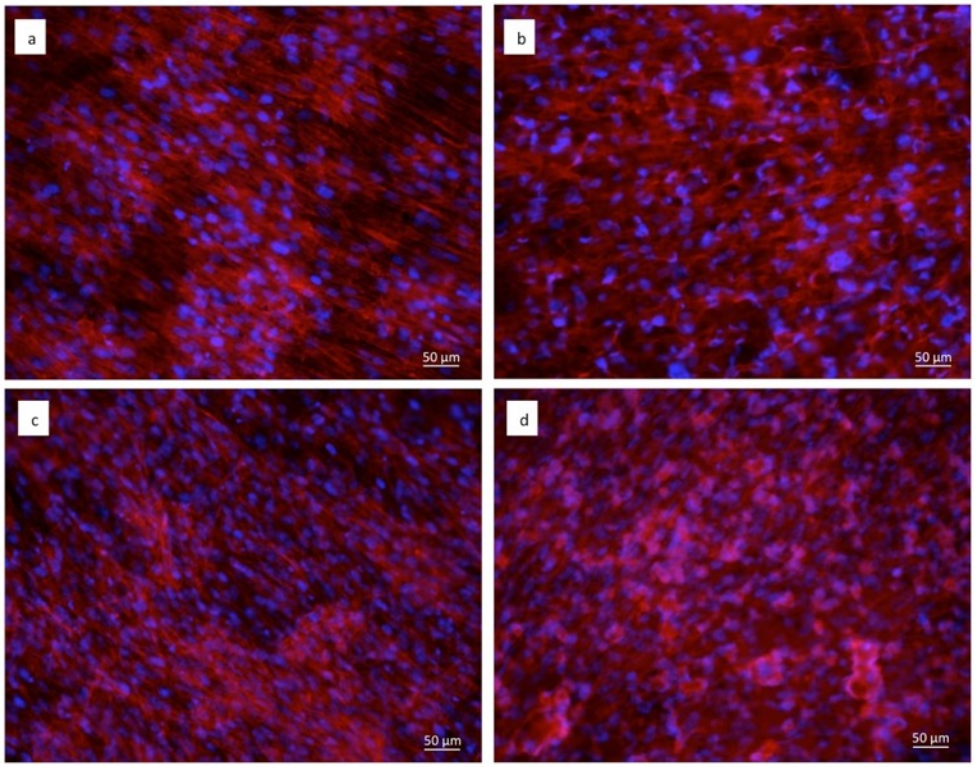

Figure 8. Immunofluorescent staining of the actin filaments with phalloidin (in red). Cell nuclei are counterstained with Hoechst (in blue). hADSCs seeded for 21 days on: (a) uncoated CpTi in DMEM High Glucose; (b) sphene-coated CpTi in DMEM High Glucose; (c) uncoated CpTi in Osteogenic Differentiation Medium; (d) sphene-coated CpTi in Osteogenic Differentiation Medium

2.3.6. In Vitro hADSC Osteogenic Differentiation

The *in vitro* osteogenic differentiation of hADSCs was first evaluated by marking of extracellular calcium deposition with Alizarin Red S staining and quantification at 21 days of culture (**Figure 9**). A difference in the presence of calcium deposits on the sphene-coated surfaces and the CpTi controls was evidenced for hADSCs cultured in the Osteogenic Differentiation Medium. Calcium deposits were significantly ($p < 0.05$) higher in the first experimental condition. The accumulation of calcium deposits by hADSCs was not observed when cells were seeded on the sphene-coated or uncoated samples in DMEM High Glucose.

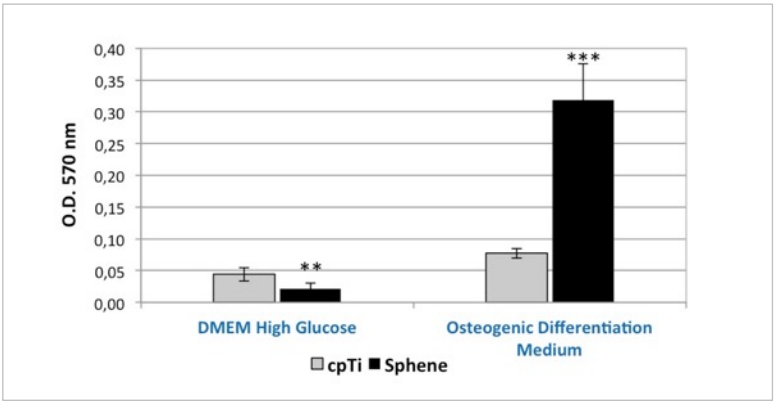

*Figure 9. Alizarin Red S quantification of calcium deposits produced by hADSCs seeded onto CpTi or Sphene surfaces in DMEM High Glucose or Osteogenic Differentiation Medium for 21 days. * $p < 0.05$, ** $p < 0.01$, *** $p < 0.001$.*

2.3.7. Real-Time PCR

Real-time PCR was used to quantify the relative expression level of several osteogenic differentiation markers. In particular, expression of runt-related transcription factor 2 (RUNX2), osterix (OSX), collagen type I (COL1A1), osteocalcin (OC), osteonectin (ON), osteopontin (OPN), alkaline phosphatase (ALPL), and receptor activator of nuclear factor kappa-B ligand (RANKL) has been investigated. Runx2 and Osterix are the main transcription factors involved on osteoblastic commitment. Collagen is the principal component of the bone matrix. Alkaline Phosphatase is involved on the calcification of the Extracellular matrix.

Osteonectin is a protein which role is related to the connection between extracellular matrix component and osteoblast. It is mostly produced during the first phases of bone regeneration or during bone remodeling [32–34].

As evident in **Figure 10a,c,** the relative expression of RUNX2, OSX, OC, OPN, and RANKL did not change significantly between the uncoated and sphene-coated surfaces, both when cells were grown in DMEM High Glucose or in Osteogenic Differentiation Medium. Similarly, there was no noticeable difference in ALPL (**Figure 10a**), COL1A1 and ON (Figure 9b) mRNA expression between CpTi and sphene-coated samples in DMEM High Glucose; instead, a slight down-regulation of ALPL (**Figure 10c**) and COL1A1 (**Figure 10d**) expression was identified in cells seeded onto the sphene surfaces in the presence of Osteogenic Differentiation Medium.

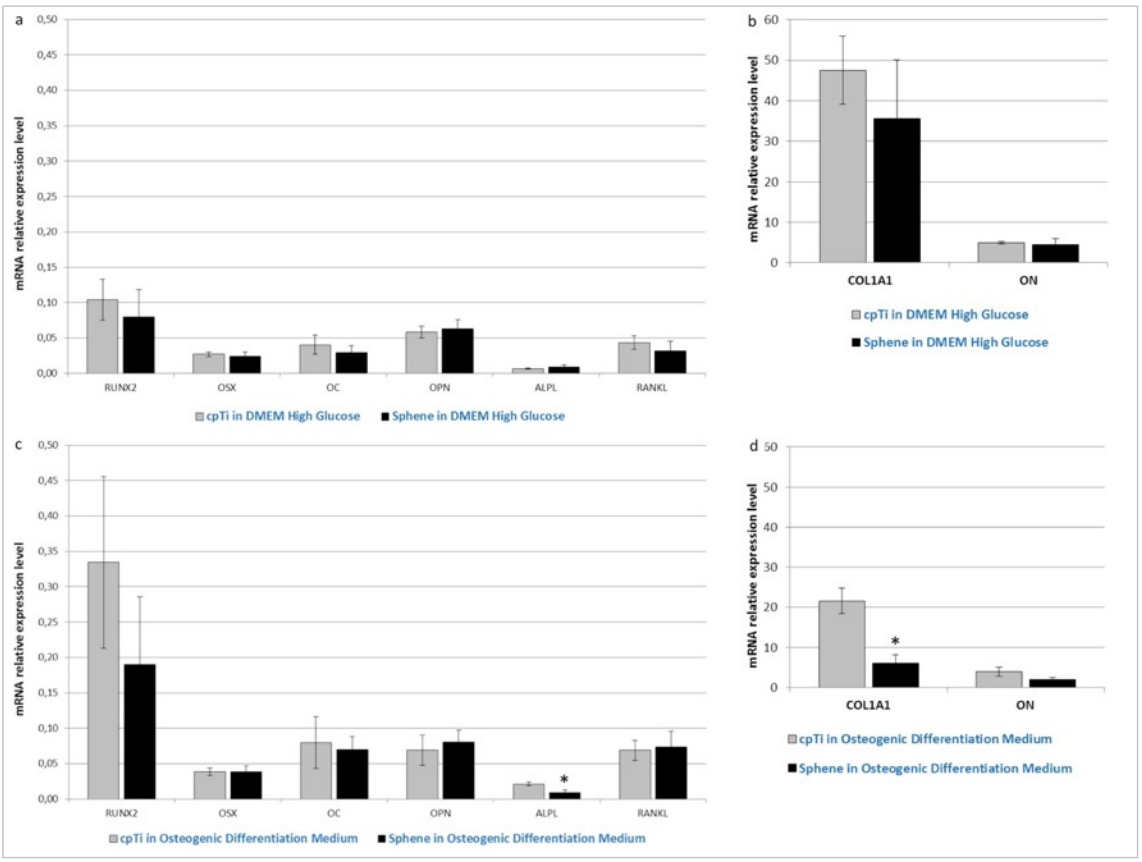

Figure 10. Real-time PCR analysis of the osteogenic differentiation markers runt-related transcription factor 2 (RUNX2), osterix (OSX), collagen type I (COL1A1), osteocalcin (OC), osteonectin (ON), osteopontin (OPN), alkaline phosphatase (ALPL), and receptor activator of nuclear factor kappa-B ligand (RANKL). Data are normalized to the expression of the transferrin receptor (TFRC) internal reference. Gray bars indicate the relative expression level of the selected genes in the hADSCs seeded onto CpTi samples in DMEM High Glucose (a,b) or Osteogenic Differentiation Medium (c,d) for 21 days. Black bars represent the gene expression level of the same markers in the hADSCs seeded onto Sphene samples in DMEM High Glucose (a,b) or Osteogenic Differentiation Medium (c,d) for 21 days.

2.4. Discussion

In the present study, the sphene-based coatings on CpTi substrates showed a rough morphology, with roughness Ra in the range of 3.25 to 4.75 μm. The morphology was characterized by small crystals made of TiO_2 and $CaTiO_3$ (valley of **Figure 4**) and islands of unregular shape that were detected by EDS analysis to be composed of sphene [27]. The quantitative XRD analysis performed on the coated substrate showed the reaction efficiency and the amount of sphene that was about 31 wt%.

Micro-roughened surfaces were demonstrated to have a positive effect on early blood cell/implant interactions [35] and osteoblast proliferation [36]. In addition, surface topography was found to influence osteoconduction in both animal studies [37,38] and

human retrieval study [39], with good results shown by rough implant surfaces. Sphene coatings examined in the present study possessed a moderately rough surface. The surface roughness quantified by 3D areal measurements showed a good correspondence with 2D measurements in both CpTi and coated CpTi.

Even though the release of Ca and Si ions has been demonstrated to favor osteoblastic proliferation and differentiation [18,19,40], one of the major drawbacks of biosilicate ceramic coatings, such as $CaSiO_3$ coatings, consists of their poor chemical stability and high degradation rate that might compromise their long-term stability [41,42]. Therefore, a limited release of these ions would enhance coating bioactivity and, on the other hand, would not interfere with the integrity of the coating itself [43].

To assess the chemical stability of the coatings, Tris-HCl was chosen due to the absence of Ca, Si or Ti ions in its composition. The results of dissolution tests in Tris-HCl showed that the dissolution happened only during the first hours of soaking and then remained constant after 1, 3 and 7 days. This behavior agrees with the results reported by Wu et al. [22], thus proving that the developed coating is comparable in terms of chemical properties to standard HA. At the same experimental conditions of the present study, a lower released Ca concentration (2.74 ppm) after 7 days of soaking in Tris-HCl was found in the sphene-coated samples here investigated as compared to the values of around 20 ppm and >110 ppm of plasma-sprayed sphene ceramic coatings and HA coatings, respectively [14]. Moreover, as found by Wang et al. [43], a higher concentration of Ca ions released to the solution was measured compared with the concentration of Si ions released after 7 days of immersion. In addition, only an irrelevant amount of Ti ions was detected by Wang et al. [43] in the Tris-HCl after one week of soaking.

The roughness of samples, after dissolution tests slightly increased compared to the starting samples. This is mainly observable in the areal measurements where a sharp increase of Sz was measured from unetched sphene to 1-day soaking time in Tris-HCl. In agreement with ICP analysis, no significant trends on roughness at increasing soaking time can be observed. Thus, this proves that little dissolution of Ca, Ti and Si, happened during the first 24 h.

The chemical composition of implant surfaces profoundly influences cell adhesion, spreading, proliferation, and differentiation [44,45]. Sphene-based substrates better supported hADSCs attachment and proliferation, compared with uncoated CpTi samples, as revealed by the MTT assay. By SEM analysis, a uniform layer of well-spread cells

could be observed when cells were cultured onto the sphene-coated surfaces in Osteogenic Differentiation Medium. The results of Alizarin Red S quantification suggested that sphene coating favorably affects the accumulation of mineralized calcium phosphate when cells are cultured in the presence of osteogenic factors.

Moreover, cells seeded onto sphene-coated surfaces expressed similar levels of osteoblasts-related genes to those expressed by cells cultured on uncoated CpTi in both culture conditions. We can hypothesize that the combination of the coating and the Osteogenic Differentiation Medium promoted a higher calcium deposition on sphene-coated surfaces than on uncoated CpTi substrates. These findings agree with Wang et al. [43], who demonstrated that sphene glass-ceramic coatings were able to support human osteoblast-like cells (HOBs) attachment, proliferation and differentiation and enhance the expression level of bone-related genes. Furthermore, it was demonstrated that sphene ceramic coatings significantly enhanced HOBs proliferation and ALP activity compared with plasma-sprayed HA coating and uncoated Ti-6Al-4V substrates [14]. Pure dense sphene ceramic disks were found to promote human bone-derived cells attachment and to significantly improve their proliferation and differentiation, as compared with α-$CaSiO_3$ ceramic disks [25]. Pure sphene ceramic disks were not only found to modulate HOBs, but also osteoclasts and endothelial cells [26]. As compared with the study of Ramaswamy et al. [26], in the current work, mesenchymal stem cells (MSCs) were preferred to human osteoblast-like cells, human osteoclasts and human microvascular endothelial to in vitro investigate the osteoconductive properties of the biomaterial, since stem cells are the main actors enrolled during the early stages of tissue regeneration. MSCs are stem cells involved on tissue regeneration, which can migrate to the damage site thanks to their receptor and to coordinate all the phase of tissue regeneration [46]. Hypoxia, which usually occurs at the injured sites due to a disruption in blood supply, has been reported to largely contribute to MSC mobilization and homing.

The hypoxia-inducible factors (HIFs) are key regulators of the cellular response to decrease in the local oxygen level, also regulating the expression of genes involved in MSC recruitment and migration to the damaged tissues [32–34,46–48].

In a good agreement with previously published work [14,25,26,43], our results suggest

that the ionic environment, determined by the dissolution of Ca and Si ions from the sphene biomaterial, may contribute to stimulate cell proliferation and differentiation. In addition, the *in vivo* assessment revealed enhanced osseointegration of both sphene-

coated and HA-coated Ti-6Al-4V implants, compared to uncoated implants, confirming the *in vitro* observations and the potential use of sphene coatings in clinical application [26].

In conclusion, sphene-based crack-free coatings were successfully produced starting from a preceramic polymer and nano-sized fillers and deposited using an automatic airbrush. The coatings presented good chemical stability, as a minimal dissolution occurred only during the first hours of soaking in Tris-HCl solution and then remained stable over the period considered. The coatings also supported hADSCs attachment, proliferation, and differentiation *in vitro*. Taken together, our findings indicate a potential for use of sphene ceramics as coating materials for orthopedic and dental implants.

In vivo studies should be performed to confirm *in vitro* observations. Further studies are ongoing to increase the reaction efficiency.

Data published in: Elsayed H, **Brunello G**, Gardin C, Ferroni L, Badocco D, Pastore P, Sivolella S, Zavan B, **Biasetto L**. Bioactive Sphene-Based Ceramic Coatings on CpTi Substrates for Dental Implants: An In Vitro Study. Materials (Basel). 2018;11(11). pii: E2234. doi: 10.3390/ma11112234.

Author Contributions: Conceptualization, H.E., B.Z. and L.B.; Data curation, H.E., **G.B.**, C.G., L.F., D.B. and L.B.; Formal analysis, H.E., **G.B.**, C.G. and L.F.; Supervision, S.S., B.Z. and L.B.; Validation, L.B.; Writing—original draft, H.E. and **G.B.**; Writing—review and editing, H.E., **G.B.**, C.G., L.F., D.B., P.P., S.S., B.Z. and L.B.

Funding: This research received no external funding.

Acknowledgments: The author would like to thank Prof. Roberto Meneghello of Department of Management and Engineering for his contribution in surface characterization. The author gratefully acknowledges the experimental support provided by Mr. Giacomo Mazzacavallo.

References

1. Kirmanidou Y, Sidira M, Drosou ME, Bennani V, Bakopoulou A, Tsouknidas A, Michailidis N, Michalakis K. New Ti-Alloys and Surface Modifications to Improve the Mechanical Properties and the Biological Response to Orthopedic and Dental Implants: A Review. Biomed. Res. Int. 2016, 2016, 2908570. DOI: 10.1155/2016/2908570.

2. Quirynen M, Al-Nawas B, Meijer HJ, Razavi A, Reichert TE, Schimmel M, Storelli S, Romeo E. Roxolid Study Group. Small-diameter titanium Grade IV and titanium-zirconium implants in edentulous mandibles: Three-year results from a double-blind, randomized controlled trial. Clin. Oral Implants Res. 2015, 26, 831–840. DOI: 10.1111/clr.12367.

3. Elias CN, Fernandes DJ, Resende CR, Roestel J. Mechanical properties, surface morphology and stability of a modified commercially pure high strength titanium alloy for dental implants. Dent. Mater. 2015, 31, e1–e13. DOI: 10.1016/j.dental.2014.10.002.

4. Niinomi M. Mechanical biocompatibilities of titanium alloys for biomedical applications. J. Mech. Behav. Biomed. Mater. 2008, 1, 30–42. DOI: 10.1016/j.jmbbm.2007.07.001.

5. Zreiqat H, Valenzuela SM, Nissan BB, Roest R, Knabe C, Radlanski RJ, Renz H, Evans PJ. The effect of surface chemistry modification of titanium alloy on signalling pathways in human osteoblasts. Biomaterials 2005, 26, 7579–7586. DOI: 10.1016/j.biomaterials.2005.05.024.

6. Liu X, Chu PK, Ding C. Surface modification of titanium, titanium alloys, and related materials for biomedical applications. Mater. Sci. Eng. R Rep. 2004, 47, 49–121. DOI: 10.1016/j.mser.2004.11.001.

7. Wennerberg A, Bougas K, Jimbo R, Albrektsson T. Implant coatings: New modalities for increased osseointegration. Am. J. Dent. 2013, 26, 105–112.

8. Narayanan R, Seshadri SK, Kwon TY, Kim KH. Calcium phosphate-based coatings on titanium and its alloys. J. Biomed. Mater. Res. B Appl. Biomater. 2008, 85, 279–299. DOi: 10.1002/jbm.b.30932.

9. Lin DY, Wang XX. A novel method to synthesize hydroxyapatite coating with hierarchical structure. Colloids Surf. B Biointerfaces 2011, 82, 637–640. DOI: 10.1016/j.colsurfb.2010.09.025.

10. Liu X, Tao S, Ding C. Bioactivity of plasma sprayed dicalcium silicate coatings. Biomaterials 2002, 3, 963–968. DOI: 10.1016/S0142-9612(01)00210-1.

11. Mohammadi H, Sepantafar M. Ion-Doped Silicate Bioceramic Coating of Ti-Based Implant. Iran. Biomed. J. 2016, 20, 189–200. DOI: 10.7508/ibj.2016.04.002.

12. Xuereb M, Camilleri J, Attard NJ. Systematic review of current dental implant coating materials and novel coating techniques. Int. J. Prosthodont. 2015, 28, 51–59. DOI: 10.11607/ijp.4124.

13. Xue W, Liu X, Zheng X, Ding C. Plasma-sprayed diopside coatings for biomedical applications. Surf. Coat. Technol. 2004, 185, 340–345. DOI: 10.1016/j.surfcoat.2003.12.018

14. Wu C, Ramaswamy Y, Liu X, Wang G, Zreiqat H. Plasma-sprayed CaTiSiO5 ceramic coating on Ti-6Al-4V with excellent bonding strength, stability and cellular bioactivity. J. R. Soc. Interface 2009, 6, 159–168. DOI: 10.1098/rsif.2008.0274.

15. Gomez-Vega JM, Saiz E, Tomsia AP, Marshall GW, Marshall SJ. Bioactive glass coatings with hydroxyapatite and Bioglass particles on Ti-based implants. 1. Processing. Biomaterials 2000, 21, 105–111. DOI: 10.1016/S0142-9612(99)00131-3.

16. Bloyer DR, Gomez-Vega JM, Saiz E, McNaney JM, Cannon RM, Tomsia AP. Fabrication and characterization of a bioactive glass coating on titanium implant alloys. Acta Mater. 1999, 47, 4221–4224. DOI: 10.1016/S1359-6454(99)00280-3.

17. Silver IA, Deas J, Erecinska M. Interactions of bioactive glasses with osteoblasts in vitro: Effects of 45S5 Bioglassw, and 58S and 77S bioactive glasses on metabolism, intracellular ion concentrations and cell viability. Biomaterials 2001, 22, 175–185. DOI: 10.1016/S0142-9612(00)00173-3.

18. Sun J, Wei L, Liu X, Li J, Li B, Wang G, Meng F. Influences of ionic dissolution products of dicalcium silicate coating on osteoblastic proliferation, differentiation and gene expression. Acta Biomater. 2009, 5, 1284–1293. DOI: 10.1016/j.actbio.2008.10.011.

19. Valerio P, Pereira MM, Goes AM, Leite MF. The effect of ionic products from bioactive glass dissolution on osteoblast proliferation and collagen production. Biomaterials 2004, 25, 2941–2948. DOI: 10.1016/j.biomaterials.2003.09.086.

20. Xynos ID, Edgar AJ, Buttery LDK, Hench LL, Polak JM. Gene-expression profiling of human osteoblasts following treatment with the ionic products of Bioglassw 45S5 dissolution. J. Biomed. Mater. Res. 2001, 55, 151–157. DOI: 10.1002/1097-4636(200105)55:2<151::AID-JBM1001>3.0.CO;2-D.

21. Wu C, Chen Z, Yi D, Chang J, Xiao Y. Multidirectional effects of Sr, Mg and Si-containing bioceramic coatings with high bonding strength on inflammation,

osteoclastogenesis and osteogenesis. ACS Appl. Mater. Interfaces 2014, 6, 4264–4276. DOI: 10.1021/am4060035.

22. Wu C, Ramaswamy Y, Gale D, Yang W, Xiao K, Zhang L, Yin Y, Zreiqat H. Novel sphene coatings on Ti-6Al-4V for orthopedic implants using sol-gel method. Acta Biomater. 2008, 4, 569–576. DOI: 10.1016/j.actbio.2007.11.005.

23. Cheng S, Wei D, Zhou Y. Formation and structure of sphene/titania composite coatings on titanium formed by a hybrid technique of microarc oxidation and heat-treatment. Appl. Surf. Sci. 2011, 257, 3404–3411. DOI: 10.1016/j.apsusc.2010.11.034.

24. Biasetto L, Elsayed H, Bonollo F, Colombo P. Polymer-derived sphene biocoating on cpTi substrates for orthopedic and dental implants. Surf. Coat. Technol. 2016, 301, 140–147. DOI: 10.1016/j.surfcoat.2016.01.018.

25. Wu C, Ramaswamy Y, Soeparto A, Zreiqat H. Incorporation of titanium into calcium silicate improved their chemical stability and biological properties. J. Biomed. Mater. Res. A 2008, 86, 402–410. DOI: 10.1002/jbm.a.31623.

26. Ramaswamy Y, Wu C, Dunstan CR, Hewson B, Eindorf T, Anderson GI, Zreiqat H. Sphene ceramics for orthopedic coating applications: An in vitro and in vivo study. Acta Biomater. 2009, 5, 3192–3204. DOI: 10.1016/j.actbio.2009.04.028.

27. Biasetto L, Elsayed H. Sphene silicate ceramic coatings on cpTi substrates: Process upgrade. Surf. Coat. Technol. 2017, 321, 416–424. DOI: 10.1016/j.surfcoat.2017.05.018.

28. Gardin C, Bressan E, Ferroni L, Nalesso E, Vindigni V, Stellini E, Pinton P, Sivolella S, Zavan B. In vitro concurrent endothelial and osteogenic commitment of adipose-derived stem cells and their genomical analyses through comparative genomic hybridization array: Novel strategies to increase the successful engraftment of tissue-engineered bone grafts. Stem Cells Dev. 2012, 21, 767–777. DOI: 10.1089/scd.2011.0147.

29. Denizot F, Lang R. Rapid colorimetric assay for cell growth and survival. Modifications to the tetrazolium dye procedure giving improved sensitivity and reliability. J. Immunol. Methods 1986, 89, 271–277. DOI: 10.1016/0022-1759(86)90368-6.

30. Hanaor DAH, Sorrell CC. Review of the anatase to rutile phase transformation. J. Mater. Sci. 2011, 46, 855–874. DOI: 10.1007/s10853-010-5113-0.

31. Muthuraman M, Patil KC. Synthesis, properties, sintering and microstructure of sphene, CaTiSiO5: A comparative study of coprecipitation, sol–gel and combustion

processes. Mater. Res. Bull. 1998, 33, 655–661. DOI: 10.1016/S0025-5408(98)00005-1.

32. Liu H, Li D, Zhang Y, Li M. Inflammation, mesenchymal stem cells and bone regeneration. Histochem. Cell Biol. 2018, 149, 393–404. DOI: 10.1007/s00418-018-1643-3.

33. Currey JD, Dean MN, Shahar R. Revisiting the links between bone remodelling and osteocytes: Insights from across phyla. Biol. Rev. Camb. Philos. Soc. 2017, 92, 1702–1719. DOI: 10.1111/brv.12302.

34. Katsimbri P. The biology of normal bone remodelling. Eur. J. Cancer Care 2017, 26, e12740. doi: 10.1111/ecc.12740.

35. Park JY, Davies JE. Red blood cell and platelet interactions with titanium implant surfaces. Clin. Oral Implants Res. 2000, 11, 530–539. DOI: 10.1034/j.1600-0501.2000.011006530.x.

36. Iwata N, Nozaki K, Horiuchi N, Yamashita K, Tsutsumi Y, Miura H, Nagai A. Effects of controlled micro-/nanosurfaces on osteoblast proliferation. J. Biomed. Mater. Res. A 2017, 105, 2589–2596. DOI: 10.1002/jbm.a.36118.

37. Franchi M, Orsini E, Trire A, Quaranta M, Martini D, Piccari GG, Ruggeri A, Ottani V. Osteogenesis and morphology of the peri-implant bone facing dental implants. Sci. World J. 2004, 4, 1083–1095. DOI: 10.1100/tsw.2004.211.

38. Franchi M, Bacchelli B, Giavaresi G, De Pasquale V, Martini D, Fini M, Giardino R, Ruggeri A. Influence of different implant surfaces on peri-implant osteogenesis: Histomorphometric analysis in sheep. J. Periodontol. 2007, 78, 879–888. DOI: 10.1902/jop.2007.060280.

39. Lazzara RJ, Testori T, Trisi PM, Porter SS, Weinstein RL. A human histologic analysis of osseotite and machined surfaces using implants with 2 opposing surfaces. Int. J. Periodontics Restorative Dent. 1999, 19, 117–129. DOI: 10.11607/prd.00.0309.

40. Fei L, Wang C, Xue Y, Lin K, Chang J, Sun J. Osteogenic differentiation of osteoblasts induced by calcium silicate and calcium silicate/_-tricalcium phosphate composite bioceramics. J. Biomed. Mater. Res. B Appl. Biomater. 2012, 100, 1237–1244. DOI: 10.1002/jbm.b.32688.

41. Ni S, Chang J. In vitro degradation, bioactivity, and cytocompatibility of calcium silicate, dimagnesium silicate, and tricalcium phosphate bioceramics. J. Biomater. Appl. 2009, 24, 139–158. DOI: 10.1177/0885328208094745.

42. Wu C, Ramaswamy Y, Kwik D, Zreiqat H. The effect of strontium incorporation into CaSiO3 ceramics on their physical and biological properties. Biomaterials 2007, 28, 3171–3181. DOI: 10.1016/j.biomaterials.2007.04.002.

43. Wang G, Lu Z, Liu X, Zhou X, Ding C, Zreiqat H. Nanostructured glass-ceramic coatings for orthopaedic applications. J. R. Soc. Interface 2011, 8, 1192–1203. DOI: 10.1098/rsif.2010.0680.

44. Bezerra F, Ferreira MR, Fontes GN, da Costa Fernandes CJ, Andia DC, Cruz NC, da Silva RA, Zambuzzi WF. Nano hydroxyapatite-blasted titanium surface affects pre-osteoblast morphology by modulating critical intracellular pathways. Biotechnol. Bioeng. 2017, 114, 1888–1898. DOI: 10.1002/bit.26310.

45. Wei J, Heo SJ, Kim DH, Kim SE, Hyun YT, Shin JW. Comparison of physical, chemical and cellular responses to nano- and micro-sized calcium silicate/poly(3-caprolactone) bioactive composites. J. R. Soc. Interface 2008, 5, 617–630. DOI: 10.1098/rsif.2007.1267.

46. Herrmann M, Verrier S, Alini M. Strategies to stimulate mobilization and homing of endogenous stem and progenitor cells for bone tissue repair. Front Bioeng. Biotechnol. 2015, 3, 79. DOI: 10.3389/fbioe.2015.00079.

47. Lampert FM, Kütscher C, Stark GB, Finkenzeller G. Overexpression of Hif-1 if-1α in mesenchymal stem cells affects cell-autonomous angiogenic and osteogenic parameters. J. Cell Biochem. 2016, 117, 760–768. DOI: 10.1002/jcb.25361.

48. Lin W, Xu L, Zwingenberger S, Gibon E, Goodman SB, Li, G. Mesenchymal stem cells homing to improve bone healing. J. Orthop. Transl. 2017, 9, 19–27. DOI: 10.1016/j.jot.2017.03.002.

Chapter 3

Bioactive Sphene-Based Ceramic Coatings on CpTi Substrates for Dental Implants: An In Vivo Study in Rat Femurs

Abstract

After the encouraging results of our preliminary *in vitro* study, fully described in **Chapter 2**, it was time to move a step forward and to investigate the influence of sphene-based bioceramic coating on implant osseointegration *in vivo*.

Animal models play a fundamental role in the development of implantable medical devices. To evaluate the *in vivo* performances of the developed sphene coating, a rat model was chosen. The already optimized suspension composition and processing setup utilized for *in vitro* study were used for implant coating.

The primary aim of this study was to compare bone-to-implant (BIC) values, measured on micro–computed tomography (micro-CT) scans, of uncoated titanium (Ti) implants (control) with those of sphene-coated implants (test) at two different time points, at 14 and 28 days of healing.

Secondary aims include: a) the evaluation of BIC in the two different bone compartments, cortical and cancellous bone, via micro-CT; b) the comparative histological analysis of peri-implant bone healing in contact with the investigated implant surfaces; c) the analysis of the synovial fluid (SF) collected from the knee joints at the time of the sacrifice.

Customized Ti implants were designed and produced. The implants were coated with sphene bioceramic by spray coating. The thickness and porosity of the coating were evaluated using micro-CT, while surface roughness of both uncoated and coated implants was determined with an optical microscope using the confocal principle.

Customized Ti implants, either sphene-coated (n=10) or uncoated (n=10), were bilaterally implanted into the proximal femurs of 10 Sprague–Dawley rats for 14 or 28 days.

Overall BIC% and BIC% in the two different bone compartments, cortical and cancellous, were assessed for each sample using micro-CT. Peri-implant bone healing was also histologically and histomorphometrically evaluated. Furthermore, SF, when collected, was forwarded for assessment of SF white blood cell (WBC) count.

Coated implants were characterized by a mean coating thickness of 61 ± 13.4 μm, Sa value of 3.38 μm and a dense structure.

No statistically significant difference in BIC values assessed using micro-CT was observed between sphene-coated and uncoated samples at both time points ($p > 0.05$).

Moreover, no differences between the two groups were detected in BIC% calculated the in cortical and cancellous bone.

Consistently with micro-CT data, from histological and histomorphometric evaluation of the peri-implant tissues, no differences could be observed between the two groups. Histological healing scenario after 14 days was characterized by the presence of an inflammatory response, extracellular matrix apposition and neo-angiogenesis. By contrast, after 28 days from surgery, no inflammatory cells were found and newly formed bone could be observed.

In addition, contrary to the control side, no SF was collected on the test side, confirming the compatibility of the coating material.

The main problem encountered in the present work was the delamination of the coating in three cases out of 10, as revealed by micro-CT analysis, which most likely occurred during implant insertion.

In conclusion, sphene ceramic resulted to be a biocompatible material for dental and orthopedic applications. Further studies are needed to address the issue of coating delamination prior to clinical testing.

Keywords: implant; osseointegration; biocompatibility; bioactive ceramic coatings; sphene; Bone-to-implant contact; micro-CT

3.1. Introduction

3.1.1. In Vivo Models to Assess Implant Osseointegration

Osseointegration, which is defined as the close contact between implant and surrounding living bone, is a fundamental condition for long-term implant success [1]. At a biological level, the process of osseointegration occurs at two different stages, known as primary implant stability and secondary implant stability [2,3]. Primary stability is represented by the initial mechanical interlocking between the implant and the surrounding bone, whereas the secondary implant stability refers to bone regeneration and remodeling occurring at the bone-implant interface. Several clinical factors affect primary stability, among which quality and quantity of the recipient bone, implant geometry and surface properties, and surgical technique adopted are determining aspects.

A secure primary stability is considered a requirement for successful secondary stability, therefore the achievement of a good primary stability is regarded as a key factor for implant osseointegration [4].

In order to improve and accelerate new bone formation at bone-implant interface, several implant surface modifications have been proposed, either by addition or subtraction techniques [5,6].

In vitro experiments can offer a great insight into the mechanisms at the tissue-implant interface, however it is not possible to completely reproduce *in vitro* the complex and dynamic *in vivo* environment. With a view to reducing the number of unnecessary animal studies, it is widely recognized that laboratory testing represents a valid tool for preliminarily testing the toxicity and the cytocompatibility of a biomaterial, thus limiting animal experiments to selected promising materials [7-9].

Nowadays, it is accepted that *in vitro* findings have to be confirmed and validated in animal models, prior to clinical trials in humans. Due to the similarity with the human bone in terms of anatomical structure and healing process, dogs, sheep, goats and nonhuman primates are preferably used for translational research. Despite the advantages of using large animal models, these are subject to relevant ethical concerns [10,11]. Even though the bone structure of smaller animals differs from that of humans to a greater extent, rabbits and rodents have been established as alternative models for assessing implant osseointegrations [8]. It is worth noting that the implant has to be scaled down to the size of the selected animal model and that the macro-design of the implant (e.g. presence of threads) will dictate the techniques for assessing osseointegration, in particular mechanical testing ones [7,8].

Different procedures are currently available for measuring implant osseointegration. These can be distinguished in two main categories: non-invasive/non-destructive methods and invasive/destructive methods [12].

One of the main advantages of non-invasive methods for assessing implant stability is that they can be used for clinical assessments of implant success or failure in humans, as they do not necessitate the retrieval of the implant. The principal methods are imaging techniques, including conventional radiography and computed tomography (CT), and resonance frequency analysis (RFA).

Imaging techniques can be used at any stage of healing following the surgery to assess the health of the implant, the bone quantity and quality, and the crestal bone loss, which

is a consequence of the osseointegration process [2]. However, several limitations exist in the use of conventional radiograph alone to make a precise evaluation of implant stability. First of all, image resolution is too low to detect changes in radiographic bone loss. In addition, crestal bone changes cannot be quantitatively measured because of distortion effects related to the presence of Ti [13]. Interestingly, in a study aiming to relate the radiographic and the histomorphometric assessments of peri-implant bone tissues of implants placed in the lower jaw of monkeys, bone density assessed on digital intra-oral radiographs was weakly correlated with bone-to-implant contact (BIC) obtained by histomorphometric evaluation [14]. As compared to intra-oral images, cone beam CT scans provide 3D information about the bone status around implants, however metal artefacts limit the accuracy of peri-implant bone evaluation [15].

RFA is a non-destructive biomechanical technique that measures the stability and stiffness of the osseointegrated dental implant interface by using vibration and a principle of structural analysis [2,16]. The reproducibility of this measure at several time points is considered of great advantage for the evaluation of implant stability over time [17]. Although extensively used in clinical research, RFA is influenced by factors such as bone tissue characteristics and implant sink depth, diameter and surface characteristics [18]. As a consequence, the long-term success of a dental implant cannot be provided with RFA, making limited its clinical value.

Beside non-invasive/non-destructive methods listed above, also invasive/destructive methods have been proposed. The use of destructive tests for assessing implant osseointegration in humans is limited due to ethical issues related to the invasiveness of these methods, however they are generally employed in preclinical animal studies [12]. Various methods belong to this category, including pull-out and push-out tests, removal torque analysis, tensional test, scanning and transmission electron microscopy (SEM and TEM, respectively) analysis, histological and histomorphometric analyses [12,13]. Even though micro-CT can be performed on living animals of small dimensions, such as mice or rats, allowing for monitoring the animals longitudinally at different time points [19,20], many factors have to be considered, such as scan duration, artefacts due to movement and animal welfare, which might be compromised by the multiple anesthetic exposures or ionizing radiations. Whereas, the scanning of isolated bones, dissected out after the sacrifice of the animal, allows for the acquisition of higher quality images [21].

The pull-out and push-out tests, together with removal torque analysis, are defined as *ex vivo* biomechanical tests, which measure the amount of force or torque required to disrupt the bone-implant interface [10,22].

Pull-out test is applicable only when non-threaded cylindrical implants are utilized. This approach involves the insertion of the implant transcortically or intramedullary in bone structures, and its consequent removal by applying a force parallel to the interface. In order to avoid inappropriate application of force, the execution of the pull-out test requires careful orientation of the implant to the pull direction. Therefore, alignment is a key factor, but once obtained it allows to evaluate only the differences in implant surface. For this reason, pull-out would represent the purest test in which the implant surface represents the only variable [23]. To date, pull-out is typically performed using long bones of different animal models. The rabbit tibia and femur are the preferred surgical sites, since rabbit is the smallest animal that can receive commercially available dental implants in long bones [23,24]. Other bones used for pull-out measurements of dental implants are the mandible and maxilla of minipigs [25] or the femur of rats [26]. Similarly to pull-out, the push-out test requires the use of cylinder-type implants, provided that the material passes entirely through the bone; if not, apical bone has to be removed, potentially altering the implant [23]. For both tests, pull-out and push-out tests, the high variability in terms of animal models, implant sizes, loading rates, healing times and outcome measurements makes difficult the comparison among the available studies [27].

Removal torque analysis works well with another implant design [16]. In fact, this technique measures the torsional force necessary for unscrewing screw-shaped implants [28]. Since removal torque primarily reflects the interfacial shear properties, the results are dependent not only on the quality of the interface, but also on the implant geometry [29].

The least used biomechanical tests to investigate implant osseointegration are represented by tensional tests [30,31], for which difficulties in translating the results of the experiments to any area-independent mechanical properties are reported [32].

Histological and histomorphometric analyses comprehend qualitative and quantitative methods that provide detailed microscopic information about the bone-implant interface. Among static parameters commonly measured, bone-to-implant contact (BIC) is probably the most frequently used one for the assessment of peri-implant bone healing and implant osseointegration [10]. Whereas, the evaluation of dynamic parameters, such

as mineral apposition rate (MAR), is less common, even though it allows for the characterization of bone remodeling kinetics around various implant surfaces [22].

The gold standards for measuring the amount of bone in direct contact with the implant surface are considered light microscopy and backscatter scanning electron microscopy (bSEM) [33].

Even though these techniques provide useful findings, they present several drawbacks. Firstly, they are both destructive techniques, which preclude the possibility to perform additional tests afterwards. Secondly, the preparation of the specimens containing Ti implants requires time, specific skills and equipment. Moreover, artefacts might be introduced during processing [34,35]. In addition, these are 2D imaging methods, and no 3D information about the bone-implant interface can be acquired [13]. As underlined by Geng et al. [34], a single histological section may not be representative of bone apposition over the whole implant and, in the meantime, it is hard to obtain serial sectioning of bony specimens containing metal implants.

Although the use of histomorphometric measurements is reported in studies on implant osseointegration in small animal models, such as mice [36-38] and rats [39,40], difficulties might be encountered during the preparation of bony specimens with metallic implants due to their size.

An alternative attractive approach to investigate bone-implant interface consists in the use of micro-CT, which enables the 3D evaluations of the bone surrounding the implants and does not preclude further assessments [19,33,41-43].

Several factors were reported to negatively influence the accuracy of BIC measurements with micro-CT, including the presence of metal-induced artefacts in close proximity to the metallic implant and the voxel size [44]. However, owing to the introduction of recent micro-CT scanners, characterized by voxels of smaller dimensions and by higher accelerating voltage, and thanks to the use of optimized scanning parameters, the metal-induced artefacts can be drastically reduced, thus allowing for the calculation of BIC via micro-CT [33].

Taking into account the above observations, an *in vivo* study in the proximal femur of rats was planned to determine whether the bone-implant contact of Ti implants was influenced by the presence of sphene coating. A total of 20 implants, 10 uncoated and 10 sphene-coated, were placed in the femur of 10 rats. Uncoated implants were randomly

positioned on one side, and sphene-coated implants on the contralateral side. To assess the implant osseointegration, micro-CT analysis was chosen as method to calculate BIC.

Primary aim of the present experimental study was to compare BIC values of uncoated Ti implants (control) with those of sphene-coated implants (test) at two different time points, at 14 and 28 days of healing.

Secondary aims comprise: a) the evaluation of BIC values of both uncoated and sphene-coated implants measured in two different bone compartments, cortical and cancellous bone; b) the comparative histological analysis of peri-implant bone healing using uncoated and sphene-coated implants; c) the evaluation of synovial fluid (SF) total white blood count in the knee joints at the time of the sacrifice to characterize the degree of inflammation.

3.1.2. Training and Preparation of the Relevant Documents for Ethics Committee Approval

Animal experimentation can be carried out in Italy only once the Ministry of Health has given its authorization (art. 31, paragraph 7, Legislative Decree No. 26/2014).

The research projects involving the use of animals, like in the present case, have to be firstly evaluated and approved locally. The research projects conducted at University of Padova have to be submitted to the Institutional Body for Animal Welfare (Organismo Preposto al Benessere degli Animali - O.P.B.A.) established as per Legislative Decree No. 26/2014 ("Implementing directive 2010/63/EU on the protection of animals used for scientific purposes").

The documents must be prepared in the Italian language, meeting the requirements of the O.P.B.A. The documentation to send comprises the following papers:

1. annex VI ("allegato VI") – Under the Italian Law Legislative Decree No. 26/2014, Annex VI is the key proof to obtain the authorization issued from Ministry of Health. Annex VI contains information related to the background of the study and a detailed description of experimental procedures. Moreover, in Annex VI, the investigator justifies the use of an *in vivo* animal model with respect to the 3Rs rules (Refinement, Reduction and Replacement) [45];
2. research project proposal;
3. non-technical summary of the research project;
4. annex E – self-declaration of their good repute by the Principal Investigator.

The main preparatory phases of the project are summarized in **Figure 1**.

Figure 1. Timeline of project phases and Brunello Giulia's training.

The project "Studio pilota sull'osteointegrazione di impianti rivestiti in sphene in un modello di femore di ratto" ("Pilot study of the osseointegration of sphene-coated implants in rat femur") was submitted to the O.P.B.A. in November 2017.

After a preliminary screening of the drafts, the O.P.B.A. can directly forward the project to the Italian Ministry of Health or can request amendments to the papers.

In the present case, the project was "accepted under condition" in January 2018 and the modified documents were sent back to the O.P.B.A. in March 2018. At this point, the project was transmitted to the Ministry of Health by the O.P.B.A. The Ministry finally expressed positive opinion on 20th June 2018 (Authorization **No. 441/2018-PR**) (see **Annex 1**).

Moreover, in order to conduct the *in vivo* experiments, the PhD candidate, Brunello Giulia, in compliance with current regulations, attended an approved training course for rodents and lagomorphs at University of Padova on 22nd June 2017. The following year, she also attended a training course at Queen Mary University of London, London (UK), and obtained the Personal Licence under the Animals (Scientific Procedures) Act 1986.

3.2. Experimental procedure

3.2.1. Samples Preparation and Coating Deposition

Customized cylindrical titanium implants, 1.45 mm in diameter and 3 mm in length, characterized by ZirTi® surface, sand-blasted with zirconium oxide and etched with mineral acids, were kindly provided by Sweden & Martina (Due Carrare, Padova, Italy).

The implant design was featured by a coronal extension, connected to the implant itself, for handling the implant during coating deposition and insertion (**Figure 2**).

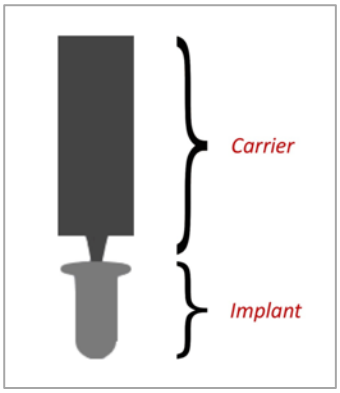

Figure 2. Schematic representation of the customized implant, characterized by a the implant itself (in light grey) and by a coronal portion (in dark grey) for carrying the implant and easily detachable after implant insertion.

Sphene coating on Ti implants was developed by the preceramic polymer processing route as extensively described in **Chapter 2**, using preceramic polymer SILRES®MK, isopropanol, nano–sized $CaCO_3$ (90 nm) and TiO_2 (25 nm) particles as raw materials.

As for sample preparation for the *in vitro* study, the suspension was homogenized by sonication (15 minutes) and subsequently positioned into an automatic airbrush (Prona-RA-C2). During the coating deposition, the solution was maintained homogenous by magnetic stirring.

Before coating process, the Ti implants were ultrasonically cleaned in acetone, alcohol, and deionized water for 10 minutes for each step, and then air-dried. The implants were secured to a rotatable substrate holder, composed of a clamping system and a DC 3V micromotor (CX.KR280-2865, Commex, Pianiga, Italy). The implants were rotated at high speed (10000 rpm) and the coating was applied on the implant surface. Optimized parameters in terms of distance, pressure and deposition time were adopted after preliminary optimization tests. The pressure was set at 3 bars and the airbrush nozzle, 1 mm in diameter, was maintained at a specific distance from the implant (35 cm). A coating time of 1 s was selected. A schematic overview of the coating systems is reported in **Figure 3**.

After spray coating deposition, the coated implants were left to dry and afterwards heat-treated in static air at 950 °C for 1 hour, with a heating rate of 5 °C/min.

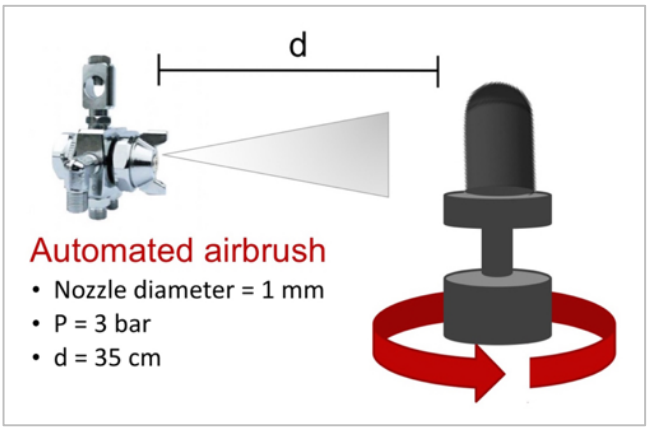

Figure 3. Schematic representation of the coating system, composed of an automated airbrush and a rotatable implant holder.

Both uncoated and sphene-coated ZirTi implants were tested *in vivo* to investigate the influence of surface modification on implant osseointegration. Henceforth, the two implants will be identified as *uncoated* and *sphene-coated* implants (**Figure 4**). Before *in vivo* experiments, all the implants were sterilized by autoclavation for 20 minutes at 121°C.

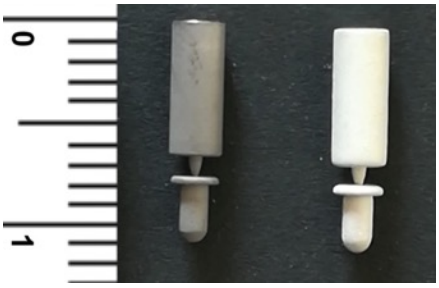

Figure 4. Customized uncoated (left) and sphene-coated (right) implants.

3.2.2. Surface and Coating Characterization

The surface topography of both uncoated and sphene-coated implants was investigated using an optical 3D profilometer (Sensofar S Neox) in confocal mode. A 20 × objective (NA 0.45, field of view 877 × 660 µm) was used, with maximum spatial resolution of 0.65 µm and optical resolution of 0.31 µm. Each implant was individually positioned with the cylinder axis in parallel to the sample table.

An area covering half of the implant was scanned. Squared areas of 1 mm x 1 mm, extracted from the scanned surface, were examined. To describe the surface topography the following areal parameters, Sa and Sz, were calculated. In order to eliminate form contributions, the area was corrected with a polynomial of second order and, afterwards, the data were filtered by applying a Gaussian filter with a sampling length equal to 0.8 mm, in accordance with ISO 25178 [46]. Data evaluation was performed with MountainsMap® (Digital Surf, Besançon, France).

Coating thickness and porosity were analyzed using a metrological X-ray CT system MCT 225 (Nikon Metrology, UK), with a specified maximum permissible error (MPE) for length measurements equal to (9 + L/50) μm (where L is the length in mm). The parameters used for CT scanning are listed in **Table 1**.

Table 1. CT scanning parameters.

Parameter	Value
Voltage	110 kV
Current	62 μA
Exposure time	1415 ms
Projections	3142
Voxel size	3 μm
Temperature	20 °C

3D image reconstruction was performed with CT Pro 3D software (Nikon Metrology, UK). For elaboration of CT volumetric voxel data, the software VGStudio MAX 3.2 (Volume Graphics GmbH, Germany) was used.

After the import of the reconstructed volume, the surface of the full part including the coating was determined, selecting one region of interest (ROI), containing air only, and a second one containing only grey values corresponding to the coating, being less dense than the Ti implant. From the obtained surface, a new ROI was created containing the full implant (ROI_{I+C}). Subsequently, a second segmentation was performed, selecting one ROI containing only values corresponding to the coating (serving as background) and a second one containing only values corresponding to the implant. Once again, ROI_I was

created, corresponding to the Ti implant only. Then, ROI_I was subtracted from ROI_{I+C} to obtain the ROI of the coating (ROI_C).

For calculation, the portion of the implant corresponding to the part which would be inserted into the bone was selected, cropping ROI_C 150 μm apically from the head of the implant. Within this volume, mean coating thickness and porosity were calculated.

3.2.3. Surgical Procedure

Ten healthy 25-week old male Sprague–Dawley rats, weighing approximately 300–350 g, were used in this study. All the animals acclimated for one week prior to surgery under climate-controlled conditions and fed with standard laboratory diet and water *ad libitum* at the Experimental Surgery Center of University of Padova.

The surgical procedure was performed under general anesthesia using sevoflurane 3% and 1.5-2%, for induction and maintenance, respectively. Tramadol (5 mg/kg) was given for perioperative pain control.

Following anesthesia, the animals were positioned in supine position, the surgical fields were shaved and the skin was disinfected with 10% povidone-iodine.

Each rat underwent bilateral implantation of sphene-coated implant on one femur and of uncoated implant (control) on the contralateral one. The implant side was randomly assigned.

On each side, the proximal aspect of the femur was exposed via lateral skin incision, followed by blunt dissection of the muscles. The implant sites were prepared under constant irrigation with sterile saline using a tungsten carbide round bur for low-speed handpiece (**Figure 5a**). The holes were slightly underprepared in order to achieve primary stability. The implants were placed into the proximal epiphysis of bilateral femurs of each rat by press-fitting (**Figure 5b**). At this point the carriers were gently detached from the implant and removed (**Figure 5c**).

A primary-intention closure was obtained with double-layer suture technique. The muscles were carefully sutured with 4-0 Vicryl (Ethicon, Inc., Somerville, NJ) and the skin was closed with 3-0 Vicryl. Postoperative analgesia was achieved with administration of Tramadol (5 mg/kg) twice daily for 5 days. Cefazolin (1 mg/kg) was administered intra-muscularly for 5 days to avoid wound infections.

Five animals were randomly sacrificed after 14 and 28 days of healing, by an overdose of anesthesia. After the sacrifice, synovial fluid was immediately collected from rat knee

joints. Finally, femurs were dissected out and fixed in 4% phosphate-buffered formalin, pH 7, for micro-CT examinations and, subsequently, for histological analysis.

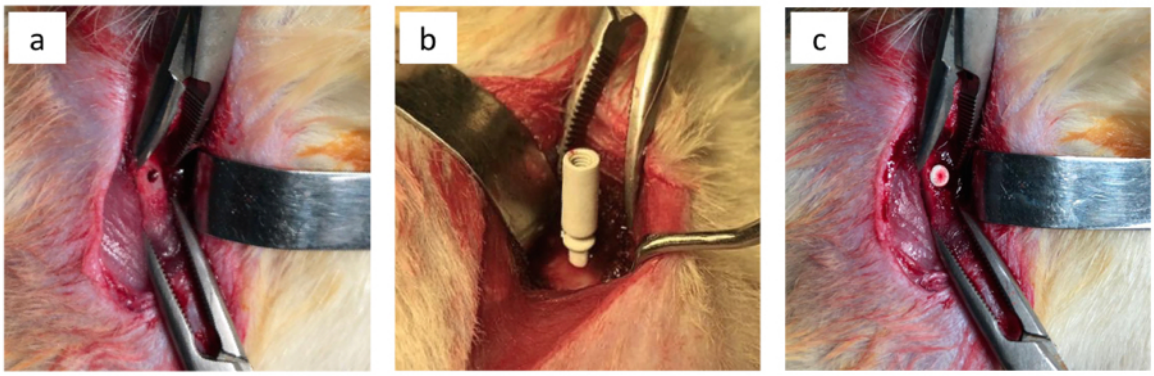

Figure 5. Surgical procedure: a) implant site preparation; b) implant positioning; c) removal of the carrier after implant placement.

3.2.4. Synovial Fluid Analysis

SF was aspirated from both the knee joints of each rat. If present, the volume of the aspirate was recorded and the sample was analysed for total white blood cell (WBC) counts (WBC/mm^3) to assess the degree of inflammation of the joints. For WBC/mm^3 < 2.000, the SF was considered a non-inflammatory fluid without any stratification within that range. Whereas, for values above this threshold, it was designated as an inflammatory fluid and the increased levels of WBC/mm^3 were associated with a higher degree of inflammation [47,48].

3.2.5. Micro-CT Analysis

For micro-CT analysis, metrological X-ray CT system MCT 225 (Nikon Metrology) was used, previously described in **section 3.2.2**. Since the samples were conserved in 10% formalin solution, they were carefully retrieved from the container and fixed using a low-density rigid foam support, which was then positioned onto the rotary table. The samples were positioned with respect to the X-ray beam in order to minimize the presence of image artefacts. Before each scan, the samples were left inside the temperature-controlled CT cabinet for 1 h at 20°C, for thermal and mechanical stabilization.

The optimized CT-scanning parameters used for CT acquisition are summarized in **Table 2**.

Table 2. CT scanning parameters.

Parameter	Value
Voltage	170 kV
Current	40 µA
Exposure time	1415 ms
Projections	2000
Voxel size	6.5 µm
Temperature	20 °C

3D image reconstruction was performed as above (see **Section 3.2.2**). A similar procedure was carried out for both uncoated and sphene-coated implants. The workflow is summarized in **Figure 6**.

For uncoated samples, after the import of the reconstructed volume, the surface of the Ti implant was determined, selecting one ROI, containing bone, and a second one containing only grey values corresponding to the Ti implant. From the obtained surface, a new ROI was created containing the Ti implant (ROI_I) (**Figure 7**). Subsequently, a second surface determination was performed, selecting one ROI containing only values corresponding to the air (serving as background) and a second one containing only values corresponding to the bone. Thus, ROI_{B+I} was created. Then, ROI_I was subtracted from ROI_{B+I} to obtain the ROI of the bone (ROI_B) (**Figure 8**).

ROI_I was expanded by 1 voxel (ROI_{I+1}). Afterwards, the intersection of ROI_{I+1} and ROI_B resulted in the creation of a new ROI (ROI_{INT}).

Outcome variable was a 3D bone to implant-contact value (BIC%), obtained analyzing the intersection between ROI_{I+1} and ROI_B.

Most of the times the implants were partially left outside the bone during surgery due to the configuration of the implant sites. Therefore, the measurements were done within ROI_{INT}, starting from where the cortical bone began, up to and including the apex of the implants and the surrounding bone tissue. When the head of the implant (the flat horizontal portion) was in contact with the cortical bone, the measurements were done cropping the ROI_{INT} 150 µm apically to the head of the implant, in order to avoid metal-induced artefacts (**Figure 9**).

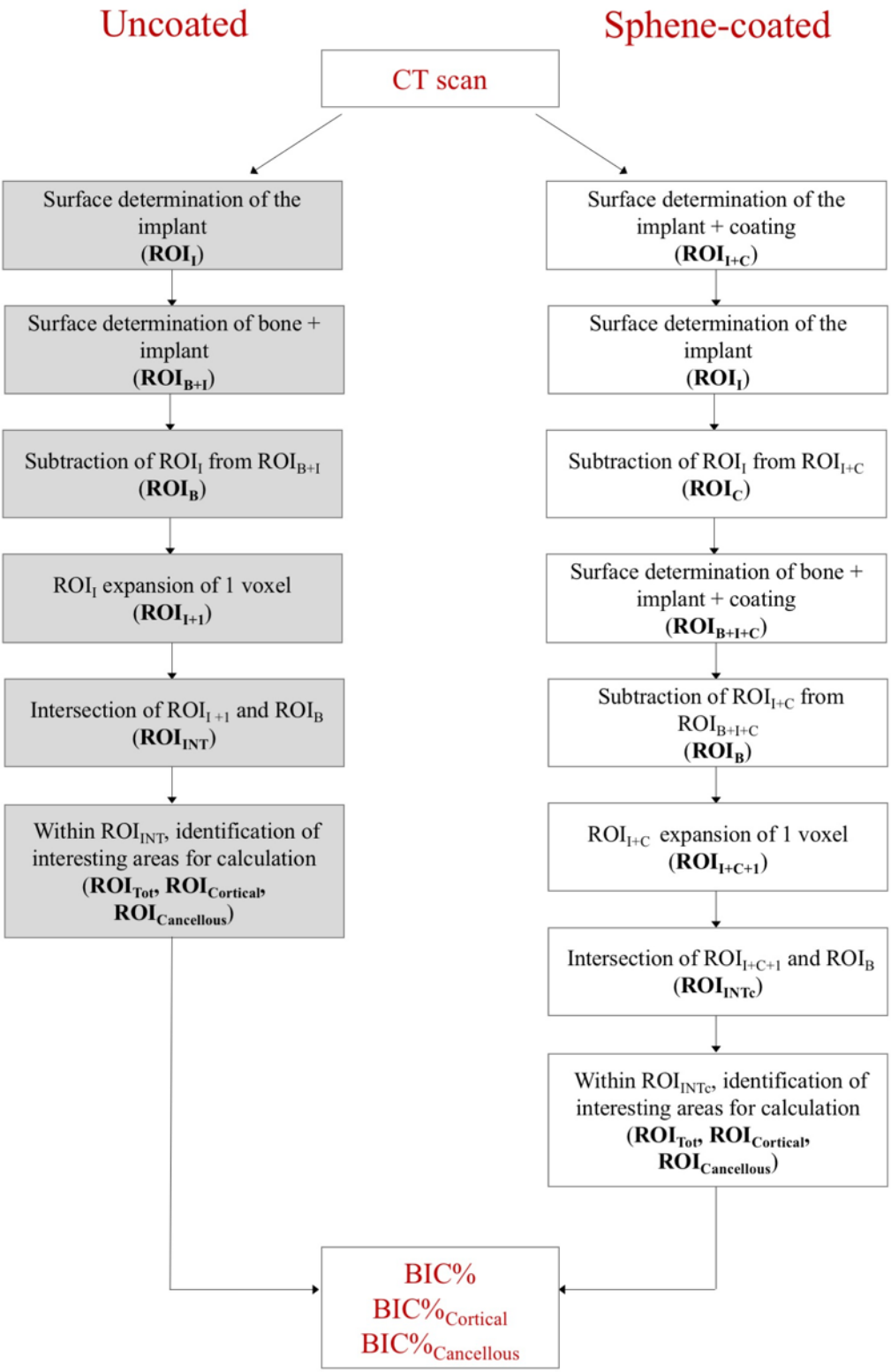

Figure 6. Workflow of micro-CT analysis.

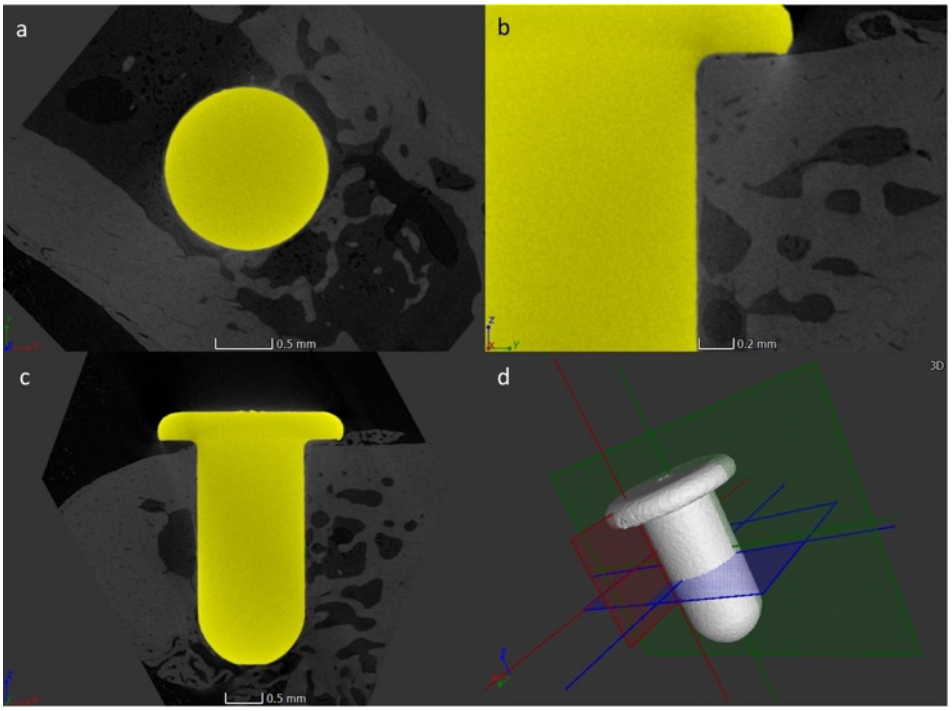

Figure 7. Representative micro-CT images of uncoated Ti implant inserted in the rat femur after 28 days of healing with indicated the selection of the ROI$_I$ (in yellow): (a) transverse cross-sectional view; (b) detail of the coronal part of the implant; (c) cross-sectional view parallel to the long axis of the implant; (d) 3D reconstruction.

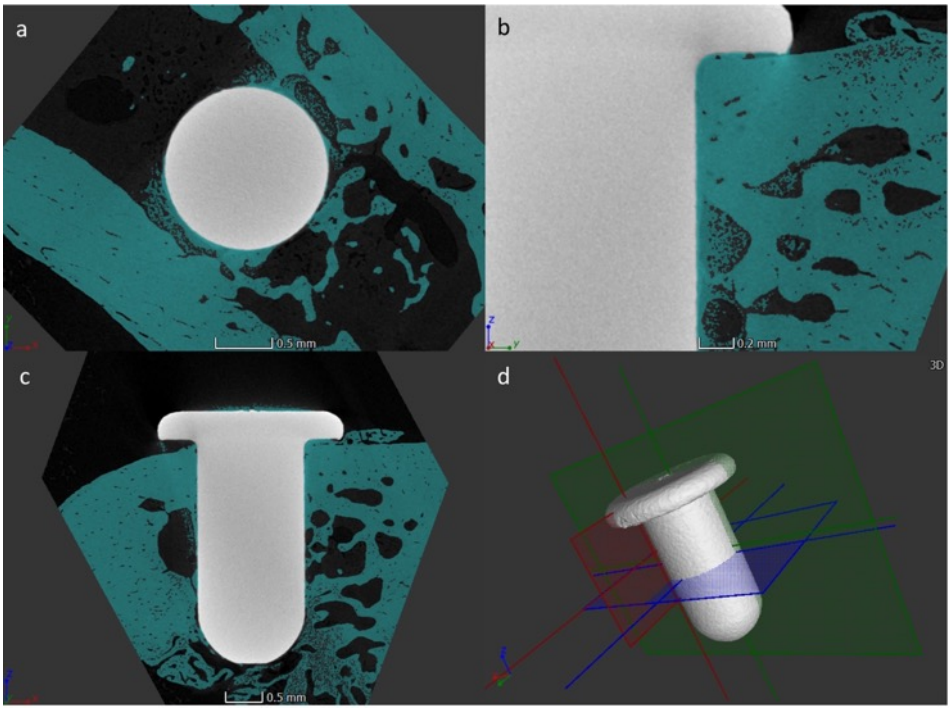

Figure 8. Representative micro-CT images of uncoated Ti implant inserted in the rat femur after 28 days of healing with indicated the selection of the ROI$_B$ (in light blue): (a) transverse cross-sectional view; (b) detail of the coronal part of the implant; (c) cross-sectional view parallel to the long axis of the implant; (d) 3D reconstruction.

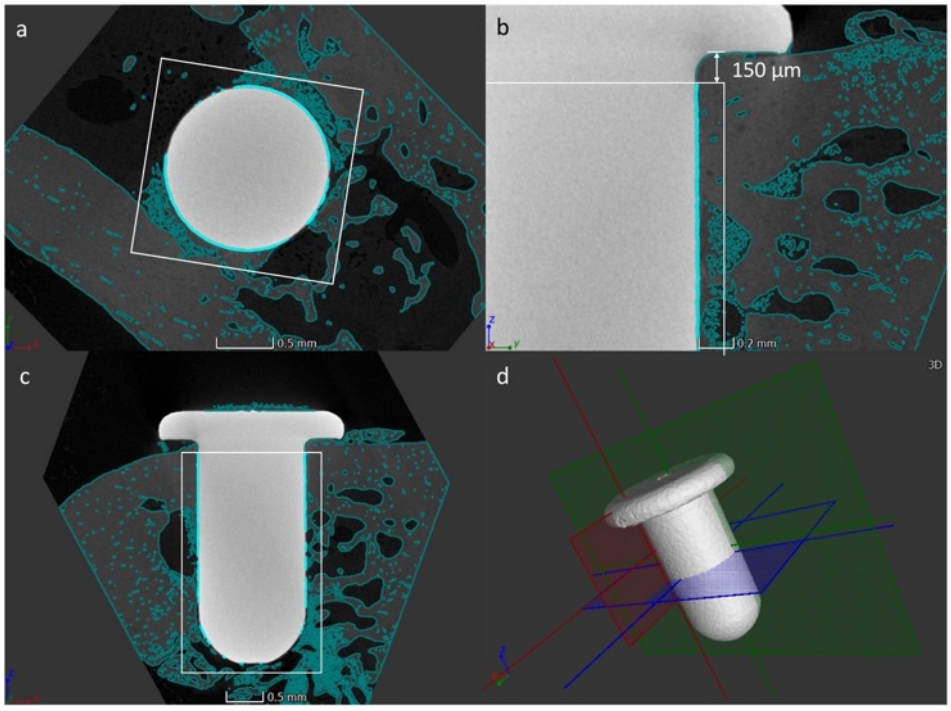

Figure 9. Representative micro-CT images of uncoated Ti implant inserted in the rat femur after 28 days of healing. Indicated in fluorescent blue, the intersection of ROI_{I+I} with the ROI_B (ROI_{INT}) is shown, illustrating the contact of the bone with the implant. The portion of the implant considered for measurements is identified by the white square. (a) Transverse cross-sectional view; (b) detail of the coronal part of the implant; (c) cross-sectional view parallel to the long axis of the implant; (d) 3D visualization.

An example of the steps of the process used for coated samples is provided in **Figures 10-12**. In case of sphene-coated implants, the surface of the Ti implant including the coating was determined, selecting a ROI, containing bone, and a second one containing only grey values corresponding to the coating, being less dense than the Ti implant. From the obtained surface, a new ROI was created containing the full implant (ROI_{I+C}) (**Figure 10**). Subsequently, a second surface determination was performed, selecting one ROI containing only values corresponding to the coating (serving as background) and a second one containing only values corresponding to the Ti implant. So, ROI_I was created, corresponding to the Ti implant only. Then, ROI_I was subtracted from ROI_{I+C} to obtain the ROI of the coating (ROI_C). Another surface determination was performed, selecting one ROI containing only values corresponding to the air (serving as background) and a second one containing only values corresponding to the bone. From the obtained surface, ROI_{B+I+C} was created. ROI_{I+C} was subtracted from ROI_{B+I+C} to obtain the ROI of the bone (ROI_B) (**Figure 11**).

In case of sphene-coated implants, as the coating represented the outer layer of the full implant, instead of ROI_{I+1}, ROI_{I+C+1}, obtained from the expansion of ROI_{I+C} by1 voxel, was used. At this point, ROI_{I+C+1} and ROI_B were intersected, thus creating a new ROI (ROI_{INTc}) (**Figure 12**).

Similarly to the uncoated samples, for calculation of BIC % as well as for mean thickness of the coating, only the portion inserted into the bone and cropped at least 150 µm apically from the head of the implant was selected within ROI_{INTc}.

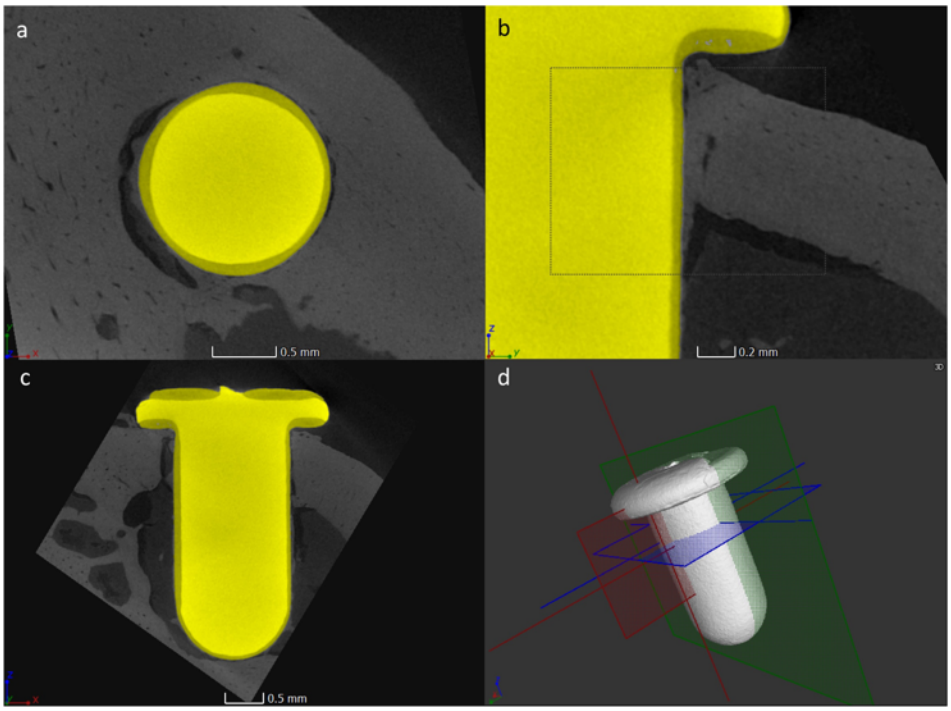

Figure 10. Representative micro-CT images of sphene-coated Ti implant inserted in the rat femur after 28 days of healing with indicated the selection of the ROI_{I+C} (in yellow): (a) transverse cross-sectional view; (b) detail of the coronal part of the implant; (c) cross-sectional view parallel to the long axis of the implant; (d) 3D reconstruction.

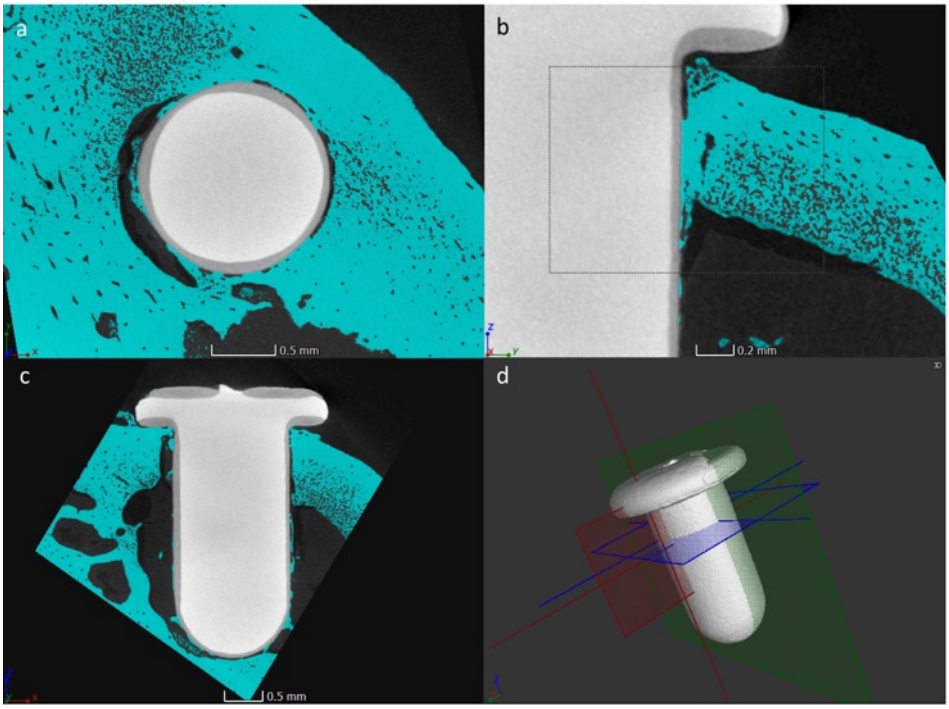

Figure 11. Representative micro-CT images of sphene-coated Ti implant inserted in the rat femur after 28 days of healing with indicated the selection of the ROI_B (in light blue): (a) transverse cross-sectional view; (b) detail of the coronal part of the implant; (c) cross-sectional view parallel to the long axis of the implant; (d) 3D reconstruction.

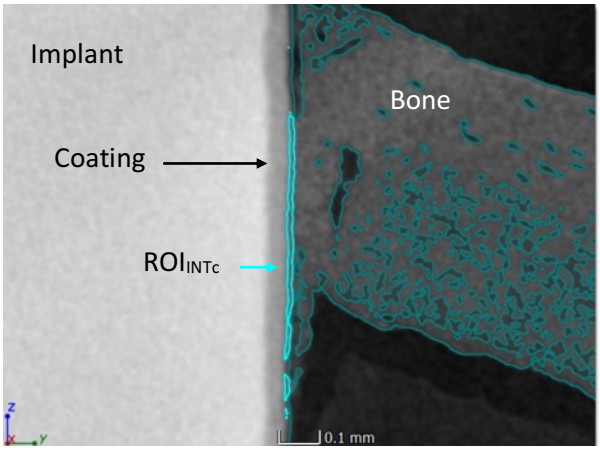

Figure 12. Cross-sectional view with indication of the Ti implant, the coating, the bone and the ROI_{INTc} (detail of the area identified with dotted-line bounding boxes in Figures 10b and 11b).

Moreover, the epiphyses of long bones are characterized by an inner porous part, the cancellous bone, and by a highly-dense outer layer, known as cortical bone. In order to investigate the effect of the coating on implant osseointegration, not only at two different time points, but also in the two different bone compartments, within ROI_{INT} and ROI_{INTc}, sub-ROIs perpendicular to the long axis of the implant, 0.3 mm in height, were randomly drawn one for each bone compartment (**Figures 13-14**). The BIC% obtained in these zones will be referred hereafter as $BIC\%_{Cortical}$ and $BIC\%_{Cancellous}$.

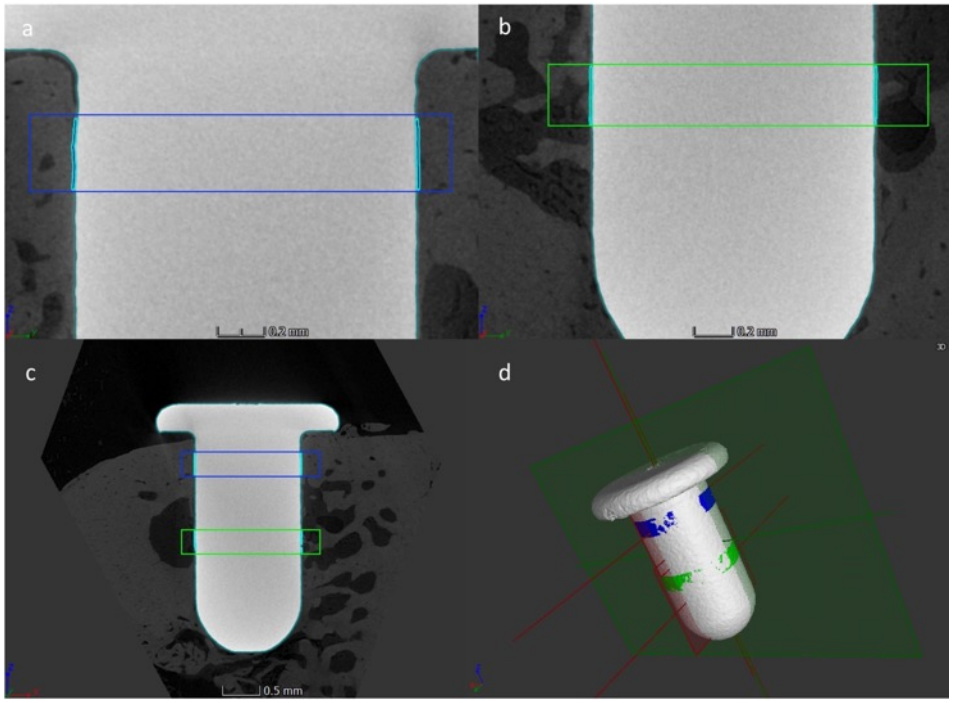

Figure 13. Representative micro-CT images of an uncoated Ti implant inserted in the rat femur after 28 days of healing with indications in blue and green for the ROIs for calculation of $BIC\%_{Cortical}$ and $BIC\%_{Cancellous}$, respectively. In light blue the intersection volume between the ROI_{I+1} and ROI_B in the portions considered for calculation. (a) Detail of the cortical part; (b) detail of cancellous part; (c) cross-sectional view parallel to the long axis of the implant; (d) 3D reconstruction.

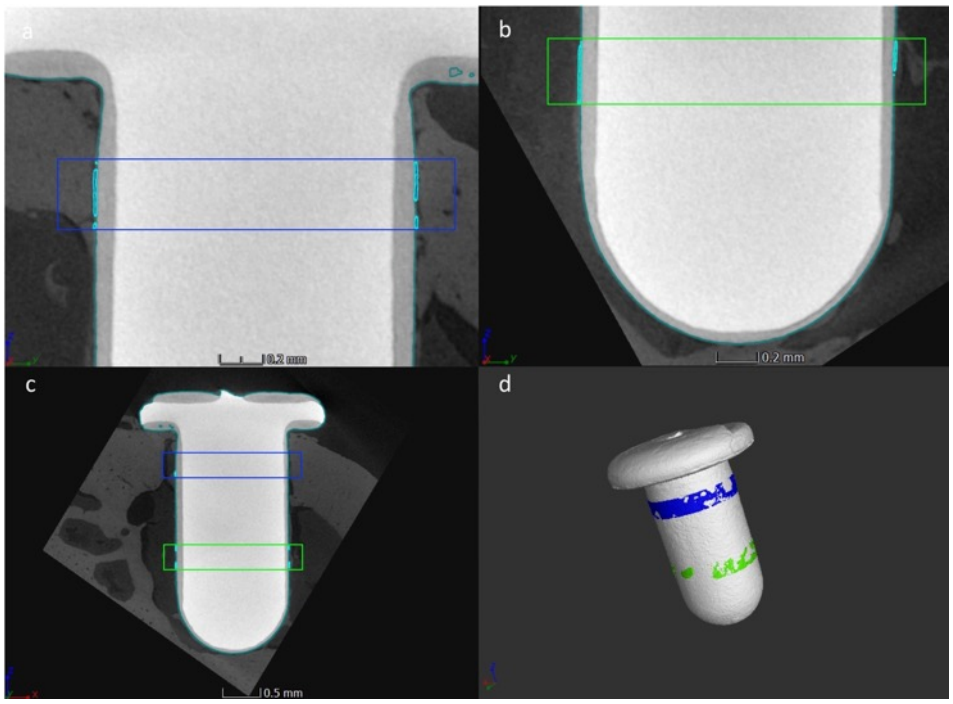

Figure 14. Representative micro-CT images of sphene-coated Ti implant inserted in the rat femur after 28 days of healing with indications in blue and green for the ROIs for calculation of $BIC\%_{Cortical}$ and $BIC\%_{Cancellous}$, respectively. In light blue the intersection volume between the ROI_{I+C+1} and ROI_B sin the portions considered for calculation. (a) Detail of the cortical part; (b) detail of cancellous part; (c) cross-sectional view parallel to the long axis of the implant; (d) 3D reconstruction.

3.2.6. Histological Processing

After micro-CT analysis, the implants were carefully retrieved from the bone and the femurs were fixed in 4% phosphate-buffered formalin, pH 7, for 10 days, then transferred to a solution of 70% ethanol until processing. The samples were dehydrated with increasing concentrations of alcohol, up to 100%. The specimens were then sectioned along the longitudinal axis of the implant using a diamond disc at about 150 mm thick cross section and prepared by grinding to approximately 50-60 μm thickness. Sections were finally stained with hematoxylin and eosin (H&E) and Masson's trichrome staining for histomorphometric analysis by means of optic microscopy.

3.2.7. Histological Assessment

Histomorphometric analysis was carried out on 3 sections per sample chosen randomly and observed under Leitz Orthoplan light microscope (LM, Leica Microsystem Inc., Bannockburn, IL, USA) equipped with a computerized image analyzer system (Qwin, Leica Microsystem Imaging Solution Ltd, Cambridge, UK). From each section 5 images were taken. The standard region of interest (ROI) was determined in a region of 1218 × 898 μm (1.09×10^6 μm^2). Within the ROI, bone growth and maturation were examined using the Leica Qwin software. The area was analyzed for the presence or absence of polymorphonuclear cells, phagocytic cells, fibroblasts, endothelial cells, collagen fibers and new bone in order to evaluate bone healing in control and tests groups at both time points. Each parameter was scored from 0 (absence) to 3 (abundantly present).

3.2.8. Statistical Analyses

Continuous data were expressed as mean and standard deviation (SD), and categorical data as frequency and percentage. Continuous data were compared between the two study arms using a paired Student t test, while categorical data using McNemar test. BIC data were compared between 14 and 28 days using Student t test. A p-value less than 0.05 was considered statistically significant. Data analysis was performed using R 3.5 (R Foundation for Statistical Computing, Vienna, Austria).

3.3. Results

3.3.1. Surface and Coating Analysis

Surface roughness was investigated by means of confocal microscopy. Results are reported in **Table 3**.

Table 3. Surface roughness of uncoated and sphene-coated implants.

Implant	Sa (µm)	Sz (µm)
Uncoated	2.55	50.74
Sphene-coated	3.38	59.06

An increase in surface roughness was found after coating deposition. As shown in **Figure 15**, the surface of the sphene coating was characterized by the presence of numerous peaks distributed on the whole surface, which were absent on the uncoated Zirti surface. Yellow and red peaks in **Figure 15b** well correspond to the edges of the white agglomerates detected by SEM observations (see **Chapter 2, Figure 3b**) and with previous investigations using a stylus profilometer (see **Chapter 2, Figure 5b**).

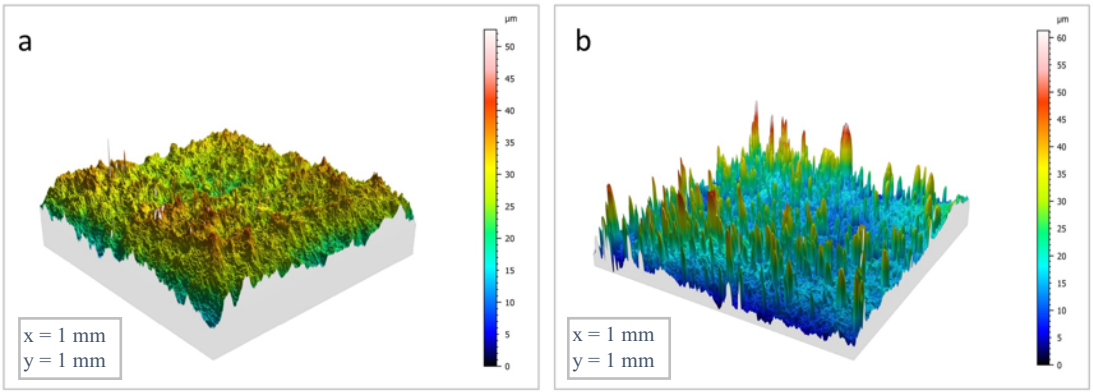

Figure 15. 3D maps of: a) uncoated implant; b) sphene-coated implant.

The mean thickness of the coating was 61 ± 13.4 µm (**Figure 16**).

No porosity inside the coating was found, however the presence of porosity or defects smaller than the resolution of 3 µm cannot be excluded.

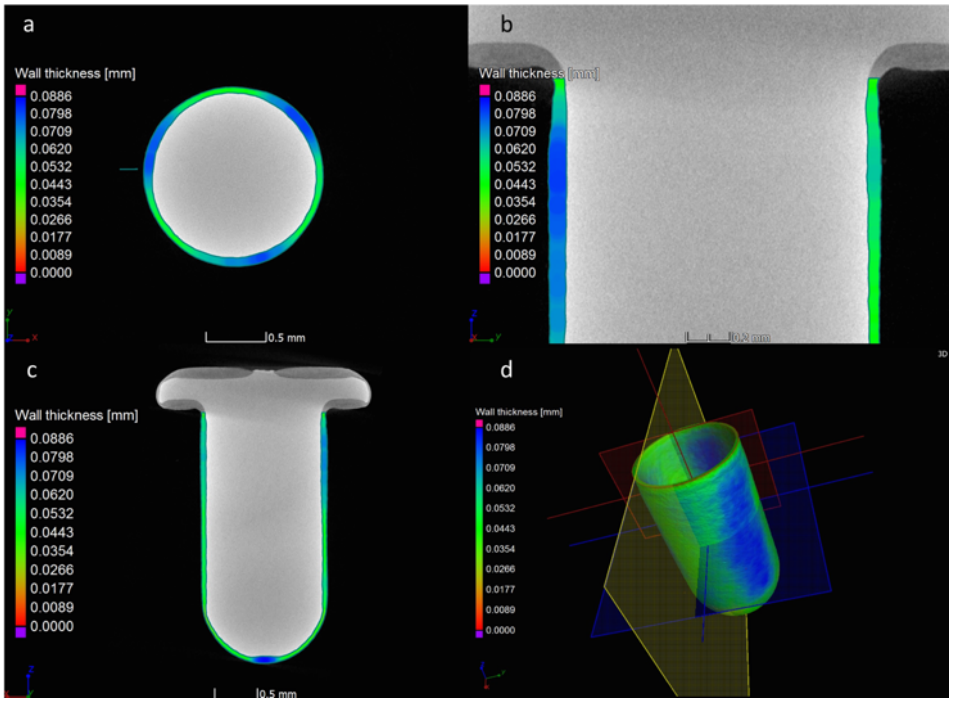

Figure 16. Micro-CT images of a sphene-coated implant with coating thickness color map: (a) transverse cross-sectional view; (b) details cross-sectional view parallel to the long axis of the implant; (c) cross-sectional view parallel to the long axis of the implant; (d) 3D reconstruction.

3.3.2. Clinical Observations In Vivo Experiments

The surgical procedures were performed without any complication. The healing period was uneventful and all the animals survived during the experimental period. At femur retrieval, at 14 and 28 days after implant placement, no macroscopic signs of inflammation or adverse reactions were detected in the surrounding tissues. No implant dislocation had occurred, and all the 20 implants were still in place at the moment of the sacrifice.

3.3.3. Synovial Fluid Analysis

Overall, SF was found in knee joints on the control side (6/10, 60%), but not on the test side (0/10, 0%), where sphene-coated implants had been positioned (p=0.04). The presence of SF on the control side was observed in samples at both 14 days (4/5 [80%] in uncoated vs. 0/5 [0%] in sphene-coated, p=0.13) and at 28 days (2/5 [40%] in uncoated vs. 0/5 [0%] in sphene-coated, p=0.48). Data are summarized in **Figure 17**.

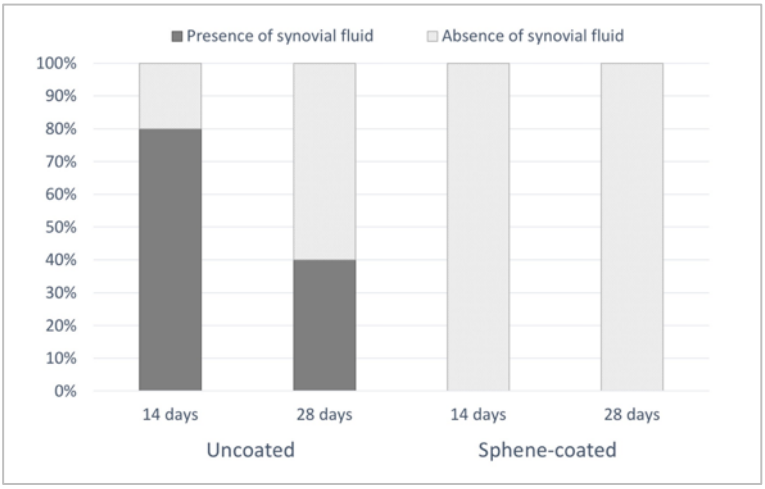

Figure 17. Presence of synovial fluid in the knee joints of operated rats at 14 and 28 days postoperatively.

When present, the volume of synovial fluid aspirate varied between 5 and 200 µL. It has to be noted that in 5 cases out of 6 the total white blood cell count was equal to 100 WBC/mm^3, which was within the non-inflammatory range. Whereas only one control sample, retrieved after 28 days of healing, presented with a clinically relevant amount of white blood cells (7000 WBC/mm^3), albeit in absence of symptoms.

3.3.4. Micro-CT Analysis

Summary of BIC%, BIC%$_{Cortical}$ and BIC%$_{Cancellous}$ values in the uncoated and sphene-coated arms is reported in **Table 4**.

Table 4. BIC%, BIC%$_{Cortical}$ and BIC%$_{Cancellous}$ values in the uncoated and sphene-coated arms.

Arm	Sacrifice [days]	Samples	BIC%	BIC%$_{Cortical}$	BIC%$_{Cancellous}$
Uncoated	14	5	48.1 ± 19.6	44.6 ± 18.6	42.2 ± 18.4
Uncoated	28	5	57.7 ± 15.4	62.2 ± 9.4	56.2 ± 14.1
Sphene-coated	14	5	50.5 ± 17.4	55.5 ± 16.1	41.5 ± 18.2
Sphene-coated	28	5	60.4 ± 17.7	53.9 ± 17.7	56.3 ± 14.8

* Data are expressed as: mean ± standard deviation

Regarding BIC% (see **Figure 18**), the values were slightly higher in sphene-coated samples at both time points. The highest BIC% value was observed in sphene-coated samples after 28 days of healing (60.4±17.7). Compared to the 14-day time point, there was a non-significant trend toward an increase in BIC% overtime within each group (p=0.41 for uncoated; p =0.40 for sphene-coated).

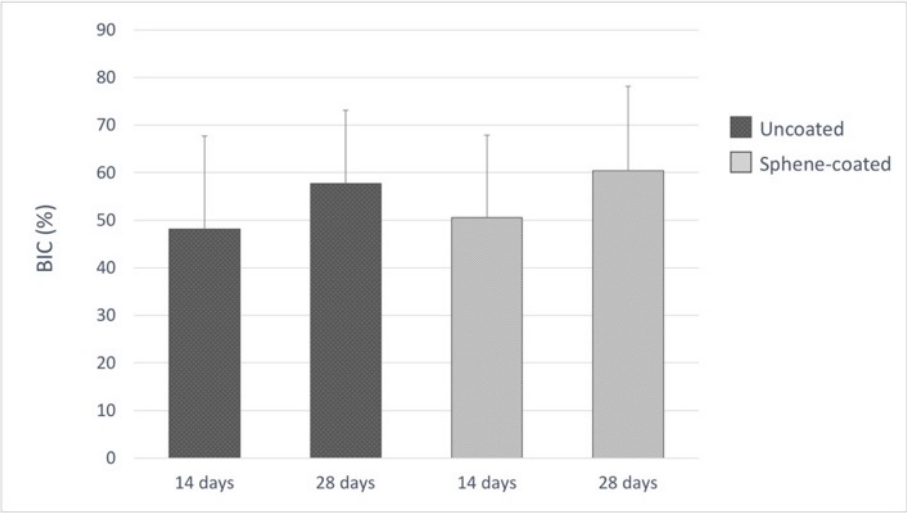

Figure 18. Effect of surface modification on BIC% values: after 14 days of healing (uncoated at 14 days vs sphene-coated at 14 days, p=0.84) and after 28 days of healing (uncoated at 28 days vs sphene-coated at 28 days, p=0.80).

The influence of implant surface modification on bone healing in the cortical portion of the bone was also investigated. The highest mean $BIC\%_{Cortical}$ was registered in the uncoated group after 28 days from implant placement (**Figure 19**). Even though an increase in $BIC\%_{Cortical}$ could be observed overtime in uncoated-samples, no statistically significant temporal differences were found within each group (p=0.11 for uncoated; p =0.87 for sphene-coated).

With regards to $BIC\%_{Cancellous}$ (see **Figure 20**), similar values were obtained in both the study arms at 14- and 28-day healing periods ($p > 0.05$). As for BIC%, a non-significant trend toward an increase in $BIC\%_{Cancellous}$ overtime within each group was identified (p=0.21 for uncoated; p =0.20 for sphene-coated).

In general, analyzing the healing pattern of peri-implant bone in two different bone compartments, cortical and cancellous, it is to be noted that, apart from sphene-coated samples at 28 days after implant insertion, better bone-implant contact values were found in the cortical compartment.

For all the three parameters (i.e. BIC%, BIC%$_{Cortical}$ and BIC%$_{Cancellous}$), no statistically significant difference was found between the two study arms.

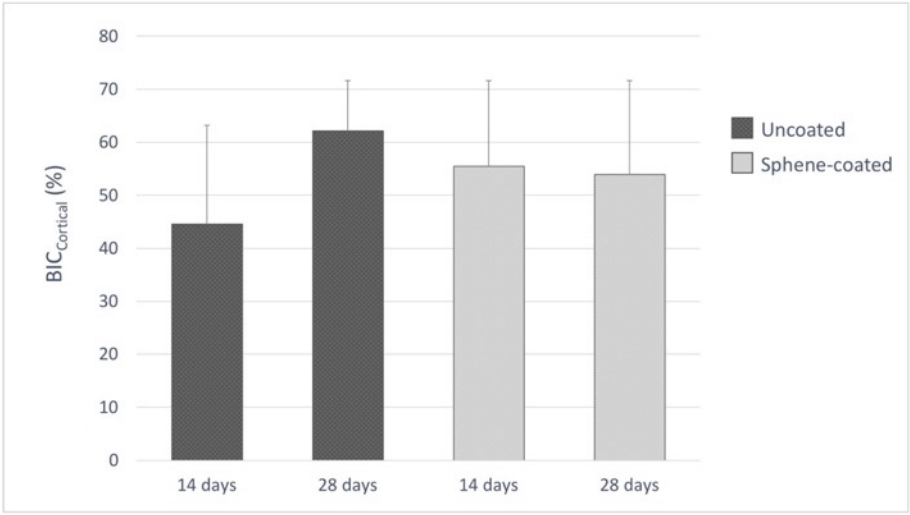

Figure 19. Effect of surface modification on BIC%$_{Cortical}$ values: after 14 days of healing (uncoated at 14 days vs sphene-coated at 14 days, p=0.35) and after 28 days of healing (uncoated at 28 days vs sphene-coated at 28 days, p=0.39).

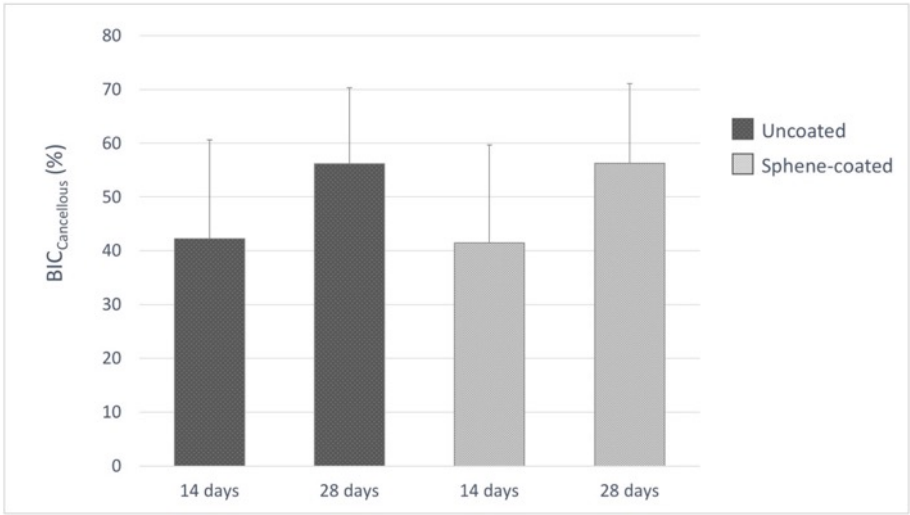

Figure20. Effect of surface modification on BIC%$_{Cancellous}$ values: after 14 days of healing (uncoated at 14 days vs sphene-coated at 14 days, p=0.95) and after 28 days of healing (uncoated at 28 days vs sphene-coated at 28 days, p=0.99).

Coating delamination was observed in three samples, of which two at 28 days postoperatively and one after 14 days from surgery. In all these samples the delamination occurred in the transition zone between the cylindrical portion of the implant and the

apical hemispherical one. Among these cases, in one case, along with the delamination of the coating, its disintegration determined the formation of particulate debris, which were detected in the cortical bone, close to an intact portion of the coating (**Figure 21**). This finding suggests that the cracking of the coating occured during implant insertion.

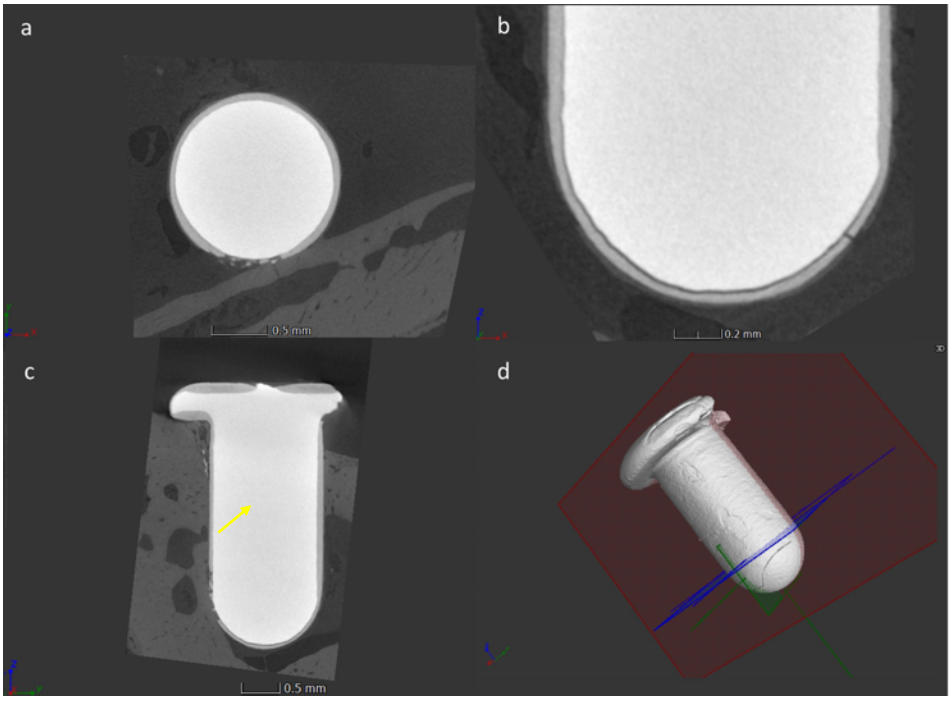

Figure 21. Micro-CT images of sphene-coated implant presenting partial delamination and disintegration of the bioceramic coating: (a) transverse cross-sectional view; (b) detail of the apical part of the implant; (c) cross-sectional view parallel to the long axis of the implant, debris are indicated by the yellow arrow; (d) 3D reconstruction.

Finally, regarding the mean thickness of the coatings in the part of the implants inserted into the bone, similar results were obtained at 14 and 28 days of healing, with values of 63.4 ± 2.7 µm and 67 ± 2.7 µm, respectively. Representative micro-CT images with color map indicating the thickness of the coating are provided in **Figure 22**.

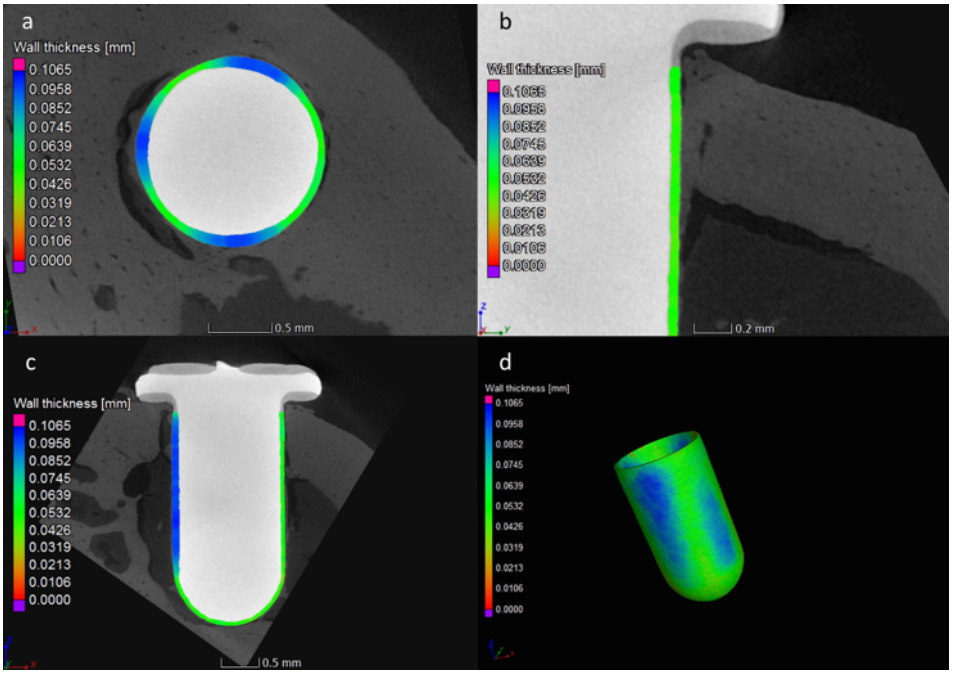

Figure 22. An example of micro-CT images of a sphene-coated implant positioned into the bone with coating thickness color map: (a) transverse cross-sectional view; (b) detail of the apical part of the implant; (c) cross-sectional view parallel to the long axis of the implant, debris are indicated by the yellow arrow; (d) 3D reconstruction

3.3.5. Histological and Histomorphometrical Analyses

Histological analysis was performed in order to observe the microstructure of peri-implant tissues. Examination of histological sections confirmed a similar healing pattern for uncoated and sphene-coated implants. The representative images 14 and 28 weeks postoperatively are presented in **Figure 23** and **Figure 24**, respectively.

After 14-day healing period, in both groups the presence of inflammatory cells and fibroblasts, as well as new vessels, could be observed. In this early phase of healing, new bone formation could not be detected. Controversy, 28 days after surgery, in both test and control conditions, peri-implant tissues were characterized by the presence of vessels embedded in extracellular matrix (ECM) and of osteogenic cells producing new bone matrix. At this stage, no sign of inflammatory process could be observed.

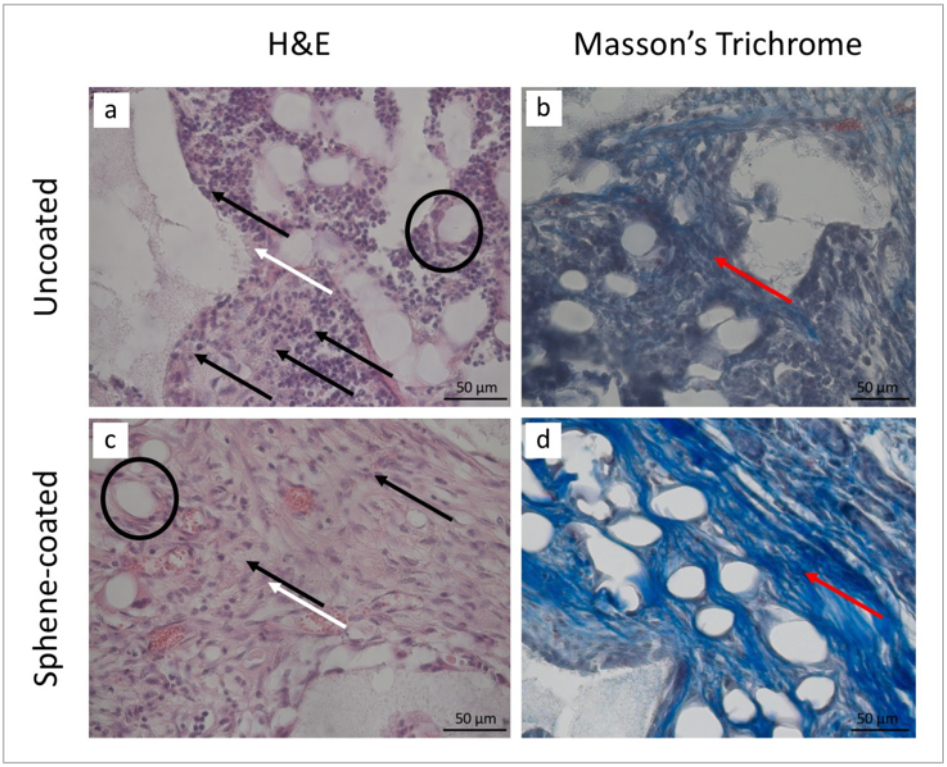

Figura 23. Staining with H&E (a,c) and Masson's trichrome (b,d) of peri-implant tissues around uncoated (a,b) and sphene-coated implants after 14 days of healing. In both experimental conditions, inflammatory cells (black arrows) and fibroblasts (white arrows) were detected. A new ECM rich in collagen fibers (red arrows) was observed, as well as the presence of several vessels (black circles).

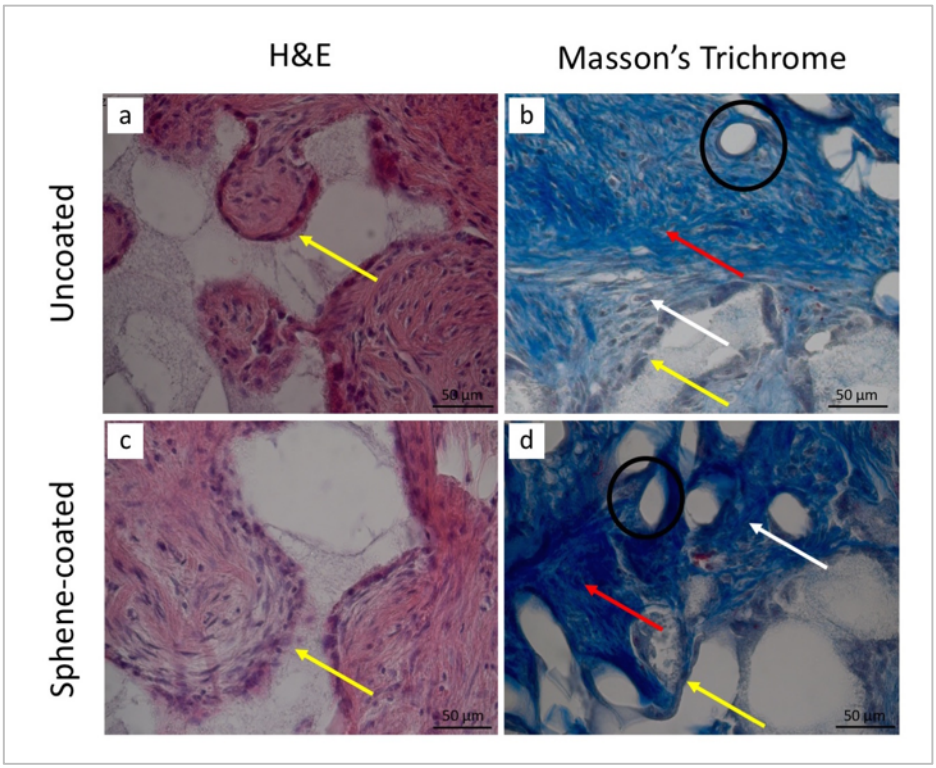

Figure 24. Staining with H&E (a,c) and Masson's trichrome (b,d) of peri-implant tissues around uncoated (a,b) and sphene-coated implants after 28 days of healing. In both experimental conditions, fibroblasts (white arrows), collagen fibers (red arrows), as well as vessels (black circles) could be observed. Moreover, osteogenic cells (white arrows) were detected.

Histomorphometric analysis of peri-implant tissues was performed and reported on **Table 5**. Similar findings were obtained in both test and control samples. Polymorphonuclear cells and phagocytic cells were abundant after 14 days and absent after 28 days from implantation. An increase in the number of fibroblasts and collagen fibers overtime could be observed, while endothelial cells were moderately present at both time points. Finally, new bone formation was detected only 28 days postoperatively.

Table 5. Results of histomorphometric measurements after 14 and 28 days from placement for uncoated and sphene-coated implants.

	Uncoated		**Sphene-coated**	
	14 days	**28 days**	**14 days**	**28 days**
Polymorphonuclear cells	3	0	3	0
Phagocytic cells	3	0	3	0
Fibroblasts	1	2	1	2
Endothelial cells	2	2	2	2
Collagen fibers	2	3	2	3
New bone	0	2	0	2

0 = absence; 1 = scarcely present; 2 = moderately present; 3 = abundantly present.

3.4. Discussion and Conclusions

The aim of the present *in vivo* study was to evaluate the performances of sphene-coated implants as compared to uncoated Ti implants in a rat femur model. Micro-CT analysis revealed slight differences, in terms of bone-to-implant contact measurements, between the two arms of the study at each time point. This result might be due to the small sample size utilized in this pilot study. Consistently, histological and histomorphometrical findings were similar for both uncoated and sphene-coated samples, in which new bone formation was observed after 28 days from implant insertion.

Interestingly, no synovial fluid aspirate could be collected on the side treated with sphene-coated implants. In contrast, synovial fluid was present in 6 cases out of 10 in the knee joints on the side where uncoated implants had been positioned. Among these cases, in one case a clinically relevant amount of white blood cells was found. Even if caution

should be used in interpreting these findings, it can be assumed that sphene ceramic is a safe and biocompatible material, with no detrimental effect on the surrounding tissues.

However, the main problem encountered was the delamination of the coating in 30 percent of the cases.

Previous studies have evaluated implant osseointegration using micro-CT imaging with encouraging results [19,33,41-43].

The choice of voxel size is critical in particular when relative thin structures, such as rodent trabeculae (about 20-60 μm thickness), are investigated [20]. Thus, in this study a voxel size of small dimension, 6.5 μm, was utilized.

One of the major problems associated with the quantification of bone surrounding a Ti implant using micro-CT imaging consists in the extent of the metal-induced artefacts, which preclude the performance of measurements close to the bone-implant interface. In Butz et al. [49], the overestimation of peri-implant bone volume within the 3 voxels (24 μm) adjacent to the implant quantified via micro-CT, as compared to histological analysis, was attributed to metal-induced artefacts. In accordance with Butz et al. [49], also other authors reported on metal-induced artifacts extending outward from the implant surface 3 times the size of the voxel when using a voxel size of 8 μm [44].

In a more recent study [33], owing to the improved quality of newer scanners and to the optimization of the scanning parameters, metal-induced artefacts were minimized, and a significant correlation was observed between BIC assessed via bSEM and BIC calculated using either manual or automated assessment of micro-CT images.

Initially, a high-resolution micro-CT 1172 (Skyscan, Aartselaar, Belgium) was utilized in this study, but the presence of metal-induced artefacts could not guarantee the accurate 3D assessment of BIC, with the risk of an overestimation of this value. Therefore, after testing different parameter settings, it was decided to change scanner and, with the metrological X-ray CT system MCT 225 (Nikon Metrology), a strong reduction of metal-induced artefacts was observed.

One of the major advantages of micro-CT is the possibility to use the whole 3D information of the bone-implant interface. Various authors advocate to use methods to perform 3D measurements of the BIC by using micro-CT [33,50-52]. However, even though they do not limit BIC calculation to 3-4 slices, like for histomorphometric analysis, and they exploit micro-CT data for calculating BIC on a high number of slices, the BIC value obtained in these studies is based on measurements on cross-sectioned

micro-CT images and not on reconstructed 3D ones. In a recent study in minipigs [53], for the calculation of the BIC, a ROI based on a circular zone from 20 to 50 μm orthogonal to the implant surface was considered. Moreover, a statistically significant correlation was observed between micro-CT and histomorphometric analysis with regard to BIC ($p < 0.0001$).

In Choi et al. [54] an algorithm was used to calculate the 3D BIC area. The latter was obtained by dividing the attached bone volume by an infinitesimally increased radius (30 μm).

A similar approach was used in the present study, in order to overcome the limitation of the software, that cannot directly measure the contact area, but volumes only. The simple geometry of the implants facilitated the calculation, which might become more complex in case of screw-type implants [54].

In the present study Ti implant with Zirti surface was used as a reference, because it is commonly used in clinical practice and because, generally, blasted and etched Ti surfaces have demonstrated better results with respect to machined ones, when tested in animal models. In Sivolella et al. [55], Ti implants with Zirti surface were used in an experimental study in dog mandible. After 3 months of healing, histomorphometric analysis revealed a BIC% of 46.1%. In another study in dog, after 3 months from surgery both HA-coated (BIC% 63.5 ± 7.5) and uncoated (BIC% 57.6 ± 6.2) Ti implants with dual acid-etched surface presented with higher BIC values as compared to machined Ti implants (BIC% 37.7 ± 13.3). Moreover, a higher osseointegration was exhibited by blasted and etched Ti implants in comparison with machined Ti implants, also in rat model [56,57]. For instance, Abron et al. [56] tested different Ti implants in a rat tibia model. After 3 weeks of healing BIC assessed via bSEM was significantly higher in Ti implants with ideal pit morphology (BIC% 54 ± 7) than in machined Ti implants (BIC% 34 ± 6) ($p < 0.003$).

Consistently with Abron et al. [56], using a similar animal model, in the present study the BIC assessed by micro-CT of uncoated Ti implants with sand-blasted and acid etched surface was of 48.1 ± 19.6 and 57.7% ± 15.4, after 2 or 4 weeks of healing, respectively.

Although slightly higher BIC% values are reported for sphene-coated samples (see **Table 4**), no statistically significant difference was found between sphene-coated and uncoated samples, at both time points ($p > 0.05$).

Micro-CT findings were confirmed by histological and histomorphometric analyses, which demonstrated no marked differences in healing pattern between the two the implant surfaces. Bone healing after implant insertion involves several phases, such the activation of the immune system, neo-angiogenesis and new bone formation [58,59]. A sequence of different cell types characterized each phase. The initial wound healing process includes an inflammatory response and new blood vessel formation is considered a prerequisite for osteogenesis [58]. In the present work, after 14 days from implant insertion, peri-implant tissues were characterized by the presence of inflammatory cells, fibroblasts and phagocytic cells, as well as by the apposition of new ECM and neo-angiogenesis. Twenty-eight days postoperatively, in both experimental conditions, no sign of inflammatory response could be observed, whereas newly formed bone was detected.

The biocompatibility of sphene coating was demonstrated not only in the present work, but also in the only other study, to the best of our knowledge, investigating the *in vivo* behavior of sphene-coated implants [60]. Sphene-coated Ti-6Al-4V implants, produced by sol-gel and applied by dip-coating, were tested *in vivo* in sheep femur model [60]. Six weeks after surgery, histomorphometric analysis revealed that, when positioned in cortico-cancellous bone, sphene-coated implants showed mean BIC% of approximately 75%, comparable with HA-coated ones, but significantly higher than that of uncoated implants, with BIC% below 20%. These findings are in contrast with what reported in the present study, where no marked differences were observed between control and test groups. This discrepancy might also be due to the different uncoated control sample used in the two studies (i.e. Ti-6Al-4V and Ti implants with Zirti surface).

In accordance with a recent study in rabbit tibiae [61], apart from sphene-coated implants after 28 days of healing, osseointegration was higher, on average, in the cortical compartment compared to the cancellous one. However, as for BIC%, no statistically significant difference was found between the uncoated and coated implants with regards to both $BIC\%_{Cortical}$ and $BIC\%_{Cancellous}$.

Although the release of Ca and Si ions was found to stimulate osteoblastic proliferation and differentiation [62], one of the shortcomings of silicate-based ceramic coatings (i.e. wollastonite coatings) is their high degradation rate, which might affect their integrity [63,64].

As compared to other silicate bioceramics, the degradation kinetic of sphene ceramics tends to be very slow [65]. In previous investigation, sphene-coated samples produced

using the same technique proposed in the present work, resulted to be chemically stable in Tris-HCl [66]. Here, the mean coating thickness before and after implantation was assessed, in order to verify if any modification occurred in the early healing phases, confirming the absence of rapid degradability of the proposed coating.

Due to the slow degradation rate of sphene ceramics, it is likely that coating thickness reduction might become visible with longer implantation periods.

As for HA coatings [67], the delamination of the sphene-based coating from the substrate was found to be an issue of major concern. In a previous study, scratch tests were carried out on samples coated using two different solutions and deposited with an automated airbrush either for 1 s or 2.5 s [68]. The best results were obtained by using the same suspension composition and deposition time (1 s) used in the present study, with a critical normal load Lc 8.6 ± 0.2 N. Therefore, it was chosen to maintain the same composition and process parameters for the following *in vitro* [66] and then *in vivo* studies.

Contrary to previous works [66,68], in this study the coating was not applied onto flat plates, but onto rotating cylindrical implants. As observed on micro-CT images, in all the three cases the delamination started in the transition zone between the cylindrical portion of the implant and the apical hemispherical one, involving the latter.

The weak adhesion of the coating in this area might be due to the deposition method, as in this portion of the implant the coating was not sprayed orthogonally to the surface. Additionally, the movement of the implant during healing phases is regarded as one of the factors affecting implant osseointegration [69]. In this experimental study, the press fit of non-threaded implants into underprepared sites allowed for primary implant stability. It is likely that delamination occurred during implant insertion, as suggested by the presence of debris in one sample in the cortical part of the bone. As revealed by a finite element analysis [70], when undersized drilling protocols are chosen, high strain values are measured in the cortical part of the bone and the press-fit phenomenon is largely dependent on the cortical bone, although the implants are inserted in both cortical and cancellous bone. It has to be noted that undersized drilling protocols can be chosen also in the clinical practice with commonly used screw-type implants, for instance when immediate loading protocols are chosen [71]. Even though lower stresses can be generated during implant insertion using other drilling protocols and implant macro designs, it is necessary to improve the adhesion strength in any case.

Regarding the presence of SF, no aspirate could be collected from the joints on the side treated with sphene-coated implants. Whilst, when uncoated implants were positioned, SF was detected in 4 and 2 cases, at 14 and 28 days of healing, respectively. However, only in one case SF was inflammatory, even though no other signs or symptoms were recorded. Taking everything into account, on one hand these findings confirmed the biocompatibility of the proposed sphene-based coating, on the other hand there were not sufficient data to determine the cause of joint inflammation, with certainty. Among the possible causes, post-operative infection or the surgical trauma itself could be responsible for high white blood cell count in that control case.

Author contributions:

The candidate performed most of the work and was involved in all the steps of the research, from planning, to experimental work and data analysis.

Acknowledgments: This work was partially supported by Sweden & Martina (Due Carrare, Padova, Italy), which provided the customized implants.

This multidisciplinary study was performed in collaboration with:

- Prof. Stefano Sivolella – School of Dentistry, Department of Neuroscience, University of Padova (UNIPD), Italy
- Prof. Barbara Zavan – Regenerative Medicine Laboratory, Medical Sciences Department of Ferrara University, Italy
- Prof. Simone Carmignato – TE.SI. Laboratory, UNIPD, Italy
- Dr. Anna Scanu – Rheumatology Unit, Department of Medicine, UNIPD, Italy.

The author gratefully acknowledges the support provided by Markus Baier, Francesco Cavallin, Hamada Elsayed, Letizia Ferroni, Chiara Gardin, Roberto Luisetto and Elia Sbettega.

References

1. Albrektsson, T.; Brånemark, P.I., Hansson, H.A.; Lindström, J. Osseointegrated titanium implants. Requirements for ensuring a long-lasting, direct bone-to-implant anchorage in man. Acta Orthop. Scand. 1981, 52, 155–170. DOI: 10.3109/17453678108991776.

2. Atsumi, M.; Park, S.H.; Wang, H.L. Methods used to assess implant stability: current status. Int. J. Oral Maxillofac. Implants. 2007, 22, 743–754.

3. Meredith, N. Assessment of implant stability as a prognostic determinant. Int. J. Prosthodont. 1998, 11, 491–501.

4. Davies, J.E. Mechanisms of endosseous integration. Int. J. Prosthodont. 1998, 11, 391–401.

5. Zreiqat, H.; Valenzuela, S.M.; Nissan, B.B.; Roest, R.; Knabe, C.; Radlanski, R.J.; Renz, H.; Evans, P.J. The effect of surface chemistry modification of titanium alloy on signalling pathways in human osteoblasts. Biomaterials 2005, 26, 7579–7586. DOI: 10.1016/j.biomaterials.2005.05.024.

6. Cordeiro, J.M.; Barão, V.A. Is there scientific evidence favoring the substitution of commercially pure titanium with titanium alloys for the manufacture of dental implants? Mater. Sci. Eng. C Mater. Biol. Appl. 2017, 71, 1201–1215. DOI: 10.1016/j.msec.2016.10.025.

7. Pearce, A.I.; Richards, R.G.; Milz, S.; Schneider, E.; Pearce, S.G. Animal models for implant biomaterial research in bone: a review. Eur. Cell. Mater. 2007, 13, 1–10. DOI: 10.22203/eCM.v013a01.

8. Wancket, L.M. Animal Models for evaluation of bone implants and devices: comparative bone structure and common model uses. Vet. Pathol. 2015, 52, 842–850. DOI: 10.1177/0300985815593124.

9. Sivolella, S.; Brunello, G.; Ferroni, L.; Berengo, M.; Meneghello, R.; Savio, G.; Piattelli, A.; Gardin, C.; Zavan, B. A Novel in vitro technique for assessing dental implant osseointegration. Tissue Eng. Part C Methods 2016, 22, 132–141. DOI: 10.1089/ten.TEC.2015.0158.

10. Coelho, P.G.; Granjeiro, J.M.; Romanos, G.E; Suzuki, M.; Silva, N.R.; Cardaropoli, G.; Thompson, V.P.; Lemons, J.E. Basic research methods and current trends of dental implant surfaces. J. Biomed. Mater. Res. B Appl. Biomater. 2009, 88, 579–596. DOI: 10.1002/jbm.b.31264.

11. Oortgiesen, D.A.W.; Meijer, G.J.; de Vries, R.B.M.; Walboomers, X.F.; Jansen, J.A. Animal models for the evaluation of tissue engineering constructs. In: Pallua N,

Suscheck CV, eds. Tissue Engineering. Springer: Berlin Heidelberg, 2011, 131–154. DOI: 10.1007/978-3-642-02824-3_8.

12. Swami, V.; Vijayaraghavan, V.; Swami, V. Current trends to measure implant stability. J. Indian Prosthodont. Soc. 2016, 16, 124–130. DOI:10.4103/0972-4052.176539.

13. Shah, F.A.; Thomsen, P.; Palmquist, A. Osseointegration and current interpretations of the bone-implant interface. Acta Biomater. 2019, 84, 1–15. DOI: 10.1016/j.actbio.2018.11.018.

14. Stokholm, R.; Spin-Neto, R.; Nyengaard, J.R.; Isidor, F. Comparison of radiographic and histological assessment of peri-implant bone around oral implants. Clin. Oral Implants Res. 2016, 27, 782–786. DOI: 10.1111/clr.12683.

15. Ritter, L.; Elger, M.C.; Rothamel, D.; Fienitz, T.; Zinser, M.; Schwarz, F.; Zöller, J.E. Accuracy of peri-implant bone evaluation using cone beam CT, digital intra-oral radiographs and histology. Dentomaxillofac Radiol. 2014, 43, 20130088. DOI: 10.1259/dmfr.20130088.

16. Sul, Y.T.; Johansson, C.B.; Jeong, Y.; Wennerberg, A.; Albrektsson, T. Resonance frequency and removal torque analysis of implants with turned and anodized surface oxides. Clin. Oral Implants Res. 2002, 13, 252–259. DOI: 10.1034/j.1600-0501.2002.130304.x.

17. Glauser, R.; Sennerby, L.; Meredith, N.; Rée, A.; Lundgren, A.; Gottlow, J.; Hämmerle, C.H. Resonance frequency analysis of implants subjected to immediate or early functional occlusal loading. Successful vs. failing implants. Clin. Oral Implants Res. 2004, 15, 428–434. DOI: 10.1111/j.1600-0501.2004.01036.x.

18. Aparicio, C.; Lang, N.P.; Rangert, B. Validity and clinical significance of biomechanical testing of implant/bone interface. Clin. Oral Implants Res. 2006, 17, 2–7. DOI: 10.1111/j.1600-0501.2006.01365.x.

19. Stadelmann, V.A.; Potapova, I.; Camenisch, K.; Nehrbass, D.; Richards, R.G.; Moriarty, T.F. In vivo MicroCT monitoring of osteomyelitis in a rat model. Biomed. Res. Int. 2015, 2015, 587857. DOI: 10.1155/2015/587857.

20. Bouxsein, M.L.; Boyd, S.K.; Christiansen, B.A.; Guldberg, R.E.; Jepsen, K.J.; Müller, R. Guidelines for assessment of bone microstructure in rodents using micro-computed tomography. J. Bone Miner. Res. 2010, 25, 1468–1486. DOI: 10.1002/jbmr.141.

21. Longo, A.B.; Salmon, P.L.; Ward, W.E. Comparison of ex vivo and in vivo micro-computed tomography of rat tibia at different scanning settings. J. Orthop. Res. 2017, 35, 1690–1698. DOI: 10.1002/jor.23435.

22. Novaes AB Jr, de Souza SL, de Barros RR, Pereira KK, Iezzi G, Piattelli A. Influence of implant surfaces on osseointegration. Braz Dent J. 2010;21(6):471–481. DOI: 10.1590/S0103-64402010000600001.

23. Baker, D.; London, R.M.; O'Neal, R. Rate of pull-out strength gain of dual-etched titanium implants: a comparative study in rabbits. Int. J. Oral Maxillofac. Implants 1999, 14, 722–728.

24. Müller, M.; Hennig, F.F.; Hothorn, T.; Stangl, R. Bone-implant interface shear modulus and ultimate stress in a transcortical rabbit model of open-pore Ti6Al4V implants. J. Biomech. 2006, 39, 2123–2132. DOI: 10.1016/j.jbiomech.2005.05.036.

25. Aparicio, C.; Padrós, A.; Gil, F.J. In vivo evaluation of micro-rough and bioactive titanium dental implants using histometry and pull-out tests. J. Mech. Behav. Biomed. Mater. 2011, 4, 1672–1682. DOI: 10.1016/j.jmbbm.2011.05.005.

26. Li, Y.; Gao, Y.; Shao, B.; Xiao, J.; Hu, K.; Kong, L. Effects of hydrofluoric acid and anodised micro and micro/nano surface implants on early osseointegration in rats. Br. J. Oral Maxillofac. Surg. 2012, 50, 779–783. DOI: 10.1016/j.bjoms.2011.12.008.

27. Seong, W.J.; Grami, S.; Jeong, S.C.; Conrad, H.J.; Hodges. J.S. Comparison of push-in versus pull-out tests on bone-implant interfaces of rabbit tibia dental implant healing model. Clin. Implant Dent. Relat. Res. 2013, 15, 460–469. DOI: 10.1111/j.1708-8208.2011.00357.x.

28. Johansson, C.B.; Han, C.H.; Wennerberg, A.; Albrektsson, T. A quantitative comparison of machined commercially pure titanium and titanium-aluminum-vanadium implants in rabbit bone. Int. J. Oral Maxillofac. Implants 1998, 13, 315–321.

29. Yeo, I.S.; Han, J.S.; Yang, J.H. Biomechanical and histomorphometric study of dental implants with different surface characteristics. J. Biomed. Mater. Res. B Appl. Biomater. 2008, 87, 303–311. DOI: 10.1002/jbm.b.31104.

30. Kitsugi, T.; Nakamura, T.; Oka, M.; Yan, W.Q.; Goto, T.; Shibuya, T.; Kokubo, T.; Miyaji, S. Bone bonding behavior of titanium and its alloys when coated with titanium oxide (TiO2) and titanium silicate (Ti5Si3). J. Biomed. Mater. Res. 1996, 32, 149–156. DOI: 10.1002/(SICI)1097-4636(199610)32:2<149::AID-JBM1>3.0.CO;2-T.

31. Brånemark, R.; Ohrnell, L.O.; Skalak, R.; Carlsson, L.; Brånemark, P.I. Biomechanical characterization of osseointegration: an experimental in vivo

investigation in the beagle dog. J. Orthop. Res. 1998, 16, 61–69. DOI: 10.1002/jor.1100160111.

32. Meenakshi, S.; Raghunath, N.; Raju, S.N.; Srividya, S.; Indira, P.N. Implant stability a key determinant in implant integration. Trends Prosthodont. Dent. Implantol. 2013, 4, 28–48.

33. Meagher, M.J.; Parwani, R.N.; Virdi, A.S.; Sumner, D.R. Optimizing a micro-computed tomography-based surrogate measurement of bone-implant contact. J. Orthop. Res. 2018, 36, 979–986. DOI: 10.1002/jor.23716.

34. Geng, H.; Todd, N.M.; Devlin-Mullin, A.; Poologasundarampillai, G.; Kim, T.B.; Madi, K.; Cartmell, S.; Mitchell, C.A.; Jones, J.R.; Lee, P.D. A correlative imaging based methodology for accurate quantitative assessment of bone formation in additive manufactured implants. J. Mater. Sci. Mater. Med. 2016, 27, 112. DOI: 10.1007/s10856-016-5721-6.

35. Gielkens, P.F.; Schortinghuis, J.; de Jong, J.R.; Huysmans, M.C.; Leeuwen, M.B.; Raghoebar, G.M.; Bos, R.R.; Stegenga, B. A comparison of micro-CT, microradiography and histomorphometry in bone research. Arch. Oral Biol. 2008, 53, 558–566. DOI: 10.1016/j.archoralbio.2007.11.011.

36. Chikazu, D.; Tomizuka, K.; Ogasawara, T.; Saijo, H.; Koizumi, T.; Mori, Y.; Yonehara, Y.; Susami, T.; Takato, T. Cyclooxygenase-2 activity is essential for the osseointegration of dental implants. Int. J. Oral Maxillofac. Surg. 2007, 36, 441–446. DOI: 10.1016/j.ijom.2006.11.011.

37. Liu, W.; Zhang, S.; Zhao, D.; Zou, H.; Sun, N.; Liang, X.; Dard, M.; Lanske, B.; Yuan, Q. Vitamin D supplementation enhances the fixation of titanium implants in chronic kidney disease mice. PLoS One 2014, 9, e95689. DOI:10.1371/journal.pone.0095689. Erratum in: PLoS One 2014, 9, e99972.

38. Zheng, X.; Mo, A.; Wang, Y.; Guo, Y.; Wu, Y.; Yuan, Q. Effect of FK-506 (tacrolimus) therapy on bone healing of titanium implants: a histometric and biomechanical study in mice. Eur. J. Oral Sci. 2017, 125, 28–33. DOI: 10.1111/eos.12320.

39. Pelegrine, A.A.; Moy, P.K.; Moshaverinia, A.; Escada, A.L.D.A.; Calvo-Guirado. J.L.; Claro, A.P.R.A. Development of a novel nanotextured titanium implant. An experimental study in rats. J Clin. Med. 2019, 8, 954. DOI: 10.3390/jcm8070954.

40. Zhou, W., Tangl, S.; Reich, K.M.; Kirchweger, F.; Liu, Z.; Zechner, W.; Ulm, C.; Rausch-Fan, X. The Influence of type 2 diabetes mellitus on the osseointegration of titanium implants with different surface modifications-A histomorphometric study in

high-fat diet/low-dose streptozotocin-treated rats. Implant Dent. 2019, 28, 11–19. DOI: 10.1097/ID.0000000000000836.

41. Vandeweghe, S., Coelho, P.G.; Vanhove, C.; Wennerberg, A.; Jimbo, R. Utilizing micro-computed tomography to evaluate bone structure surrounding dental implants: a comparison with histomorphometry. J. Biomed. Mater. Res. B Appl. Biomater. 2013, 101, 1259–1266. DOI: 10.1002/jbm.b.32938.

42. He, T.; Cao, C.; Xu, Z.; Li, G.; Cao, H.; Liu, X.; Zhang, C.; Dong, Y. A comparison of micro-CT and histomorphometry for evaluation of osseointegration of PEO-coated titanium implants in a rat model. Sci, Rep. 2017, 7, 16270. DOI: 10.1038/s41598-017-16465-4.

43. Yu, Y.J.; Zhu, W.Q.; Xu, L.N.; Ming, P.P.; Shao, S.Y.; Qiu, J. Osseointegration of titanium dental implant under fluoride exposure in rabbits: Micro-CT and histomorphometry study. Clin. Oral Implants Res. 2019 Jul 26. [Epub ahead of print] DOI: 10.1111/clr.13517.

44. Liu, S.; Broucek, J.; Virdi, A.S.; Sumner, D.R. Limitations of using micro-computed tomography to predict bone-implant contact and mechanical fixation. J. Microsc. 2012, 245, 34–42. DOI: 10.1111/j.1365-2818.2011.03541.x.

45. Russell, U.M.S.; Burch, R.L. The principles of human experimental techniques. London, 1959.

46. ISO - International Organization for Standardization. Available online: https://www.iso.org/obp/ui/#iso:std:iso:25178:-2:ed-1:v1:en (accessed on 20 Sept 2019)

47. Scanu, A.; Oliviero, F.; Ramonda, R.; Frallonardo, P.; Dayer, J.M.; Punzi, L. Cytokine levels in human synovial fluid during the different stages of acute gout: role of transforming growth factor β1 in the resolution phase. Ann. Rheum. Dis. 2012, 71, 621–624. DOI: 10.1136/annrheumdis-2011-200711.

48. Punzi, L.; Oliviero, F. Arthrocentesis and synovial fluid analysis in clinical practice: value of sonography in difficult cases. Ann. N. Y. Acad. Sci. 2009, 1154, 152–158. DOI: 10.1111/j.1749-6632.2009.04389.x.

49. Butz, F.; Ogawa, T.; Chang, T.L.; Nishimura. I. Three-dimensional bone-implant integration profiling using micro-computed tomography. Int. J. Oral Maxillofac. Implants. 2006, 21, 687–695.

50. Bernhardt, R.; Kuhlisch, E.; Schulz, M.C.; Eckelt. U.; Stadlinger. B. Comparison of bone-implant contact and bone-implant volume between 2D-histological sections and

3D-SRμCT slices. Eur. Cell. Mater. 2012, 23, 237–247; discussion 247-8. DOI: 10.22203/eCM.v023a18.

51. Jimbo, R.; Coelho, P.G.; Vandeweghe, S.; Schwartz-Filho, H.O.; Hayashi. M.; Ono, D.; Andersson, M.; Wennerberg, A. Histological and three-dimensional evaluation of osseointegration to nanostructured calcium phosphate-coated implants. Acta Biomater. 2011, 7, 4229–4234. DOI: 10.1016/j.actbio.2011.07.017.

52. Palmquist, A.; Shah, F.A.; Emanuelsson, L.; Omar, O., Suska, F. A technique for evaluating bone ingrowth into 3D printed, porous Ti6Al4V implants accurately using X-ray micro-computed tomography and histomorphometry. Micron. 2017, 94, 1–8. DOI: 10.1016/j.micron.2016.11.009.

53. Bissinger, O.; Probst, F.A.; Wolff, K.D.; Jeschke. A.; Weitz, J.; Deppe, H.; Kolk, A. Comparative 3D micro-CT and 2D histomorphometry analysis of dental implant osseointegration in the maxilla of minipigs. J. Clin. Periodontol. 2017, 44, 418–427. DOI: 10.1111/jcpe.12693.

54. Choi, J.Y.; Park, J.I.; Chae, J.S.; Yeo, I.L. Comparison of micro-computed tomography and histomorphometry in the measurement of bone-implant contact ratios. Oral Surg. Oral Med. Oral Pathol. Oral Radiol. 2019, 128, 87–95. DOI: 10.1016/j.oooo.2018.12.023.

55. Sivolella, S.; Bressan, E.; Salata, L.A.; Urrutia, Z.A.; Lang, N.P.; Botticelli, D. Osteogenesis at implants without primary bone contact - an experimental study in dogs. Clin. Oral Implants Res. 2012, 23, 542–549. DOI: 10.1111/j.1600-0501.2012.02423.x.

56. Abron, A.; Hopfensperger, M.; Thompson, J.; Cooper, L.F. Evaluation of a predictive model for implant surface topography effects on early osseointegration in the rat tibia model. J. Prosthet. Dent. 2001, 85, 40–46. DOI: 10.1067/mpr.2001.112415.

57. Marinho, V.C.; Celletti, R.; Bracchetti, G.; Petrone, G.; Minkin, C.; Piattelli, A. Sandblasted and acid-etched dental implants: a histologic study in rats. Int. J. Oral Maxillofac. Implants. 2003, 18, 75–81.

58. Terheyden, H.; Lang, N.P.; Bierbaum, S.; Stadlinger, B. Osseointegration--communication of cells. Clin Oral Implants Res. 2012, 23, 1127–1135. DOI: 10.1111/j.1600-0501.2011.02327.x.

59. Bressan, E.; Botticelli, D.; Sivolella, S.; Bengazi, F.; Guazzo, R.; Sbricoli, L.; Ricci, S.; Ferroni, L.; Gardin, C.; Velez, J.U.; Zavan, B. Adipose-derived stem cells as a tool for dental implant osseointegration: an experimental study in the dog. Int. J. Mol. Cell. Med. 2015, 4, 197–208.

60. Ramaswamy, Y.; Wu, C.; Dunstan, C.R.; Hewson, B.; Eindorf, T.; Anderson, G.I.; Zreiqat, H. Sphene ceramics for orthopedic coating applications: an in vitro and in vivo study. Acta Biomater. 2009, 5, 3192–3204. DOI: 10.1016/j.actbio.2009.04.028.

61. Soto-Peñaloza, D.; Caneva, M.; Viña-Almunia, J.; Martín-de-Llano, J.J.; Peñarrocha-Oltra, D.; Peñarrocha-Diago, M. Bone-healing pattern on the surface of titanium implants at cortical and marrow compartments in two topographic sites: an experimental study in rabbits. Materials 2018, 12, 85. DOI: 10.3390/ma12010085.

62. Fei, L.; Wang, C.; Xue, Y.; Lin, K.; Chang, J.; Sun, J. Osteogenic differentiation of osteoblasts induced by calcium silicate and calcium silicate/β-tricalcium phosphate composite bioceramics. J. Biomed. Mater. Res. B Appl. Biomater. 2012, 100, 1237–1244. DOI: 10.1002/jbm.b.32688.

63. Wu, C.; Ramaswamy, Y.; Kwik, D.; Zreiqat, H. The effect of strontium incorporation into CaSiO3 ceramics on their physical and biological properties. Biomaterials 2007, 28, 3171–3181. DOI: 10.1016/j.biomaterials.2007.04.002.

64. Ni, S.; Chang, J. In vitro degradation, bioactivity, and cytocompatibility of calcium silicate, dimagnesium silicate, and tricalcium phosphate bioceramics. J. Biomater. Appl. 2009, 24, 139–158. DOI: 10.1177/0885328208094745.

65. Wu, C.; Chang, J. A review of bioactive silicate ceramics. Biomed. Mater. 2013, 8, 032001. DOI: 10.1088/1748-6041/8/3/032001.

66. Elsayed, H.; Brunello, G.; Gardin, C.; Ferroni, L.; Badocco, D.; Pastore, P.; Sivolella, S.; Zavan, B.; Biasetto, L. Bioactive sphene-based ceramic coatings on cpTi substrates for dental implants: an in vitro study. Materials 2018, 11, 2234. DOI: 10.3390/ma11112234.

67. Ogiso, M.; Yamashita, Y.; Matsumoto, T. The process of physical weakening and dissolution of the HA-coated implant in bone and soft tissue. J. Dent. Res. 1998, 77, 1426–1434. DOI: 10.1177/00220345980770060701.

68. Biasetto, L.; Elsayed, H. Sphene silicate ceramic coatings on cpTi substrates: Process upgrade. Surf. Coat. Technol. 2017, 321, 416–424. DOI: 10.1016/j.surfcoat.2017.05.018.

69. Albrektsson, T.; Albrektsson, B. Osseointegration of bone implants. A review of an alternative mode of fixation. Acta Orthop. Scand. 1987, 58, 567–577. DOI: 10.3109/17453678709146401.

70. Frisardi, G.; Barone, S., Razionale, A.V.; Paoli, A.; Frisardi, F.; Tullio, A.; Lumbau, A.; Chessa, G. Biomechanics of the press-fit phenomenon in dental implantology: an

image-based finite element analysis. Head Face Med. 2012, 8, 18. DOI: 10.1186/1746-160X-8-18.

71. Ostman, P.O.; Hellman, M.; Sennerby, L. Direct implant loading in the edentulous maxilla using a bone density-adapted surgical protocol and primary implant stability criteria for inclusion. Clin. Implant Dent. Relat. Res. 2005, 7, S60–S69. DOI: 10.1111/j.1708-8208.2005.tb00076.x.

Chapter 4

Bioactive Sphene-Based Ceramic Scaffolds for Bone Regeneration: an In Vitro Study

ABSTRACT

The work presented in this chapter consists in the characterization and *in vitro* assessment of the biological behavior of porous sphene ceramic scaffolds, produced by means of extrusion-based 3D printing, known as direct ink writing (DIW).

After the successful production and mechanical characterization of sphene ceramic scaffolds (Bernardo E., Colombo P., and Elsayed H., in collaboration with Mazzer A.- DII-UNIPD), critical aspects, including *in vitro* cytocompatibility of the scaffolds, needed to be addressed before experimental studies in animal models.

Sphene scaffolds were fabricated by direct ink writing of an ink composed of a silicone polymer and inorganic fillers (fumed silica, TiO_2 and $CaCO_3$). The green bodies were firstly cross-linked at 250 °C and, then, fired at 1300°C for 3 h in air. For the production of the scaffolds, already optimized ink composition and processing parameters were utilized.

Microstructural characterization of the scaffolds after heat treatment was performed by means of optical stereomicroscopy and scanning electron microscopy (SEM).

The methyl thiazolyl-tetrazolium (MTT) assay was performed in order to evaluate the viability of human adipose-derived stem cells (hADSCs) seeded onto 3D-printed scaffold, either in presence of osteogenic differentiation medium or endothelial differentiation medium, for 14, 21 and 28 days.

Real-time PCR (Polymerase Chain Reaction) was also performed to verify *in vitro* osteogenic and endothelial differentiation of ADSCs cells.

Highly porous crack-free 3D-printed scaffolds were successfully fabricated by direct ink writing. MTT test confirmed the *in vitro* biocompatibility of sphene ceramic scaffolds. Moreover, osteogenic and endothelial differentiation of ADSCs was confirmed by real-time PCR.

The so produced porous sphene ceramic scaffolds are suitable candidates as bone grafting materials.

After *in vitro* positive results, *in vivo* study will be performed to investigate the osteoconductive effect of sphene ceramic scaffolds in critical-sized bone defect in calvaria. To this aim, detailed study protocol was developed and ethical approval from the Italian Ministry of Health was obtained.

Keywords: scaffold; sphene; bioactive ceramic; direct ink writing; bone regeneration

4.1. Introduction

Bone defects may arise due to a variety of causes, such as trauma, infections, tumors or congenital conditions. One of the major challenges in dentistry, as well as in maxillofacial surgery and orthopedics, still remains the reconstruction of extensive bone defects [1,2].

In clinical practice, a wide variety of materials of both natural and synthetic origin have been used [3,4]. The ideal bone graft should be biocompatible and should possess osteoconductive, osteoinductive and osteogenic properties. Moreover, it should preferably be resorbable and replaced by newly formed bone, while maintaining adequate mechanical strength and structural support in the meantime, especially in load-bearing applications [5-7].

Even though autogenous bone graft is considered the "gold standard" material for bone regeneration, its application is limited by supply and morbidity at the donor site after harvesting [8-10].

As alternative to autogenous bone grafting, allogeneic bone grafting, derived either from human cadavers or living donors, is utilized, despite possible rejection reactions or transmission of infections [11]. To overcome these limitation, synthetic bone materials have been proposed.

One of the requirements for a good bone substitute is to present an interconnected porous structure, mimicking the hierarchical structure of native bone. One of the major advantages of Additive Manufacturing (AM) technologies, as compared to conventional ones (e.g. gas foaming, freeze drying, emulsification), is the possibility to control the macro- and micro- porosity of the scaffolds [12,13].

Moreover, shaping the bone grafts manually in order to fit it into a bone defect is a complex procedure requiring time and high level of operator skills [14,15]. AM technologies offer the great advantage to produce custom-made bone blocks, tailored to specific bone defects, starting from patients' computerized tomography (CT) scans [13,16].

Bioceramic scaffolds for bone tissue regeneration can be obtained using various AM technologies, such as stereolithography (SLA), Selective Laser Sintering (SLS) and Binder Jetting 3D Printing [13,17,18].

Another approach, known as Direct Ink Writing (DIW), originally developed for printing polymers, is nowadays exploited for the production of bioceramic scaffolds [19,20]. With this technique, active fillers in form of powders are mixed with the polymer and extruded through the nozzle at room temperature. The ink has to possess adequate rheologic features (pseudoplastic fluid with yield stress), in order to guarantee the maintenance of the shape once printed [20,21]. Moreover, it was demonstrated that by using DIW it is possible to have high precision control of the scaffold features at macro- and micro-level, thus influencing cell growth and differentiation within the bone scaffold [17].

Recently, various ceramic scaffolds, such as silica-bonded calcite ($SiO_2/CaCO_3$) or wollastonite-diopside ($CaSiO_3 – CaMgSi_2O_6$) scaffolds, were successfully 3D-printed by DIW, starting from inks comprising a silicon polymer and powder precursors [20,21]. The so produced ceramic scaffolds, after heat treatment, presented an average compressive strength in the range of 2.9-5.5 MPa, depending on the material and the geometry of the scaffolds [20,21]. Moreover, preliminary cell culture tests confirmed their biocompatibility [20].

As one of the main requirements for bone scaffolds, in particular for load bearing application, is to possess adequate mechanical properties, 3D-printed sphene ceramic scaffolds with porous structure and improved compressive strength was developed by our group.

In the study presented in this chapter, 3D-printed sphene ceramic scaffolds previously characterized at DII-UNIPD were used. The scaffolds, after heat treatment at 1300°C, were fully composed of sphene crystalline phase and presented a geometrical density (ϱ) of 1.4876 ± 0,06 g/cm^3, an open porosity (P_{open}) of 53.71 ± 1.98% and a compressive strength (σ_{comp}) of 17.91 MPa. The volume shrinkage after ceramization was approximately of 40%. [Data gently provided by Elsayed H.].

The primary objective of the current research was to evaluate the biocompatibility of the sphene ceramic scaffold as well as its effect on the osteogenic and endothelial differentiation of hADSCs *in vitro*. The secondary aim consisted in the morphological and microstructural characterization of the scaffolds.

4.2. Experimental Procedure

4.2.1. Direct Ink Writing of Sphene Scaffolds

The polymer-derived ceramics (PDCs) route, previously described for the production of sphene-based coatings in **Chapters 2** and **3**, was used also for the preparation of the sphene ($CaTiSiO_5$) ceramic scaffolds.

The molar ratio between the oxides constituting the material, $CaO:TiO_2:SiO_2$, is 1:1:1.

For the fabrication of the ink, a commercially available polymethylsiloxane, SILRES® MK (Wacker-Chemie GmbH, München, Germany) was used as preceramic polymer, which has a silica yield of ~84 wt% after heating in air at 1000 °C [22]. In order to obtain the required amount of SiO_2, nano-sized silica (fumed silica, Aerosil R106, Evonik Germany) was used. As the latter is pure silica, it possesses a ceramic yield of 100 wt%, after ceramization. The addition of fumed silica allowed for the adequate rheological behavior of the ink, as previously demonstrated [23,24].

CaO was provided by $CaCO_3$, in the form of micro-sized particles (~10 μm, Industrie Bitossi, Vinci, Italy), while TiO_2 was added in form of nano-sized particles (~21 nm, Evonik Degussa GmbH, Germany).

Briefly, for the ink production, MK silicone resin, in powder form, was dissolved in isopropanol with 30 vol%. Then, fumed silica was mixed with MK in isopropanol. TiO_2 and, then, $CaCO_3$ active fillers were incorporated into the polymer. It is fundamental to prepare a perfectly homogenous suspension without traces of powder aggregates, which might lead to nozzle clogging during printing.

At each passage described above, the solution was firstly mixed manually and, then, by using automatic mixing equipment at 2000 rpm (initially for 3 min 30 sec, for 3 min after adding fumed silica, for 2 min after the addition of TiO_2 and finally for 3 min 30 sec after incorporating $CaCO_3$).

The composition of the ink is reported in **Table 1**, with the addition of 1.7 g of isopropanol.

Table 1. Ink composition.

Component	Amount [g]
MK polymer	3.28
Fumed silica	0.31

TiO_2	4.07
$CaCO_3$	5.11

For the fabrication of the scaffolds, a 20x40 Delta Turbo printer (Wasp, Massa Lombarda, Italia) was used (see **Figure 1a**). The ink was loaded into a syringe and then extruded through a conical nozzle, characterized by a diameter of 410 µm (Nordson Italia S.p.a., Milano, Italy) (**Figure 1b**). The extrusion was performed at room temperature.

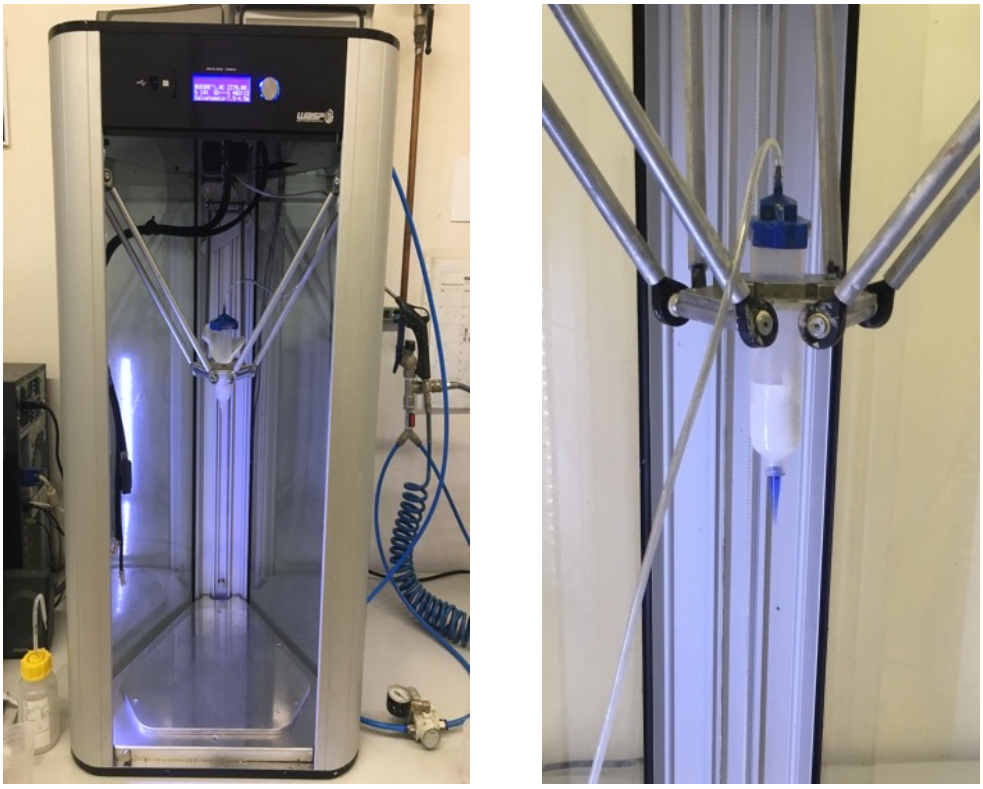

Figure 1. Photographs of: a) 3D-printer 20x40 Delta Turbo; b) detail of the 3D-printer equipped with syringe containing the preceramic ink.

For the *in vitro* study the scaffolds were designed and produced in the form of prisms with dimensions 10 mm x 10 mm x 4 mm, as resulted from the overlapping of 12 layers of cylindrical rods, periodically arranged along *x* and *y* axes, with successive layers at 90 degree angles to each other (**Figure 2**). The distance between two continuous parallel rods in the same layer was set at 700 µm. A layer thickness of 0.35 mm was selected.

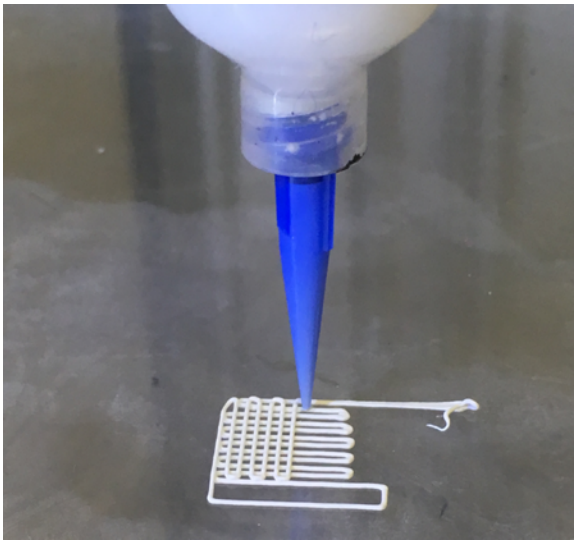

Figure 2. Detail of the printing process.

The substrate utilized for the deposition of the scaffolds was a plastic plate, with a thin layer of sunflower oil on the top, in order to facilitate the removal of the scaffolds from the substrate.

After printing, the scaffolds were left to dry for two days in ambient conditions, in order to allow the complete evaporation of the solvent (isopropanol). Then the scaffolds underwent a crosslinking process at 250°C for 1 h (heating rate 0.5 °C/min), followed by ceramization for 3 h at 550 °C, 1 h at 650 °C, 3 h at 850 °C, and finally 3 h at 1300°C (same heating rate as cross-linking treatment).

4.2.2. Morphological and Microstructural Characterization of the Scaffolds

Ceramized scaffolds were visually analyzed by means of optical stereomicroscopy (AxioCamERc 5s Microscope Camera, Carl Zeiss Microscopy, Thornwood, New York, USA). In addition, the samples were analyzed by scanning electron microscopy (FEI Quanta 200 ESEM, Eindhoven, Netherlands).

4.2.3. Cell Culture

Human adipose-derived stem cells (hADSCs) were isolated from the adipose tissue of healthy patients undergoing cosmetic surgery procedures, after they signed informed consent. Experiments carried out with the use of human-derived cells were performed in accordance with the ethical principles outlined in the Declaration of Helsinki. The adipose

tissues were digested, and stem cells isolated and expanded as described in a previously published protocol [25].

Briefly, cells were isolated by sequential collagenase and trypsin digestion. After the discard of floating adipocytes, the cells from the stromalvascular fraction were pelleted, rinsed with media, and centrifuged. This step was followed by red cell lysis in NH_4Cl for 10 min at room temperature. The remaining viable cells were counted using the trypan blue exclusion assay and seeded at a density of 10^6 cells/cm^2 for *in vitro* expansion in Dulbecco's modified Eagle's medium (DMEM; EuroClone, Milan, Italy) supplemented with 10% Fetal Bovine Serum (FBS; Bidachem S.p.A., Milan, Italy) and 1% penicillin/streptomycin (P/S; EuroClone). After 10 day of culture, cells were seeded onto 3D-printed sphene scaffolds at a density of 10^6 cells/cm^2 in presence of differentiative medium and cultivate up to 28 days.

For MTT assay, two different cell culture media were used (i.e. osteoinductive medium and endothelial differentiation medium). Whereas, for rt-PCR a medium for concomitant osteogenic and vasculogenic commitment was utilized. The composition of the culture media is provided in **Table 2**.

Table 3. Culture medium compositions.

Culture medium	Composition
Osteogenic differentiation medium	DMEM containing 10% fetal calf serum, 1% l-glutamine, 50 mg/mL l-ascorbic acid (Sigma Aldrich Italia, Milan, Italy), 10 ng/mL fibroblast growth factor (FGF) (Calbiochem, San Diego, CA, US), 10nM dexamethasone, and 10mM b-glycerophosphate.
Endothelial differentiation medium	M199 (Seromed, Berlin, Germany) containing 10% fetal calf serum, 1% l-glutamine, 50 mg/mL l-ascorbic acid (Sigma Aldrich Italia), 10 ng/mL ECGF (Calbiochem), and 100 mg/mL human basic FGF (Seromed)
Differentiation medium co-commitment (osteogenic and vasculogenic)	M199 (Seromed) containing 10% fetal calf serum, 1% l-glutamine, 50 mg/mL l-ascorbic acid (Sigma Aldrich Italia), 10 ng/mL ECGF (Calbiochem), 100 mg/mL human basic FGF (Seromed), 10nM dexamethasone, and 10mM β-glycerophosphate.

4.2.4. MTT Assay

In order to determine the proliferation rate of cells on 3D-printed sphene ceramic porous scaffolds, the methyl thiazolyl-tetrazolium (MTT) assay was performed at

predetermined times (i.e. 14, 21 and 28 days) according to the method of Denizot and Lang, with minor modifications [26]. The assay is based on mitochondria viability, i.e. only functional mitochondria can oxidize an MTT solution, turning the light yellow shade of the solution into the typical blue-violet end product.

After harvesting the culture medium, the cells were incubated for 3 h at 37°C in 1 mL of 0.5 mg/mL MTT solution prepared in phosphate buffer solution (PBS). Then, the MTT solution was removed with a pipette and 0.5 mL of 10% dimethyl sulfoxide in isopropanol was added for 30 min of incubation at 37 °C. For each sample, optical density (O.D.) values were determined at a wavelength of 570 nm in duplicate on 200 µL aliquots deposited in 96-well plates using a multilabel plate reader (Victor 3 Perkin Elmer, Milano, Italy).

4.2.5. Real-Time PCR

Total RNA was extracted from hADSCs, cultured in presence of differentiation medium for co-commitment on 3D-printed sphene scaffolds for 14, 21 and 28 days, using a Total RNA Purification Plus Kit (Norgen Biotek Corporation, Thorold, ON, Canada).

For the first-strand cDNA synthesis, for each sample 1 µg of total RNA was reverse transcribed using M-MLV Reverse Transcriptase (Invitrogen, Carlsbad, CA, USA), accordingly to the user's manual.

Human primers selection was conducted for each target gene using a Primer 3 software. The human primer sequences are provided in **Table 3**.

Real-time polymerase chain reaction (PCR) was performed using the selected primers at a concentration of 300 nM and FastStart SYBR Green Master (Roche Diagnostics, Mannheim, Germany) on a Rotor-Gene 3000 (Corbett Research, Sydney, Australia).

The thermal cycling conditions were as follows: 15 min denaturation at 95 °C; then 40 cycles of denaturation for 15 s at 95 °C; annealing for 30 s at 60 °C; and, finally, elongation for 20 s at 72 °C. Values were normalized to the expression of reference GAPDH. The experiments were performed in triplicate.

Table 3. Human primer sequences. VWF (von Willebrand factor), CD31 (PECAM-1, platelet/endothelial cell adhesion molecule 1), OC (osteocalcin), OPN (osteopontin), ON (osteonectin), RUNX (runt-related transcription factor), ALP (alkaline phosphatase), Collagen type I, and GAPDH (glyceraldehyde 3-phosphate dehydrogenase).

Gene	FORWARD (5' → 3')	REVERSE (5' → 3')	Product Length

VWF	GCTTCACTTACGTTCTGCATGA	CCTTCACTCGGACACACTCATTG	174 bp
CD31	TCCAGCCAACTTCACCATCC	TGGGAGAGCATTTCACATACGA	171 bp
OC	GCAGCGAGGTAGTGAAGAGAC	AGCAGAGCGACACCCTA	193 bp
OPN	TGGAAAGCGAGGAGTTGAATGG	GCTCATTGCTCTCATCATTGGC	192 bp
ON	TGCATGTGTCTTAGTCTTAGTCACC	GCTAACTTAGTGCTTACAGGAACCA	183 bp
RUNX	CGTGGATCCATGGCT	CCTCGATCGAAGGACT	102 bp
ALP	TCAGAGGGAAGGAGATAGAGAGTC	AGCCAGAAACCATATGTCAAGAGA	112 bp
Collagen type I	TGAGCCAGCAGATCGAGA	ACCAGTCTCCATGTTGCAGA	128 bp
GAPDH	TCAACAGCGACACCCAC	GGGTCTCTCTCTTCCTCTTGTG	203 bp

4.2.6. Statistical Analyses

For data analysis, one-way analysis of variance (ANOVA) was used. t-tests were used to determine data significance, with p-value < 0.05 considered statistically significant. All tests were done using SPSS 16.0 software (SPSS Inc., Chicago, IL, USA) (licensed to the University of Padua, Padova, Italy).

4.3. Results

4.3.1. Morphology and Microstructural Characterization

At macro-level, the scaffolds appeared to maintain the shape and to possess a highly regular structure. As visible in **Figure 3**, heat treatment at 1300°C led to volume shrinkage of the 3D-printed scaffolds.

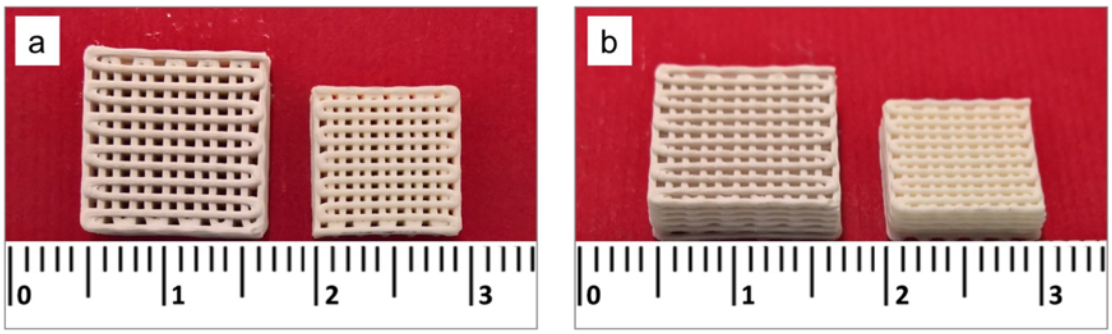

Figure 3. Overview of 3D-printed sphene scaffolds before (left) and after ceramization (right): a) top view at an angle;

The morphology of the 3D-printed scaffold is shown in **Figure 4**. The optical stereomicroscopy image testifies the uniformity of the structure and the absence of micro-cracks, that might originate during the polymer-to-ceramic transformation.

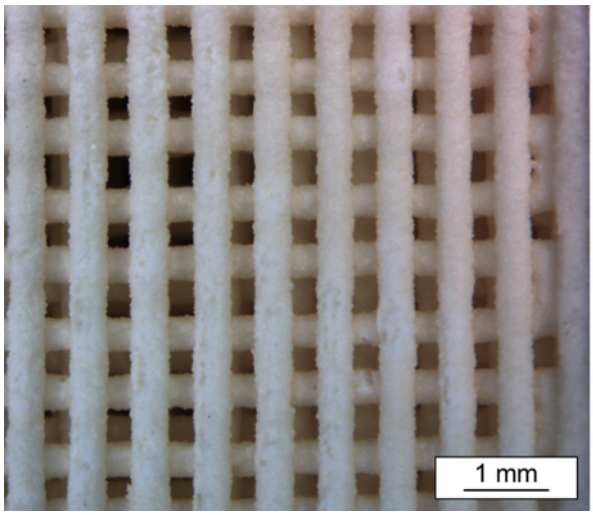

Figure 4. Morphology of 3D-printed sphene scaffold after ceramization (top view).

This is further confirmed by SEM images at different magnifications (see **Figure 5**). The scaffold was characterized by a highly porous structure with inter-connective macropores. The space between adjacent rods on the x–y plane was almost of 500 μm, resulting in a pore size suitable for bone tissue engineering. Indeed, pores in the range of 150–800 μm were found to favor osteogenesis and neo-angiogenesis [27].

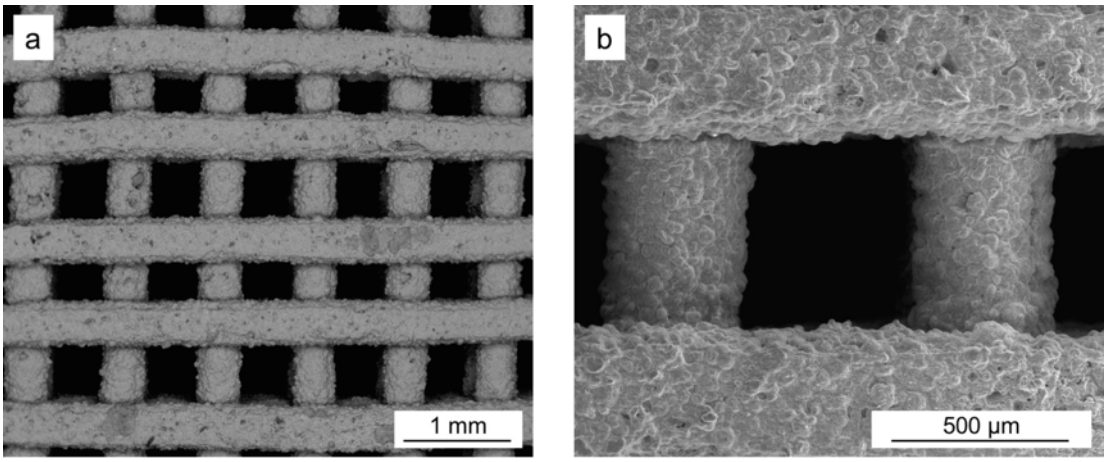

Figure 5. SEM images of 3D-printed sphene scaffold after ceramization: a) top view; b) higher magnification.

4.3.2. MTT Assay

The results of MTT assay showed that the 3D-printed sphene ceramic scaffolds had no toxic effect on hADSCs, as cells were able to proliferate on the scaffolds in presence of both differentiation media (see **Figure 6**). The O.D. values recorded for cells loaded on scaffolds in presence of osteogenic differentiation medium were slightly higher than in presence of endothelial differentiation medium at each time points, however no statistically significant difference was found between the two experimental conditions. Moreover, the rising in O.D. values overtime confirmed not only the vitality of the cells, but also their ability to proliferate.

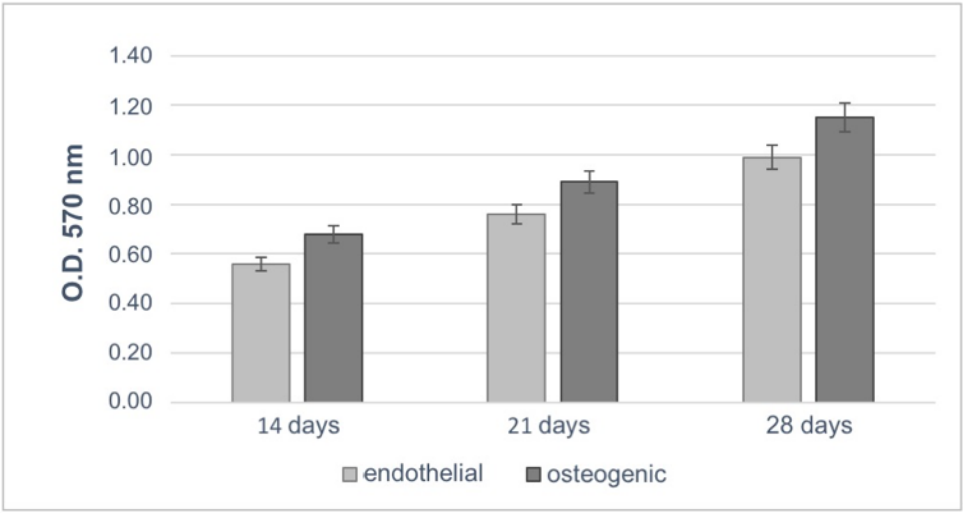

Figure 6. MTT assay of hADSCs cultured for 14, 21 and 28 days on 3D-printed sphene ceramic scaffolds in endothelial differentiation medium or osteogenic differentiation medium.

4.3.3. Real-Time PCR

The time course of vasculogenic and osteogenic mRNA expression, analyzed by semiquantitative real-time PCR in hADSCs cultured on 3D-printed sphene ceramic scaffolds in osteogenic plus vasculogenic medium after 7, 14, and 21 days, is shown in **Figure 7** and **Figure 8**, respectively.

As regards endothelial commitment, expression for von Willebrand factor and CD31 was detectable at each time points, confirming that cells were able to commit to the endothelial cells (**Figure 7**).

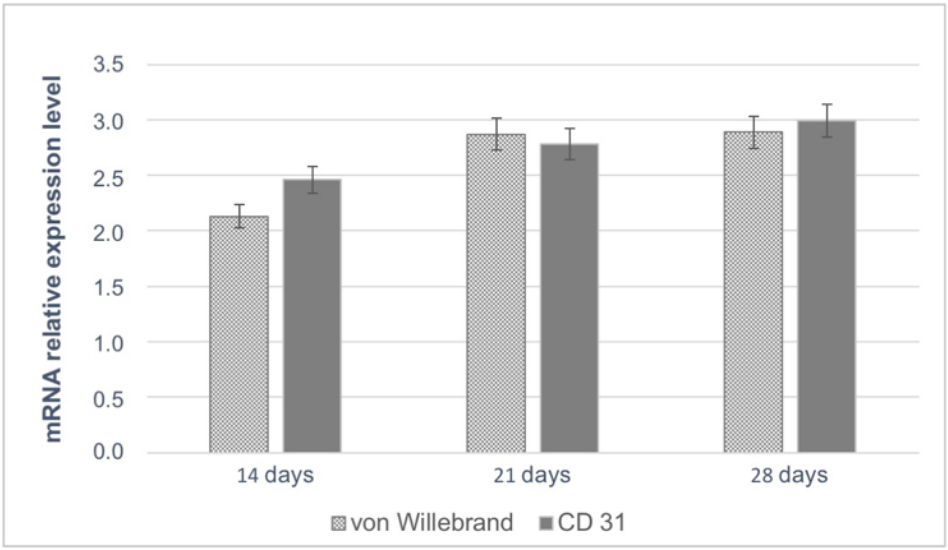

Figure 7. Real-time PCR analysis of the endothelial differentiation markers VWF (von Willebrand factor) and CD31 after 14, 21 and 28 days of culture. Data were normalized to the expression of reference GAPDH.

The expression of various osteogenic differentiation markers was also detectable, with increasing values of mRNA expression levels overtime. Specific markers were selected, including collagen, which is the main component of the bone matrix, and alkaline phosphatase, whose role is related to the calcification of the extracellular matrix. Also the expression of osteonectin was analyzed, as it is a protein selectively binding to both hydroxyapatite and collagen [28,29].

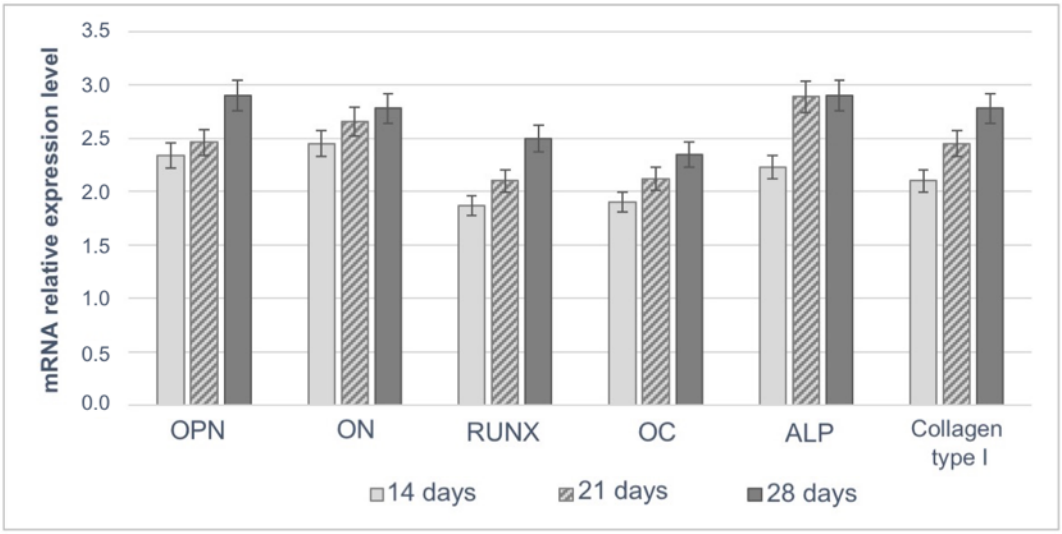

Figure 8. Real-time PCR analysis of the osteogenic differentiation markers OC (osteocalcin), OPN (osteopontin), ON (osteonectin), RUNX (runt-related transcription factor), ALP (alkaline phosphatase) and Collagen type I after 14, 21 and 28 days of culture. Data were normalized to the expression of reference GAPDH.

4.4. Discussion

Highly regular porous sphene ceramic scaffolds were successfully produced by DIW. The biocompatibility of the 3D-printed scaffolds was investigated in terms of proliferation rate of hADSCs seeded onto the samples up to 28 days by means of the MTT test. The cells were able to proliferate in both osteogenic and endothelial differentiation media and the proliferation was found to increase over the course of time. Moreover, gene expression tests for endothelial and osteogenic markers strongly supported a correct commitment to both endothelial and bone cells.

In our previous study on sphene ceramic as coating material for titanium implants [30], the coating resulted to be composed not only of sphene ($CaTiSiO_5$, 31 wt%), but also of rutile (TiO_2, 60 wt%) and perovskite ($CaTiO_3$, 9 wt%). The high percentage of rutile could be due to the heat treatment temperature used (950 °C, in air), which might have allowed the nucleation and growth of rutile crystals before sphene synthesis. Whilst, previously performed XRD analysis on 3D-printed scaffolds used in this work confirmed the full crystallization occurring in the samples of the desired silica phase, i.e. sphene. Firing in air atmosphere at 1300 °C led to crack-free scaffolds with pure sphene crystalline phase. This is in accordance with what reported in Muthuraman & Patil [31], in which the complete formation of sphene by the sol-gel method was achieved at 1300 °C.

For coating production [30], the lower heat treatment temperature was chosen, in order not to affect the integrity of the metallic substrate, resulting in multiple crystalline phases. One of the aims of future studies will be to produce coatings fully composed of sphene, assuming to obtain better results with increasing amount of sphene. A direct comparison between the *in vitro* behavior of sphene-based coatings [30] and that of 3D-printed sphene scaffolds here presented cannot be drawn, due to the different morphology of the samples and different culture media. In order to analyze the role of the percentages of sphene and other oxides, such as rutile, on the *in vitro* behavior of a biomaterial, ideally either 3D-printed scaffolds or coatings presenting various amounts of sphene should be investigated under the same experimental conditions.

As in Elsayed et al. [30], sphene scaffolds supported hADCS attachment and proliferation when cultured in osteogenic differentiation medium, as revealed by MTT assay. Moreover, in the present work the ability to proliferate was also confirmed for cells loaded in presence of endothelial differentiation medium.

It has been demonstrated that most silicate bioceramics, including akermanite ($Ca_2MgSi_2O_7$), hardystonite ($Ca_2ZnSi_2O_7$), diopside ($CaMgSi_2O_6$), bredigite ($Ca_7MgSi_4O_{16}$) and sphene ($CaTiSiO_5$), support the cell attachment and proliferation [32-35]. The release of silicon ions from silicate bioceramics in the culture media is considered to enhance the proliferation and the osteogenic differentiation of stem cells, thus suggesting excellent *in vitro* bioactive properties [36]. Si ions were found to elicit the proliferation, differentiation and bone-related gene expression of bone marrow stromal cells (BMSCs) [37]. In an *in vitro* study of Wu et al. [33], sphene ceramics were found to influence the proliferation and differentiation of human primary osteoblast-like cells (HOBs). In Ramaswamy et al. [38], sphene ceramics not only supported the attachment of HOBs, presenting highly structured actin filaments and expressing increased mRNA levels of osteoblast-related genes, but also favored the attachment of human endothelial cells. Interestingly, rt-PCR analysis revealed higher expression levels of the endothelial marker VECadherin, when cells were seeded onto sphene samples, than onto $CaSiO_3$ ceramics.

It is, indeed, fundamental not only to verify that bone scaffolds are conductive for osteoblasts, but also for endothelial cells. Blood vessels are indispensable for the maintenance of bone homeostasis. Moreover, vascular networks play a critical role during bone formation, carrying oxygen, nutrients and waste products, as well as transporting inorganic ions, such as calcium and phosphate ions, which are necessary for mineralization [39-42].

In a recent work of Inomata & Honda [39], osteoblast-like cells and human umbilical vein endothelial cells were found to enhance each other's functions, such as osteoblastic differentiation and endothelial cell tube formation, when co-cultured on a microfiber scaffold composed of poly (lactic-co-glycolic acid) (PLGA), β-tricalcium phosphate (β-TCP), and silicon-doped vaterite (SiV). Similarly, in Deb et al. [43] porous bioactive glass–ceramic scaffolds were found to support endothelial and human osteoblast cell proliferation in co-culture.

Contrary to other works [38,39,43], in the current study mesenchymal stem cells (i.e. ADSCs) were used rather than osteoblast-like cells or microvascular endothelial cells to *in vitro* investigate the osteoconductive and angiogenetic properties of the scaffold. Stem cells, indeed, play an essential role during the early phases of tissue regeneration,

migrating to the damage site thanks to their receptor and coordinating all the stages of tissue regeneration [44].

ADSCs, cultured up to 28 days on 3D-printed sphene scaffolds in a medium for concomitant osteogenic and vasculogenic commitment, were found to support cell differentiation, as confirmed by rt-PCR analysis. Also silica-bonded calcite scaffolds produced using the same technique, i.e. DIW, were able to stimulate the proliferation of bone marrow stromal cells *in vitro* [20]. As ADSCs, bone marrow stromal cells can differentiate into various mesenchymal cell lineages, including osteoblasts [45]. It is worth noting that, after 2 weeks of culture, cells exhibited a different phenotype depending on the medium. In non-stimulated condition, cells on 3D-printed silica-bonded calcite scaffolds showed a fibroblast-like morphology, whereas in presence of osteogenic medium cells displayed a mature osteoblast phenotype [20].

Although positive *in vitro* tests are generally considered as an important prerequisite for the success of a biomaterial, *in vivo* osseointegration ability of 3D-printed sphene ceramic scaffolds has to be assessed in animal models prior to clinical trials in human beings [46].

To our knowledge, no one has already produced and tested *in vivo* 3D-printed porous sphene ceramic scaffolds in a bone defect model, thus confirming the originality of our project.

4.5. Future Developments: from *In Vitro* to *In Vivo*

As already discussed in the previous chapter (see **Chapter 3**, **section 3.1.1.**), after testing a new biomaterial *in vitro*, it is necessary to confirm the results in animal models.

In light of the positive findings we recently obtained *in vitro* and of data reported in literature about other bioceramic 3D-printed scaffolds [20,21,47,48], sphene ceramic scaffolds produced by DIW appeared to be good candidates as bioactive bone substitutes for dental and orthopedic applications. Therefore, animal experiments in rat calvaria were planned for assessing bone response to this new biomaterial.

4.5.1. Critical Size Defect Model

In order to test a bone grafting material, various experimental approaches have been developed, including the “critical size defect” (CSD) model [49,50]. An intrabony defect

of critical dimensions is defined as a defect which does not heal spontaneously within the lifetime of the animal [51,52]. CSD models have been described for both small and large animals. Even though the latter are advantageous in terms of defect dimension, similarity to the human bone and biomechanical situation, their use is limited due to high experimental costs, long follow-up and ethical concerns. On the contrary, rodents were found to be reliable and predictable models, suitable for testing bone response to biomaterials. The main advantages of using rodents consist in the ease of handling and in the reduced experimental costs and timing [46,53,54]. The critical size defect model in rat calvaria is one of the most commonly used animal models for evaluating bone healing [49]. The size of the CSD varies depending on the animal model and on the site. Calvarial single defect of 8 mm in diameter or bilateral through-and-through defects with a diameter of 5.0 mm could be considered as CSDs [49,55].

Moreover, it is reported the use of critical size rat calvarial defect model for investigating the biocompatibility and bone repairing capacity of 3D-printed bone scaffolds [56-58].

4.5.2. Experimental Design for the In Vivo Study and Ethical Approval

The osteoconductive properties of the 3D-printed scaffolds will be investigated using a critical size rat calvarial defect model. Bone healing in defects filled with 3D-printed sphene ceramic scaffolds will be evaluated by means of micro-CT and histological analysis after 4 and 8 weeks of healing, as in Zhang et al. [56]. The selection of this model and time points, previously used by other authors [56-58], will favor the comparison between this study and others.

Two symmetrical full-thickness bone defects, 5 mm in diameter, will be carefully created in rat's calvarial bone using a trephine bur. Sphene ceramic scaffold will be randomly positioned on one side, whereas the contralateral defect will remain empty, without any grafting material, as illustrated in **Figure 9**.

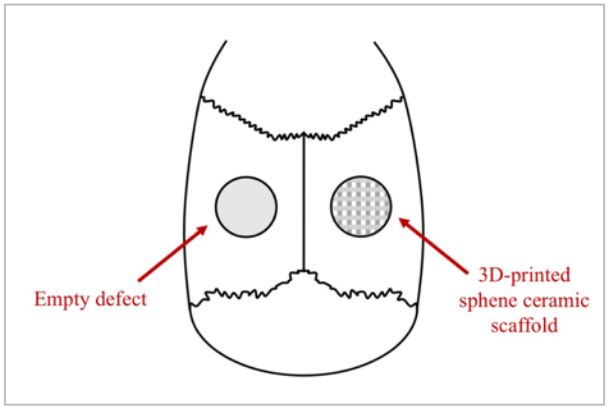

Figure 9. Schematic representation of critical size rat calvarial defect model. One bone defect, 5 mm in diameter, will be performed in each parietal bone and will be either left empty or filled with sphene ceramic scaffold.

To this aim, 3D-printed sphene ceramic scaffolds have already been produced using the same ink composition, printing setup and heat treatment described in **section 4.2.1**. However, for the *in vivo* study the scaffolds have not been printed in the form of prisms, but of cylinders with dimensions 5 mm in diameter and 2.3 mm in height (see **Figure 10**), in order to match the morphology of the bone defect.

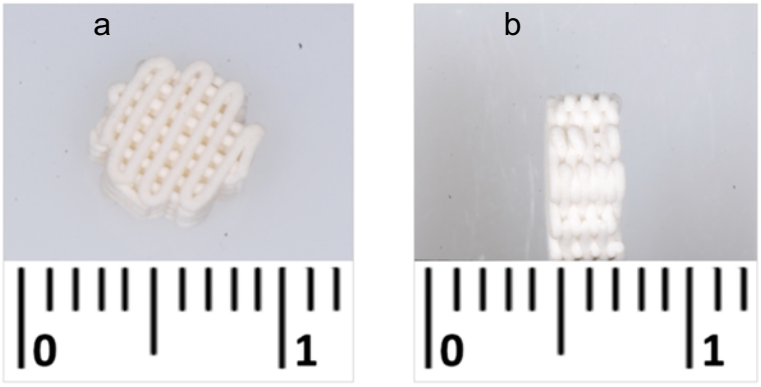

Figure 10. Cylindrical 3D-printed sphene ceramic scaffolds after ceramization for in vivo study: a) top view; b) lateral view.

As discussed in **Chapter 3**, **section 3.1.1**., micro-CT analysis is a recently introduced non-destructive approach to assess bone healing. Contrary to conventional histological and histomorphometric analyses, it does not require the sectioning of the sample, which might affect the three-dimensional anisotropic information of bone architecture [59]. BV/TV (bone volume/total volume) is the main parameter obtained from micro-CT data, which allows to identify the quantity of newly formed bone as compared to the bone

defect to fill. The primary aim of this *in vivo* study consists in the evaluation of BV/TV of rat CSDs either left empty (control) or filled with 3D-printed sphene ceramic scaffolds (test group). BV/TV will be calculated in 20 rats, randomly sacrificed after 4 weeks (n = 10) or 8 weeks of healing (n = 10). The secondary aim consists in the comparative histological analysis bone healing in presence or not of the scaffold. To the best of our knowledge, there is no study in the literature investigating the *in vivo* performances of sphene ceramic scaffolds fabricated by DIW, therefore sample size calculation was based on similar studies using our same experimental model [56,60-62].

A sample size equal to 10 rats was calculated in order to demonstrate a mean difference of 15% in BV/TV between test and control side four weeks after surgery, with a power of 80% and a type I error equal to 5%. A further sample size of 10 rats was calculated in order to demonstrate a mean difference of 30% in BV/TV between test and control side 8 weeks after surgery, with a power of 80% and a type I error equal to 5%. Sample size calculation was performed using R 3.3 (R Foundation for Statistical Computing, Vienna, Austria).

Similarly to what described in **Chapter 3 - section 3.1.2**, the protocol and all the relevant documents for ethics committee approval were firstly submitted to the Body for Animal Welfare (Organismo Preposto al Benessere degli Animali - O.P.B.A.) of University of Padova and, then, forwarded to the Italian Ministry of Health for approval. The main preparatory phases of the project are summarized in **Figure 11**.

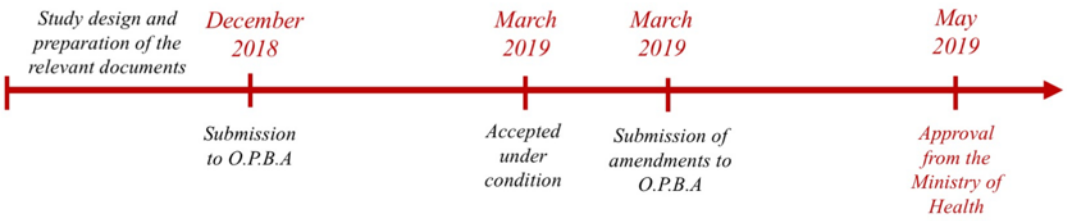

Figure 11. Timeline of project phases.

The project "Studio pilota sull'osteointegrazione di innesti di biomateriale ceramico 3D printed in un modello di calvaria di ratto" ("Pilot study of the osseointegration of 3D-printed bone substitutes in a rat calvaria defect model") received the authorization from

the Ministry of Health in May 2019 (Authorization **No. 402/2019-PR**) (see **Annex 2**) and the study is now ongoing.

Author contribution:

The candidate produced the 3D-printed scaffolds using already optimized parameters, contributed to the experimental work and data analysis and was the main contributor to writing the documents for the ethics committee approval.

Acknowledgments:

Scaffold production and characterization were performed in collaboration with Prof. Paolo Colombo, Prof. Enrico Bernardo and Dr. Hamada Elsayed, Centre for Mechanics of Biological Materials, Department of Industrial Engineering (DII), University of Padova, Italy.

Biological tests were performed in collaboration with Prof. Barbara Zavan, Head of the Regenerative Medicine Laboratory, Medical Sciences Department of Ferrara University, Italy.

References

1. Tonetti, M.S.; Hämmerle, C.H.; European Workshop on Periodontology Group C. Advances in bone augmentation to enable dental implant placement: Consensus Report of the Sixth European Workshop on Periodontology. J. Clin. Periodontol. 2008, 35, 168–172. DOI: 10.1111/j.1600-051X.2008.01268.x.

2. Chiapasco, M.; Casentini, P.; Zaniboni, M. Bone augmentation procedures in implant dentistry. Int. J. Oral Maxillofac. Implants 2009, 24, 237–259.

3. Merli, M.; Merli, I.; Raffaelli, E.; Pagliaro, U.; Nastri, L.; Nieri, M. Bone augmentation at implant dehiscences and fenestrations. A systematic review of randomised controlled trials. Eur. J. Oral Implantol. 2016, 9, 11–32.

4. Esposito, M.; Grusovin, M.G.; Felice, P.; Karatzopoulos, G.; Worthington, H.V.; Coulthard, P. The efficacy of horizontal and vertical bone augmentation procedures for dental implants - a Cochrane systematic review. Eur. J. Oral Implantol. 2009, 2, 167–184. DOI: 10.1007/978-3-642-05025-1_13.

5. Moore, W.R.; Graves, S.E., Bain, G.I. Synthetic bone graft substitutes. ANZ J. Surg. 2001, 71, 354–361. DOI: 10.1046/j.1440-1622.2001.02128.x.

6. Navarro, M.; Michiardi, A.; Castaño, O.; Planell, J.A. Biomaterials in orthopaedics. J. R. Soc. Interface. 2008, 5, 1137–1158. DOI: 10.1098/rsif.2008.0151.

7. Rezwan, K.; Chen, Q.Z.; Blaker, J.J.; Boccaccini, A.R. Biodegradable and bioactive porous polymer/inorganic composite scaffolds for bone tissue engineering. Biomaterials 2006, 27, 3413–3431. DOI: 10.1016/j.biomaterials.2006.01.039.

8. Felice, P.; Marchetti, C.; Iezzi, G.; Piattelli, A.; Worthington, H.; Pellegrino, G.; Esposito, M. Vertical ridge augmentation of the atrophic posterior mandible with interpositional bloc grafts: bone from the iliac crest vs. bovine anorganic bone. Clinical and histological results up to one year after loading from a randomized-controlled clinical trial. Clin. Oral Implants Res. 2009, 20, 1386–1393. DOI: 10.1111/j.1600-0501.2009.01765.x.

9. Myeroff, C.; Archdeacon, M. Autogenous bone graft: donor sites and techniques. J. Bone Joint Surg. Am. 2011, 93, 2227–2236. DOI: 10.2106/JBJS.J.01513.

10. Shalash, M.A.; Rahman, H.A.; Azim, A.A.; Neemat, A.H.; Hawary, H.E.; Nasry, S.A. Evaluation of horizontal ridge augmentation using beta tricalcium phosphate and demineralized bone matrix: A comparative study. J. Clin. Exp. Dent. 2013, 5, e253–259. DOI: 10.4317/jced.51244.

11. Dimitriou, R.; Jones, E.; McGonagle, D.; Giannoudis, P.V. Bone regeneration: current concepts and future directions. BMC Med. 2011, 9, 66. DOI: 10.1186/1741-7015-9-66.

12. Ma, H.; Feng, C.; Chang, J.; Wu, C. 3D-printed bioceramic scaffolds: From bone tissue engineering to tumor therapy. Acta Biomater. 2018, 79, 37–59. DOI: 10.1016/j.actbio.2018.08.026.

13. Brunello, G.; Sivolella, S.; Meneghello, R.; Ferroni, L.; Gardin, C.; Piattelli, A.; Zavan, B.; Bressan, E. Powder-based 3D printing for bone tissue engineering. Biotechnol. Adv. 2016, 34, 740–753. DOI: 10.1016/j.biotechadv.2016.03.009.

14. Markiewicz, M.R.; Bell, R.B. Modern concepts in computer-assisted craniomaxillofacial reconstruction. Curr. Opin. Otolaryngol. Head Neck Surg. 2011, 19, 295–301. DOI: 10.1097/MOO.0b013e328348a924.

15. Oka, K.; Murase, T.; Moritomo, H.; Goto, A.; Sugamoto, K.; Yoshikawa, H. Corrective osteotomy using customized hydroxyapatite implants prepared by preoperative computer simulation. Int. J. Med. Robot. 2010, 6, 186–193. DOI: 10.1002/rcs.305.

16. Yao, Q.; Wei, B.; Guo, Y.; Jin, C.; Du, X.; Yan, C.; Yan, J.; Hu, W.; Xu, Y.; Zhou, Z.; Wang, Y.; Wang, L. Design, construction and mechanical testing of digital 3D anatomical data-based PCL-HA bone tissue engineering scaffold. J. Mater. Sci. Mater. Med. 2015, 26, 5360. DOI: 10.1007/s10856-014-5360-8.

17. Yuan, H.; Xing, K.; Hsu, H.Y. Trinity of three-dimensional (3D) scaffold, vibration, and 3d printing on cell culture application: a systematic review and indicating future direction. Bioengineering 2018, 5, E57. DOI: 10.3390/bioengineering5030057.

18. Zhang, L.; Yang, G.; Johnson, B.N.; Jia, X. Three-dimensional (3D) printed scaffold and material selection for bone repair. Acta Biomater. 2019, 84, 16–33. DOI: 10.1016/j.actbio.2018.11.039.

19. Gmeiner, R.; Deisinger, U.; Schönherr, J.; Lechner, B.; Detsch, R.; Boccaccini, A.R.; Stampfl, J. Additive manufacturing of bioactive glasses and silicate bioceramics J. Ceram. Sci. Technol. 2015, 6, 75–86. DOI: 10.4416/JCST2015-00001.

20. Fiocco, L.; Elsayed, H.; Badocco, D.; Pastore, P.; Bellucci, D.; Cannillo, V.; Detsch, R.; Boccaccini, A.R.; Bernardo, E. Direct ink writing of silica-bonded calcite scaffolds from preceramic polymers and fillers. Biofabrication 2017, 9, 025012. DOI: 10.1088/1758-5090/aa6c37.

21. Elsayed, H.; Rincón Romero, A.; Ferroni, L.; Gardin, C.; Zavan, B.; Bernardo. E. Bioactive glass-ceramic scaffolds from novel 'inorganic gel casting' and sinter-crystallization. Materials 2017, 10, 171. DOI: 10.3390/ma10020171.

22. Parcianello, G.; Bernardo, E.; Colombo, P. Cordierite ceramics from silicone resins containing nano-sized oxide particle fillers. Ceram. Int. 2013, 39, 8893–8899. DOI: 10.1016/j.ceramint.2013.04.083.

23. Zocca, A.; Franchin, G.; Elsayed, H.; Gioffredi, E.; Bernardo, E.; Colombo, P. Direct ink writing of a preceramic polymer and fillers to produce hardystonite Ca2ZnSi2O7 bioceramic scaffolds J. Am. Ceram. Soc. 2016, 99, 1960–1967. DOI: 10.1111/jace.14213.

24. Paquien, I.J.; Galy, J.; Gérard, J.F.; Pouchelon, A. Rheological studies of fumed-silica–polydimethylsiloxane suspensions Colloids Surf. 2005, 260, 165–172. DOI: 10.1016/j.colsurfa.2005.03.003.

25. Gardin, C.; Bressan ,E.; Ferroni, L.; Nalesso, E.; Vindigni, V.; Stellini, E.; Pinton, P.; Sivolella, S.; Zavan, B. In vitro concurrent endothelial and osteogenic commitment of adipose-derived stem cells and their genomical analyses through comparative genomic hybridization array: novel strategies to increase the successful engraftment of tissue-engineered bone grafts. Stem. Cells Dev. 2012, 21, 767–777. DOI: 10.1089/scd.2011.0147.

26. Denizot, F.; Lang, R. Rapid colorimetric assay for cell growth and survival. Modifications to the tetrazolium dye procedure giving improved sensitivity and reliability. J. Immunol. Methods 1986, 89, 271–277. DOI: 10.1016/0022-1759(86)90368-6.

27. Gao, C.; Deng, Y.; Feng, P.; Mao, Z.; Li, P.; Yang, B.; Deng, J.; Cao, Y.; Shuai, C.; Peng, S. Current progress in bioactive ceramic scaffolds for bone repair and regeneration. Int. J. Mol. Sci. 2014, 15, 4714–4732. DOI: 10.3390/ijms15034714.

28. Katsimbri, P. The biology of normal bone remodelling. Eur. J. Cancer Care 2017, 26, e12740. DOI: 10.1111/ecc.12740.

29. Liu, H.; Li, D.; Zhang, Y.; Li, M. Inflammation, mesenchymal stem cells and bone regeneration. Histochem. Cell Biol. 2018, 149, 393–404. DOI: 10.1007/s00418-018-1643-3.

30. Elsayed, H., Brunello, G.; Gardin, C.; Ferroni, L.; Badocco, D.; Pastore, P.; Sivolella, S.; Zavan, B.; Biasetto, L. Bioactive sphene-based ceramic coatings on cpTi substrates for dental implants: an in vitro study. Materials 2018, 11, 2234. DOI: 10.3390/ma11112234.

31. Muthuraman, M.; Patil, K.C. Synthesis, properties, sintering and microstructure of sphene, CaTiSiO5: A comparative study of coprecipitation, sol–gel and combustion processes. Mater. Res. Bull. 1998, 33, 655–661. DOI: 10.1016/S0025-5408(98)00005-1.

32. Wu, C.; Ramaswamy, Y.; Chang, J.; Woods, J.; Chen, Y.; Zreiqat, H. The effect of Zn contents on phase composition, chemical stability and cellular bioactivity in Zn–Ca–Si system ceramics. J. Biomed. Mater. Res. B 2008, 87, 346–353. DOI: 10.1002/jbm.b.31109.

33. Wu, C.; Ramaswamy, Y.; Soeparto, A.; Zreiqat, H. Incorporation of titanium into calcium silicate improved their chemical stability and biological properties. J. Biomed. Mater. Res. A, 2008, 86, 402–410. DOI: 10.1002/jbm.a.31623.

34. Wu, C.; Chang, J. Degradation, bioactivity, and cytocompatibility of diopside, akermanite, and bredigite ceramics. J. Biomed. Mater. Res. B, 2007, 83, 153–160. DOI: 10.1002/jbm.b.30779.

35. Wu, C.; Chang, J.; Ni, S.; Wang, J. In vitro bioactivity of akermanite ceramics. J. Biomed. Mater. Res. A 2006, 76, 73–80. DOI: 10.1002/jbm.a.30496.

36. Wu, C.; Chang, J. A review of bioactive silicate ceramics. Biomed. Mater. 2013, 8, 032001. DOI: 10.1088/1748-6041/8/3/032001.

37. Han, P.; Wu, C.; Xiao, Y. The effect of silicate ions on proliferation, osteogenic differentiation and cell signaling pathways (WNT and SHH) of bone marrow stromal cells. Biomater. Sci. 2013, 1, 379–392. DOI: 10.1039/C2BM00108J.

38. Ramaswamy, Y.; Wu, C.; Dunstan, C.R.; Hewson, B.; Eindorf, T.; Anderson, G.I., Zreiqat, H. Sphene ceramics for orthopedic coating applications: an in vitro and in vivo study. Acta Biomater. 2009, 5, 3192–3204. DOI: 10.1016/j.actbio.2009.04.028.

39. Inomata, K.; Honda, M. Co-Culture of Osteoblasts and Endothelial Cells on a Microfiber Scaffold to Construct Bone-Like Tissue with Vascular Networks. Materials 2019, 12, 2869. DOI: 10.3390/ma12182869.

40. Black, C.R.; Goriainov, V.; Gibbs, D.; Kanczler, J.; Tare, R.S.; Oreffo, R.O. Bone tissue engineering. Curr. Mol. Biol. Rep. 2015, 1, 132–140. DOI: 10.1007/s40610-015-0022-2.

41. Pirraco, R.P.; Marques, A.P.; Reis, R.L. Cell interactions in bone tissue engineering. J. Cell. Mol. Med. 2010, 14, 93–102. DOI: 10.1111/j.1582-4934.2009.01005.x.

42. Grosso, A.; Burger, M.G.; Lunger, A.; Schaefer, D.J.; Banfi, A.; Di Maggio, N. It takes two to tango: coupling of angiogenesis and osteogenesis for bone

regeneration. Front. Bioeng. Biotechnol. 2017, 5, 68. DOI: 10.3389/fbioe.2017.00068.

43. Deb, S.; Mandegaran, R.; Di Silvio, L. A porous scaffold for bone tissue engineering/45S5 Bioglass derived porous scaffolds for co-culturing osteoblasts and endothelial cells. J. Mater. Sci. Mater. Med. 2010;21, 893–905. DOI: 10.1007/s10856-009-3936-5.

44. Herrmann, M.; Verrier, S.; Alini, M. Strategies to stimulate mobilization and homing of endogenous stem and progenitor cells for bone tissue repair. Front Bioeng. Biotechnol. 2015, 3, 79. DOI: 10.3389/fbioe.2015.00079.

45. Bianco, P.; Riminucci, M.; Gronthos, S.; Robey, P.G. Bone marrow stromal stem cells: nature, biology, and potential applications. Stem Cells 2001, 19 180–92. DOI: 10.1634/stemcells.19-3-180.

46. Wancket, L.M. Animal Models for evaluation of bone implants and devices: comparative bone structure and common model uses. Vet. Pathol. 2015, 52, 842–850. DOI: 10.1177/0300985815593124.

47. Fu, S.; Liu, W.; Liu, S.; Zhao, S.; Zhu, Y. 3D printed porous β-Ca(2)SiO(4) scaffolds derived from preceramic resin and their physicochemical and biological properties. Sci. Technol. Adv. Mater. 2018, 19, 495–506. DOI: 10.1080/14686996.2018.1471653.

48. Adel-Khattab, D.; Giacomini, F.; Gildenhaar, R.; Berger, G.; Gomes, C.; Linow, U.; Hardt, M.; Peleska, B.; Günster, J.; Stiller, M.; Houshmand, A.; Ghaffar, K.A.; Gamal, A.; El-Mofty, M.; Knabe, C. Development of a synthetic tissue engineered three-dimensional printed bioceramic-based bone graft with homogenously distributed osteoblasts and mineralizing bone matrix in vitro. J. Tissue Eng. Regen. Med. 2018, 12, 44–58. DOI: 10.1002/term.2362.

49. Vajgel, A.; Mardas, N.; Farias, B.C.; Petrie, A.; Cimões, R.; Donos, N. A systematic review on the critical size defect model. Clin. Oral Implants Res. 2014, 25, 879–893. DOI: 10.1111/clr.12194.

50. Muschler, G.F.; Raut, V.P.; Patterson, T.E.; Wenke, J.C.; Hollinger, J.O. The design and use of animal models for translational research in bone tissue engineering and regenerative medicine. Tissue Eng. B. 2010, 16, 123–145. DOI: 10.1089/ten.TEB.2009.0658.

51. Schmitz, J.P.; Hollinger, J.O. The critical size defect as an experimental model for craniomandibulofacial nonunions. Clin. Orthop. Relat. Res. 1986, 299–308. DOI:10.1097/00003086-198604000-00036.

52. Hollinger, J.O.; Kleinschmidt, J.C. The critical size defect as an experimental model to test bone repair materials. J. Craniofac. Surg. 1990, 1, 60–68. DOI: 10.1097/00001665-199001000-00011.

53. Pearce, A.I.; Richards, R.G.; Milz. S.; Schneider, E.; Pearce, S.G. Animal models for implant biomaterial research in bone: a review. Eur. Cell Mater. 2007, 13, 1–10. DOI: 10.22203/eCM.v013a01.

54. Poser, L.; Matthys, R.; Schawalder, P.; Pearce, S.; Alini, M.; Zeiter, S. A standardized critical size defect model in normal and osteoporotic rats to evaluate bone tissue engineered constructs. Biomed. Res. Int. 2014, 2014, 348635. DOI: 10.1155/2014/348635.

55. Gomes, P.S.; Fernandes, M.H. Rodent models in bone-related research: the relevance of calvarial defects in the assessment of bone regeneration strategies. Lab. Anim. 2011, 45, 14–24. DOI: 10.1258/la.2010.010085.

56. Zhang, H.; Mao, X.; Du, Z.; Jiang, W.; Han, X.; Zhao, D.; Han, D.; Li, Q. Three dimensional printed macroporous polylactic acid/hydroxyapatite composite scaffolds for promoting bone formation in a critical-size rat calvarial defect model. Sci. Technol. Adv. Mater. 2016, 17, 136–148. DOI: 10.1080/14686996.2016.1145532.

57. Bae, E.B.; Park, K.H., Shim, J.H.; Chung, H.Y., Choi, J.W.; Lee, J.J.; Kim, C.H.; Jeon, H.J.; Kang, S.S.; Huh. J.B. Efficacy of rhBMP-2 lLoaded PCL/β-TCP/bdECM scaffold fabricated by 3D printing technology on bone regeneration. Biomed. Res. Int. 2018, 2018, 2876135. DOI: 10.1155/2018/2876135.

58. Diomede, F.; Gugliandolo, A.; Cardelli, P.; Merciaro, I.; Ettorre, V.; Traini, T.; Bedini, R.; Scionti, D.; Bramanti, A.; Nanci, A.; Caputi, S.; Fontana, A.; Mazzon, E.; Trubiani, O. Three-dimensional printed PLA scaffold and human gingival stem cell-derived extracellular vesicles: a new tool for bone defect repair. Stem Cell Res. Ther. 2018, 9, 104. DOI: 10.1186/s13287-018-0850-0.

59. Yeom, H.; Blanchard, S., Kim, S.; Zunt, S.; Chu, T.M. Correlation between micro-computed tomography and histomorphometry for assessment of new bone formation in a calvarial experimental model. J. Craniofac. Surg. 2008, 19, 446–452. DOI: 10.1097/SCS.0b013e318052fe05.

60. Bartov, M.S.; Gromov, A.V.; Poponova, M.S.; Savina, D.M.; Nikitin, K.E.; Grunina, T.M.; Manskikh, V.N.; Gra, O.A.; Lunin, V.G.; Karyagina, A.S.; Gintsburg, A.L. Modern approaches to studies of new osteogenic biomaterials on the model of regeneration of critical-size cranial defects in rats. Bull Exp Biol Med. 2016, 162, 273–276. Erratum in: Bull Exp Biol Med. 2017, 162, 707.

61. Horváthy, D.B.; Vácz, G.; Toró, I., Szabó, T.; May, Z.; Duarte, M.; Hornyák, I.; Szabó, B.T.; Dobó-Nagy, C.; Doros, A., Lacza, Z. Remineralization of demineralized bone matrix in critical size cranial defects in rats: A 6-month follow-up study. J. Biomed. Mater. Res. B Appl. Biomater. 2016, 104, 1336–1342. DOI: 10.1002/jbm.b.33446.

62. Chamieh, F.; Collignon, A.M.; Coyac, B.R.; Lesieur, J.; Ribes, S.; Sadoine, J.; Llorens, A.; Nicoletti, A.; Letourneur, D.; Colombier, M.L.; Nazhat, S.N.; Bouchard, P.; Chaussain, C.; Rochefort, G.Y. Accelerated craniofacial bone regeneration through dense collagen gel scaffolds seeded with dental pulp stem cells. Sci. Rep. 2016, 6, 38814. DOI: 10.1038/srep38814.

Concluding Remarks and Future Perspectives

The main objective of the current work was to study a specific silicate-based bioactive ceramic, sphene, as implant coating material for titanium dental implants, both in terms of synthesis process and coating technology. The final goal consists in the use of the developed bioceramic coating as a safe and bioactive material within the clinical setting. Sphene-based ceramic coatings were successfully synthesized via polymer-derived ceramics route, using a silicone preceramic polymer containing nanosized active fillers as precursors for the formation of the desired ceramic phase. The airbrush coating technique was used for coating deposition. In order to verify the efficacy and the biocompatibility of this new biomaterial, it underwent both *in vitro* and *in vivo* animal investigations.

In vivo study in rat femurs demonstrated the biocompatibility of sphene-coated implants, which exhibited a similar healing pattern of uncoated implants used as control with an already optimized implant surface. Interestingly, no sign of inflammation was detected in presence of sphene, thus confirming the biocompatibility of the material.

The results of dissolution tests in Tris-HCl showed that the dissolution happened only during the first hours of soaking and then remained constant up to one week. Consistently, the comparison of coating thickness before and after implantation in rat femurs up to 28 days confirmed the stability of the coating.

Even though scratch test revealed good adhesion between the bioceramic coating and the substrate, the presence of delamination in some samples after 2 and 4 weeks of healing in rat femur was detected by micro-CT analysis.

Future developments of sphene-based coatings obtained in this project might be the increase of the amount of sphene in the coating composition and the improvement of the adhesion strength between the coating and the substrate, to be assessed by means of pull-off tests. Moreover, as screw-type implants of larger dimensions compared to the ones utilized in this rat femur model are commonly used in humans, it would be interesting to test screw-type sphene-coated implants in large animal study.

Concerning the bone scaffolds, sphene scaffolds were successfully 3D-printed by direct ink writing, starting from an ink made of a silicone preceramic polymer and nano-sized fillers. The printed scaffolds resulted fully composed of ceramic sphene phase, after ceramization at 1300 °C. Moreover, they exhibited highly ordered and interconnected porosity and presented a remarkable compressive strength. In addition, they showed a

pronounced ability to stimulate cell adhesion, proliferation and differentiation when cultured with ADSCs up to 28 days.

In the light of these encouraging results obtained in this preliminary *in vitro* phase, the rat calvarial critical size defect model will be used to evaluate the osteoconductive properties of these porous sphene ceramic scaffolds, before moving to larger animals for potential translation to human applications.

List of Publications Related to This Thesis

List of Published Articles:

- **Brunello G**, Elsayed H. Biasetto L. Bioactive Glass and Silicate-Based Ceramic Coatings on Metallic Implants: Open Challenge or Outdated Topic? Materials (Basel). 2019;12(18):2929. doi: 10.3390/ma12182929. (Brunello G. Co-corresponding author)

- Elsayed H, **Brunello G**, Gardin C, Ferroni L, Badocco D, Pastore P, Sivolella S, Zavan B, Biasetto L. Bioactive sphene-based ceramic coatings on cpTi substrates for dental implants: an in vitro study. Materials (Basel). 2018;11(11):E2234. doi: 10.3390/ma11112234.

Presentations given at conferences

a. Oral presentations:

- Elsayed H, **Brunello G**, Gardin C, Ferroni L, Sivolella S, Zavan B, Biasetto L. Sphene bioceramic coatings for dental and orthopedic implant: process study and coating characterization. Conference proceeding (Brunello G presenting author - oral communication at 31st International Conference on Surface Modification Technologies - SMT 31, Mons 5-7 July 2017)

b. Poster presentations

- Schiavon L, **Brunello G**, Elsayed H, Stellini E, Sivolella S, Biasetto L. Bioceramic bone substitutes in preclinical in vivo research: A systematic review. J Osseointegr 2019;11(2):182-3. (poster presented at XXVI Congresso Nazionale Collegio dei Docenti Universitari di discipline Odontostomatologiche, Naples 11-13 April 2019)

- **Brunello G**, Biasetto L, Elsayed H, Sibillin M, Zavan B, Sivolella S. Bioactive Sphene coatings for dental implant applications. J Osseointegr 2017; 9(1):98 (poster presented at XXIV Congresso Nazionale Collegio dei Docenti Universitari di discipline Odontostomatologiche, Milan 6-8 April 2017)

Annex 1

Ministero della Salute

DIREZIONE GENERALE DELLA SANITÀ ANIMALE E DEI FARMACI VETERINARI
UFFICIO 6

Autorizzazione n. 441/2018-PR

IL DIRETTORE GENERALE

Vista la domanda di autorizzazione del progetto di ricerca **"Studio pilota sull'osteointegrazione di impianti rivestiti in sphene in un modello di femore di ratto"**, ex articolo 31 del decreto legislativo 4 marzo 2014, n. 26, acquisita con prot. 965E9.20 del 14/03/2018, inoltrata dall'**Università degli Studi di Padova, sede legale in Padova, Via VIII Febbraio, 2**, per il tramite dell'Organismo preposto al benessere degli animali di cui all'articolo 25 del menzionato d.lgs. n. 26/2014, e finalizzata all'esecuzione di un progetto di ricerca come descritto nella documentazione allegata alla domanda;

Visto l'articolo 31, comma 1, del d.lgs. n. 26/2014, nel quale il Ministero della salute è individuato quale autorità competente al rilascio dell'autorizzazione all'esecuzione di progetti di ricerca che prevedono l'utilizzo di animali a fini scientifici secondo le finalità di cui all'articolo 5, comma 1, in continuità con la precedente normativa di cui al decreto legislativo 27 gennaio 1992, n. 116;

Visti gli articoli 12, 13, 14, 15, 16 e 17 del succitato d.lgs. n. 26/2014, che stabiliscono le modalità di utilizzazione degli animali nelle procedure condotte a fini scientifici;

Visti gli articoli 31, 32, 34 e 35, nonché gli Allegati IV, VI, VII e IX del d.lgs. n. 26/2014, che fissano i requisiti generali per il rilascio di autorizzazione per progetti di ricerca;

Vista la nota n. 18449 del 14/06/2018 con cui l'Istituto Superiore di Sanità ha comunicato l'esito positivo della valutazione tecnico-scientifica sul progetto di ricerca;

Considerato che ricorrono i requisiti stabiliti dal d.lgs. n. 26/2014 per il progetto da autorizzare;

Preso atto che il responsabile del progetto di ricerca, ai sensi dell'articolo 3, comma 1, lettera g) del d.lgs. n. 26/2014, è il **Dr. Stefano SIVOLELLA**;

Considerato che lo **stabilimento utilizzatore del Centro di Ricerca Interdipartimentale di Chirurgia Sperimentale, Università di Padova, sito in Padova, Via Giustiniani 2, è regolarmente autorizzato con decreto n. 102/2004-A del 30/09/2004, ai sensi del D.lgs. 116/92;**

Visto l'articolo 4, comma 2 e l'articolo 16 del decreto legislativo 30 marzo 2001, n. 165 e successive modifiche, recanti le funzioni dei dirigenti di uffici dirigenziali;

Responsabile del procedimento: Dr. Vincenzo Ugo SANTUCCI
Referenti: Zappulla - f.zappulla-esterno@sanita.it; Aleandri - g.aleandri-esterno@sanita.it

AUTORIZZA

1. **L'Università degli Studi di Padova, sede legale in Padova, Via VIII Febbraio, 2**, all'esecuzione del progetto di ricerca ex articolo 31 del decreto legislativo 4 marzo 2014, n. 26, in conformità a quanto indicato nella richiesta di autorizzazione citata in premessa ed, in particolare, con riferimento a:

"Studio pilota sull'osteointegrazione di impianti rivestiti in sphene in un modello di femore di ratto"

2. Il **Dr. Stefano SIVOLELLA** quale responsabile del progetto di ricerca, ai sensi dell'articolo 3, comma 1, lettera g) del d.lgs. n. 26/2014;

3. L'**Università degli Studi di Padova, sede legale in Padova, Via VIII Febbraio, 2**, all'esecuzione del progetto di ricerca di cui al punto 1 nello **stabilimento utilizzatore del Centro di Ricerca Interdipartimentale di Chirurgia Sperimentale, Università di Padova, sito in Padova, Via Giustiniani 2, è regolarmente autorizzato con decreto n. 102/2004-A del 30/09/2004, ai sensi del D.lgs. 116/92**.

Alla conclusione del progetto di ricerca, il responsabile di cui all'articolo 3, comma 1, lettera g) del d.lgs. n. 26/2014 dovrà inviare alla scrivente Amministrazione la documentazione necessaria ai fini della valutazione retrospettiva, come previsto dall'articolo 32 del citato decreto.

La presente autorizzazione ha una durata di ventiquattro mesi e può essere revocata secondo quanto previsto dall'articolo 31, comma 15 del d.lgs. n. 26/2014.

20 GIU 2018

IL DIRETTORE GENERALE
(Dott. Silvio BORRELLO)

Responsabile del procedimento: Dr. Vincenzo Ugo SANTUCCI
Referenti: Zappulla - f.zappulla-esterno@sanita.it; Aleandri - g.aleandri-esterno@sanita.it

Annex 2

Ministero della Salute

DIREZIONE GENERALE DELLA SANITÀ ANIMALE E DEI FARMACI VETERINARI
UFFICIO 6

Autorizzazione n. 402 **/2019-PR**

IL DIRETTORE GENERALE

Vista la domanda di autorizzazione del progetto di ricerca **"Studio pilota sull'osteointegrazione di innesti di biomateriale ceramico 3D printed in un modello di calvaria di ratto"**, ex articolo 31 del decreto legislativo 4 marzo 2014, n. 26, acquisita con prot. 965E9.25 del 02/04/2019, inoltrata dall'**Università degli Studi di Padova, sede legale in Padova, Via VIII Febbraio, 2**, per il tramite dell'Organismo preposto al benessere degli animali di cui all'articolo 25 del menzionato d.lgs. n. 26/2014, e finalizzata all'esecuzione di un progetto di ricerca come descritto nella documentazione allegata alla domanda;

Visto l'articolo 31, comma 1, del d.lgs. n. 26/2014, nel quale il Ministero della salute è individuato quale autorità competente al rilascio dell'autorizzazione all'esecuzione di progetti di ricerca che prevedono l'utilizzo di animali a fini scientifici secondo le finalità di cui all'articolo 5, comma 1, in continuità con la precedente normativa di cui al decreto legislativo 27 gennaio 1992, n. 116;

Visti gli articoli 12, 13, 14, 15, 16 e 17 del succitato d.lgs. n. 26/2014, che stabiliscono le modalità di utilizzazione degli animali nelle procedure condotte a fini scientifici;

Visti gli articoli 31, 32, 34 e 35, nonché gli Allegati IV, VI, VII e IX del d.lgs. n. 26/2014, che fissano i requisiti generali per il rilascio di autorizzazione per progetti di ricerca;

Vista la nota n. 16261 del 28/05/2019 con cui l'Istituto Superiore di Sanità ha comunicato l'esito positivo della valutazione tecnico-scientifica sul progetto di ricerca;

Considerato che ricorrono i requisiti stabiliti dal d.lgs. n. 26/2014 per il progetto da autorizzare;

Preso atto che il responsabile del progetto di ricerca, ai sensi dell'articolo 3, comma 1, lettera g) del d.lgs. n. 26/2014, è il **Prof. Stefano SIVOLELLA**;

Considerato che **lo stabilimento utilizzatore del Centro di Ricerca Interdipartimentale di Chirurgia Sperimentale, Università di Padova, sito in Padova, Via Giustiniani, 8, è regolarmente autorizzato con decreto n. 102/2004-A del 30/09/2004, ai sensi del D.lgs. 116/92**;

Visto l'articolo 4, comma 2 e l'articolo 16 del decreto legislativo 30 marzo 2001, n. 165 e successive modifiche, recanti le funzioni dei dirigenti di uffici dirigenziali;

Responsabile del procedimento: Dr. Vincenzo Ugo SANTUCCI
Referente: G. Aleandri - g.aleandri-esterno@sanita.it

AUTORIZZA

1. L'**Università degli Studi di Padova, sede legale in Padova, Via VIII Febbraio, 2**, all'esecuzione del progetto di ricerca ex articolo 31 del decreto legislativo 4 marzo 2014, n. 26, in conformità a quanto indicato nella richiesta di autorizzazione citata in premessa ed, in particolare, con riferimento a:

"Studio pilota sull'osteointegrazione di innesti di biomateriale ceramico 3D printed in un modello di calvaria di ratto"

e all'impiego di un numero complessivo di 20 ratti, come indicato al punto 10 dell'Allegato VI.

2. Il **Prof. Stefano SIVOLELLA** quale responsabile del progetto di ricerca, ai sensi dell'articolo 3, comma 1, lettera g) del d.lgs. n. 26/2014;

3. L'**Università degli Studi di Padova, sede legale in Padova, Via VIII Febbraio, 2**, all'esecuzione del progetto di ricerca di cui al punto 1 **presso lo stabilimento utilizzatore del Centro di Ricerca Interdipartimentale di Chirurgia Sperimentale, Università di Padova, sito in Padova, Via Giustiniani, 8, regolarmente autorizzato con decreto n. 102/2004-A del 30/09/2004, ai sensi del D.lgs. 116/92**.

Alla conclusione del progetto di ricerca, il responsabile di cui all'articolo 3, comma 1, lettera g) del d.lgs. n. 26/2014 dovrà inviare alla scrivente Amministrazione la documentazione necessaria ai fini della valutazione retrospettiva, come previsto dall'articolo 32 del citato decreto.

La presente autorizzazione ha una durata di ventiquattro mesi e può essere revocata secondo quanto previsto dall'articolo 31, comma 15 del d.lgs. n. 26/2014.

PER IL DIRETTORE GENERALE
(Dott. Silvio BORRELLO)
IL DIRIGENTE
(Dott.ssa Marina BELLUCCI)

30 MAG 2019

Responsabile del procedimento: Dr. Vincenzo Ugo SANTUCCI
Referente: G. Aleandri - g.aleandri-esterno@sanita.it